General Disclaimer

One or more of the Following Statements may affect this Document

- This document has been reproduced from the best copy furnished by the organizational source. It is being released in the interest of making available as much information as possible.

- This document may contain data, which exceeds the sheet parameters. It was furnished in this condition by the organizational source and is the best copy available.

- This document may contain tone-on-tone or color graphs, charts and/or pictures, which have been reproduced in black and white.

- This document is paginated as submitted by the original source.

- Portions of this document are not fully legible due to the historical nature of some of the material. However, it is the best reproduction available from the original submission.

Produced by the NASA Center for Aerospace Information (CASI)

GPO PRICE $ _____

CFSTI PRICE(S) $ _____

Hard copy (HC) 3.00

Microfiche (MF) .65

ff 653 July 65

FACILITY FORM 602

N68-23721 (ACCESSION NUMBER) (THRU)

34 (PAGES) 1 (CODE)

NASA-CR-62072 (NASA CR OR TMX OR AD NUMBER) 07 (CATEGORY)

SCATTEROMETER DATA ANALYSIS PROGRAM

FINAL REPORT

REPORT NO. 57667-2

21 SEPTEMBER 1967

PREPARED FOR

NASA MANNED SPACECRAFT CENTER

HOUSTON, TEXAS

UNDER CONTRACT NO. NAS 9-6059

Prepared by: W. L. Floyd
W. L. Floyd
Project Engineer

Approved by: R F Chadwick
R. F. Chadwick
Program Manager

LIBRARY COPY

OCT 17 1967

MANNED SPACECRAFT CENTER
HOUSTON, TEXAS

RYAN AERONAUTICAL COMPANY
5650 KEARNY MESA ROAD
SAN DIEGO, CALIFORNIA 92017

MAY 1968
RECEIVED
NASA STI FACILITY
INPUT BRANCH



TABLE OF CONTENTS

SECTION	TITLE	PAGE
1.0	INTRODUCTION	1
1.1	SCOPE	2
1.2	OBJECT	3
1.3	LAND RADAR REFLECTIVITY MODEL	4
1.4	MODELING CONSIDERATIONS	6
1.4.1	Applicable Models	8
1.4.2	Simulation	9
1.4.3	Specular and Scatter Concepts	10
1.4.4	Parameters	11
1.4.5	Errors in Models	13
1.5	EXTENT OF MODEL DEVELOPMENT	14
2.0	TECHNICAL DISCUSSION	19
2.1	RYAN REDOP TECHNIQUES	19
2.1.1	Derivation of Signal Return Equations	26
2.1.2	Predicted Results	30
2.1.3	System Equations and Sign Sense Technique	31
2.2	A DISCUSSION OF SPECTRUM ANALYZERS	37
2.3	THE EFFECTS OF FILTERING AND DETECTION ON THE STATISTICAL PROPERTIES OF A CW SIGNAL	41

TABLE OF CONTENTS (Continued)

SECTION	TITLE	PAGE
2.4	ERROR ANALYSIS	52
2.4.1	Discussion of Errors	53
2.4.2	Summary of Error Analysis	76
2.5	ANALYSIS OF NEAR-VERTICAL RETURN	84
2.6	EQUAL BEAMWIDTH EQUATIONS	86
2.7	METHODS OF OBTAINING THE SLOPE OF THE σ_o CURVES	88
2.8	FERRITE MODULATOR (BASIC CALIBRATOR)	92
2.9	TRANSFORMATION OF EVANS AND PETTENGILL DATA	103
3.0	SYSTEM DESCRIPTION	107
3.1	FUNCTIONAL DESCRIPTION	107
3.1.1	Operational Characteristics	107
3.2	EQUIPMENT DESCRIPTION	108
3.2.1	Antennas	109
3.2.2	Microwave Plumbing	111
3.2.3	Klystron	111
3.2.4	Blower	112
3.2.5	Microwave Detectors	112
3.2.6	Ferrite Modulator	113
3.2.7	Power Monitor Crystal	113

TABLE OF CONTENTS (Continued)

SECTION	TITLE	PAGE
3.2.8	Control Panel	114
3.2.9	Preamplifiers	114
3.2.10	Boost Amplifier	115
3.2.11	Klystron Power Supply	116
3.2.12	Monitoring Voltmeter	116
3.2.13	Audio Oscillator	117
3.2.14	Tape Recorder	117
4.0	DATA REDUCTION	132
4.1	SPECTRUM ANALYSIS	132
4.2	DIGITAL SPECTRUM ANALYSIS	137
4.3	ANALOG ANALYSIS EQUATIONS	139
4.4	DIGITAL COMPUTER PROGRAMS	143
4.4.1	Digital Computer Program Requirements	143
4.4.2	Basic Computer Program	158
4.4.3	Ryan Advanced Computer Program	163
4.4.4	Advanced RF Reflectivity Computer Program	179
4.5	SCATTEROMETER DATA TABLES	200
5.0	DATA ANALYSIS	208
5.1	SCATTEROMETER DATA ANALYSIS TECHNIQUES	209

TABLE OF CONTENTS (Continued)

SECTION	TITLE	PAGE
5.2	TERRAIN CHARACTERISTICS OF SCATTEROMETER TEST AREAS	211
5.3	LUNAR ANALOG DATA	227
5.4	OTHER SOURCES OF REFLECTIVITY DATA	228
5.5	WATER DATA	230
5.6	THEORETICAL MODELS	254
5.7	SEPARATION OF SPECULAR AND SCATTER COMPONENTS	264
5.8	BEST FIT CURVES	276
6.0	SUMMARY	283
6.1	REFINEMENTS IN THE NEW LMLR MODEL	284
7.0	CONCLUSIONS AND RECOMMENDATIONS	290

APPENDICES

A	GLOSSARY OF GEOLOGIC TERMS	293
B	LIST OF SYMBOLS	295
C	SYSTEM TEST PROCEDURES	298
C.1	PREFLIGHT PROCEDURE	299
C.2	IN-FLIGHT PROCEDURE	303
C.2.1	Turn On Procedure	303
C.2.2	Data Acquisition Procedure	304

TABLE OF CONTENTS (Continued)

APENDICES	TITLE	PAGE
C.3	POST-FLIGHT CHECK	305
C.4	OPERATIONAL GROUND CHECK	305
C.4.1	List of Test Equipment	306
C.4.2	Preliminary Connection of Test Equipment	306
C.4.3	Preliminary Settings of Equipment	307
C.4.4	Operational Ground Check Procedure	307
C.5	IN-FLIGHT PREVENTIVE MAINTENANCE	310
C.6	PERIODIC MAINTENANCE	310
C.7	PRE-MISSION TESTS	311

REFERENCES 314

LIST OF ILLUSTRATIONS

FIGURE	TITLE	PAGE
A1	Comparison of Measured Data to LMLR Model	5
1	Comprehensive Reflectivity Model as an Assembly of σ_0 Plots Reflectivity	16
2	Ryan REDOP Technique	21
3	Redop Scatterometer Block Diagram	22
4	Typical Overland Frequency Spectrum	23
5	Airborne System Block Diagram	31
6	Microwave Mixer Signal and Noise Density Versus Frequency	32
7	Narrow Band Power Spectral Analyzer Block Diagram	38
8	Discrete Frequency Spectrum Analyzer Block Diagram	40
9	Narrow Band Cross Power Spectral Analyzer Block Diagram	42
10	Analog Analysis Block Diagram	44
11	Coordinate Transformation	44
12	Rayleigh Distribution	44
13	Effect of Measured Signal-to-Noise Ratio upon Accuracy of Measured Signal Signal-to-Noise Ratio	51
14	Antenna Reference Axes	62
15	Photo Panel Reading Error	82
16	Velocity Sensor Reading Error	83
17	H-Plane and E-Plane Cross Sections	86

LIST OF ILLUSTRATIONS (continued)

FIGURE	TITLE	PAGE
18	Best Fit Method Block Diagram	89
19	Average Slope Method	91
20	H Vector Component Rotation with Propogation	94
21	Ferrite Isolator	94
22	H and E Vectors for The TE_{10} Propogation Mode	95
23	Relationship Between Incidence Angle And Delay Time	104
24	H-Plane Antenna Pattern	119
25	E-Plane Antenna Pattern	120
26	Redop Antenna	121
27	Microwave Plumbing	121
28	Scatterometer Calibration Levels Using KM-4 Ferrite Modulator	122
29	Redop Control Panel	123
30	Redop Control Panel Schematic	124
31	Redop Control Panel Schematic	125
32	Hushed Transistor Amplifier	126
33	Preamplifier Schematic	127
34	Model 121A Amplifier Schematic	128
35	Klystron Power Supply	129
36	Klystron Filament Supply	130

LIST OF ILLUSTRATIONS (continued)

FIGURE	TITLE	PAGE
37	Klystron High Voltage Power Supply	131
38	Sweeping Filter Spectrum Analysis	134
39	Analog Parallel Filter Spectrum Analysis	136
40	System Geometry	141
41	Determination of Resolution Cell Size	141
42	Effect of Irregular Ground on Resolution Cell	148
43	Determination of Point Where Beam Intersects Ground	148
44	Calculation of Climb or Glide Angle	156
45	Relation Between Ground Cell and Air Cell	165
46	Tape Data Time for Intermediate Incidence Angles	168
47	Relating θ_{max} To Ground Cell	186
48	Finding Intermediate Angle Radar Data Tape Times	188
49	Finding Distance and Time Adjustment to Correct Nominal Angles	190
50	Time Table - Partially Filled	193
51	Resolution Cell Size and Time Defined at 30^{o}	194
52	Generalized Desired Analog and Digital Tape Formats for Radar Data Tapes	196
53	Broken Lava - Photograph	218

LIST OF ILLUSTRATIONS (continued)

FIGURE	TITLE	PAGE
54	Sunset Crater Cinder Area - Photograph	220
55	Ambog Crater Lava Flow - Photograph	222
56	Pisgah Crater Northern Lava Flow - Photograph	224
57	Pisgah Crater Southern Lava Flow - Photograph	225
58	Lavic Dry Lake - Photograph	226
59	White Sands Missile Range Desert with Dunes - Photograph	232
60	White Sands Missile Range Desert - Photograph	233
61	White Sands Missile Range AFSWC Site - Photograph	234
62	White Sands Missile Range SS Scat Site - Photograph	235
63	White Sands Missile Range Pearl Site - Photograph	236
64	White Sands Missile Range Salt Site - Photograph	237
65	Pisgah Crater Area Desert - Photograph	238
66	Pisgah Crater Area Lavic Dry Lake - Photograph	239
67	White Sands Missile Range Lava - Photograph	240
68	San Francisco Volcanic Fields Broken Lava - Photograph	241
69	Pisgah Crater Area Lava Flow - Photograph	242

LIST OF ILLUSTRATIONS (continued)

FIGURE	TITLE	PAGE
70	San Francisco Volcanic Fields Alluvium - Photograph	243
71	Sunset Crater Area Cinder Hills - Photograph	244
72	Amboy Crater Area Sand Filled Lava Flow - Photograph	245
73	Comparison of Lunar Analog to Lunar Reflectivity Data	246
74	Incidence Angle in Degrees	247
75	University of New Mexico Reflectivity Data	248
76a	Comparison of Acoustical Data with Scatterometer Data (Rough Sand)	249
76b	Comparison of Acoustical Data with Scatterometer Data (Slightly Rough Sand)	250
76c	Comparison of Acoustical Data with Scatterometer Data (Smooth Plywood)	251
77	Comparison of Measured Data to LMLR Model	252
78	Mission 20, Flight 2, (8 Runs), Bermuda Area	253
79	Terrain Prediction Through R and K Values	262
80	Terrain Prediction	263
81	Least Squares Curve Fit	280
82	Power Function Curve Fit	281

LIST OF ILLUSTRATIONS (continued)

FIGURE	TITLE	PAGE
83	Power Function Curve Fit on Semi-Log Grid	282
84	Range of Scatterometer Data	286
85	Comparison of Lunar Analog to Lunar Reflectivity Data	287
86	Comparison of Measured Data to LMLR Model	288
87	Surveyor 1 Photos of Lunar Surface	289
88	Ryan Redop System Block Diagram	300
89	Redop Mission Report Sheet	301
90	Redop Operational Ground Check Sheet	309
91	Redop Calibration Log	312

LIST OF TABLES

TABLE	TITLE	PAGE
I	Errors In The Magnitude of Sigma Zero	78
II	Errors In Incidence Angle	80
III	Indirectly Related Errors	81
IV	K_{BW} For Several Values of Incidence Angle	142
V	Composite Roll-Off Function For Over Land Missions	201
VI	Composite Roll-Off Function For All Over Water Missions (Excluding Mission 20)	203

LIST OF TABLES (continued)

TABLE	TITLE	PAGE
VII	Composite Roll-Off Function For Mission 20 Only	203
VIII	Scatterometer Antenna Pattern Factor (Fore)	204
IX	Scatterometer Antenna Pattern Factor (Aft)	206
X	Lunar Analog Sites And The Lunar Surface	213

SECTION I

INTRODUCTION

Early in the Apollo Program, the plan for a radar directed lunar descent focused attention upon two important but relatively unknown areas of concern. The first was related to radar acquisition of sufficiently detailed glide path information for a lunar descent in the absence of active terrain based sources of information. The second was concerned with the radar reflectivity characteristics of lunar terrain. It became apparent that a radar design program was essential, and that another program to accumulate a library of backscattering information on lunar-like terrain would be essential for assisting the radar designers.

A 13.3 GHz radar doppler (REDOP) Scatterometer was installed in a Convair 240 aircraft at the Manned Space Center (MSC). During the 1966-1967 fiscal years, the Scatterometer was flown over various sites in the continental United States selected to simulate the lunar terrain.

Specific techniques developed for use in the MSC RF Reflectivity Program are unique in many respects. The program represents the first time that scattering data has been gathered at all angles of incidence simultaneously for a known and identifiable terrain resolution element. Each resolution element is characterized by a plot of the radar backscattering cross-section (σ_o) versus incidence angle (θ). The precise scattering envelope for a recognizable

resolution element, coupled with known geophysical characteristics of the terrain, provides a wealth of scientific data.

1.1 SCOPE

The primary purpose of the RF Reflectivity Program was to provide measurements of the backscattering coefficient per unit surface area σ_o for various types of earth terrain. The absolute magnitude and angular dependence of the backscattering cross-section per unit surface area $\sigma_o(\theta)$ is measured by relating the echo power density for each Doppler frequency to its respective incidence angle.

The accuracy and altitude capability of radar for use in surface track systems depends upon surface reflectivity characteristics. (For a rough surface, it is usually sufficient to discuss the values of σ_o as functions of its pertinent variables to describe surface reflectivity.) Therefore, another objective of the reflectivity program was to learn as much as possible about the reflectivity characteristics of various earth surfaces. This information will aid in the design and evaluation of radar for earth, lunar, and planetary missions. The reflectivity program included the following areas of study:

- Reflectivity of various types of surfaces including sand, desert, and volcanic formations.
- Reflectivity as a function of time for a given surface.
- Reflectivity as a function of altitude above the surface.

- The reflectivity signature of various types of terrain discontinuities, and the possible use of this information for selection of a landing site.

The data obtained from this study can be used by the space radar designer to infer the absolute value of radar reflectivity of the surface of the moon and planets. The reflectivity data will aid in the determination of the Landing Radar system's altitude capability and will assist in the evaluation of the sidelobe effects. In addition, the reflectivity data will be used to determine the accuracy compensations which must be provided in the radar set to correct for terrain bias and altitude effects. These data can also be used in compiling error budgets for assignment to uncompensated terrain bias effects. Future study will also provide an estimate of the fluctuation of the terrain bias characteristics as a function of time. Presently, only the relatively long-time average reflectivity characteristic is available to the radar designers.

1.2 OBJECT

One object of the RF Reflectivity Program is to provide a reflectivity model for the LM Landing Radar. The system performance of the LM Landing Radar is analyzed by computer programs: a terrain reflectivity model is one input to the program. The signal power calculations, sidelobe levels, and terrain bias errors are directly

calculated from the antenna beam pattern, flight trajectory, and the reflectivity model. In addition, system altitude performance depends directly upon signal power return; thus, a valid reflectivity model is vital to the LM Landing Radar.

1.3 LAND RADAR REFLECTIVITY MODEL

The high altitude* Landing Radar Reflectivity Model, given by the average of all (four $\sigma_o(\theta)$ plots) of the lunar analog data, is presented by Figure A1. This reflectivity model, or a plot of $\sigma_o(\theta)$ for vertical polarization, shows good agreement with lunar radar measurements by Evans and Pettengill and the Surveyor I and III Spacecrafts. The σ_o values for all four sources of measured data were significantly higher than the σ_o values for the present Landing Radar Reflectivity Design Model. The procedure, methods, and equipment required for producing σ_o lunar analog plots, as well as plots of other surfaces of interest to the Principal Investigators, i.e., farmland and sea, are given in Sections 2-5.

Section 2 presents the working REDOP system equations and various analyses of the data-taking and data-reduction process.

Section 3 is a discussion of the pertinent REDOP system hardware and includes the details about system calibration.

---

* For the purpose of this report, high altitude refers to altitudes above 1,000 feet. A program is currently being pursued which will establish lunar reflectivity characteristics for altitudes below 1,000 feet.

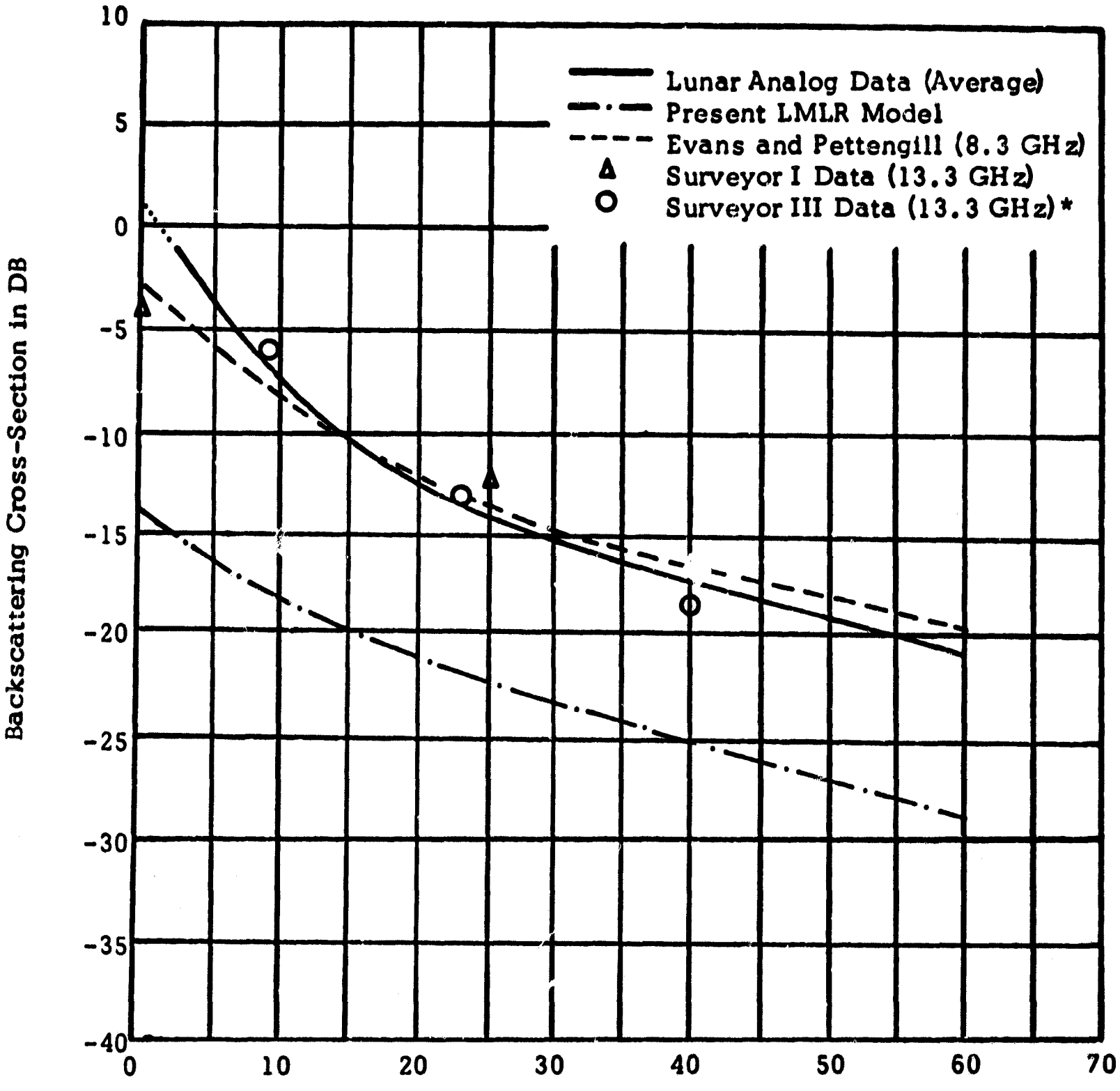


Figure A1 Comparison of Measured Data to LMLR Model

Section 4 is a description of present and future data reduction processes including the digital computer program.

Section 5 presents representative data samples of the lunar analog reflectivity measurements. In addition, possible applicable theoretical models for the study of various lunar-like terrains are summarized. Photographs of the lunar-like terrains and their corresponding ground truth information are displayed.

Section 6 is a summary of the data that was obtained during this program, and Section 7 presents the recommended areas for further study.

Appendices A, B, and C present a Glossary of the geologic terms used in this report, a definition of symbols, and REDOP system test procedures, respectively.

1.4 MODELING CONSIDERATIONS

For the design of a radar with return signals from a discrete target or extensive rough surface area, the total return power can be computed from an appropriate mathematical model (usually the radar equation). For discrete targets, the backscattering cross-section has been accurately determined for a number of wavelengths for a large number of different shapes. For the deterministic or statistical large rough surface, computation of the total received power for a pulse or continuous-wave radar system is largely dependent upon

the selection of a σ_o from an inadequate amount of published σ_o values. This condition is further aggravated when one realizes that σ_o is a function of a large number of pertinent variables: wavelength, altitude, angle of incidence, etc. In contrast, the parameters of the radar equation, transmitted power gain, etc., are easily controllable and amenable to straightforward laboratory or field calibrations except for σ_o and, possibly, the radar range R.

The designer of a lunar landing radar, or altimeter, is invariably faced with the question of what is the correct $\sigma_o(\theta)$ (including the standard deviation) to use with a particular terrain? It is soon learned that a very limited amount of reliable radar backscattered data from the moon is available either from experiment (use of probes and earth-based radar) or from theory. Because of the limited validated data available to the engineer, conjectures and estimates are relied upon for the analysis or design of a radar. It is interesting to note that even such limited information utilized in a mathematical model has proven to be of value. The fact remains, however, that sufficient models of σ_o for the required terrain types are still not available to provide the comprehensive foundation necessary for R & D.

Wavelength, polarization, and altitude are but a few of the variables which must be considered in greater extent in experimental programs before a sufficiently complete set of σ_o are generated for model requirements.

1.4.1 Applicable Models

Because of the complexity of the backscattering surface, either for land or sea, a number of different models have been proposed by various researchers. On nearly all models, one has control over the type of radar to be used but usually not in picking out the type of terrain over which the radar is to be operated. Usually, in the final analysis, σ_o (as functions λ, θ, and polarization) is the total model sought for analyzing a specific radar, and the information provided is usually found sufficient to define the upper and lower bounds of the radar. To date, a large variety of models have been produced and applied to the study of radar systems and are tailored to include some of the salient features of the radar system.

(1) Mathematical Models

Simple analytical expressions have been found adequate for the analysis of certain backscattering surfaces. Lambert's cosine law for a diffuse surface has figured predominantly in many studies.

- Extensive areas, such as the oceans, which have a periodic surface structure, require more sophisticated models which include the pronounced effects experienced by different polarizations.
- The surfaces of the moon and earth are extremely complex in structure and composition and are categorized

as statistically rough surfaces for modeling. Results obtained from the application of such models are expressed in some of the following statistical terms: (1) average scattering heights and slopes of the terrain, (2) variance of the scattered power, (3) power spectral densities, and (4) scattering element height-spatial autocorrelation functions.

Such models of a randomly varying surface provide the designer with statistical and not discrete-valued parameters for resolving the radar problem. Consequently, care must be exercised in the application of the statistical model if the desired information is to be obtained within a so-called "statistical" resolution capability. Such applications call for additional supporting information obtained from photographs and visual inspection of the terrain along with an analysis of the physical aspects of the terrain. This supporting information has been defined as "ground truth" and is vital for increasing the usefulness of the model.

1.4.2 Simulation

Significant radar backscattering results have been obtained through simulation. Complete radar problems have been simulated by electrical acoustical, and computer techniques. To increase the confidence level

of purely mathematical model outputs, correlation and comparison of simulated results are helpful. The maximum degree of confidence is established by developing a model in the real world from backscattered radar data obtained over the terrain of interest in this case, lunar-like terrains; however, data can be obtained more rapidly and generally at a reduced expense by simulation. Such data can provide early inputs to the estimate and development of a proposed mathematical model.

1.4.3 Specular and Scatter Concepts

Surface roughness must be defined in terms of the radar exploring wavelength. A seemingly rough surface, by visual observation, becomes relatively smooth at an exploring wavelength of 1 meter. Also, if the surface is perfectly smooth (optically), homogeneous, and of infinite extent, the method of images can be used for computing the received power.

Beyond some transition, which is a function of scatterer heights, the angle of incidence, and the wavelength, the return is based upon a specular or quasi-specular theory as compared to a scattering theory. Because of the lack of a clear-cut transition (based usually upon theory) between these two regions of radar return, a host of models have been developed in the past to separate the specular and scatter regions. These models are discussed in Section 5.

1.4.4 Parameters

A mathematical, or physical model (simulated), of the back-scattering terrain is usually developed to serve two very important design functions:

- to provide a means of identifying the type of scattering surface and possibly some of its physical characteristics.
- to provide inputs (parametric data) for the evaluation of radar systems.

The assembly or construction of a model can follow many different paths and appear in as many different forms. Consider the general integral form of the radar equation,

integral form of the radar equation,

$$P_R = \int \frac{P_t G^2(\theta, \phi) \lambda^2 \sigma_o(\theta, \phi)\, dR}{32 \pi^2 R^3}$$

which in itself can be considered a mathematical model. In this model, it will be assumed that all the parameters are well-behaved and well-defined (as verified by laboratory measurements), except for the parameter $\sigma_o(\theta, \phi)$. For a statistical model σ_o (as it is usually presented or modeled), which is usually dictated by a rough surface of a random nature, includes such regular parameters as wavelength and angle of incidence, and the more complex statistical parameters associated with the surface: (1) standard deviation of the scatterer heights, (2) standard deviation of scatterer slopes, and (3) the

autocorrelation function. However, the bulk of published data are not too involved models of σ_o and are functions of the angle of incidence only.

What is urgently needed by the engineering and scientific community is a complete library of parametric plots of σ_o as functions of the angle of incidence, wavelength, and altitude, and variations on the parameters of polarization, scatterer-height arrangements, coupling, seasonal variations, etc., taken over the same area. Unfortunately, it is readily apparent that σ_o data have been compiled independently by different groups in the past for a large number of terrain types; consequently, comparisons, correlations, or extrapolations between the σ_o plots becomes difficult and questionable. No standardization was attempted, and in most cases only the variable θ was adequately considered. Very little dynamic data (taken with an aircraft) were collected for altitudes less than 1,000 feet over rough terrain, especially lunar-like surfaces; therefore, there is a pronounced gap in the low-altitude region of data. Another gap is apparent for long-wavelength σ_o plots because data has been collected mainly in the microwave region with very little taken at VHF and UHF.

As a start for covering the gap for σ_o plots of rough surfaces under 1,000 feet, two models of σ_o as functions of altitude have been postulated by both Ryan and MIT. Clearly, due to the extremely complex nature of the model (quasi-specular terrain, sidelobe effects,

beamwidth limiting, and correlation effects), experimental data are absolutely essential for validation and refinement of the postulated models.

Ground truth will have to be carefully correlated with the return signals for establishing the validity of these models. Without ground truth information, the probability of breaking out the values of the modeling parameters such as $\frac{\sigma}{\lambda}$ (normalized scatterer height deviation) and $\frac{\sigma}{L}$ (scatter-height spatial separation ratio, slope) becomes extremely low.

1.4.5 Errors in Models

The best radar data-gathering program is only as good as calibrations and control that go into the entire radar system, the recording of the data, and the data-reduction program. For example, an undetected fixed error in power, gain, etc., results in a fixed bias in σ_o plots. Thus, an error accounting must become part of any data-gathering or model validation program. Such an error analysis of the Ryan Scatterometer is presented later. Publishing of the calibration procedure and error analysis greatly increases the confidence level of the data and allows meaningful correlations to be made with data from outside programs.

1.5 EXTENT OF MODEL DEVELOPMENT

Numerous aircraft flights were taken by the MSC with the Ryan Scatterometer over lunar-type surfaces at altitudes over 1,000 feet. The scope of this effort was not entirely limited to the development of a lunar analog model but was also designed to collect information for the Earth Resources Program. The end item of these data-gathering flights, after the doppler analog data were processed by the computer, was a large number of $\sigma_o(\theta)$ plots for a wavelength of 2.26 cm, for vertical polarization, and altitudes from 1,000 to 8,000 feet. A summary of the lunar analog models is given in Section 6.

The $\sigma_o(\theta)$ plots correlated with the ground truth collected by the various support groups constituted a reflectivity model for a selected terrain. Sometimes the model was only applicable to a small part of the terrain because the characteristics changed rapidly within the overall selected area. In brief, models of the lunar analog surfaces were generated from the flight data, with the aid of a computer and supporting ground truth information. The reverse process usually prevails in similar modeling programs, a theoretical model is first postulated with an attempt at validation by experiment later.

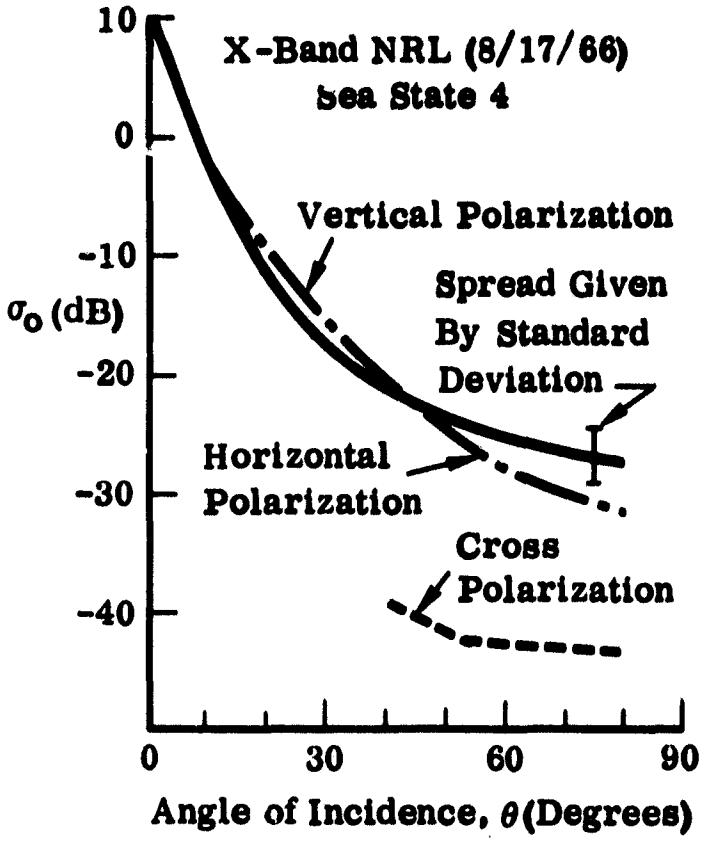
A sizable library of accurate σ_o plots has resulted from the Ryan-directed effort for NASA. The procedure and methods to generate such comprehensive information has been established and can easily be extended to the generation of a more complete model. A more

complete model would include a number of related plots of σ_o with the independent variables of the angle of incidence, wavelength, and altitude. Polarization would be a fixed parameter for all cases (vertical, horizontal, and cross polarization). An even more elaborate model could contain σ_o plots showing the complex dielectric constant of the surface as a parameter. Such a comprehensive reflectivity model is depicted by the essentially hypothetical σ_o plots in Figure 1. Average values are shown by the solid lines. The spread in the data is given by the standard deviation and is represented by the dotted lines.

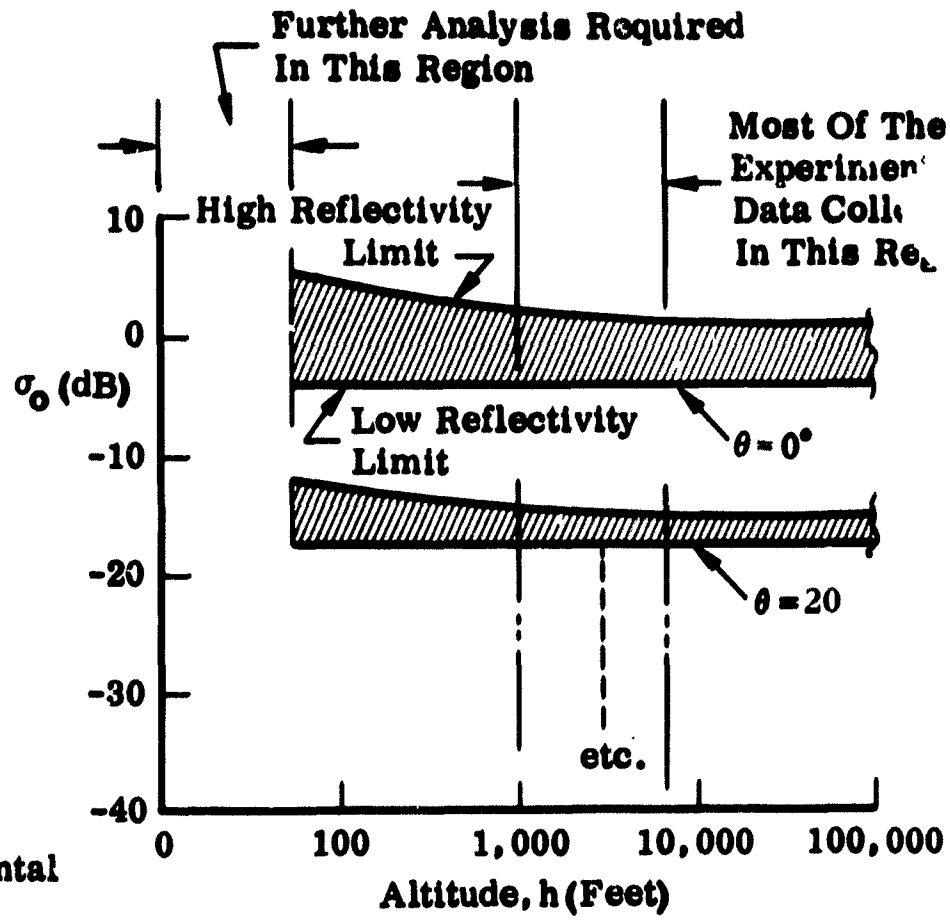
Other statistical parameters are explicit in the mathematical forms of σ_o, and their role in modeling is held in abeyance until Section 5.

The past year's effort as herein reported was concerned primarily with the generation of mostly σ_o plots for lunar-type surfaces (vertical polarization only) as shown in Figure 1A. The altitude variations of $\sigma_o(h)$ with θ as a parameter are hypothesized in Figure 1B. Some REDOP data was recorded below 1,000 feet; however, most of the data was recorded at 1,000, 2,500, 4,000, and 8,000 feet over desert, farmland, and sea surfaces. Considerable experimental data are available; however, further data are required to do the following:

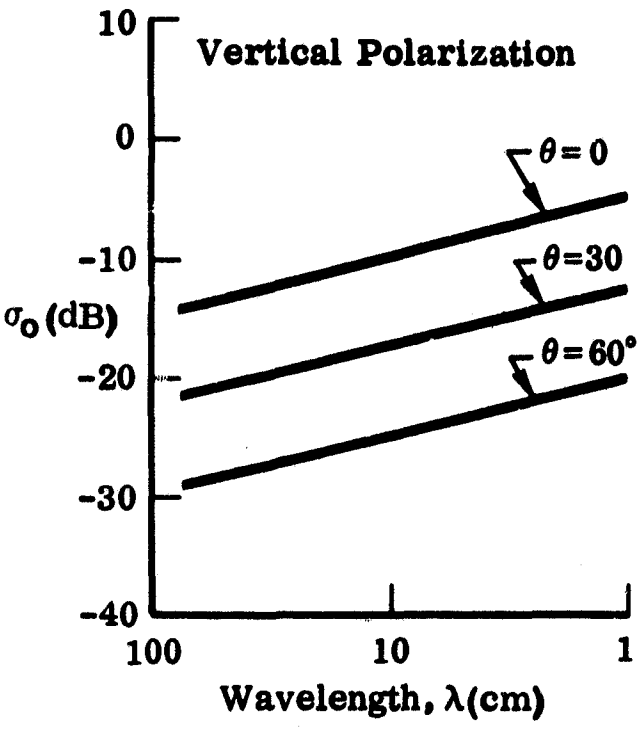
(1) to complete the low-altitude model for altitudes 0-1,000 feet, Figure 1B, for landing radar designs.



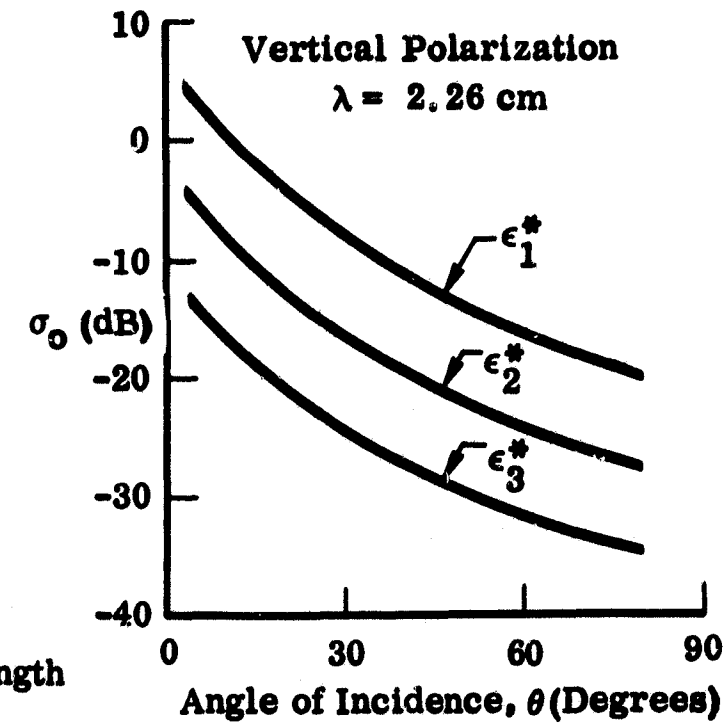
A) Sea Return For Vertical, Horizontal and Cross Polarizations



B) Hypothesized Low-Altitude Model



C) Model Structure Showing Wavelength Dependence



D) Model Structure Showing Complex Dielectric Constant Dependence

Figure 1. Comprehensive reflectivity model as an assembly of σ_o plots reflectivity

(2) to continue the compilation of σ_o plots at the higher altitudes for a larger variety of terrains.

(3) to gather data at a longer wavelength, or different wavelength, over previously flown areas, Figure 1C.

(4) to start a study of the effects on σ_o plots for varying surface complex dielectric constants.

In particular, the low-altitude region has been avoided by most researchers in the past. As a consequence, there is a definite need for experimental evidence of the reflecting characteristics of terrains at these low-altitudes. Presently developed low-altitude models are questionable when return power and fading rate and depth are considered in the context of a quasi-specular surface.

Some data are available above 10,000 feet altitudes; however, this does not appear to be as complex a modeling region as the low-altitude region. Large interspersed specular scatterers do not greatly affect the overall signal return when they are in essence only an infinitesimal part of the reradiating area element being considered.

Two σ_o models have been proposed for the low-altitude region by Ryan and MIT. A reconsideration must be made of an old set of modeling questions as the radar approaches the surface. A few are as follows:

(1) What are the received signals and final receiver output signals for a doppler or pulse system for a quasi-specular surface?

(2) At what altitudes do antenna beamwidth-limited returns occur?

(3) Are the electromagnetic characteristics of the quasi-specular surface of greater significance?

The two proposed low-altitude models differ mainly in their convergence properties as the altitude approaches zero. Further analysis, beyond the present effort, of the theory and experimental low-altitude data is required to establish a valid low-altitude model for the lunar-analog surface.

SECTION 2

TECHNICAL DISCUSSION

This Section presents a technical discussion of the MSC REDOP Scatterometer system. Equations are derived for signal density as a function of incidence angle and doppler frequency. The technique for separating the positive and negative doppler is also presented. In addition, a discussion of various spectrum analyzers and the effects of filtering on the statistical properties of the signal are included. The final part of this Section is an error analysis of the complete data taking and data reduction process.

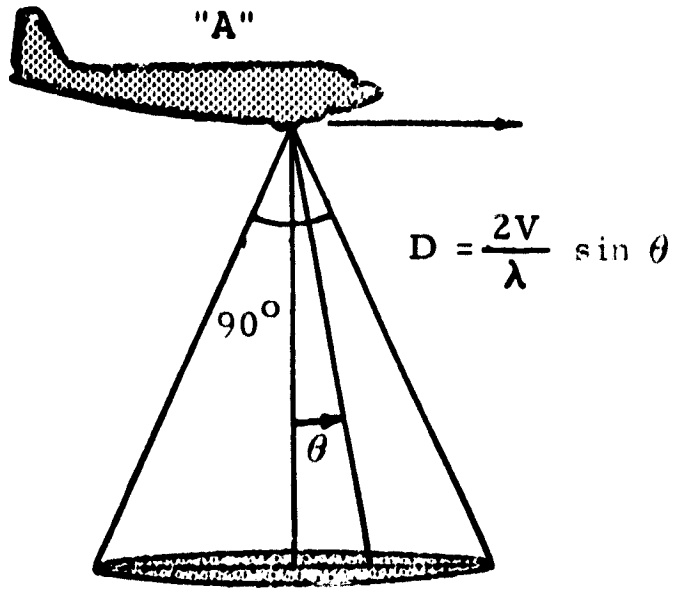
2.1 Ryan Redop Techniques

The techniques used by the REDOP Scatterometer are unique in the field of reflectivity measurements. This method permits measurement of the backscattering cross section per unit surface quickly and accurately by relating the echo power density at a given doppler frequency to angle of incidence of the radiation.

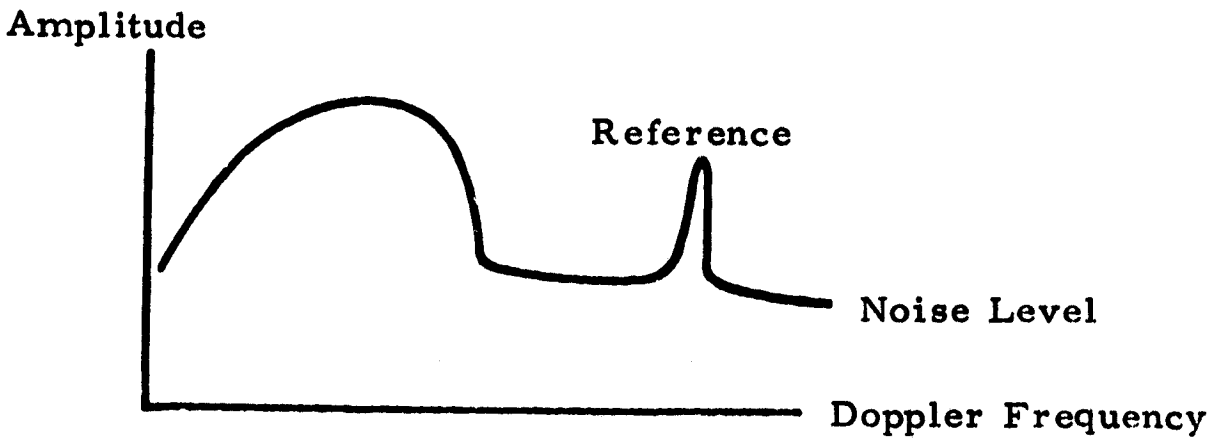
Figure 2 illustrates the basic principle of operation. The RF energy is radiated by an antenna which has a wide beam fore-aft and a narrow transverse beam. The return energy may be separated into the return as a function of incidence angle by the doppler

frequency. The doppler frequency is a function of aircraft velocity and angle of incidence. Return power is a function of radar system parameters, altitude, and surface reflectivity characteristics.

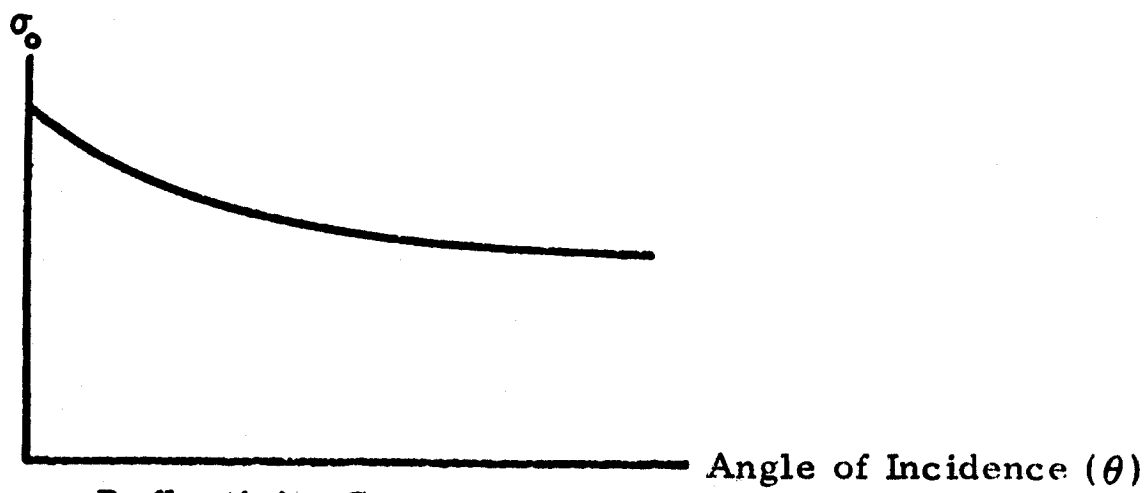
The amplitude of the return as a function of frequency is illustrated in Figure 2 and shows the effect of a designed amplifier roll off to prevent receiver saturation for signals at the radar. The data may be corrected for system parameters and converted to σ_o versus θ as shown. Figure 3 is a block diagram of the REDOP Scatterometer. The transmitting antenna radiates an extremely broad beam (≈120 degrees beamwidth) along the fore-aft axis of the aircraft and a narrow (≈3.5 degrees beamwidth) along the port-starboard axis of the aircraft. The center of the beam is oriented along the vertical axis of the aircraft. The E-vector of the antenna is in the wide beam direction. Therefore, this antenna is used to transmit vertical polarization. The receiving antenna is identical to the transmitting antenna, thus the two-way beamwidth is about 100 degrees by 2.5 degrees. As the aircraft is flown, data is received from all angles of incidence simultaneously. The data is detected by a direct-to-audio technique and amplified. The audio data is recorded on an FM tape recorder. After the flight, the tape data is played back through the spectrum analyzer to obtain the output signal amplitude versus frequency. A typical spectrum analyzer output is shown in Figure 4.



Antenna Beam Orientation



Frequency Domain Plot of Return Signal



Reflectivity Curve

Figure 2 Ryan REDOP Technique

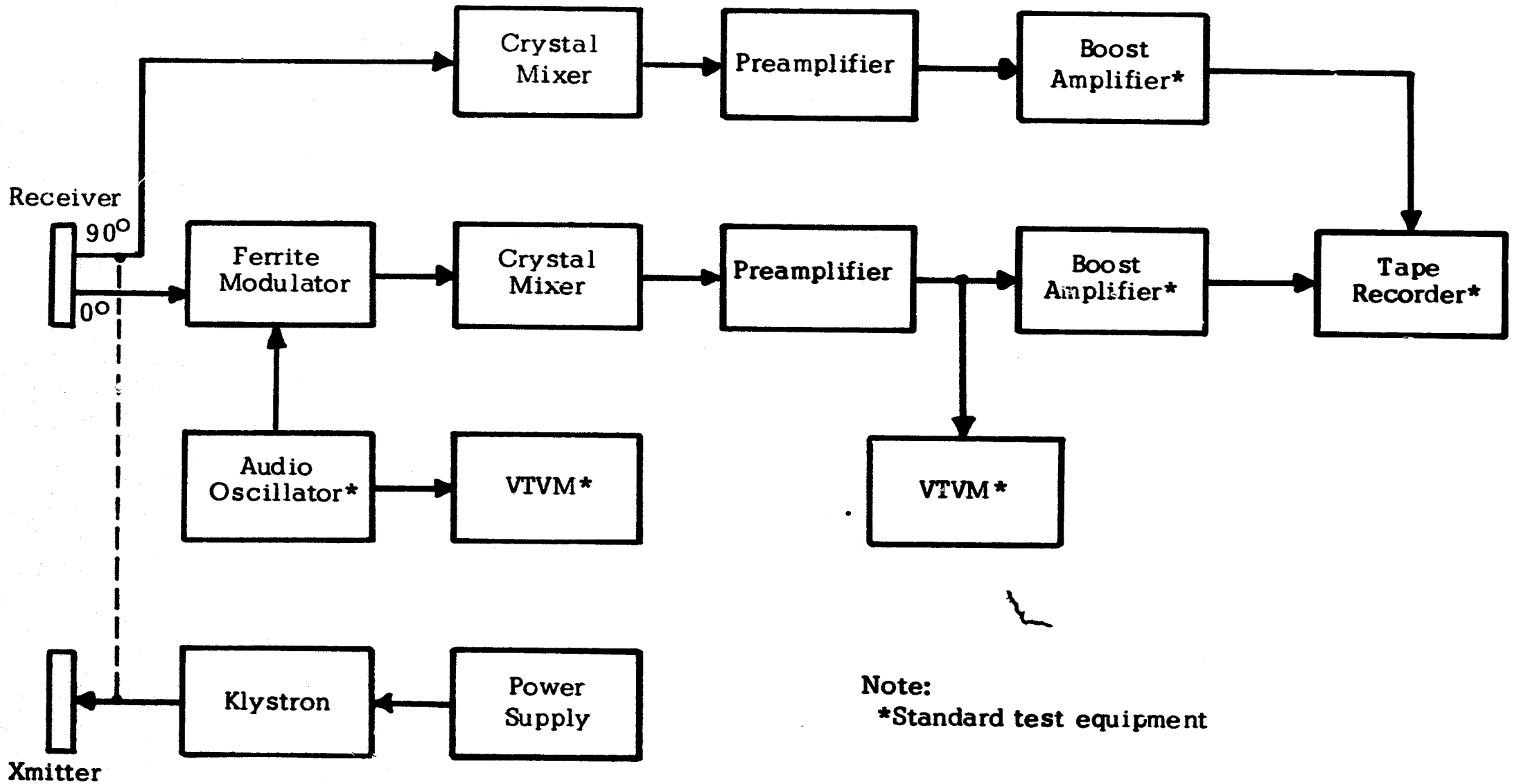


Figure 3. REDOP Scatterometer Block Diagram

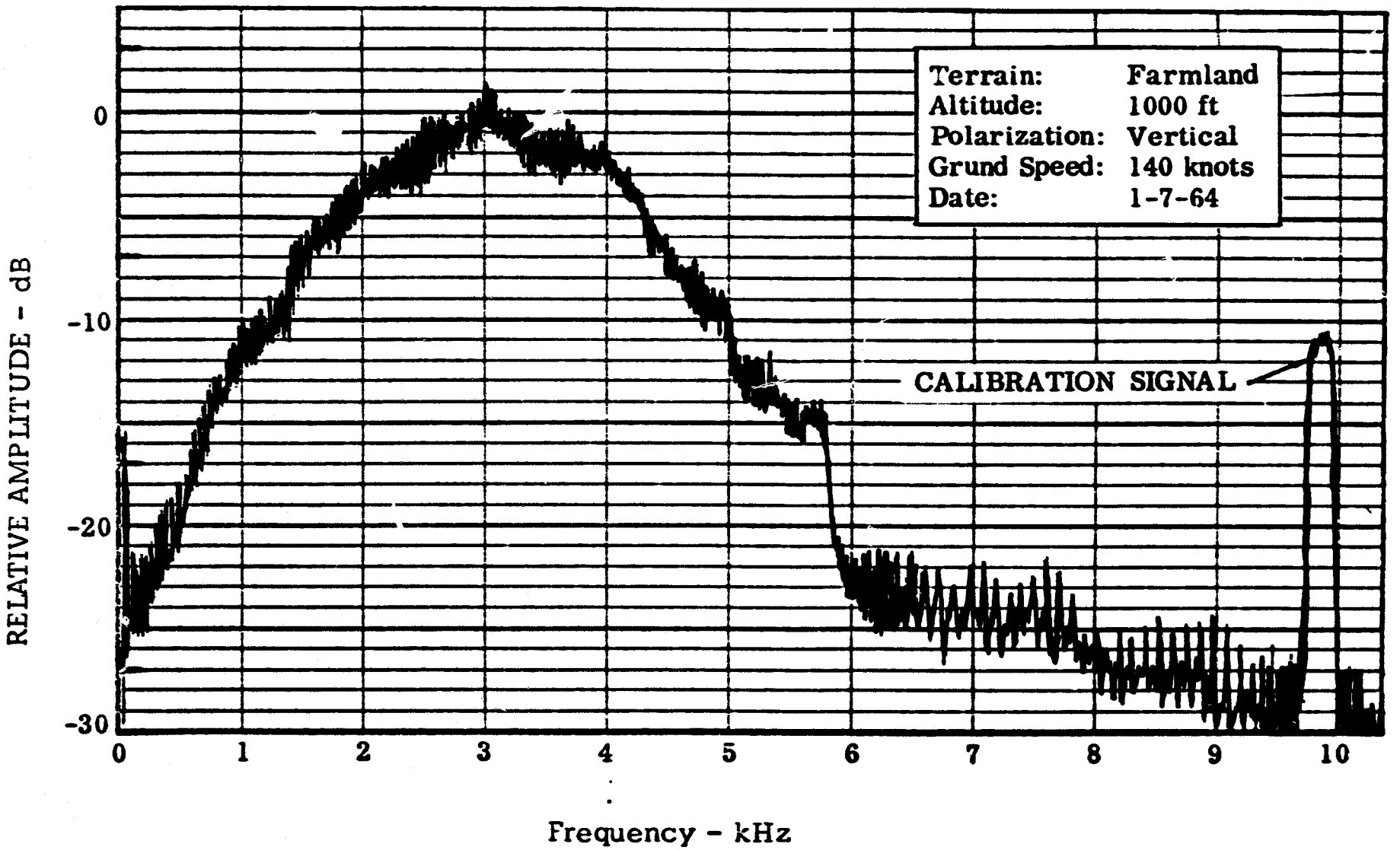


Figure 4 Typical Overland Frequency Spectrum

To calibrate the system a ferrite modulator is used to provide an absolute power reference level of the transmitted signal. The σ_o versus θ information is obtained by subtracting out all known factors of the system from the ferrite modulator reference level.

The spectrum analyzer recordings can be reduced using the following equation to obtain signal amplitude as a function of angle of incidence.

$$W_S = \frac{P_T G_o^2 \lambda^3 \sigma_o(\theta) f(\theta)}{(4\pi)^3 h^2 V_g} \int_{-\pi/2}^{\pi/2} f_1(\theta, \phi)\, d\phi$$

Where

P_T = transmitted power

G_o = antenna gain

λ = transmitted wavelength

$\sigma_o(\theta)$ = radar backscattering cross section per unit surface area

$f(\theta)\int_{-\pi/2}^{\pi/2} f_1(\theta, \phi)\, d\phi$ = two-way antenna pattern factor

h = altitude above terrain

V_g = aircraft ground speed

In the REDOP system, a klystron transmitter is used. The klystron power is divided in the directional coupler to feed the transmitting antenna and the receivers. Almost all the klystron power is transmitted to the ground (the crystal bias powers are one-half milliwatt each compared to a total klystron output power of one and one-half watts). The power transmitted to the ground is received and added to the crystal bias power. The power received from the ground is about -80 dbm compared to -3 dbm for the crystal bias power.

The crystal bias and ground return power in one channel are modulated by the ferrite modulator. In the other channel, the two signals are not modulated. Since the amount of modulation on the output of the ferrite modulator is proportional to the input microwave power, the modulation of the ground return power is negligible compared to the modulation of the bias power. The ferrite modulator thus passes the ground return without modulation.

An audio oscillator drives the ferrite at a frequency of 10 KHz which is several kilocycles above the maximum frequency of the ground return. While recording data, the output level of the oscillator is monitored by a voltmeter. The microwave power removed by the ferrite in the modulation process is absorbed by a dummy load. The remainder of the power goes to a crystal mixer whose outputs are the audio frequencies contained in the modulated bias power and the ground return. The audio power in each channel is amplified by a low-noise amplifier and by a boost amplifier to drive the FM tape recorder.

2.1.1 Derivation of Signal Return Equations

The power density in the incident radiation at the surface of the earth, S^i, may be expressed in terms of the antenna characteristics G_T (q); transmitted power, P_T, and range, R, as follows,

$$S^i = \frac{P_T}{4\pi R^2} G_T (q)$$

where the quantity $P_T/4\pi R^2$ is the power density which would result from isotropic radiation of the transmitted power and G(q) is the power gain of the antenna over the gain of an isotropic radiator in a direction determined by the space cordinate, q, measured from the beam axis. The antenna gain, G(q), may be written in terms of its maximum value, G_o, and a pattern factor, F(q), as follows,

$$G(q) = G_o f(q)$$

The backscattered power density, S^s, from a signal scattering element is related to the incident power density by,

$$S^s = S^i \frac{\sigma}{4 \pi R^2}$$

where the backscattering cross section, σ , is defined as the area normal to the axis of the beam intercepting that amount of power which, when scattered isotropically, produces an echo equal to that observed from the target.

The surface of the earth may be assumed to consist of a large number of independent scattering elements. It is convenient, therefore, to define a quantity, σ_o, as the average backscattering cross section per unit surface area.

$$\sigma_o = \frac{\sigma}{\text{Area Illuminated}}, \qquad \sigma = \int \sigma_o \, da$$

The differential backscattered power density from an incremental surface area da having an angle of incidence equal to θ becomes,

$$dS^s = S^i \frac{\sigma_o(\theta)\, da}{4\pi R^2}$$

The amount of echo power received is related to the backscattered power density and to the effective receiving area of the antenna, A_e, as follows:

$$P_R = A_e S^s$$

where the effective receiving area, A_e, may be written in terms of antenna gain and the wavelength of the radiation,

$$A_e = \frac{G(q)\, \lambda^2}{4\pi}$$

The differential scattered power received per incremental surface area then becomes,

$$dP_R = A_e dS^s = \frac{P_T G_o^2 [f(q)]^2 \lambda^2 \sigma_o(\theta)\, da}{(4\pi)^3 R^4}$$

The antenna pattern factor can be expressed in terms of the usual beam coordinates θ and ϕ as follows,

$$f(q)^2 = f(\theta, \phi)$$

where $f(\theta, \phi)$ is the two-way pattern factor. The differential surface area, da, may also be expressed in terms of the coordinates θ and ϕ, and the range to the surface R,

$$da = \frac{R^2}{\cos\theta} \, d\theta \, d\phi$$

The amount of power received from an incremental area on the surface bounded by the angles $(\theta - \frac{\Delta\theta}{2}$ to $\theta + \frac{\Delta\theta}{2})$ and $(\phi - \frac{\pi}{2}$ to $\phi + \frac{\pi}{2})$ then becomes,

$$\Delta P_R = \frac{P_T G_o \lambda^2 \sigma_o(\theta, \phi)}{(4\pi)^3 R^2 \cos\theta} \int_{\theta_o - \frac{\Delta\theta}{2}}^{\theta_o + \frac{\Delta\theta}{2}} \int_{-\pi/2}^{\pi/2} f(\theta, \phi) \, d\theta \, d\phi$$

The two-way antenna beamwidths will be in the order of 100 degrees in the θ dimension and 2.5 degrees in the ϕ dimension at normal incidence (zero degrees θ). The pattern parameter will, therefore, be a slowly changing function of θ and the integrals above may be written as follows,

$$\int_{\theta_o - \frac{\Delta\theta}{2}}^{\theta_o + \frac{\Delta\theta}{2}} \int_{-\pi/2}^{\pi/2} f(\theta, \phi) \, d\theta \, d\phi = f(\theta)\Delta\theta \int_{-\pi/2}^{\pi/2} f_1(\theta, \phi) \, d\phi$$

where

$$f(\theta, \phi) = f(\theta) f_1(\theta, \phi)$$

The amount of received power as a function of frequency can be obtained by substituting the equivalent increment of frequency for the angular increment, $\Delta\theta$. To this end it is noted that for the antenna beam configuration as previously discussed, the doppler frequency, f, can be expressed by,

$$f = \frac{2V}{\lambda} \sin\theta$$

and,

$$\frac{df}{d\theta} = \frac{2V}{\lambda} \cos\theta \quad , \quad \frac{d\theta}{df} = \frac{\lambda}{2V\cos\theta}$$

An angular increment of $\frac{\lambda}{2V\cos\theta}$ radians is thus equivalent to a frequency increment of 1 cycle per second. The amount of echo power received in an increment of frequency 1 cps wide, which will be referred to as the signal power density, W_s, may then be written as follows,

$$W_s = \frac{P_T G_o^2 \lambda^3 \sigma_o(\theta,\phi) f(\theta)}{(4\pi)^3 2Vh^2} \int_{-\pi/2}^{\pi/2} f_1(\theta,\phi)\, d\phi$$

where

$$h^2 = R^2 \cos^2\theta$$

For values of in excess of a few degrees, $\sigma_o(\theta,\phi)$, becomes equal to $\sigma_o(\theta)$. If the two-way beam width in the ϕ dimension is 2.5 degrees, an angular error of only 8 percent results from approximately the (θ,ϕ) angular dependence by a (θ) dependence at $\theta = 3$ degrees and becomes smaller as θ increases.

A folding over of the power spectrum about zero frequency will take place in the direct-to-audio signal detection process. This foldover is removed during processing by a sign-sense detector such that signals coming from the fore beam are separated from those from the aft beam. The value of the backscattering cross-section per unit surface area, $\sigma_o(\theta)$, may be determined from flight test recordings of the signal power density at a given altitude h, in conjunction with the following equation,

$$W_{..} = \frac{P_T G_o^2 \lambda^3 \sigma_o(\theta)\, f(\theta)}{(4\pi)^3 h^2 V} \int_{-\pi/2}^{\pi/2} f_1(\theta, \phi)\, d\phi$$

The functions $f(\theta)$ and $f_1(\theta, \phi)$ are taken directly from the antenna pattern data. The integration of $f_1(\theta, \phi)$ over the coordinate ϕ may be done either numerically or by approximating the function by an integrable expression.

2.1.2 Predicted Results

The predicted signal power density is determined on the basis of existing reflectivity data and proposed system parameters. A velocity

of 170 knots (287 feet per second) was typical for the NASA aircraft.

For illustrative purposes, the pattern function $f_1(\theta, \phi)$ will be approximated by a Gaussian function in the ϕ direction, the side lobes being of little consequence (See Figures 24 and 25, pages 119 and 120 for plots of the antenna patterns.) The integration of $f_1(\theta, \phi)$ over all ϕ then becomes equal to the two way half-power beamwidth in radians along the ϕ coordinate. Figure 6 is a plot of expected signal and noise density versus frequency.

2.1.3 System Equations and Sign Sense Technique

System equations were derived for the scatterometer. These equations include the effect of unequal gain in the two channels of the airborne system and show how it can be compensated for in the sign sense detector. The derivation of the equations is given below. Figure 5 is a block diagram of the airborne system.

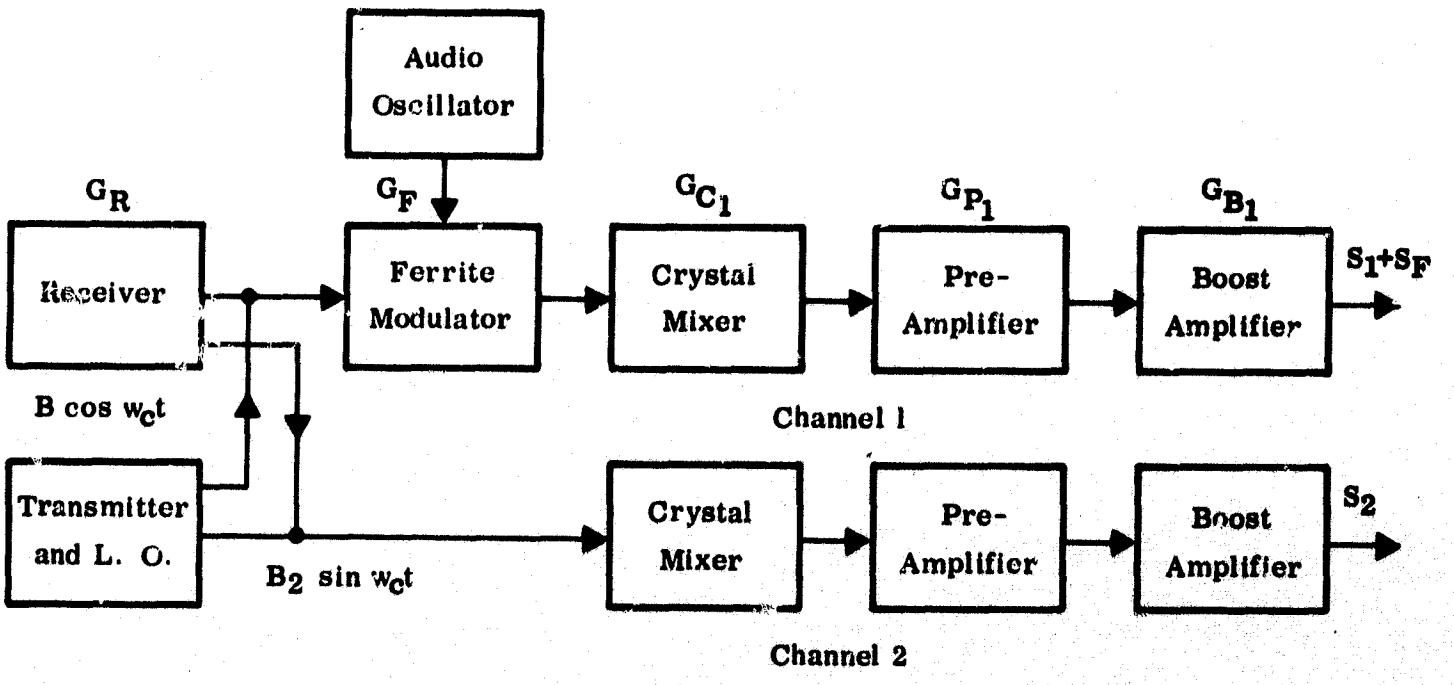


Figure 5

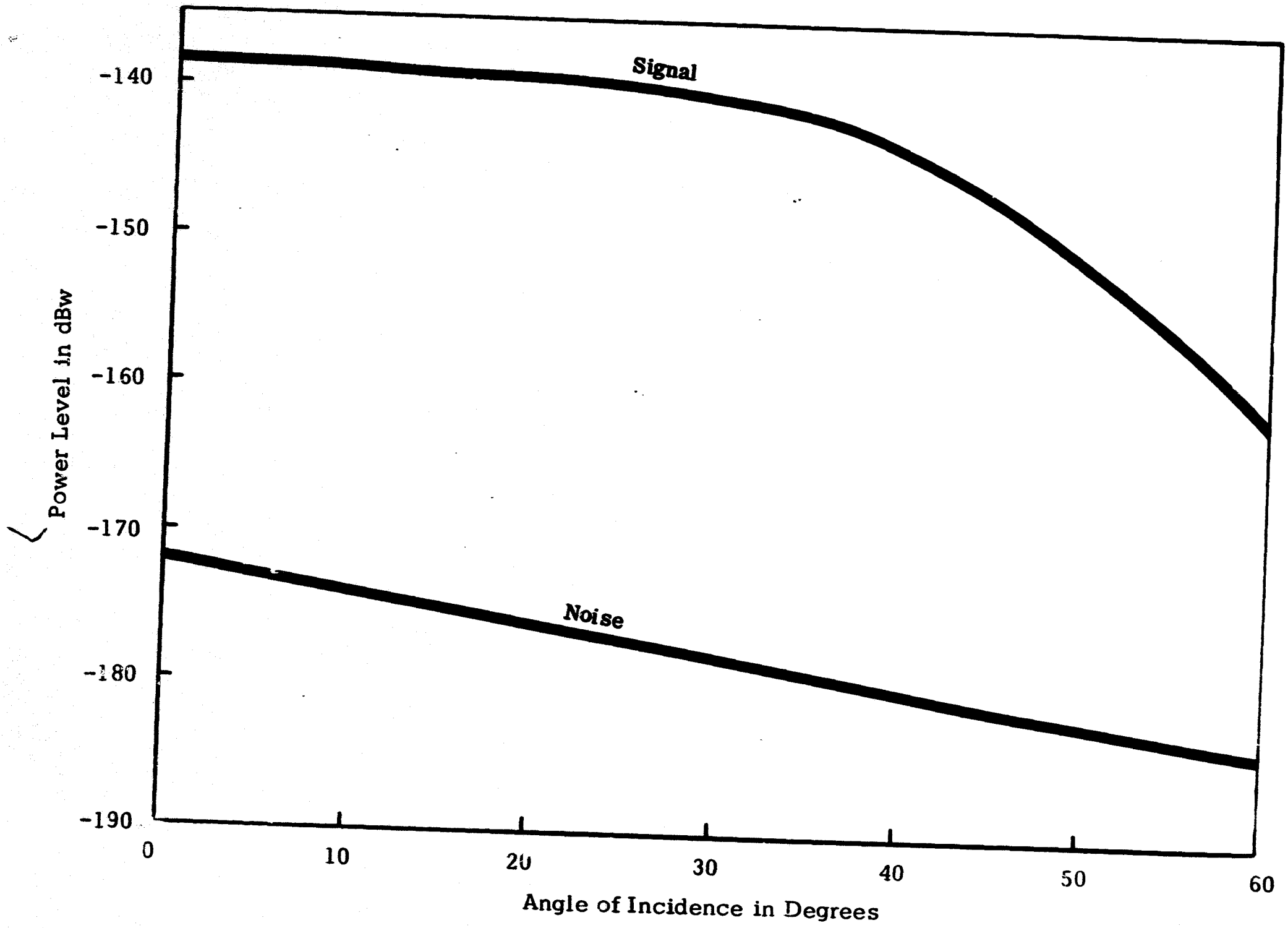
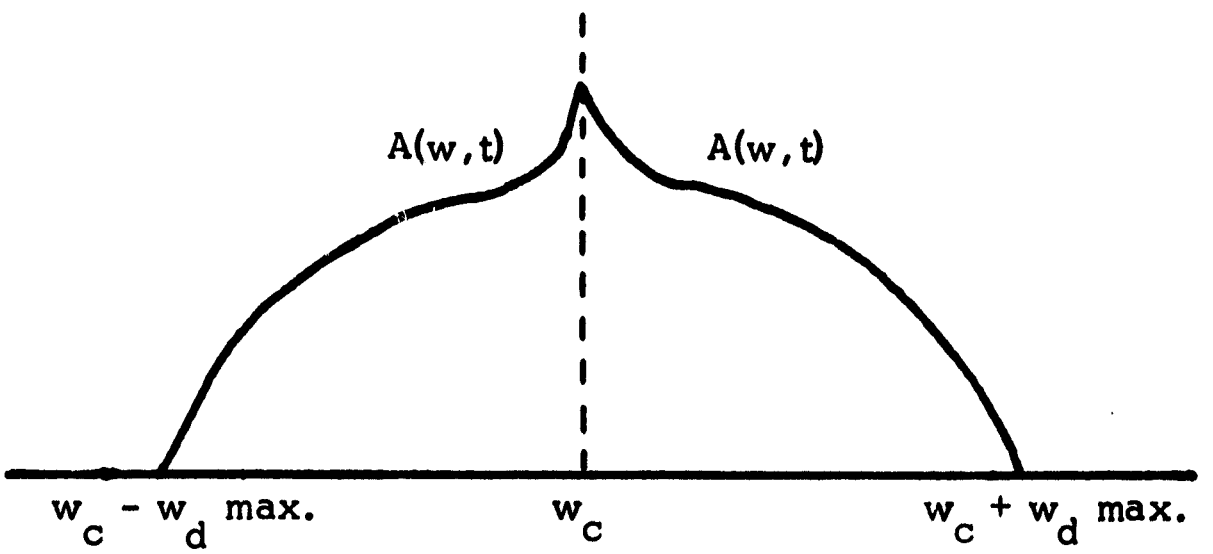


Figure 6 Microwave Mixer Signal and Noise Density Versus Frequency

The total gain of channel 1, plus the receiver is $G_1 = G_R G_F G_{C_1} G_{P_1} G_{B_1}$, and of channel 2 is $G_2 = G_R G_{C_2} G_{P_2} G_{B_2}$

The input spectrum can be represented by,



Where $A(f_w, t)$ is the negative return signal spectrum and $A(f_w^-, t)$ is the positive return signal spectrum.

Let the input spectrum be broken into two parts representing the positive and negative components.

Positive Component $\quad W(f^+) = A^+(w^+, t) \cos (w_c + w_d^+)t$

Negative Component $\quad W(f^-) = A^-(f_w^-, t) \cos (w_c - w_d^-)t$

The local oscillator/transmitter signal is mixed in quadrature with the received signal after it has been split into two equal components. The local oscillator signal can be represented by,

$$B_1 \cos w_c t$$

and,

$$B_2 \sin w_c t$$

The product is,

$$W(w)\ B_1 \cos w_c t$$

and, $W(w)\ B_2 \sin w_c t$

where $W(w) = W(w^+) + W(w^-)$

Assuming that variations in amplitude as a function of time are negligible during the sampling interval, the product becomes,

$$B_1 \cos w_c t \left[A(w^+) \cos (w_c + w_d^+)t + A(w^-) \cos (w_c - w_d^-)t\right]$$

$$B_2 \sin w_c t \left[A(w^+) \cos (w_c + w_d^+)t + A(w^-) \cos (w_c - w_d^-)t\right]$$

Simplifying and eliminating the terms that are at microwave frequency, we have,

$$1/2\ B_1 \left[A(w^+) \cos w_d^+ t + A(w^-) \cos w_d^- t\right]$$

and,

$$1/2\ B_2 \left[A(w^+) \sin w_d^+ t + A(w^-) \sin w_d^- t\right]$$

Applying the proper gain factors for channels 1 and 2, we have,

$$S_1 = 1/2\ G_1 B_1 \left[A(w^+) \cos w_d^+ t + A(w^-) \cos w_d^- t\right]$$

and,

$$S_2 = 1/2\ G_2 B_2 \left[A(w^+) \sin (- w_d^+ t) + A(w^-) \sin w_d^- t\right]$$

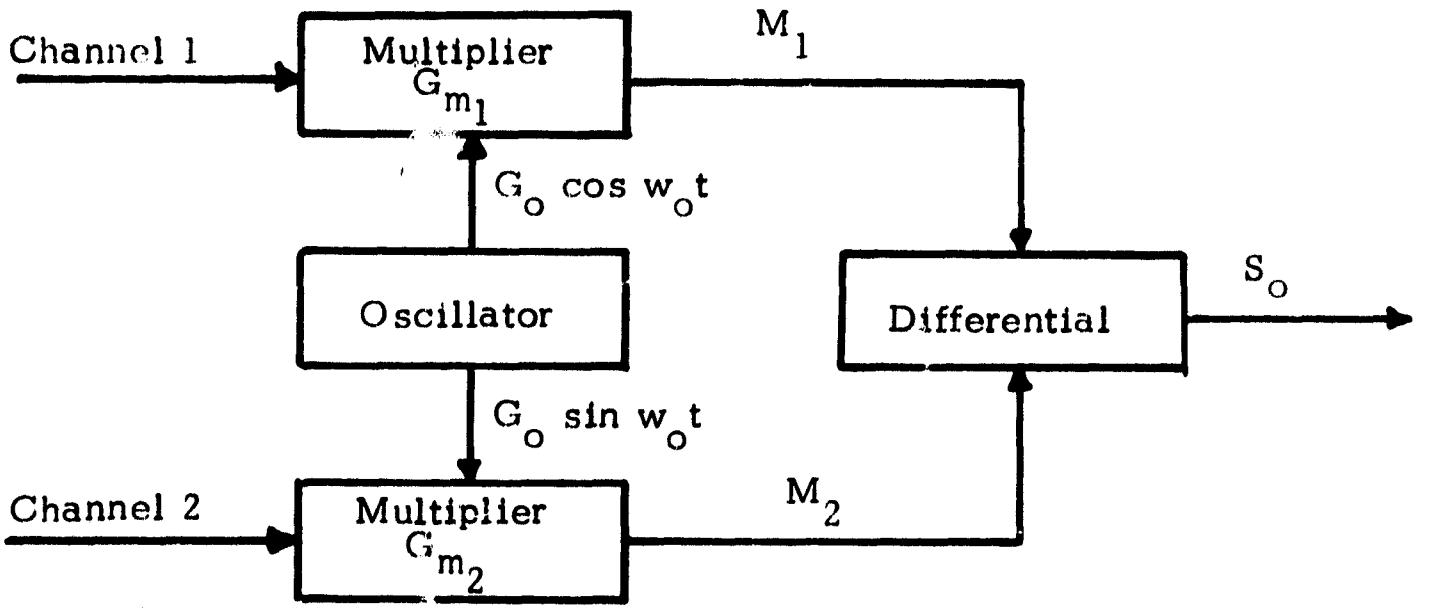
where S_1 and S_2 are the output signals of channels 1 and 2, respectively.

In addition, channel 1 has a signal from the ferrite modulator which can be represented by,

$$S_F = \frac{G_1 B_1}{G_R}\ G_a \cos w_a t$$

where G_a is the product of the audio oscillator gain and the ferrite modulator sensitivity.

The sign sensing technique presently being used is represented in the block diagram below:



The output of multiplier 1 is

$$M_1 = \frac{G_1 B_1 G_a G_{m_1} G_o}{2 G_R} \left[\cos (w_o + w_a)t + \cos (w_o - w_a)t\right]$$

$$+ \frac{G_1 B_1 G_{m_1} G_o}{4} \left[A(w^+) \left\{\cos (w_o + w_d^+)t + \cos (w_o - w_d^+)t\right\}\right.$$

$$\left. + A(w^-) \left\{\cos (w_o + w_d^-)t + \cos (w_o - w_d^-)t\right\}\right]$$

$$M_2 = \frac{G_2 B_2 G_{m_2} G_o}{4} \left[A(w^+) \left\{\cos (w_o + w_d^+)t - \cos (w_o - w_d^+)t\right\}\right.$$

$$\left. + A(w^-) \cos (w_o - w_d^-)t - \cos (w_o + w_d^-)t\right\}\right]$$

The output of the sign sense detector gives separation of the two sidebands, if, and only if,

$$B_1 G_1 G_{m_1} = G_2 G_{m_2} B_2$$

which can be done by adjusting G_{m_1} or G_{m_2}. Then,

$$S_o = \frac{G\, B\, G_a\, G_m\, G_o}{2\, G_R} \left[\cos (w_o + w_a)t + \cos (w_o - w_a)t\right]$$

$$+ \frac{B\, G\, G_m\, G_o}{2} \left[A(w^+) \cos (w_o + w_d^-)t + A(\bar{w}) \cos (w_o - w_d^-)t\right]$$

$w_o + w_a$ and $w_o - w_a$ are two calibration signals on the output that are generated by the ferrite modulator. The level of the ferrite modulator signals compared to the level of the received signal is proportional to the product of the voltage of the audio oscillator, the ferrite modulator constant and the local oscillator bias power. Therefore, the ferrite modulator provides a calibration signal that is independent of all other parameters. The value of the calibration signal can be determined by the calibration constants. The only effect of the ferrite modulator on the received signal is a slight decrease in power (-0.3 db) due to insertion loss. This does not introduce a calibration error, since the loss is relative to the received and calibration signals. No modulation of the received signal occurs.

2.2 A DISCUSSION OF SPECTRUM ANALYZERS

This section presents a comparison of three types of spectrum analyzers: the narrow band power spectral analyzer (presently being used), the discrete frequency spectrum analyzer, and the narrow band cross-power spectrum analyzer. A spectrum analyzer is essential to data reduction and processing; thus, a discussion of the very types used are pertinent to illustrate their effects on the processed data.

The Narrow Band Power Spectral Analyzer - This type of spectral analyzer is presently being used to reduce the scatterometer data. In the past, this type of spectral analyzer gave sufficient information for the design of doppler trackers and doppler performance evaluations. The drawback to this type of analyzer is that it makes no distinction between signal and noise since all phase information is lost. A block diagram of this analyzer is shown in Figure 7.

The Discrete Frequency Spectral Analyzer - The frequency spectrum of the recorded data is continuous, but since the spectral analysis is performed on recorded samples of finite length, the analytic resolution is 1/T cycles per second where T is the sample length in seconds. The resultant discrete frequency spectrum of the sample is found by the Fourier Series expansion coefficients a_n and b_n where

$$a_n = \int_0^T f(t) \cos \frac{2\pi nt}{T} \, dt$$

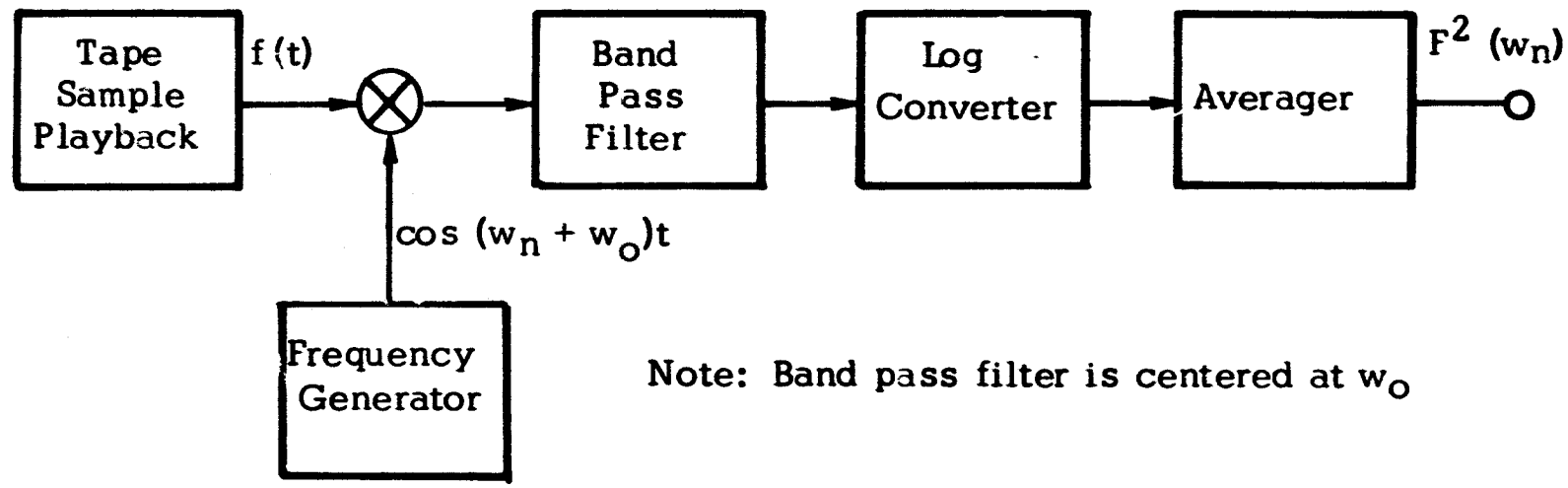


Figure 7 Narrow Band Power Spectral Analyzer

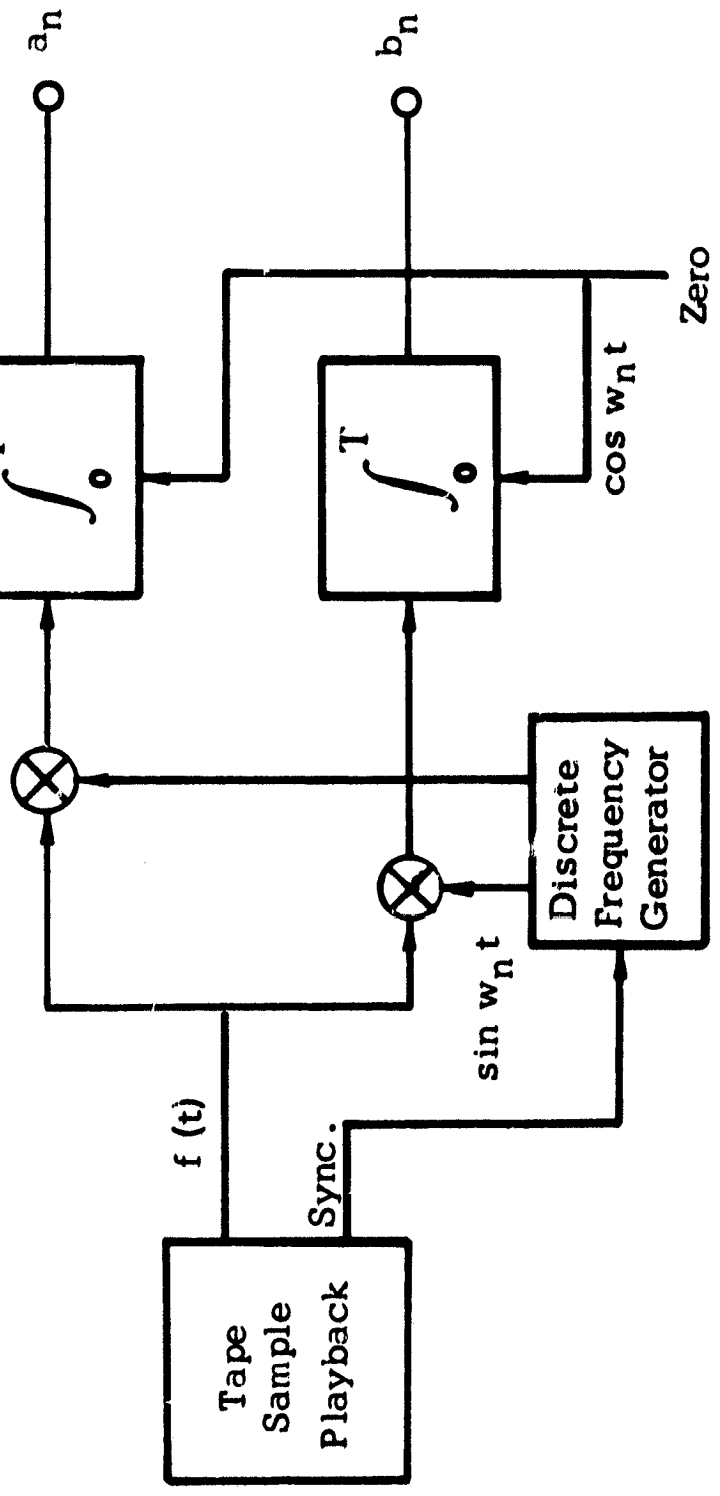
$$b_n = \int_0^T f(t) \sin \frac{2\pi nt}{T} \, dt$$

A block diagram of an analog analyzer for determining the Fourier coefficients is shown in Figure 8. A synchronizing signal is recorded on the tape to insure proper phasing of the discrete frequency generator outputs with the recorded signal f(t). A section of blank tape is spliced into the tape loop to permit time for reading out and zeroing the integrators between operations.

This technique is used when the data is processed directly on the digital computer. The two advantages of this method are (1) it is sensitive to the phase of the signal and (2) discrete frequency magnitudes and abrupt discontinuities are more readily distinguished.

The Narrow Band Cross Power Spectral Analyzer - The recorded signal differs from the received signal in that it includes additive noise from the amplifiers, the tape recorder, the tape playback, distortions from non-linear processes and 60 and 400 cycle noise spikes. These are held to a minimum by operating with strong signals within the linear limits of the system (where possible).

Under certain conditions where the signal return is very weak (or else the spectral components of interest are weak) with respect to the input noise sources of the amplifier or tape recorders, the influence



Note: This analyzer determines the Fourier series coefficients a_n and b_n for a recording of length T

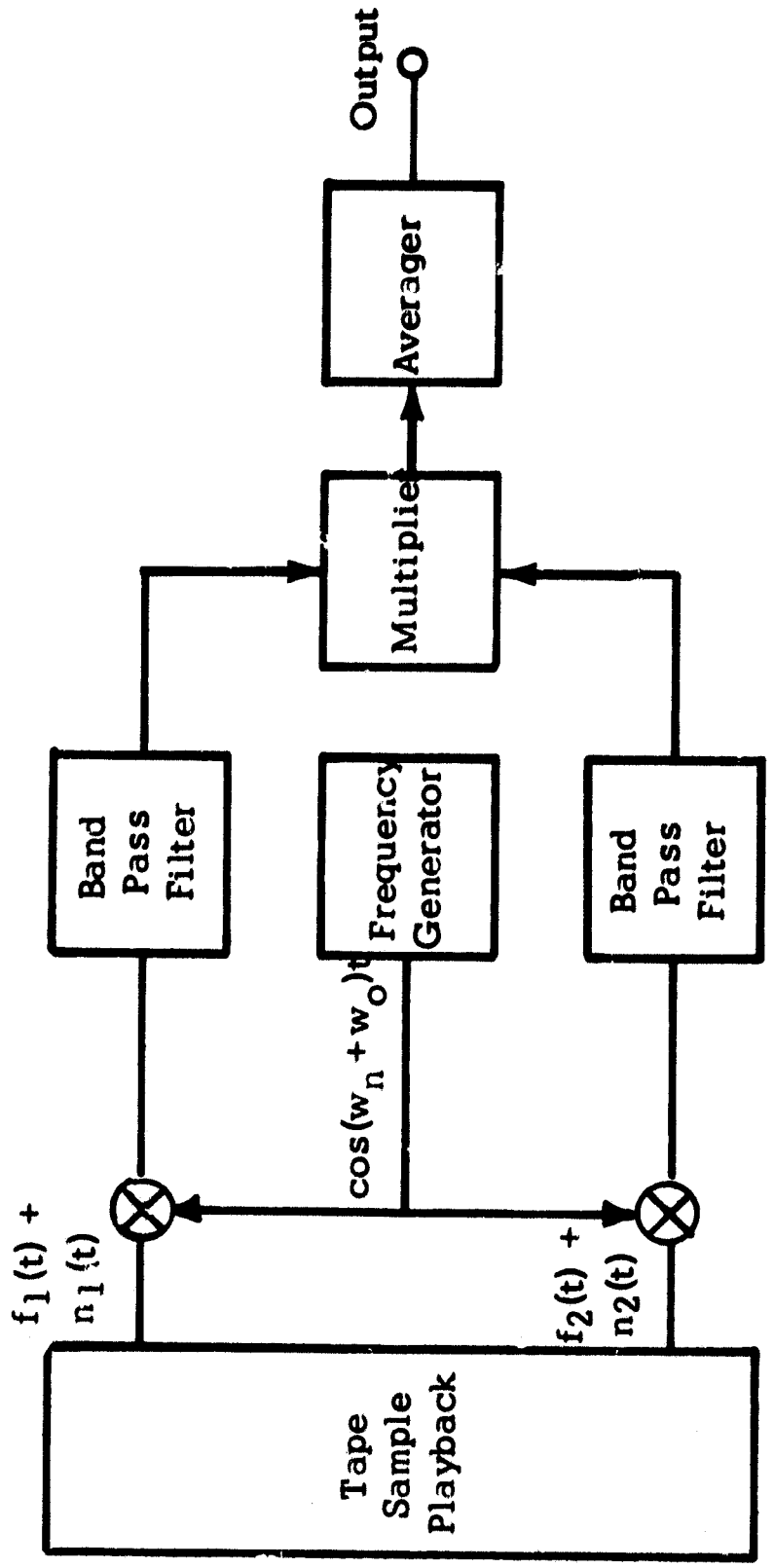
Figure 8 Discrete Frequency Spectrum Analyzer

of the noise can be rejected to any extent necessary by use of the Narrow Band Cross Power Spectral Analyzer. This requires detecting and recording the signal on two channels instead of one, which is presently done in the scatterometer. The recorded signals are thereby correlated while the additive noise is not (assuming that the two channels have independent noise sources). The averaged cross product of a narrow frequency band is a measure of true signal power spectral density because the noise products are averaged out within the limits of the averager time constant.

A block diagram of a Narrow Band Cross Power Spectral Analyzer is given in Figure 9. A system similar in principle to the Cross Power Spectral Analyzer is used in the Ryan doppler cross-correlation tracker. This tracker is able to seek out and track signals of less than -6 db signal-to-noise density ratio and reject non-doppler signals such as power supply ripple and near zone reflections from vibrating objects.

2.3 THE EFFECTS OF FILTERING AND DETECTION ON THE STATISTICAL PROPERTIES OF A CW SIGNAL

The purpose of this discussion is to evaluate the effects of utilizing a narrow band filter followed by a linear detector for the purpose of analyzing the return of the REDOP system over a small terrain element. For the purpose of this discussion, the following assumptions will be made:



Note: The desired signals $f_1(t)$ and $f_2(t)$ are correlated and produce output in a true power spectrum $F^2(w_n)$. The noise signals $n_1(t)$ and $n_2(t)$ are uncorrelated and produce an average of zero on the output. The noise rejection is proportional to the averager time constant.

Figure 9 Narrow Band Cross Power Spectral Analyzer

(1) The filter response in the frequency domain will be assumed to be gaussian.

(2) The input to the filter will be assumed to consist of broad-band gaussian noise (the signal component) plus white noise* (detector noise).

(3) The width of each filter will be assumed to be small compared to its center frequency so that the concept of an envelope will have physical significance.

Figure 10 is a block diagram of the process. The output of the narrow band filter in the time domain is a sinusoidal wave with slowly varying amplitude and phase or,

$$f(t) = R(t) \cos \left[\omega_c t + \phi(t)\right]$$

where $f_c = \omega_c/2\pi$ is the center frequency of the filter and R(t) and $\phi(t)$ are the time-domain functions of the amplitude (envelope) and phase.

If the center frequency and bandwidth of the filter are invariant, the statistical properties of the amplitude and phase can be determined by a Fourier analysis of the waveform over the interval $0<t<T$.

---

* It should be noted that the noise in the REDOP actually decreases monatonically with frequency; however, it can be shown that this has no effect upon the statistical properties of the output signal and is, therefore, an unnecessary complication.

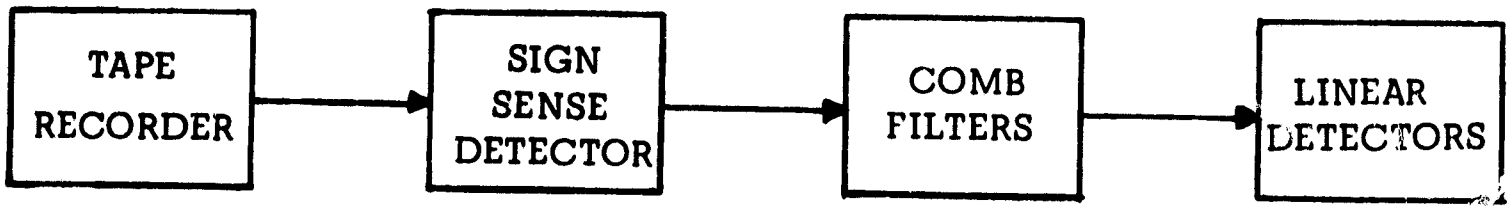


FIGURE 10 ANALOG ANALYSIS BLOCK DIAGRAM

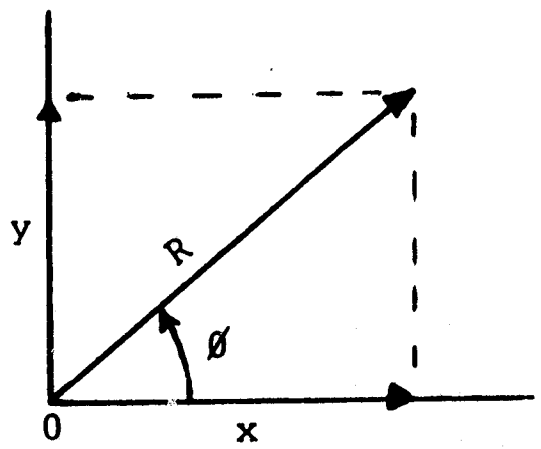


FIGURE 11 COORDINATE TRANSFORMATION

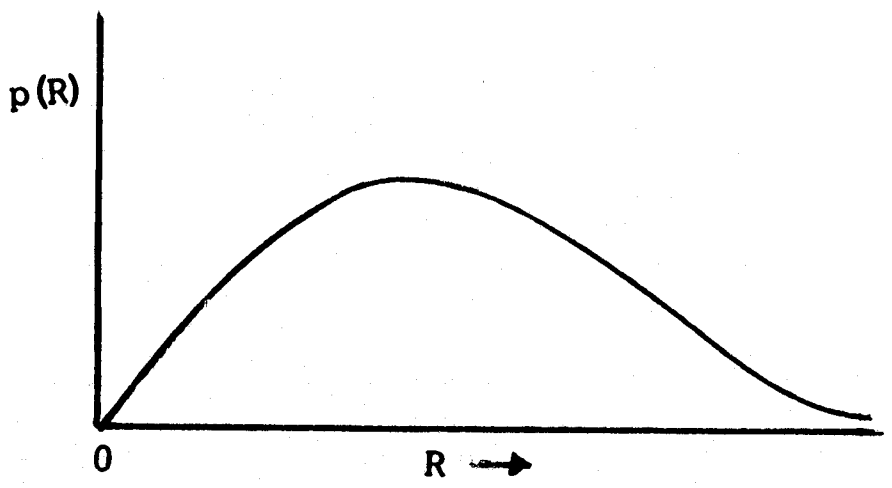


FIGURE 12 RAYLEIGH DISTRIBUTION

Thus, we see that x(t) and y(t) are an orthogonal set, which in terms of R(t) and ϕ (t) becomes,

$$x(t) = R(t) \cos \phi (t)$$

$$y(t) = R(t) \sin \phi (t)$$

Figure 11 shows the relation between the two sets.

Obviously,

$$R(t) = \left[x^2 (t) + y^2 (t) \right]^{1/2}$$

and,

$$\phi(t) = \tan^{-1} \left(\frac{y(t)}{x(t)} \right)$$

where $R(t) \geq 0$ and $0 \leq \phi (t) \leq 2\pi$. Since x(t) and y(t) are only defined in the region where the filter exists, the bandwidths of x(t) and y(t) will be equal to the bandwidth of the filter and centered about zero frequency.

The random variables x_t and y_t which represent possible values of x(t) and y(t), respectively, are defined as sums of gaussian random variables whose means are zero, and hence, are gaussian random variables with zero mean. The variance is,

$$\sigma^2(x_t) = \sigma^2(y_t) = \sigma^2(f_t)$$

$$f(t) = \sum_{n=1}^{\infty} (x_n \cos n\omega_o t + y_n \sin n\omega_o t)$$

where $\omega_o = 2\pi/T$

$$x_n = \frac{2}{T} \int_0^T f(t) \cos n\,\omega_o t\, dt$$

$$y_n = \frac{2}{T} \int_0^T f(t) \sin n\,\omega_o t\, dt$$

The coefficients can be shown to be gaussian random variables, which become uncorrelated as the expansion interval increases without limit. The center frequency of the filter can be incorporated by letting $n\omega_o = (n\omega_o - \omega_c) + \omega_c$ and expanding. The expression for f(t) then becomes,

$$f(t) = x(t) \cos \omega_c t - y(t) \sin \omega_c t$$

where

$$x(t) = \sum_{n=1}^{\infty} \left[x_n \cos (n\omega_o - \omega_c)t + y_n \sin (n\omega_o - \omega_c)t \right]$$

$$y(t) = \sum_{n=1}^{\infty} \left[x_n \sin (n\omega_o - \omega_c)t - y_n \cos (n\omega_o - \omega_c)t \right]$$

x(t) and y(t) will be equal to the bandwidth of the filter and centered about zero frequency.

The random variables x_t and y_t which represent possible values of x(t) and y(t), respectively, are defined as sums of gaussian random variables whose means are zero, and hence, are gaussian random variables with zero mean. The variance is,

$$\sigma^2(x_t) = \sigma^2(y_t) = \sigma^2(f_t)$$

The covariance of x_t and y_t is zero. Therefore, x_t and y_t are independent gaussian random variables. Their joint probability density is,

$$p(x_t, y_t) = \frac{1}{2\pi\sigma^2(f_t)} \exp\left[\frac{-(x_t^2 + y_t^2)}{2\sigma^2(f_t)}\right]$$

The joint probability density function of the amplitude and phase random variables R_t and ϕ_t can be obtained from that of x_t and y_t The Jacobian of the transformation is,

$$|J| = R_t$$

and therefore,

$$p(R_t, \phi_t) = \frac{R_t}{2\pi\sigma^2(f_t)} \exp\left[\frac{-R_t^2}{2\sigma^2(f_t)}\right]$$

The probability density function of R_t can be obtained by the equation,

$$p(R_t) = \int_0^{2\pi} p(R_t, \phi_t)\, d\phi$$

or,

$$p(R_t) = \frac{R_t}{\sigma^2(f_t)} \exp\left[\frac{-R_t^2}{2\sigma^2(f_t)}\right]$$

which is a Rayleigh distribution (see Figure 12).

It should be recalled, this analysis was based upon having random (noise-like) signals plus white noise as inputs to the filter. If the bandwidth of the filter is narrower than bandwidth of the input, the output of the detector is thus constrained to be a Rayleigh distribution. Therefore, the statistical properties of the signal return itself will be masked by the analysis techniques employed. The output of the detector is expected to exhibit an 18 db fading range whether the input to the filter is all noise, all signal, or a combination thereof.

Thus, one exception to the above would be right at the nadir over terrain whose specular return has a narrower bandwidth than the analysis system. In this case, the output of the detector will be the true fading characteristics of the signal input.

The measurement of signal power in the presence of noise will become increasingly inaccurate as the signal-to-noise ratio decreases.

However, since the signal and noise are independent random variables, their powers will add directly. Thus, the magnitude of the error in signal power measurements can be accurately determined. A compensation can be made for this error when required.

The reason for this error is that the spectrum analysis equipment, which can consist of either a single sweeping filter or a bank of comb filters, measures the composite of signal and noise.

$$P_M = P_S + P_N$$

Where P_S is the signal power and P_N is the noise power. The ratio of the measured power to the noise power is,

$$\frac{P_M}{P_N} = \frac{P_S + P_N}{P_N}$$

Since the measured signal-to-noise power ratio will normally be in db,

$$\left(\frac{P_M}{P_N}\right)_{db} = 10 \log \left(\frac{P_S + P_N}{P_N}\right)$$

The error in using the measured signal-to-noise power is,

$$\xi p_{db} = \left(\frac{P_M}{P_N}\right)_{db} - \left(\frac{P_S}{P_N}\right)_{db}$$

or,

$$\xi p_{db} = 10 \log \left(\frac{P_S + P_N}{P_S} \right)$$

$(\xi_p)_{db}$ is plotted versus $\left(\frac{P_M}{P_N} \right)_{db}$ in Figure 13.

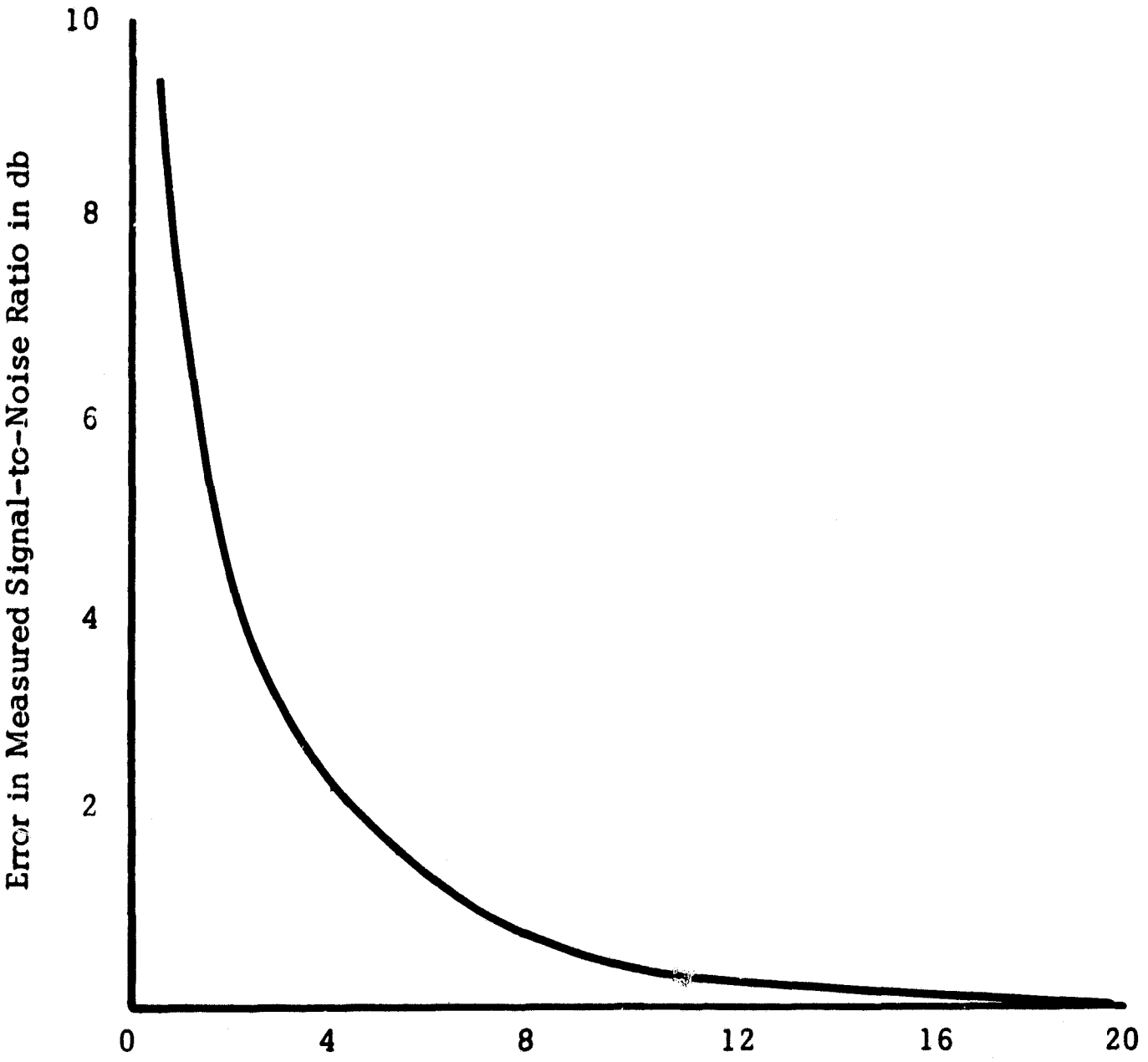


Figure 13 Effect of Measured Signal-to-Noise Ratio Upon Accuracy of Measured Signal-to-Noise Ratio

2.4 Error Analysis

The purpose of this analysis is to define the range of errors assigned to the data obtained from the R. F. Reflectivity Program currently in progress. The error sources can be divided in five groups for the purpose of analysis.

A. Errors in the Measurement of Radar System Parameters

- A.1 Transmitted Power
- A.2 Wavelength
- A.3 Two-Way Antenna Pattern Factor
- A.4 Roll-off Characteristics R(D)
- A.5 Phase Shift Due to Thermal Changes
- A.6 Two-Way Antenna Gain
- A.7 Boresight Accuracy

B. Aircraft Installation

C. Errors in Directly Related Aircraft Information

- C.1 Velocity
- C.2 Altitude

D. Errors in Values of Indirectly Related Aircraft Information

- D.1 Pitch
- D.2 Roll
- D.3 Drift

E. Errors in Signal Density Measurement

- E.1 Ferrite Modulator Calibration
- E.2 Analog Reduction Process
- E.3 Digital Reduction Process

2.4.1 Discussion of Errors

This section presents a detailed discussion of the errors outlined above.

A. Errors in the Radar System.

A.1 Transmitted Power

The transmitted power accuracy depends upon the following factors:

- The measured klystron power
- Klystron filament voltage
- Waveguide losses
- Antenna and waveguide VSWR
- Klystron high voltage

Measured Klystron Power.

The accuracy of the Klystron power measurement is dependent upon the accuracy of the precision attenuator and the power meter used for this measurement. The accuracy of the precision attenuator is specified as a maximum of $\pm$ 2% of the reading in db. For these measurements the attenuator setting was 36.5 db. The maximum error is 0.73 db or $\pm$ 0.42 db rms (assuming a rectangular distribution of the errors). The accuracy of the power meter is specified as $\pm$ 5% of full scale. Thus, the maximum error was $\pm$ .22 db or $\pm$ .13 db rms (again using a

rectangular error distribution).

Klystron Filament Voltage.

The klystron output power will vary with filament voltage. The filament voltage regulation is 0.1%. Measured variations of output power from the klystron are:

6.0 volts = 1.057 watts

6.3 volts = 1.092 watts

The total output power variation is 0.14 db for a voltage change of 0.3 volts. Assuming the change is linear between these limits, the variation due to filament voltage regulation (6 millivolts) is 0.003 db or 0.0017 db rms, which is negligible.

Another consideration of filament voltage error is the precision to which the filament voltage can be adjusted. The meter used in this adjustment has a 1% tolerance giving a possible variation of: 0.063 volts or 0.03 db, which is negligible (again assuming a linear variation of power out with filament voltage).

In practice, however, the curve of output power versus filament voltage tends to flatten out above 6.3 volts. Adjusting the filament voltage on the high side of the meter tolerance will make the variation somewhat less than the 0.03 db figure.

Waveguide Losses.

All waveguide losses are included in the respective antenna pattern and power level measurements.

Antenna and Waveguide VSWR.

The Klystron output power is a function of the VSWR of the antenna and waveguide. Thus, for calibration purposes, the output power was measured with a VSWR equal to that of the actual system.

Klystron High Voltage.

The Klystron output is always peaked using the high voltage adjust. Once peaked, the high voltage variation is 85 millivolts out of 1600 volts or 0.005%. Thus, this variation is negligible compared to the variation in the other parameters.

A.2 Wavelength

A second parameter that will effect the accuracy of the scatterometer measurements is the wavelength of the transmitted signal. The specified frequency and frequency deviation of the klystron are 13.3 GHz and $\pm$ 5 MHz, respectively. The maximum error in wavelength is $\pm$ 0.038% or 0.022% rms. Since the measured value of sigma zero is proportional to the wavelength cubed the total effect is $\pm$ 0.066% rms or $\pm$ 0.006 db.

A.3 Two-Way Antenna Range Pattern Factor

The maximum antenna range pattern factor measurement errors were determined for the purpose of this analysis. An evaluation of the accuracy of the antenna patterns in the H-plane and the E-plane is given below.

The angular position errors encountered in the antenna pattern measurements by the automated antenna range are $\pm$ 10 minutes of arc. This figure was determined by manually measuring the 3 db points of the H-plane at the 0^{o} "port-starboard" positions, and comparing this with the 3 db points measured by the pattern plotting equipment. Converting this error from minutes of arc to degrees, the error becomes .166 degrees.

The pattern range has no automated plotting capabilities in the elevation axis, therefore, it was necessary to plot the E-plane by hand. This was accomplished by manually rotating the elevation axis of the antenna mount in 20 minute increments, rotating the pattern recorder the same amount, and depressing the recorder pen. Therefore, the gain measurement function is defined in twenty (20) minute increments. The pattern measurement accuracy is $\pm$ 2 minutes of an arc or $\pm$ 0.03 degrees.

By comparing the H-plane pattern maximum with the E-plane pattern at the angle at which the E-plane measurements were taken, it is possible to measure the difference. The error in measurement is

$\pm$ 0.5 db out to $\pm$ 60°. At angles beyond 60°, the error is greater due to reflections from the Pratt and Whitney mount.

The absolute and relative gains of the patterns are both within $\pm$ 0.5 db, since the relative gain accuracy is a function of equipment drift and reflected signals. Equipment stability offered no problems and reflected signals are negligible at angles up to 60°.

A.4 Roll-Off Characteristics

The amplifiers used in the Ryan Scatterometer system are two Millivac Instruments Model VS-64A hushed transistor amplifiers and two Kin Tel Model 121A boost amplifiers. The output of the boost amplifiers is coupled through a large capacitor and an isolation transformer. The amplifiers, capacitors and transformers are included in the measurements of the amplifier roll-off and frequency response curves. The errors in the amplifier section of the Scatterometer are due to the effects of amplifier stability and error in measuring the amplifier roll-off characteristics.

Amplifier Stability

The stability of the Millivac instruments, Model VS-64A, hushed transistor amplifier is given as 1.0 db. Assuming a rectangular distribution, the rms error is 0.58 db. The stability of the Kin Tel Model 121A boost amplifier is given as $\pm$ 0.1%. Again assuming rectangular distribution, the error is $\pm$0.1 db rms.

Error in Measurement

The errors in measuring the amplifier roll-off characteristics are caused by errors in the Ballantine 302C voltmeter, which is used for measuring the amplifier roll-off. The accuracy of this amplifier is $\pm$ 3% of full scale (20 db). Thus, the error in measurement is $\pm$ 0.3 db or $\pm$ 0.17 db rms.

A.5 Phase Shift Errors Due to Thermal Changes

Phase shift errors between the two channels will cause a reduction in the ability to separate the fore and aft beam data. Phase shift errors can result from klystron frequency changes and from relative phase shifts in the two scatterometer channels. The klystron frequency (wavelength) will vary slightly with changes in the aircraft ambient temperature. The klystron sensitivity to temperature variations is $\pm$ 100 KHz/degrees C. It is estimated that the temperature extremes in the aircraft will be from 40°F to 140°F, which is a variation of approximately 55 degrees centigrade. Thus, the variation in transmitted wavelength over this temperature range is 0.036°, which is negligible.

No information is available on the amplifier phase shift variation with changes in aircraft ambient temperature. These amplifiers were designed for laboratory use; therefore, it is

recommended that measurements be made of the effects of temperature upon phase shift.

A.6 Two-Way Antenna Gain

The two-way antenna gain was measured on the Ryan precision boresight range. The antenna was set at boresight zero. The output of the crystal mixer on the receiving antenna was fed to the pattern recorder and a reference mark was made with the pen. The transmitting and receiving antennas under test were then replaced by waveguide horns, each having a known gain of 19.26 db. The output of the crystal was again fed to the recorder and a mark was made. The difference between the two lines is the gain difference between the standard horns and the scatterometer antennas.

Since the gain was determined by a comparison method, it is only necessary to know the absolute value of the reference antennas. Two identical waveguide horns were used as a gain reference, and their absolute gain value was determined by three methods.

(1) By knowing the physical dimensions of the horn and calculating the gain according to a method outlined in the I.R.E. PGAP, October, 1956. Result, 19.30 db per horn.

(2) Experimentally by the method described in Volume 12,

Microwave Antenna Theory and Design,

Radiation Laboratory Series, pp 585-587.

Result, 19.26 db per horn.

(3) According to a graph provided by the horn manufacturers, Microwave Associates.

Result, 19.30 db per horn.

The boresight data shows the gain reference to be 0.4 db higher than the system reference. Thus, the two-way antenna system gain at the output of the hybrid mixer is (2X 19.26 - 0.4) db = 38.12 db.

A.7 Boresight Accuracy

Two-way antenna patterns were measured to define the gain changes as a function of angle. There is sufficient gain ripple in the radiation pattern as a function of angle to require that the measurements be referred accurately to angular reference planes located on the antenna. For these reasons the antenna was boresighted as described below.

To establish a frame of reference for angular measurements on the antenna it was necessary to utilize the Pratt and Whitney precision boresight mount. This mount was optically aligned to 0^{o} azimuth and 0^{o} elevation and then the antenna was placed in a horizontal position on the mount. The object was to align the antenna to the boresight mount. At this point it was necessary

to define points on the antennas which could be used to align fore-aft, port-starboard and skew planes. Figure 14 shows the alignment points which were chosen.

Fore-Aft

A clinometer was placed across the radome at point (a), the antenna was then adjusted up and down until the clinometer read 0^{o}. Since the antenna is in a horizontal position, these adjustments establish the 90^{o} fore-aft reference.

Port-Starboard

To establish 0^{o} port-starboard as indicated by the point (b), fiberglass blocks were epoxied onto the radome surface and a clinometer was placed across the blocks. The procedure was completed by moving the antenna until the clinometer read 0^{o}.

Skew

The points marked "c" establish 0^{o} skew. With fore-aft and port-starboard aligned, the boresight elevation mount was rotated 90^{o}, thus placing the antenna at vertical or 0^{o} fore-aft. Port-starboard was left at 0^{o}. A plumb line was then dropped across the surface of the radome and a small punch was used to mark the points where this line crossed the opposite sides of the radome.

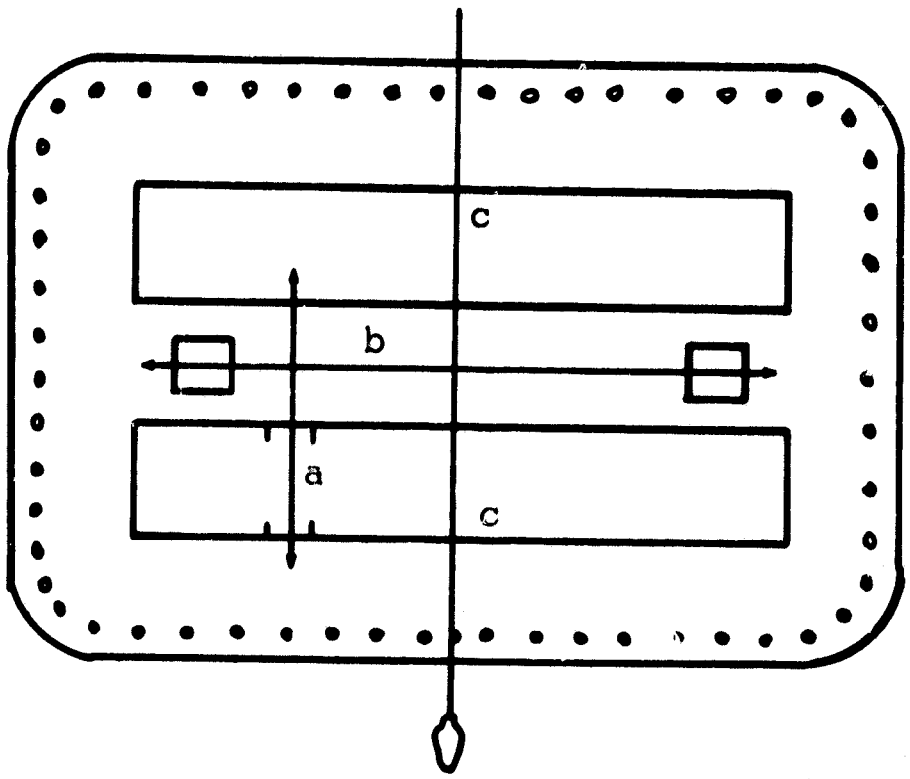


Figure 14 Antenna Reference Axes

Evaluation of Alignments

The accuracy of these mechanical alignments with respect to the boresight table are 2 minutes of an arc in the fore-aft and port-starboard planes and 4 minutes of an arc in the skew plane. This results in errors of 0.033 degrees and 0.066 degrees, respectively.

Since there is interaction between fore-aft and port-starboard adjustments, it was necessary to repeat the adjustments several times until 0^{o} was obtained in both planes.

B. Aircraft Installation Errors

To establish a reference for the aircraft installation error, it is necessary to define the procedure. The aircraft was first leveled using standard leveling procedures. A jig was then manufactured from a piece of flat stock complete with a collar around the edge. This jig was inserted into a hole cut into the base of the fuselage for the Ryan antenna. After leveling the jig very accurately using a clinometer, a scribe was used to describe the contour of the fuselage around the collar. The jig was then shipped to Ryan for precision tooling. As this was accomplished, the jig was used to shape the Ryan Scatterometer antenna. The antenna was then precision boresighted on the boresight pattern range and shipped to MSC for installation into the aircraft. The antenna was leveled. The difference between the aircraft level and the Ryan antenna measurements is as follows:

B.1 Pitch Error

The measured pitch installation error is 0.4 degrees (nose up). The resultant error in sigma zero is 0.8 db for the worst case. However, this error source will be completely removed by shifting the antenna gain table by 0.4 degrees.

B.2 Roll Error

The measured roll installation error is 0.3 degrees (right wing high). The resultant error in sigma zero is 0.3 db at the vertical. The error of a given angle may be determined by the equation $\vec{\theta}_i \approx \vec{\theta}_o + \vec{R}$. For example, the error at $\theta_o = 3$ degrees is 0.03 degrees. Beyond 3 degrees the error diminishes rapidly.

B.3 Azimuth Error

The azimuth installation error is $\pm$ 10 minutes of an arc maximum. The azimuth installation error causes a slight smearing of the resolution cells (0.17 degrees). This error is well within the maximum allowable azimuth error (due to all sources) of 2.5 degrees.

C. Directly Related Flight Parameters

The flight parameters which have a direct relation to the recorded data are altitude and velocity. The accuracy of the equipment measuring these parameters will, therefore, have an effect upon the accuracy of determining sigma zero.

C.1 Radar Altitude

The accuracy of determining altitude for reflectivity measurements depends upon the accuracy of:

- The AN/APN-22 System
- The readout instrument
- Reading the Photo Panel film.

The accuracy of the radar altitude is dependent upon the tolerance of the AN/APN-22 system. In the absence of detailed information giving the error tolerances, we shall assume the system accuracy to be $\pm$ 5.0% (2 sigma) of the measured altitude.

The sensitivity of sigma zero to altimeter errors may be obtained by taking a partial derivative of sigma zero with respect to the altitude, h.

$$\frac{\partial \sigma_o}{\sigma_o} = \frac{2 \Delta h}{h}$$

Thus, the APN-22 causes a maximum error of 0.41 db or 0.24 db rms.

The tolerance of the satellite instrument mounted on the photo panel, in the absence of accurate information, shall be assumed to be $\pm$ 2% (2 sigma) of the total altitude. The error in sigma zero due to the error of this instrument is $\pm$ 0.18 db or $\pm$ 0.1 db rms.

The accuracy to which the altimeter reading may be interpreted is the major source of system error. Since the instrument is

calibrated in a logarithmic scale, the present reading accuracy is a step function, the most extreme inaccuracy occurring at the 1000, 5000 and 10,000 foot levels. The maximum error below 10,000 feet is 20%. The rms errors below 10,000 feet is 11.6% of the measured altitude. The error in sigma zero is $\pm$ 1.5 db $\pm$ 0.87 db rms.

It is recommended that the barometric altitude be used on missions at or above 10,000 feet due to the large errors in interpreting the logarithmic meter on the photo panel.

C.2 Velocity

The accuracy of measurement of the aircraft ground speed used in analysis of the scatterometer data depends upon the following:

- AN/APN-131
- Readout instrument accuracy
- Reading accuracy from photo panel film

The accuracy of the AN/APN-131 system is assumed to be $\pm$ 2% (2 sigma) of the total velocity in the absence of detailed information on the system.

The sensitivity of the error in sigma zero to velocity errors can be found by the following equation,

$$\frac{\partial \sigma_o}{\sigma_o} = \frac{\Delta V}{V}$$

The error in sigma zero due to this effect is $\pm$ 0.085 db or $\pm$ 0.049 db rms.

The accuracy of the readout instrument is assumed to have the same tolerance as the AN/APN-131 system. Again, by substituting this error into a partial equation, the resultant error in sigma zero may be found. This error is $\pm$ 0.085 db or $\pm$ 0.049 db rms.

The measured error in velocity on a given mission from the beginning to the end of a run has been approximately 20 knots. Since fixed frequency filters are used to represent fixed incidence angles in the present data reduction procedures, large errors can occur due to velocity variations. The effect of velocity changes will be greatest at the highest frequencies (largest incidence angles) where the rate of change of power with respect to frequency is at its maximum value.

D. Indirectly Related Aircraft Information

Aircraft pitch, roll and drift angles will affect the accuracy of determining the sigma zero versus theta information. When the magnitudes of these angles are known, the resultant errors can be determined. Thus, the primary concern is the accuracy to which pitch, roll and drift are known. The errors due to these parameters include errors in the measuring equipment and the errors in reading these parameters on the photo panel. These errors will add to the smearing or blurring of the recorded data.

The data will not be analyzed if the blurring is more than one-half of a resolution cell. The effect of the errors will also depend upon the availability of the pitch, roll and drift data and the ability of the computer program to compensate for the pitch, roll and drift angles.

D.1 Pitch Errors

The pitch error of the on-board equipment is assumed to be $\pm$ 0.4 degrees in the absence of accurate information. The reading error of the pitch angle information is $\pm$ 0.44 degrees.

D.2 Roll Errors

The roll error of the on-board equipment is assumed to be $\pm$ 0.4 degrees in the absence of accurate information. The reading error in the roll angle information is $\pm$ 0.44 degrees.

D.3 Drift Errors

The drift error of the on-board equipment is assumed to be $\pm$ 0.5 degrees, in the absence of accurate input data. The reading error in the drift angle information is $\pm$0.5 degrees.

E. Errors in Signal Density Measurement

Errors in the measurement of signal density can be divided into errors in the calibration of the ferrite modulator and errors in the data reduction process.

E.1 Ferrite Modulator Calibration

The ferrite modulator consists of a ferrite device in a waveguide section. The ferrite modulator is installed on the receiver side of the scatterometer between the coupler and the microwave detector. A coil is wrapped around the outside of the ferrite. The coil is excited by an audio oscillator.

The ferrite modulator was precisely calibrated using a standard noise bench. The purpose of the bench is to determine the noise figure of diodes used in various doppler navigation systems. The noise bench is calibrated for an operating frequency of 13.3 GHz. The primary calibration source for the noise bench is a precision noise lamp.

The ferrite modulator calibration consisted of the following basic steps: (1) Determination of RF power into the ferrite modulator; (2) Measurement of ferrite modulator insertion loss; (3) Measurement of power output versus coil voltage, RF power, frequency and temperature.

The RF power into the ferrite modulator was determined by replacing the ferrite modulator with a power meter on the actual antenna assembly. Thus, this measurement included the following

factors: The actual klystron power to be used in the flight test program, the attenuation in this power due to the intentional transmitter-receiver leakage power, the waveguide losses, and the unintentional transmitter-receiver leakage power.

The ferrite modulator insertion loss was determined by measuring the RF power with and without the modulator in place. This reading was very accurate since only the differential value was required. The measured value was 0.3 db.

The output power was measured as a function of coil voltage, RF power, frequency and temperature. The output power was measured to be proportional to the square of the coil voltage (directly proportional to the coil power) for coil voltages between 40 mv and 1 volt, and directly proportional to the input RF power for RF powers between 0 and -10 dbm. The modulator output power decreased with increasing audio frequency. The modulator power output was constant ($\pm$ 0.2 db) within the temperature range of interest (+10 to +60 degrees centigrade).

The equations for the signal power density received from the ground (W_s) and the sideband power out of the ferrite modulator are,

$$W_s = \frac{P_T G_o^2 \lambda^3 \sigma_o(\theta, \phi) f'(\theta) L_f}{2(4\pi)^3 V h^3}$$

and $P_m = P_T B L_f G_f V_c^2$

where P_T is the transmitted signal power, L_f is the ferrite modulator insertion loss, B is transmitter-receiver coupling factor, G_f is the ferrite modulator gain factor for the modulation frequency (10 KHz), and V_c is the coil voltage.

The absolute value of sigma zero is computed from the ratio of W_s/P_m. When this ratio is computed, the transmitted power (P_T) and the modulator insertion loss (L_f) cancel out. Therefore, the ferrite modulator makes the computation of sigma zero independent of these two parameters (or to errors in the measurement of these two parameters).

The error in the measurement of the ferrite modulator power output is determined by the errors in the measurement of the following four parameters: the transmitter-receiver coupling factor, the ferrite modulator gain factor, the setting of the coil voltage, and the setting of the coil frequency.

The transmitter-receiver coupling factor is measured with a power probe. The maximum error in this measurement is $\pm$ 0.5 db. Assuming an equally probable error distribution, the rms error in measurement is $\pm$ 0.29 db. The ferrite modulator gain factor is also measured to an accuracy of $\pm$ 0.5 db or an rms error of $\pm$ 0.29 db using a rectangular error distribution. The meter

used to read these voltages is a Ballentine Model 302C whose accuracy is ± 3% of the reading or ± 0.3 db maximum. Again, using a rectangular error distribution, the rms error is ±0.17 db.

The accuracy of the coil frequency depends upon the stability and repeatability of the audio oscillator. The audio oscillator used is a Hewlett-Packard Model 241A. The long term stability of this audio oscillator is 0.04% or ± 0.02 db. The repeatability is 0.02% or ± 0.01 db.

E.2 Analog Reduction Process

The analog reduction process consists of preparing a dubbed copy of the flight data tapes to be analyzed and using one or more of the following analog analysis procedures to reduce the data.

The analog analysis process can be divided into two categories. The first category is data verification procedures and the second is data analysis procedures. The purpose of the data verification procedures is to establish the data quality. The data analysis procedures are those methods employed to prepare the data for automatic processing on the digital computer.

Two methods have been used for data verification. One method is to cut a short loop from the tape dub and play this loop into a sweeping filter spectrum analyzer. The output of the spectrum analyzer is amplitude versus frequency. The amplitude

of the spectrum analyzer is fed through a logrithmic converter (so that the amplitude will be in db) and into the vertical scale of the x-y plotter. The frequency (analog) output of the spectrum analyzer is fed to the x-axis of the plotter. The analyzer is then swept over the frequency band of interest to yield a plot of amplitude versus frequency. A time-stationary sigma zero versus angle of incidence plot can be derived from the recorded signal spectrum.

The second method of verifying the data consists of using the same equipment as above in a slightly different configuration. This configuration consists of using the entire test run, setting the spectrum analyzer at a specific frequency, and sweeping the x-y plotter in real time. The resultant recording is the time history of the amplitude of a specific frequency band. The tape recorder is stopped at the end of the run and rewound. Then the center frequency of the spectrum analyzer filter is shifted to a new value and another time history plot is made. This process is normally repeated for about six incidence angles, the 10 KHz calibration signal and the system noise.

The first process in preparing the data for the digital computer is a frequency domain separation of the signal with a bank of parallel filters. The filter outputs are detected, averaged and recorded in dc form on separate channels of an analog tape.

recorder. The analog tape is then processed by an analog-to-digital converter and recorded on digital tape for use in computer processing.

The accuracy of the analog processing is presently unknown. However, large errors have been encountered due to various sources of signal-to-noise ratio degradation. A test tape is being prepared which is designed to determine the errors in the analog analysis process. The various error sources include gain stability, dynamic range, phase shifts, errors in setting filter frequencies and bandwidths, errors in the linear detectors, errors in the dc analog recording, and errors in the analog-to-digital conversion. Addendums to this error analysis will be provided as soon as the magnitude of these errors is known.

E.3 Digital Reduction Process

The digitized tapes from the analog reduction process are used on digital computers along with information on aircraft flight parameters and systems constants to compute the sigma zero curves. The computer output is then plotted using automatic plotting equipment. The functional accuracy of this digital computer program has been measured by a test tape to be 0.1 db maximum. However, the significant errors in the program are due to not compensating for changes in radar altitude or aircraft ground speed. Errors in the values of sigma zero and the incidence

angles can be as much as 6 db and 5 degrees, respectively, due to using constant altitude and velocity. In addition, the ground resolution cells can be smeared excessively.

2.4.2 Summary of Error Analysis

This report presents analysis of the errors in computing sigma zero. The errors are divided into the following general categories: errors attributable to the scatterometer itself, errors attributable to aircraft instrumentation, and errors attributable to the data reduction process. The errors due to these sources affects the final data in the following four areas: (1) errors in the magnitude of sigma zero, (2) errors in the incidence angle values, (3) errors in the sign sensing process, and (4) errors in the correlation of the data.

The rms errors in the magnitude of sigma zero are $\pm$ 0.64 db for the scatterometer, $\pm$ 0.95 db for the aircraft instrumentation effects, and $\pm$ 1.0 db (assumed) for the data reduction system. Thus, the total rms error in the magnitude of sigma zero is $\pm$ 1.54 db.

The rms errors in the values of the incidence angles are $\pm$0.1 degrees due to the scatterometer, $\pm$ 0.3 degrees due to aircraft instrumentation, and $\pm$ 0.1 degrees (assumed) due to the data analysis process.

The total effect upon the sign sensing system is $\pm$ 1 db in gain unbalance and $\pm$ 5 degrees in phase shift, which results in a sideband separation of 22 db.

Data correlation errors are very difficult to classify quantitatively. Errors in timing cause difficulty in the correlation of sigma zero curves with aerial photos. Thus, timing errors cause an effective blurring of the resolution cells. Aircraft pitch, roll and drift also cause a blurring of the resolution cells. In general, if the blurring of the resolution cell is determined to be greater than one-half the size of the resolution cell, the data is not processed.

The various errors are summarized in Tables I, II and III and in Figures 15 and 16. Table I presents the errors in the magnitude of sigma zero. Tables II and III present the errors in incidence angle and the azimuth angle. Figure 15 shows the altimeter reading errors as a function of altitude. Figure 16 shows the velocity sensor reading errors as a function of velocity.

TABLE I

ERRORS IN THE MAGNITUDE OF SIGMA ZERO

Error Source	Magnitude	Sensitivity	Maximum Error	RMS Error
KLYSTRON				
1. Precision Attenuator Calibration	± 2.0% **	ΔP_T	±0.73 db	±0.42 db*
2. Power Meter Calibration	± 5.0%	ΔP_T	±0.22 db	±0.13 db*
3. Filament Voltage				
A. Voltage Adjustment	± 0.1%	ΔP_T	negligible	negligible
B. Voltmeter Accuracy	± 1.0%	ΔP_T	±0.03 db	±0.02 db
FERRITE MODULATOR				
1. Initial Calibration	± 0.5 db	ΔW_s	±0.5 db	±0.29 db
2. Temperature Variations	± 0.1 db	ΔW_s	±0.1 db	±0.06 db
3. Adjustment of Voltage	± 3.0%	ΔW_s	±0.26 db	±0.15 db
WAVELENGTH				
1. Manufacturing Tolerance	± 5.0 MH_Z	$3\Delta\lambda$	negligible	negligible
TWO-WAY ANTENNA PATTERN FACTOR				
1. Relative and ABSOLUTE GAINS	± 0.5 db	ΔG	±0.5 db	0.29 db
ROLL-OFF CHARACTERISTICS				
1. Ballentine Voltmeter Accuracy	± 3.0%	ΔG	±0.26 db	0.15 db
2. Amplifier Stability				
A. Millivac Preamplifiers	± 1.0 db	ΔG	±1.0 db	0.58 db
B. Kin Tel Boost Amplifiers	± 0.1%	ΔG	±0.018 db	0.01 db

* These errors are reduced to zero by the use of the ferrite modulator.
** ± 2% of reading in db.

TABLE I

ERRORS IN THE MAGNITUDE OF SIGMA ZERO

(Continued)

Error Source	Magnitude	Sensitivity	Maximum Error	RMS Error
VELOCITY				
1. Equipment Accuracy	± 2.0%	ΔV	0.085 db	0.049 db
2. Readout Instrument	± 2.0%	ΔV	0.085 db	0.049 db
3. Reading of Photo Panel Film	± 0.5 Knots	ΔV	0.021 db	0.012 db
ALTITUDE				
1. Equipment Accuracy	± 5.0%	$2\Delta h$	0.41 db	0.24 db
2. Readout Instrument	± 2.0%	$2\Delta h$	0.18 db	0.1 db
3. Reading of Photo Panel Film	± 20.0%	$2\Delta h$	1.5 db	0.87 db
THERMAL CHANGES				
1. Klystron	100 KC/°C	ΔP_T	±0.04 db	±0.023 db
2. Tape Recorder	± 0.5 db	ΔG	±0.5 db	±0.29 db
3. Millivac Preamplifier	(DATA NOT AVAILABLE)			
4. Kin Tel Boost Amplifier	(DATA NOT AVAILABLE)			

TABLE II

ERRORS IN INCIDENCE ANGLE

Error Source	Maximum Error	RMS Error
BORESIGHT ACCURACY		
1. Fore-Aft	± 0.033 DEG	± 0.02 DEG
READING OF PHOTO PANEL		
1. Pitch Error	± 0.44 DEG	± 0.23 DEG
ON-BOARD EQUIPMENT		
1. Pitch Error	± 0.4 DEG	± 0.23 DEG
TWO-WAY ANTENNA PATTERN FACTOR		
1. Angular Position Errors	± 0.166 DEG	± 0.096 DEG
INSTALLATION ERRORS		
1. Pitch Error	± 0.4 DEG	*

* This error is of known magnitude and sense and will be removed by a change in the computer program.

TABLE III

INDIRECTLY RELATED ERRORS

Error Source	Maximum Error	RMS Error
INSTALLATION ERRORS		
1. Roll Error	- 0.3 DEG	*
2. Skew	± 0.166 DEG	± 0.09 DEG
ACCURACY OF ON-BOARD EQUIPMENT		
1. Roll	± 0.4 DEG	± 0.23 DEG
2. Drift	± 0.5 DEG	± 0.29 DEG
ACCURACY OF PHOTO PANEL READING		
1. Roll	± 0.44 DEG	± 0.23 DEG
2. Drift	± 0.5 DEG	± 0.29 DEG
BORESIGHT ACCURACY		
1. Port-Starboard	± 0.033 DEG	± 0.02 DEG
2. Skew	± 0.066 DEG	± 0.038 DEG

* This error is of known magnitude and sense and may be removed by a change in computer program.

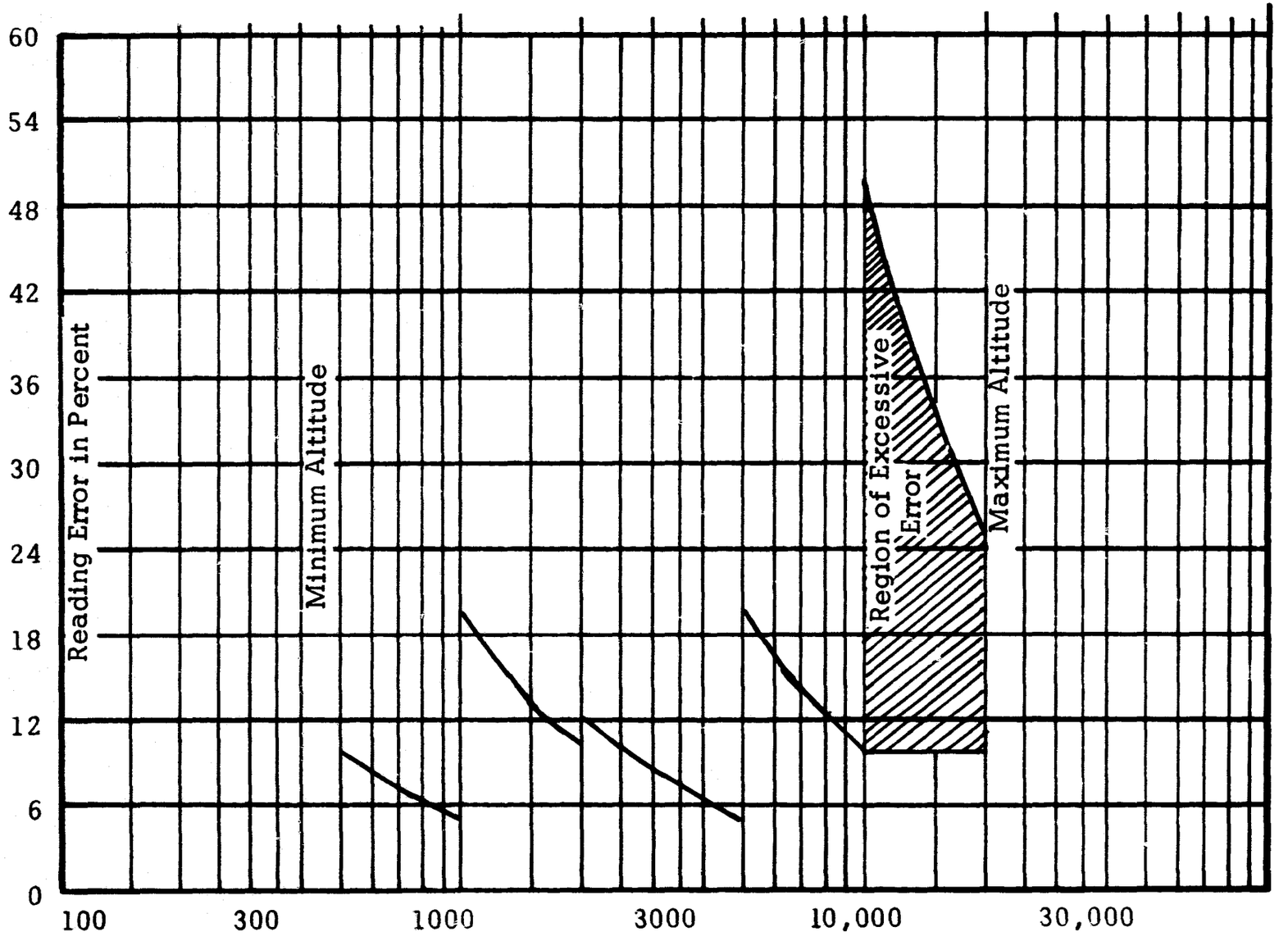

60
54
48
42
36
30
24
18
12
6
0
Reading Error in Percent
Minimum Altitude
Region of Excessive Error
Maximum Altitude
100
300
1000
3000
10,000
30,000
Photo Panel Reading Error

Figure 15

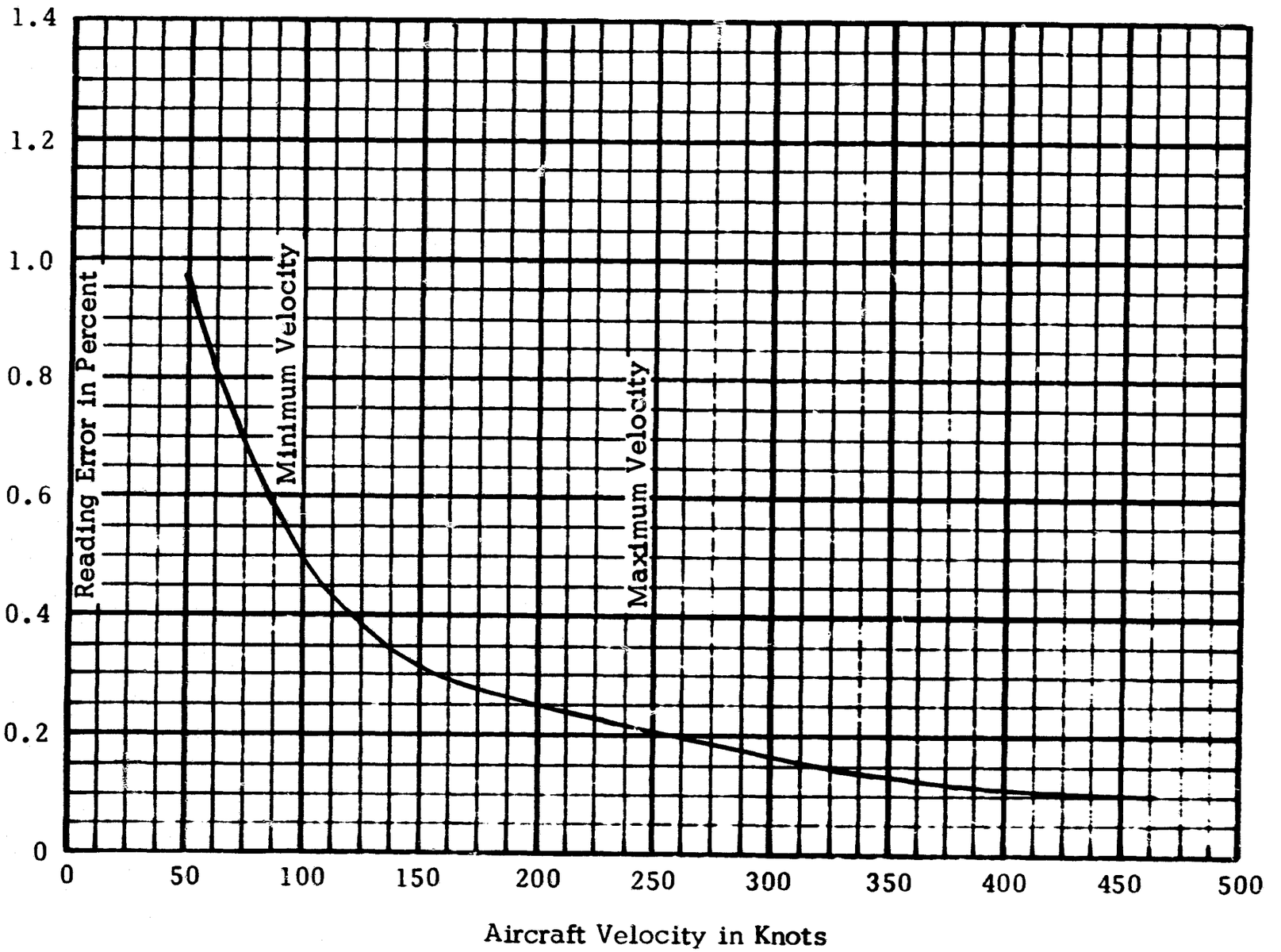


Figure 16 Velocity Sensor Reading Error

2.5 ANALYSIS OF NEAR-VERTICAL RETURN

In the present comb filter data analysis technique, the center frequencies of the filters are adjusted to correspond to incidence angles of 5, 10, 15, 20, 30, 40, 50, and 60 degrees. The bandwidths of the filters are adjusted to span one resolution cell on the ground at each incidence angle. Because of a desire to look at data from incidence angles less than 5 degrees, a study was made to determine how close to the nadir that reliable data could be obtained.

The theoretical resolution in the fore-aft direction is limited only by the bandwidth of the analysis filter at incidence angles of 2.5 degrees or greater. At incidence angles less than 2.5 degrees, the theoretical resolution decreases until it equals one-half the port-starboard beamwidth or 1.25 degrees at the nadir. The only additional theoretical limiting factor is introduction of a notch filter for isolation purposes at zero cps.

The effect of the notch filter can be readily determined by a knowledge of its bandwidth and the normal aircraft velocity. For this system, these values are 8 Hz and 160 knots, respectively. The width of the notch can be calculated from the equation,

$$\phi \approx 1.25 \frac{\xi}{V}$$

where ξ is the half bandwidth of the notch filter in Hz and V is the aircraft velocity in knots. For this case,

$$\phi \approx 0.03 \text{ degrees}$$

which is far less than the amplitude of the aircraft's phugoidal oscillations. The aircraft's vertical motion caused by these oscillations will perturbate the angular position of the notch about zero degrees.

Another method of studying the effects of the notch filter is to determine the amount of power loss due to this filter. Assuming an equally probable (rectangular) distribution of power within the analysis filter, the power loss can be easily computed. Again, assuming a nominal case of 160 knots, the width of the first analysis filter will be 370 Hz The power loss is equal to the ratio of the bandwidths, which is 0.022 or less than 0.1 db.

In addition to the theoretical limitations on how close to the nadir the data can be reliably used, spurious noise also causes certain limitations. In the case of the present scatterometer as installed in the CV-240 aircraft, the spurious noise consists of 400 and 60 Hz noise components. One of these spurious noise components could be completely eliminated by converting the system to either all 400 or all 60 Hz operation.

The present data can be analyzed at a frequency of 160 Hz, which is approximately half-way between the two spurious noise signals (on a log scale). Using a 50 Hz wide analysis filter, the two spurious signals will be attenuated by at least 24 db, which would make them insignificant. A slight computer program modification would be required to average over the proper time interval so that the resolution cell size would not be changed.

2.6 EQUAL BEAMWIDTH EQUATIONS

The present Scatterometer system can be used to simulate fixed narrow beamwidth systems such as those on Surveyor or the Lunar Module. The H-plane (transverse) beamwidth is 2.5°. A 2.5° beamwidth can be simulated in the E-plane (fore-aft direction) by proper filter bandwidth settings during the data reduction process (see Figure 17). The equations for the upper and lower bandwidth settings of the 2.5° envelope are derived below.

The basic equation under consideration is the doppler frequency equation,

$$F_d(\theta) = (45.646\ V \sin \theta)\ \text{Hz}$$

where V = aircraft velocity in knots, and θ is the angle measured from the vertical.

To obtain the center frequency setting of an analysis filter for a particular angle, say 5°, the velocity must be known in knots and the equation solved for $F_d(5^\circ)$.

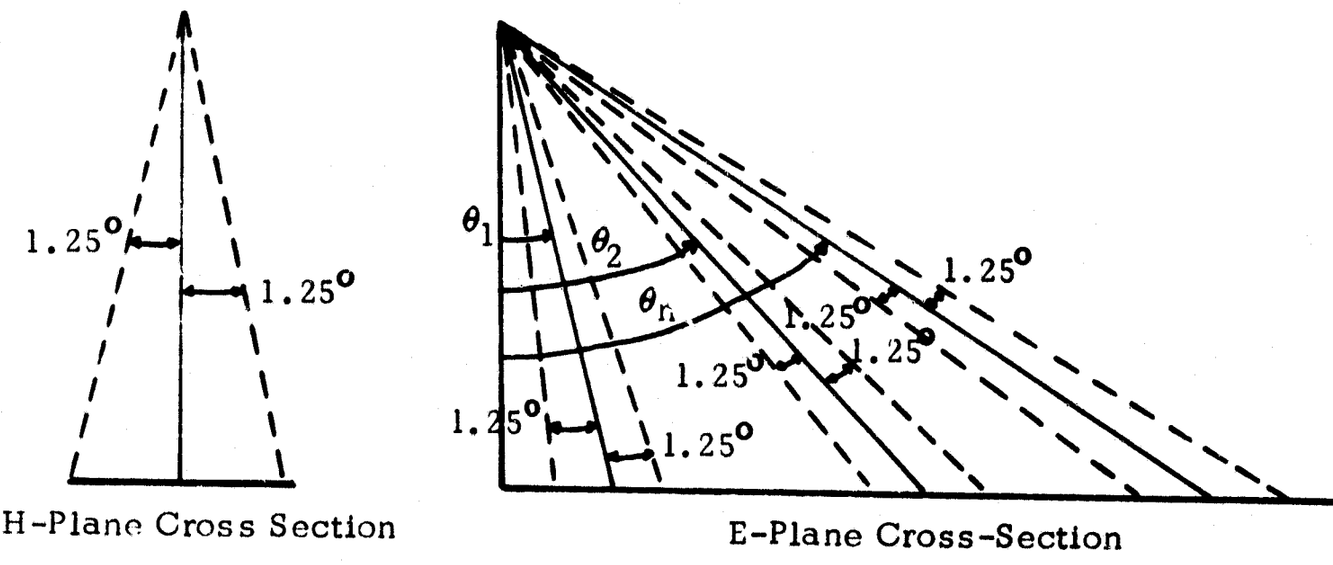


Figure 17

First, a series of constants can be defined. The center doppler frequency constant,

$$K_{f_d} = 45.646 \sin \theta \qquad \text{Hz/kt}$$

The frequency constant for $\theta + 1.25^{\circ}$,

$$K_{f_{d+}} = 45.646 \sin (\theta + 1.25^{\circ}) \qquad \text{Hz/kt}$$

The frequency constant for $\theta - 1.25^{\circ}$,

$$K_{f_{d-}} = 45.646 \sin (\theta - 1.25^{\circ}). \qquad \text{Hz/kt}$$

Finally, a bandwidth constant K_{BW} is defined as,

$$K_{BW} = K_{f_{d+}} - K_{f_{d-}}$$

To relate the center doppler frequency to the center frequency of the bandwidth the following equations were developed,

$$\text{Upper Frequency} = K_{f_d} V + \frac{K_{BW}}{2} V \qquad \text{Hz}$$

$$\text{Lower Frequency} = K_{f_d} V - \frac{K_{BW}}{2} V \qquad \text{Hz}$$

To obtain the actual filter settings to be used, a compensation must be made in the carrier frequency of the sign sense detector.

$$\text{Actual upper frequency setting} = 20 \times 10^3 - (K_{f_d} V - \frac{K_{BW}}{2} V) \qquad \text{H}$$

$$\text{Actual lower frequency setting} = 20 \times 10^3 - (K_{f_d} V + \frac{K_{BW}}{2} V) \qquad \text{H}$$

Substituting for K_{f_d} and K_{BW} in these last two equations and simplifying through the use of trigonometric formulas the final result becomes:

$$\text{Actual upper frequency setting} = 20 \times 10^3 - 45.646V (\sin \theta - A \cos \theta)$$

$$\text{Actual lower frequency setting} = 20 \times 10^3 - 45.646V (\sin \theta + A \cos \theta)$$

$$\text{where } A = \sin 1.25^{\circ} = .02181$$

2.7 METHODS OF OBTAINING THE SLOPE OF THE σ_o CURVES

The correlation of σ_o plots with associated terrains can at times be improved with plots of their derivatives.

Two methods of obtaining the slope of the σ_o curves are presented in this appendix. The first method is more precise than the second but also more complex to implement. The second is less precise, but it is simpler to implement. Either of these techniques could be added on to the present computer program as an additional routine.

The first method uses a best fit, n^{th} order, polynomial in θ for each σ_o versus θ curve, i.e.,

$$\sigma_o = \sum_{i=o}^{n} a_i (\theta)^i$$

or

$$\sigma_o = a_o + a_1\theta + a_2\theta^2 + \ldots + a_n\theta^n$$

The next step would be to take the term by term derivative of σ_o with respect to θ :

$$d\,\sigma_o/d\theta = a_1 + 2a_2\theta + 3a_3\theta^2 + \ldots a_n\theta^{n-1}$$

This process, then, results in an $(n-1)^{th}$ order polynomial of the form,

$$d\,\sigma_o/d\theta = \sum_{i=1}^{n} ia_i (\theta)^{i-1} = \sum_{i=1}^{n} b_{i-1}(\theta)^{i-1}$$

or,

$$d\,\sigma_o/d\,\theta = b_o + b_1\theta + b_2\theta^2 + \ldots + b_{n-1}(\theta)^{n-1}$$

The process is completed by solving the above for different values of and plotting the results as a curve of $d\,\sigma_o/d\,\theta$ versus θ . Figure 18 is a block diagram of this method.

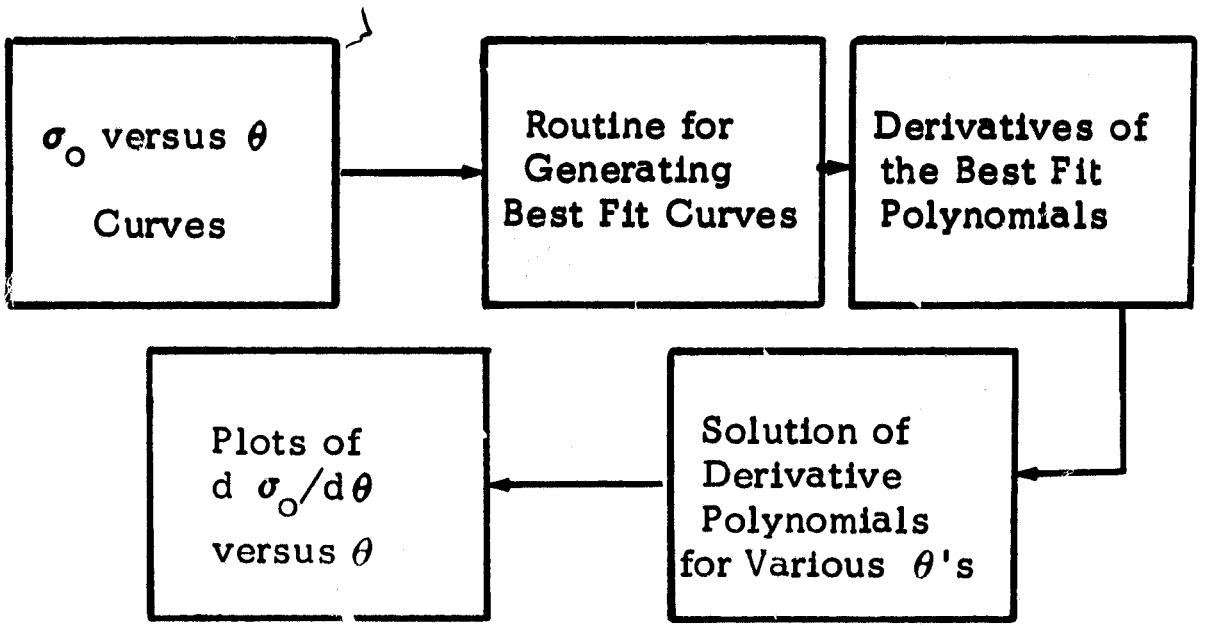


Figure 18

Best Fit Method Block Diagram

A second method would use an approximation and averaging technique to find $d\,\sigma_o/d\,\theta$ for each σ_o versus θ curve. On each curve, begin with the first three successive (θ, σ_o) points.

Assuming a straight line between the first and middle point, compute the slope using the simple tangent formula,

$$\text{Slope} = \frac{\Delta\,\sigma_o}{\Delta\,\theta}$$

Next assume a straight line between the middle and third points and compute this slope as above. The average of these two computed slopes should give an approximation to the slope at the middle point. This average slope, then, corresponds to $d\sigma_o/d\theta$ at the middle θ value and is plotted as a point on a new curve of $d\sigma_o/d\theta$ versus θ. The process continues by dropping one point and advancing to the next three points, where the 1st and 2nd points of this new group are the 2nd and 3rd points of the last set (see Figure 19). The slopes are again computed along with their average so that the result is an approximation to the slope at the new middle point. It is noted that when the process is completed, there will be n-2 points on the $d\sigma_o/d\theta$ versus θ curve, where n equals the number of points on the original σ_o versus θ curve. (The slope at the first and last points on the curve cannot be computed by this technique.)

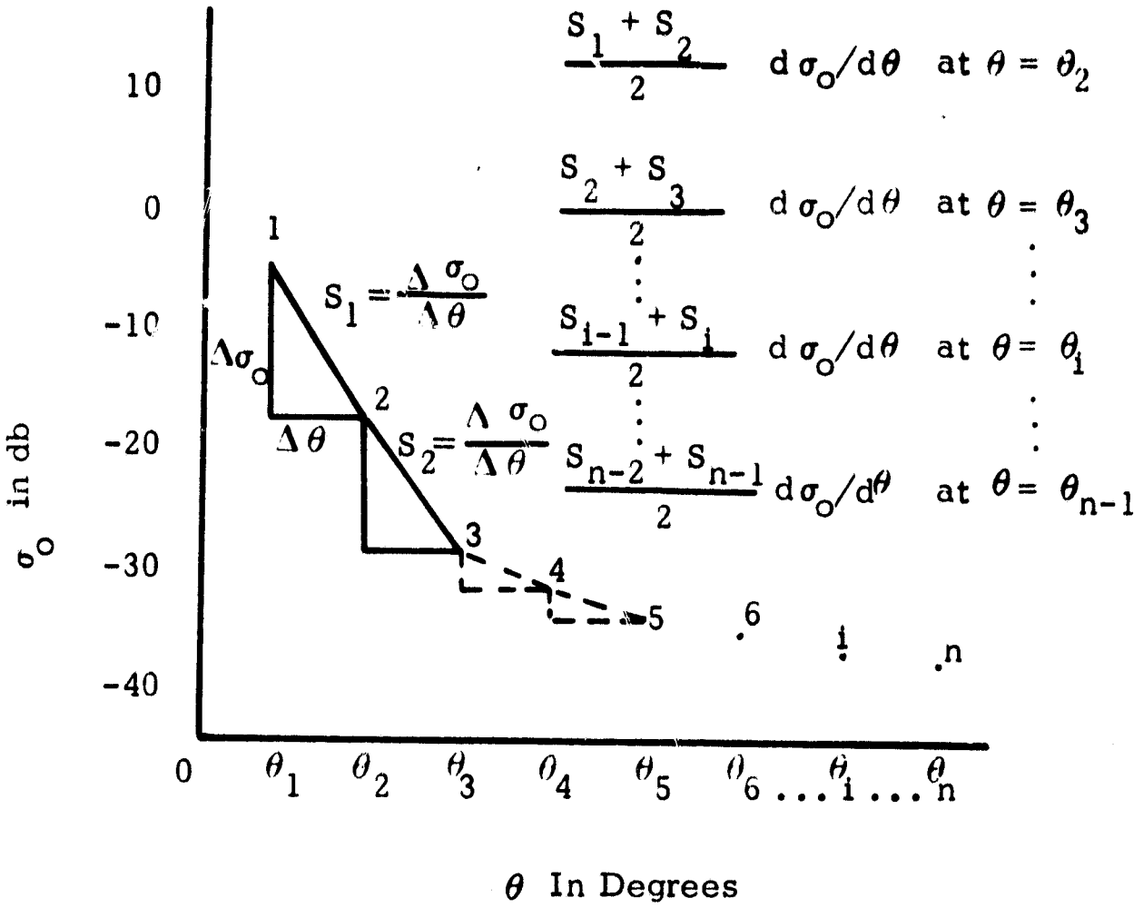


Figure 19

Average Slope Method

2.8 FERRITE MODULATOR (BASIC CALIBRATOR)

Every radar back-scattering measuring system depends upon some secondary standard or relative method for establishing the power level of the received signal. The scatterometer utilizes a ferrite modulator as a means of injecting a reference calibration 10 KHz signal on the doppler spectra. A complete description of this device is required to show the validity of the application.

In general, the behavior of an electromagnetic wave in passing through a medium may be completely characterized by Maxwell's equations and three parameters of the medium - the permeability μ, the dielectric coefficient ξ and the attenuation factor α. All three parameters will, in general, depend on frequency, but for a homogeneous isotropic material, they may be represented by (space) scalar quantities. In addition, the attenuation factor, for a homogeneous medium, will simply make a contribution of the form $I(x) = I_o e^{-\alpha x}$, where I_o is the intensity of the incidence EM wave, x is the distance traversed in the medium and I (x) is the intensity at a point x in the medium. So, in this discussion we will set $\alpha = 0$, i.e., assume a lossless material.

A material characterized by scalar μ and ξ will behave impartially with respect to EM waves impingent from various directions, that is, there are no natural axes or directions within the material. However, there do exist materials which, although homogeneous, exhibit different values of μ or ξ or both along 1, 2, or 3 axes. The familiar example

from optics is the dichroic crystal which has different values of dielectric coefficient ξ along two directions in the crystal. Thus, in the plane formed by these two axes electromagnetic waves will propagate with uniform phase velocity independent of the orientation of the electric vector. However, in the direction perpendicular to this plane, the EM wave will propagate with a phase velocity which depends on the $\vec{E}$ vector orientation. Therefore, when a plane polarized wave passes through the crystal in the perpendicular direction, the $\vec{E}$ component along the axis having the smaller value of ξ "gains" on the component which is parallel to the axis of larger ξ, and the net result is that the plane of polarization rotates at a constant rate during passage through the medium.

At microwave frequencies, it has been found that the class of materials of typical composition $Mn_a\ Zn_{(1-a)}\ Fe_2\ O_4$ or $Ni_a\ Zn_{(1-a)}\ Fe_2\ O_4$, known as ferrites, can be made to exhibit an analogous "magnetic dichroism" when placed in a strong static magnetic field. The effect of a medium which is anisotropic in μ is most naturally analyzed in terms of circular rather than plane polarized components, and the procedure is outlined in Section B2 of this Appendix. It turns out that, for an electromagnetic wave propagating through a ferrite material along the direction of the static external magnetic field, clockwise and counterclockwise components rotate at different rates. Now, any plane polarized wave may be resolved into two components rotating in opposite directions (See Figure 20) at the same angular rate. If the wave now enters the ferrite traveling in

the direction of the magnetic field, the clockwise component, $\vec{H}+$, rotates faster than $\vec{H}-$. If the direction of propagation (or the field) is reversed, then $\vec{H}-$ rotates faster. In either case, it can be seen that the resultant vector $\vec{H}$ rotates in the direction of the faster moving component at one half the difference of the angular rates.

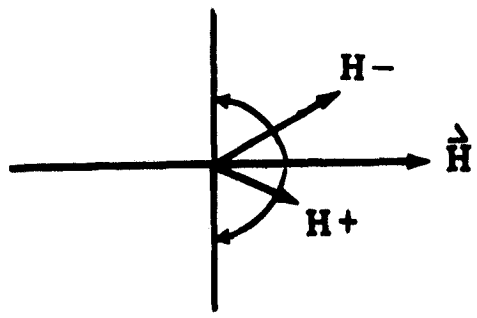


Figure 20

Ferrite devices utilizing this rotation property are commercially available and have been used extensively in the waveguide plumbing of modern radar systems. The principle applications have been (1) load isolator, (2) gyrator, and (3) circulator. All three devices operate in the same general way, and may be indicated schematically as in Figure 21.

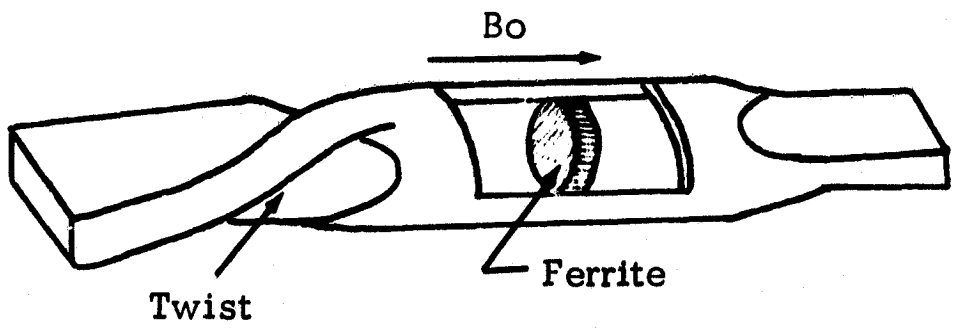


Figure 21

The orientation of the electric and magnetic vectors for the TE_{10} propagation mode are shown in Figure 22.

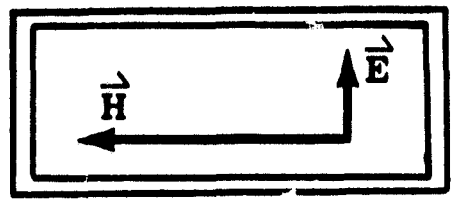


Figure 22

For a general orientation of an electromagnetic wave impinging on a section of waveguide, only that component with the orientation shown in Figure 22 will be passed. The rest of the energy will be reflected or may be absorbed in a dummy load placed at this point. Thus, in the load isolator, the twist in the waveguide and the ferrite each produce a 45° rotation. The twist preserves sense of rotation, i.e., is either plus for both directions or minus for both directions. But the ferrite will produce a plus rotation for a wave traveling in one direction and a minus rotation for a wave moving in the opposite direction. Therefore, a wave traveling in one direction experiences a rotation of $45° - 45° = 0°$ and passes through unimpeded, but a wave moving in the opposite direction undergoes a rotation $45° + 45° = 90°$ and is completely absorbed (or reflected). The gyrator utilizes two 90° rotations and the resultant angles are 0° and 180° , so no absorption occurs in either direction. The circulator utilizes a long piece of ferrite and several waveguide taps oriented in such a way that the EM wave inserted at a given tap is always in the proper phase to emerge at one adjacent tap and none of the others.

The ferrite modulator may be regarded as a special application of the load isolator discussed above. The r.f. signal is sent through the device in the direction which would normally produce absorption, i.e., towards the dummy load. Now, however, no d.c. field is applied and in the absence of modulation, the r.f. signal simply encounters an isotropic dielectric medium and passes through unchanged. The audio frequency modulation is applied longitudinally (by a solenoidal winding about the ferrite) and appears essentially as d.c. to a small segment of the r.f. signal. The previous discussion applies and there is a slow sinusoidal oscillation of the plane of polarization about the configuration shown in Figure 22. The absorption is proportional to the sine of the angle by which the polarization plane deviates from the TE_{10} configuration. For small angles (small amounts of modulation), the absorption is proportional to the angle of rotation, and if the rotation were in turn proportional to the applied modulating field, the desired amplitude modulation would result. However, we have assumed throughout this discussion that the ferrite is saturated by the external field. Clearly, this cannot be strictly true for an a.c. field, and in actual practice ferrite devices are "tuned" by applying a small twist to the output section waveguide to achieve minimum harmonic distortion.

ANALYSIS OF A FERRITE MEDIUM

The purpose of this section is not to present a rigorous and detailed mathematical analysis of EM waves in magnetized ferrite material but to make qualitative determinations of their behavior. The static external

field here is an approximation to a short time segment of the slowly varying modulation signal and the a.c. field refers to the r.f. signal. The tensor structure of the permeability μ is deduced and then used to establish the basic result that the plane of polarization of an EM wave does rotate during passage through the ferrite. Finally, some approximate results are stated relating the angle of rotation to the applied field.

For a homogeneous isotropic material, the magnetic induction $\vec{B}$ is related to the field $\vec{H}$ and the magnetization $\vec{M}$ by,

$$\vec{B} = \mu(\vec{H} + \vec{M})$$

Here μ is a scalar quantity characteristic of the material and the three vectors are colinear. For a nonisotropic material, the vectors will not, in general, be colinear and the scalar μ must be replaced by a (9 element) tensor $\hat{\mu}$.

In order to deduce the structure of $\hat{\mu}$, we will assume the following model for a ferrite:

1. The basic domain unit will consist of individual bound spinning electrons.
2. The forces on the electrons will be due to the external induction $\vec{B}$ and internal coupling which is accounted for by the usual $\frac{\mu_o \vec{M}}{3}$ term (the aligning force due to nearest neighbor coupling will be abosrbed in this term and not accounted for explicitly).
3. Dissipative forces will be neglected ($\alpha = 0$).

We start with Newton's second law of motion in angular form,

$$\vec{T} = \frac{d\vec{J}}{dt}$$

where $\vec{J}$ is the angular momentum of the spinning charge and $\vec{T}$ is the applied torque. Angular momentum $\vec{J}$ and magnetic momentum $\vec{M}$ are related by,

$$\vec{M} = \gamma \vec{J}$$

where γ is the gyromagnetic ratio and will be treated as a scalar in this discussion. Also, the torque $\vec{T}$ may be written,

$$\vec{T} = \vec{m} \times \vec{B}_{tot} = \vec{m} \times (\vec{B} + \mu_o \frac{\vec{M}}{3})$$

We also note that $\vec{m}$ and $\vec{M}$ are related by,

$$\vec{M} = N_o \vec{m}$$

where N_o is the number of magnetic dipoles per unit volume. If these substitutions for $\vec{T}$, $\vec{J}$, and $\vec{m}$ are made above, the result is,

$$\frac{d\vec{M}}{dt} = \vec{M} \times \vec{B} = \mu_o \vec{M} \times \vec{H}$$

(μ_o is the permeability of free space). Now, we assume that the ferrite is saturated by the static external field $\vec{H}_o = \frac{\vec{B}_o}{\mu_o}$, i.e., all of the dipoles are aligned with $\vec{H}_o$. Next, we introduce a small a.c. component superimposed on the static field (representing the r.f. signal, not the

modulation which is assumed to be d.c.), then,

$$\vec{H} = \vec{H}_o + \vec{H}_1 e^{j\omega t}$$

$$\vec{M} = \vec{M}_o + \vec{M}_1 e^{j\omega t}$$

Substituting above and performing the differentiation gives,

$$j\omega \vec{M}_1 = a\mu_o \quad (\vec{H}_o \times \vec{M}_1) + (\vec{H}_1 \times \vec{\mu}_o)$$

Now, if we assume that the a.c. terms are small compared with the static terms, i.e., if we neglect products of a.c. terms, then we may write the preceeding relation in component form and compare term by term with the components of the tensor relation,

$$\vec{B}_1 = \hat{\mu} \vec{H}_1$$

After a little algebra, this yields the result,

$$\mu = \begin{bmatrix} \mu & -jk & 0 \\ jk & \mu & 0 \\ 0 & 0 & \mu_o \end{bmatrix}$$

where $\mu \equiv \mu_o + \dfrac{\mu_o^3 \gamma^2 M_o H_o}{\mu_o^2 \gamma^2 H_o^2 - \omega^2}$, $k \equiv \dfrac{\omega_o^2 M_o}{\mu_o^2 \gamma^2 H_o^2 - \omega^2}$

The explicit form of the tensor $\hat{\mu}$ of course depends on the coordinates used, and to obtain this particular representation we chose $\vec{M}_o$ and $\vec{H}_o$

to lie along the Z axis. Again, this assumption implies saturation (since $\vec{M}_o$ and $\vec{H}_o$ are parallel). Up to this point, we haven't placed any restrictions on the orientation of the r.f. term. Now, we wish to consider a circularly polarized plane wave propagating in the Z direction. Writing the tensor relation in component form,

$$B_{1x} = \mu H_{1x} - jK\ H_{1y}$$
$$B_{1y} = jk\ H_{1x} + \mu H_{1y}$$
$$B_{1z} = \mu_o\ H_{1z}$$

For a circularly polarized wave along Z,

$$H_X^{\ 2} = H_Y^{\ 2}$$

and we very quickly discover the different permeability presented by the medium to clockwise (+) and counterclockwise(-) polarizations, i.e.,

CLOCKWISE	COUNTERCLOCKWISE
$H_y = -jH_x$	$H_y = +j\ H_x$
$B_x = (\mu-k)\ H_x$	$B_x = (\mu+k)\ H_x$
$B_y = (\mu-k)\ H_y$	$B_y = (\mu+k)\ H_y$
$\mu+ = \frac{B+}{H+} = (\mu-k)$	$\mu- = \frac{B-}{H-} = (\mu+k)$

Representing the plane wave by,

$$\psi = e^{j\omega t - Gz}$$

the propagation constant(s) G may be evaluated from Maxwell's equations.

The two curl equations in component form yield,

$$G E_y = -j\omega B_x$$

$$-G E_y = j\omega B_y$$

$$G H_y = j\omega \epsilon E_x$$

$$-G H_x = j\omega \epsilon E_y$$

with four solutions,

$$G_{F+} = j\omega \sqrt{\epsilon(\mu+k)} = -G_{B-}$$

$$G_{F-} = j\omega \sqrt{\epsilon(\mu-k)} = -G_{B+}$$

where F and B refer to forward and backward travel, respectively. These solutions exhibit the different propagation rates for the + and - components and form the basis for the rotation of the polarization plane discussed earlier.

To obtain an expression for the angle of rotation of a plane wave as a function of the field quantities, one must use the component equations above to obtain relations between the various F and B field components. Then, we must apply one of a number of suitable boundary conditions (since we are only interested in the angle.) For example, let

$$E_{xF+} = E_{xF-} = \frac{E_{xo}}{2} \quad \text{at } Z = 0$$

Then (using the relations obtained from the preceding component equations),

$$E_{yF+} = -E_{yF-} = -j\omega \frac{E_{xo}}{2}$$

so at some point Z,

$$E_{xF} = E_{xF+} + E_{xF-} = \frac{E_{xo}}{2} \left(e^{-j\omega \sqrt{\epsilon(\mu+k)}\, Z} + e^{-j\omega \sqrt{\epsilon(\mu-k)}\, Z} \right)$$

Now, in order to proceed, we must make an assumption valid only at very high frequencies —namely, $K \ll \mu$. From the definitions of K and μ, this will certainly be true for ω sufficiently large since $K \longrightarrow 0$ as $\omega \longrightarrow \infty$. The quantities $\mu_o \gamma H_o$ and $\mu_o \gamma M_o$ which ω must exceed, have units of frequency and experimental measurements yield values in the range 0.5 - 3.0 GHz for fields of the order of 1000 oersteds. For $k \ll \mu$, we expand the radical to 1st order and get,

$$E_{xF} \simeq E_{xo} \; e^{-j\omega \sqrt{\epsilon \mu} Z} \cos \frac{\omega_k \sqrt{\frac{\epsilon}{\mu}}}{2} Z$$

Finally, substituting for ϵ, μ, and k and using the same approximation,

$$\theta_F \simeq \frac{\sqrt{\mu_o \epsilon}\, \mu_o \gamma M_o Z}{2}$$

Applying the same boundary condition to a wave moving in the - Z direction yields,

$$\theta_F = \theta_B$$

That is, the angle of rotation is the same for the forward and backward directions and hence the medium is nonreciprocal.

2.9 TRANSFORMATION OF EVANS AND PETTENGILL DATA

Comparisons were made with the lunar data taken by Evans and Pettengill and various lunar analog terrains located in the Western United States. The common basis for comparison was the $\sigma_o(t)$ plots.

The Evans and Pettengill data were transformed into a σ_o versus θ curve by the method outlined in the RCA Report No. LTM-P-3600-4-9100-8. The time delay is converted into incidence angle as shown in Figure 23, and the power return is converted σ_o data.

The equation for converting delay time into incidence angle is,

$$\theta(t) = \cos^{-1}\left(1 - \frac{tc}{2a}\right)$$

where t is the delay time, c is the velocity of light, and a is the radius of the moon.

The total energy received from the lunar surface is the sum of the instantaneous received power times the duration of each power level.

$$E_T = \sum_{i=1} P_i(t)\Delta t_i$$

The equation for the instantaneous power received is,

$$P_i(t) = K_1 \frac{P_t GA\, \pi ac\tau}{(4\pi R^2)^2}\, \sigma_o(t)$$

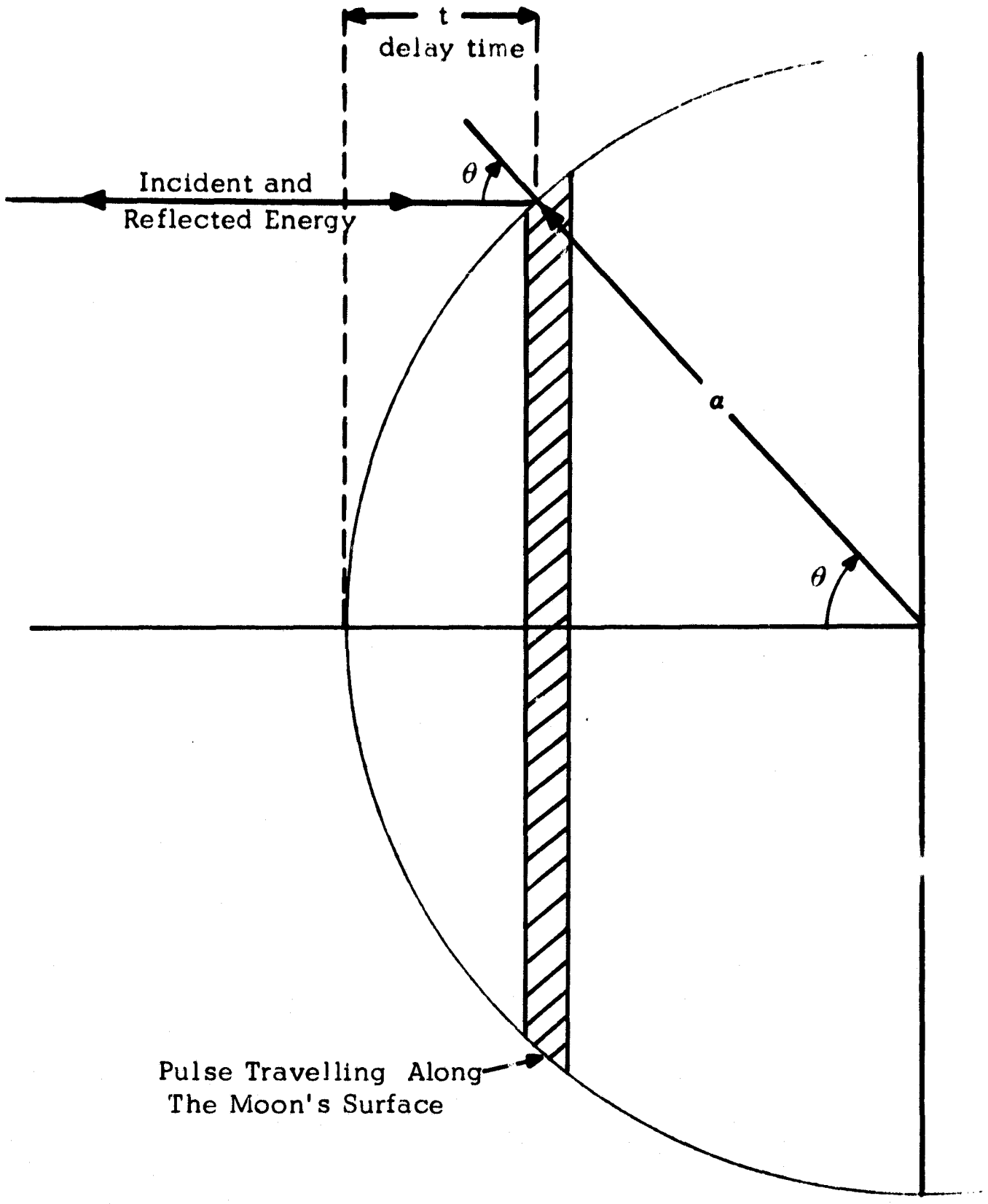


Figure 23 Relationship Between Incidence Angle and Delay Time

where K_1 is a normalizing factor*, P_t is the transmitted power, G is the antenna gain, A is the antenna aperture, R is the range to the moon**, τ is the pulse length, $\sigma_o(t)$ is the instantaneous lunar radar backscattering cross section per unit surface area.

The total radar cross-section of the moon can be related to the instantaneous cross-section by the equation,

$$\sigma_T = \pi ac \int_0^{2\,a/c} \sigma_o(t)\, dt$$

Since each term in the equation for $P_i(t)$ is consistant except $\sigma_o(t)$, then equation for E_T can be written as,

$$E_T = \frac{K \sigma_T}{\pi ac}$$

where

$$K = K_1 \frac{Pt\, G A\, \pi ac \tau}{(4\pi R^2)^2}$$

Thus, if E_T and σ_T are known, K can be determined. E_T is found by multiplying each relative power in the Evans and Pettingill data by its

---

* K_1 must be introduced since the values for $P_i(t)$ are normalized to 0 DB for t=0.

** The parameter R is treated as a constant in this analysis. A slight variation in R (0.1 DB occurs as the pulse travels over the surface of the moon from the sub-earth point to the limbs.

respective delay time, and then summing. The value for σ_T is given in their report as $0.02\pi a^2$ (2 percent of the physical cross-section of the lunar surface). However, this value seems low compared to the average measurements of σ_T given in Figure 22 of their report, which is $0.07\pi a^2$. For these reasons a compromise value of $0.05\pi a^2$ was chosen for use in this document. Using this value,

$$K = \frac{E_T}{0.05\ a/c} = 1.69 \quad ;$$

therefore,

$$\sigma(t) = 0.592\ P_1(t)$$

SECTION 3

SYSTEM DESCRIPTION

This section presents a detailed description of the REDOP system characteristics and of the units that comprise the REDOP. Both Ryan-built and commercial equipment items are included.

3.1 FUNCTIONAL DESCRIPTION

The Ryan REDOP Scatterometer transmits continuous-wave electro-magnetic energy at a frequency of 13.3 GHz. This energy is directed by the transmitting antenna towards the earth's surface. Energy received from the radar beam is detected by heterodyning it with a portion of the transmitted signal and amplified.

A portion of the energy received is detected as a reference doppler signal. The remainder of the energy is detected in microwave phase quadrature with the reference signal. Provision of the reference and quadrature components of the signal permits separation of the fore and aft signal return during data analysis.

The following data present the general operational and physical characteristics of the Ryan REDOP:

3.1.1 Operational Characteristics

Velocity	100 to 350 knots
Altitude	0 to 10,000 feet
Pitch	± 10 degrees
Roll	± 3 degrees

Weight	100 pounds*
Volume (displacement)	4 cubic feet
Power requirements	
115 volts single phase 400 cycle	175 watts
115 volts 60 cycle	80 watts
28 volts DC **	10 watts
Transmitter frequency	13.3 GHz
Two-way beamwidth	
Fore-aft	100 degrees
Port-starboard	2.5 degrees
Antenna gain	20 db
Polarization	vertical
Klystron power output	1.5 watts

3.2 EQUIPMENT DESCRIPTION

The individual units that comprise the REDOP system are described in detail in the following paragraphs. Descriptions are provided of the Ryan-built equipment, the standard commercial equipment and the tape recorder.

---

* These values could be reduced to 25 pounds and 1 cubic foot by replacing the present laboratory test equipment with aircraft-type equipment. This would also eliminate the requirement for 60-cycle power.

** For relays and indicator lights only.

3.2.1 Antennas

The REDOP antennas are two single-element slotted arrays. One array is used for transmitting and the other is used for receiving. The slot pattern in the array is cut to a Dolph-Chebyshev distribution to minimize sidelobe levels. The advantages of using an array antenna include:

- High aperture efficiency
- Lightweight construction
- Minimum overall height

Design characteristics of the planar array antenna include:

- Standing wave excitation, resulting in relative independence of beam angle change with frequency drift, temperature change and manufacturing tolerances.
- Low level sidelobes

Sidelobe Level

The design objective for the sidelobe level was 60 db below the peak of the main beam. Because of this sidelobe level requirement, a Dolph-Chebyshev design was used. To verify this approach a breadboard 13.3 GHz array was designed and fabricated. The antenna radiation patterns are shown in Figure 24 and 25. The highest sidelobe was 56 db below the main antenna lobe.

Constancy of H-Pattern

The constancy of the two-way half-power H-plane beamwidth as measured on the antenna range is shown for 10 degree increments in the fore and aft directions in the E-plane.

Two-Way Half-Power Beamwidth H-Plane

Angle, Degrees	Beamwidth
Forward	
0°	02° 29' 06"
10	02° 25' 32"
20	02° 23' 54"
30	02° 29' 14"
40	02° 25' 38"
50	02° 29' 06"
60	02° 25' 58"
70	02° 29' 16"
Aft	
10	02° 19' 24"
20	02° 23' 26"
30	02° 30' 14"
40	02° 29' 58"
50	02° 22' 24"
60	02° 28' 00"
70	02° 44' 54"

Leakage

The coupling specification requires that the transmitter leakage power in the reciving antennas be 50 db below the power transmitted. (This does not include the internal coupling of -36.5 db for direct-to-audio conversion purposes.) The measured leakage was 52 db below the transmitted power.

Figure 26 is a photograph of the antenna assembly. The antennas are mounted on an aluminum plate which has fences on its surface to enhance the transmitter-receiver isolation. The top of the fences are contoured with foam and fiber glass material to protect the antenna and provide a low drag profile. The back of the antennas are bolted to a plan which provides pressure sealing, and is contoured to fit the Convair 240 airframe.

The space between the antennas and the pan is filled with foam for strength. The antennas are vented to the outside to prevent large differential pressures in the antenna. The outside waveguide is connected to the inside waveguide through pressure windows.

3.2.2 Microwave Plumbing

The microwave plumbing section includes the interconnecting guide from the klystron to the transmitting antenna, the coupler for the power monitor crystal and the hybrid and coupler for the quadrature detectors. Figure 27 is a photograph of the microwave plumbing and its associated equipment as installed on the back of the antennas. The hybrid and coupler divides the received energy into quadrature components and couples a portion of the klystron power to each channel for mixing purposes.

3.2.3 Klystron

The transmitter chosen for this system is a two-cavity, low noise klystron developed specifically for use in Ryan CW doppler navigation systems. The nominal power output is 1.5 watts.

The frequency is 13.3 GHz ± 5 MHz (the ± 5 MHz represents a tube-to-tube variation, not a variation in the frequency output of a single tube). The frequency sensitivity is 0.1 MHz per degree centigrade. Therefore, a temperature change of 10 degrees results in a change in output frequency of only 1 MHz. Since the klystron is inside the aircraft, temperature excursions should be relatively small.

3.2.4 Blower

The blower is a cooling device for the klystron. It works off single phase, 400-cycle power and consists of motor, fan and ducting to direct the air flow on the klystron.

3.2.5 Microwave Detectors

The microwave detectors are low-noise, area-contact diodes. These diodes were developed under a Ryan contract by a major semiconductor company. This detector provides, in addition to improved reliability, a minimum 10 db lower audio noise figure than previous K_u-band detectors.

The measured noise figures of the four diodes supplied for this program are:

Serial No.	Noise Figure	Conversion Loss
1	20.2 db	-7.7 db
2	18.8 db	-6.0 db
3	18.0 db	-4.9 db
4	17.4 db	-4.4 db

These data were measured at an audio frequency of 10 KHz.

3.2.6 Ferrite Modulator

The ferrite modulator consists of a ferrite device in a waveguide section. A coil is wrapped around the outside of the ferrite. The ferrite modulator is installed between the coupler and the microwave detector. As a audio signal is placed on the coil, a field is induced into the ferrite. The field causes the microwave energy to rotate about the direction of propagation of the energy.

The amount of rotation is directly proportional to the coil voltage, and inversely proportional to the frequency of the audio signal. The energy that is rotated out of the plane of the microwave detector waveguide is absorbed in a dummy load. The remainder of the energy goes to the microwave detector. The output of the microwave detector due to the ferrite modulator is a signal at the frequency of the audio signal. A frequency of 10 KHz was chosen for the audio signal. This frequency is enough higher than the maximum doppler frequency of the return spectrum to prevent interference. The calibration curve of the ferrite modulator is shown in Figure 28.

3.2.7 Power Monitor Crystal

The power monitor crystal is a detector which receives a portion of the transmitter power and rectifies it. The rectified output can be monitored on a meter for the purpose of centering the klystron on the peak of its mode. The klystron peaking is accomplished by adjusting the output of the high voltage power supply.

3.2.8 Control Panel

The control panel was fabricated to provide an interface between the NASA-furnished equipment and the Ryan-furnished equipment. Figure 29 is a drawing of the front of the REDOP control panel. The ON-OFF switch turns on the primary power necessary for system operation. Panel lights indicate 28 Vdc for the preamplifier relays and 115 Vac at 400 cycles for the boost amplifiers and blower. A function selection switch permits monitoring of the preamplifiers, boost amplifiers or audio oscillator with a VTVM. Test points are provided for measuring the output of the power monitor crystal (klystron power). Figures 30 and 31 are wiring prints of the REDOP system control panel. It can be seen that all system interconnections are made at the control panel.

3.2.9 Preamplifiers

Two Millivac VS-64A Hushed Transistor amplifiers were modified for use as the system preamplifiers. These amplifiers were chosen because of their low noise figure, variable gain and variable frequency response. These amplifiers operate off of internal 6 volt batteries. A relay was installed for remote turn-on by application of 28 Vdc. Figure 32 is a photograph of one preamplifier.

The frequency response is adjustable on the lower and upper limits between 2Hz and 180 KHz. The gain is selected in 10 db steps between 10 db and 80 db. The input impedance is either 10KΩ or 100KΩ (selectable) and the output impedance is approximately 2KΩ.

The amplifier is divided into two cascaded 4-stage units, one unit being used on the 10 db to 40 db range, and both units for the 50 db to 80 db range. Typical settings of the preamplifiers in the Ryan REDOP installation are 10KΩ input impedance, 400 Hz to 14 KHz bandpass limits and 40 db of gain. The lower bandpass limit compensates for specular return near vertical incidence.* The upper bandpass limit of 14 KHz is used to provide a flat response for the 10 KHz reference signal. Figure 33 is a schematic drawing of the preamplifiers.

3.2.10 Boost Amplifier

The KinTel Model 121A amplifiers are used as the boost amplifiers in the Ryan REDOP installation. These amplifiers were provided by NASA. The frequency response of these amplifiers is from dc to 200 KHz. Fixed gains of 1, 10, 20, 30, 50, 100, 200, 300, 500 and 1000 are provided with a variable gain control of X1.0 to X2.2; therefore, the gain may be set to any desired value between 1 and 1000. The input impedance is greater than 10 MΩ and output impedance less than 0.2Ω in series with 50μh. Figure 34 is a schematic diagram of the Model 121A amplifier.

---

* Note: The low end roll-off does not eliminate the specular return, but reduces it by a calibrated amount.

The model 121A amplifier divides the input into a dc, a slowly varying dc, and an ac component. The dc component is handled by a carrier amplifier and the ac component by a wideband amplifier. The outputs of these amplifiers are combined in the final amplifier. The output is taker from a precision attenuator which also supplies a feedback to the wideband and carries amplifiers. This makes stable operation possible over the wide band of selectable gains. Local feedback loops are used in the wideband, carrier and output amplifiers to further improve the gain stability for long periods of time.

3.2.11 Klystron Power Supply

A Micro-Power Model D-FD-00-00-BW power supply was modified for use with the FE-102 klystron. This unit supplies 6 Vdc for the klystron cathode. The klystron anode is connected to power supply ground. Figure 35 shows the front panel of this power supply. The power supply used 115 VAC 60 cycle power.

One section of the power supply provides the filament voltage and a time delay relay between the 60 Hz power source and the high voltage module. The time delay allows the klystron to warm up before applying high voltage. Figure 36 is a schematic of the filament supply module and Figure 31 is a schematic of the high voltage module.

3.2.12 Monitoring Voltmeter

The voltmeter was supplied by NASA, MSC, for the purpose of monitoring the outputs of the two preamplifiers, the two boost amplifiers and the audio oscillator. On-board tests showed that the voltmeter

was causing ground loop problems; therefore, a Ryan battery-powered Ballentine voltmeter is now being used.

3.2.13 Audio Oscillator

The audio oscillator is an adjustable signal source capable of putting out signals in the range of 1 Hz to 100 KHz. The audio oscillator is being used to drive the ferrite modulator at 10 KHz. The output voltage is normally set at 1 volt rms.

3.2.14 Tape Recorder

The tape recorder supplied by NASA is a Precision Instrument 14-Channel unit. Both AM and FM channels are available. The frequency response of the channels is 100 Hz to 100 KHz on the AM channels, and dc to 10 KHz on the FM channels at normal take speed (30 ips). The required frequency response for the REDOP is dc to 10 KHz, thus FM channels are used. The FM channels provide better signal-to-noise capability and have fewer dropouts than the AM channels. The normal flutter and wow of the tape recorder are very small. Occasionally a particular combination of reels may cause flutter; however, this is readily apparent in flight and can be corrected by changing one or both tape reels.

Two recording heads are used on the tape recorder. One head provides all odd numbered tape channels and the other provides the even numbered tape channels. The channels for recording the REDOP data were chosen carefully because of the requirement that the signals

be in quadrature in order to separate the positive and negative halves of the spectrum.

It is of interest to determine how much tape head misalignment can be tolerated without causing excessive phase shift. The worst case is at the maximum frequency (10 KHz). At a frequency of 10 KHz and for a tape speed of 30 inches per second, each channel records 333 cycles per inch of tape. Thus, each cycle of data is 0.003 inches long. Since there are 360 degrees per cycle, one degree is 8.3 μ inches of tape. If the maximum allowable phase shift is 5 degrees, the maximum allowable relative misalignment between recording and playback heads is 42 μ inches.

This effect is minimized by using adjacent tracks on the same head of the tape recorder. Actual measurements of recorder relative phase shift have shown it to be within acceptable limits.

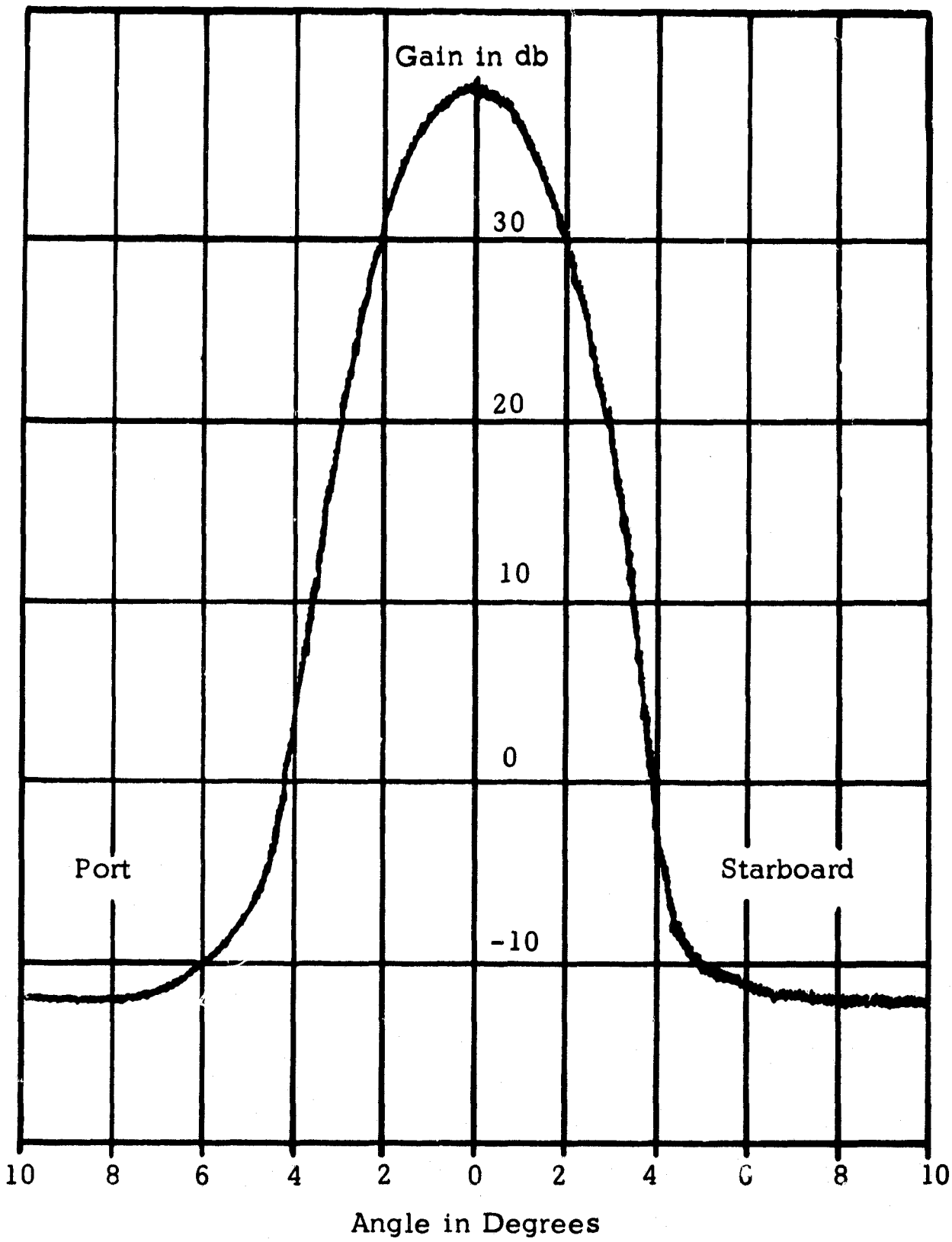


Figure 24 H-Plane Antenna Pattern

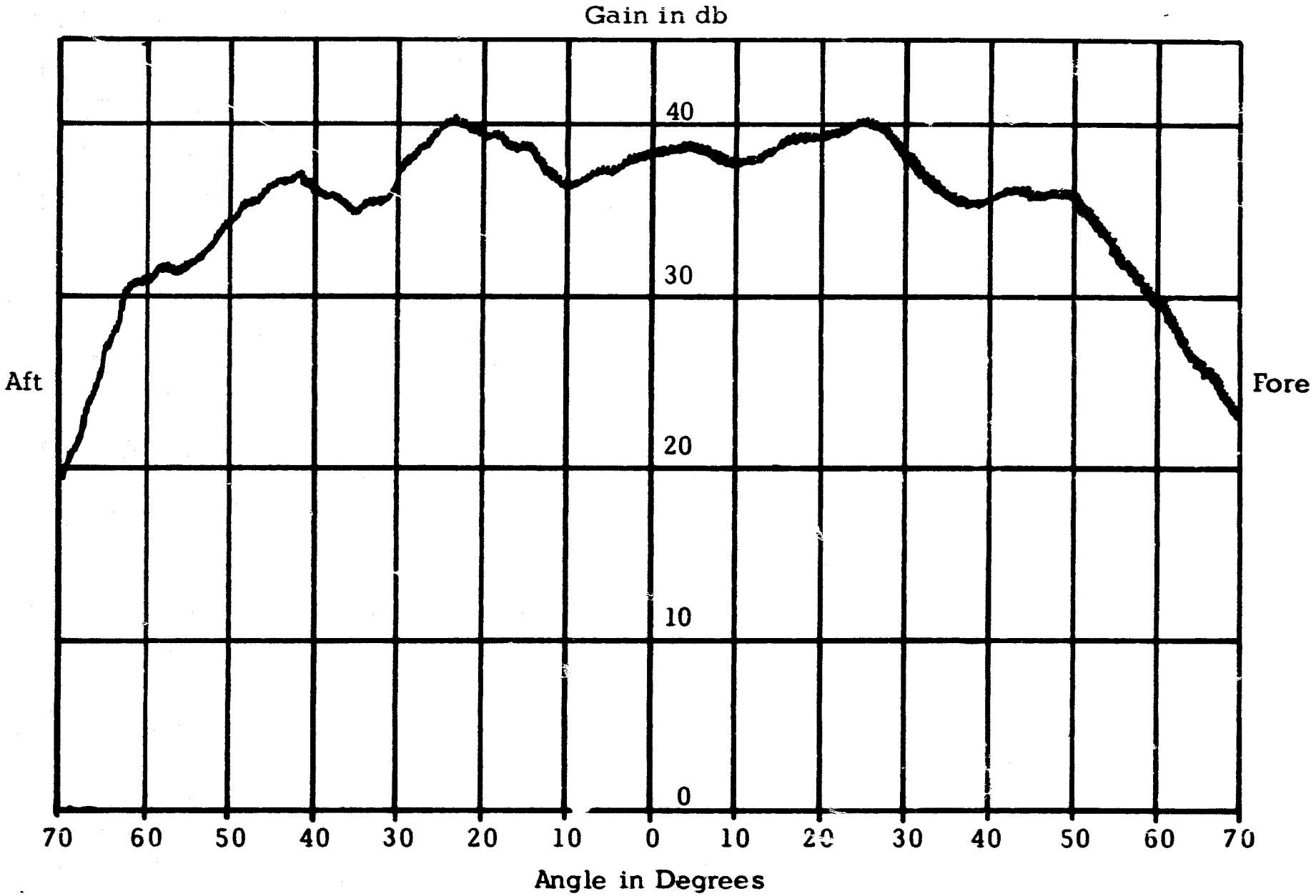


Figure 25 E-Plane Antenna Pattern

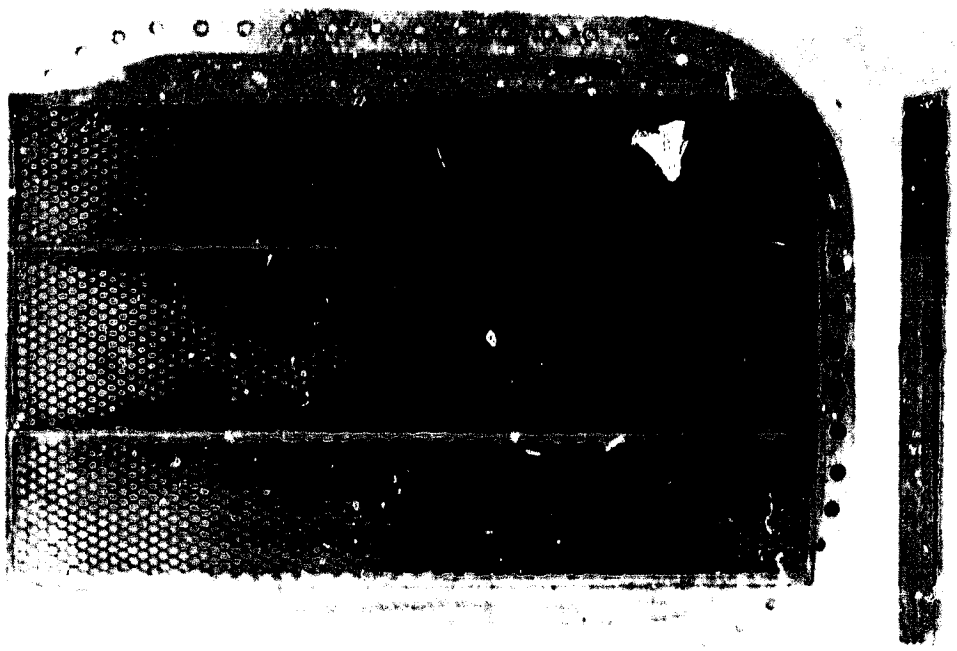


Figure 26 Redop Antenna



Figure 27 Microwave Plumbing

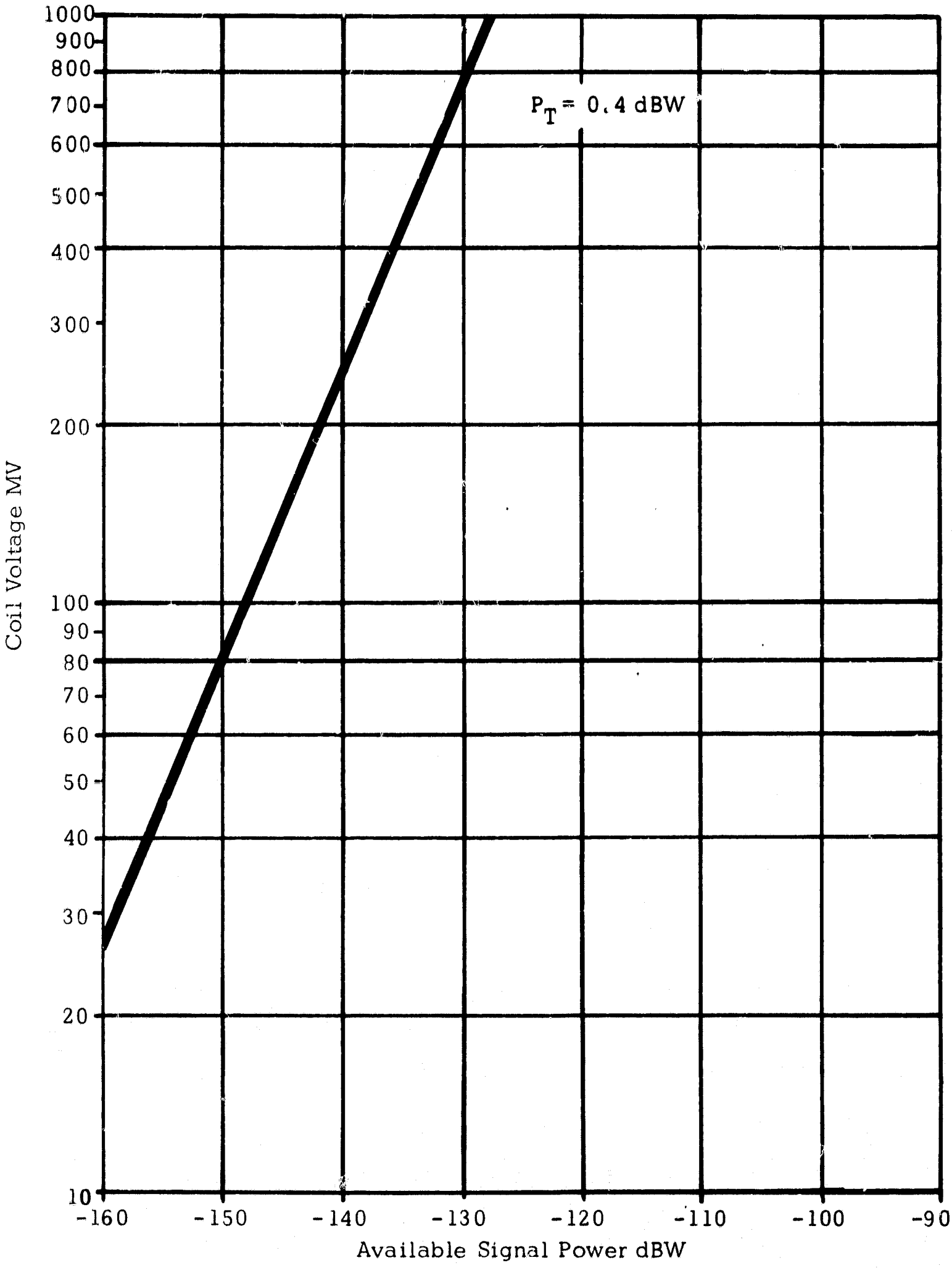


Figure 28 Scatterometer Calibration Levels
Using KM-4 Ferrite Modulator

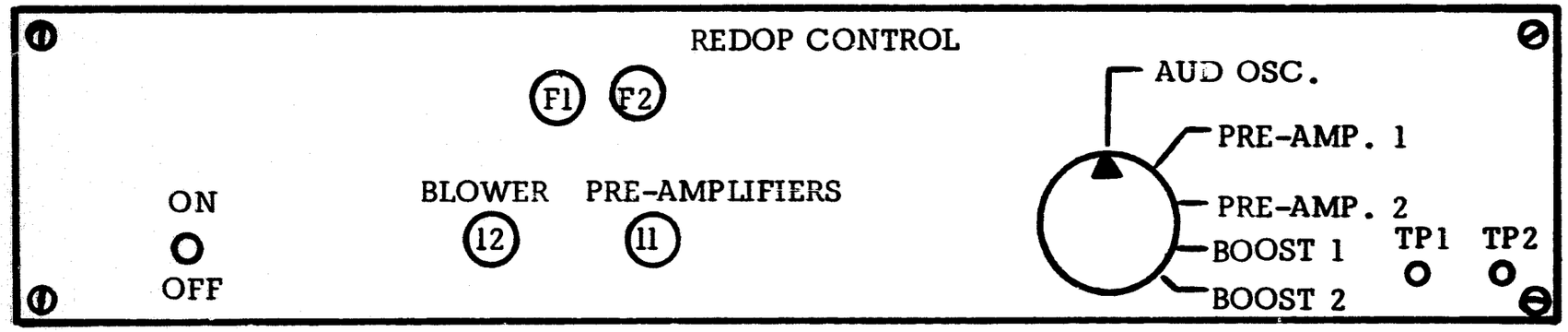


Figure 29 REDOF CONTROL PANEL

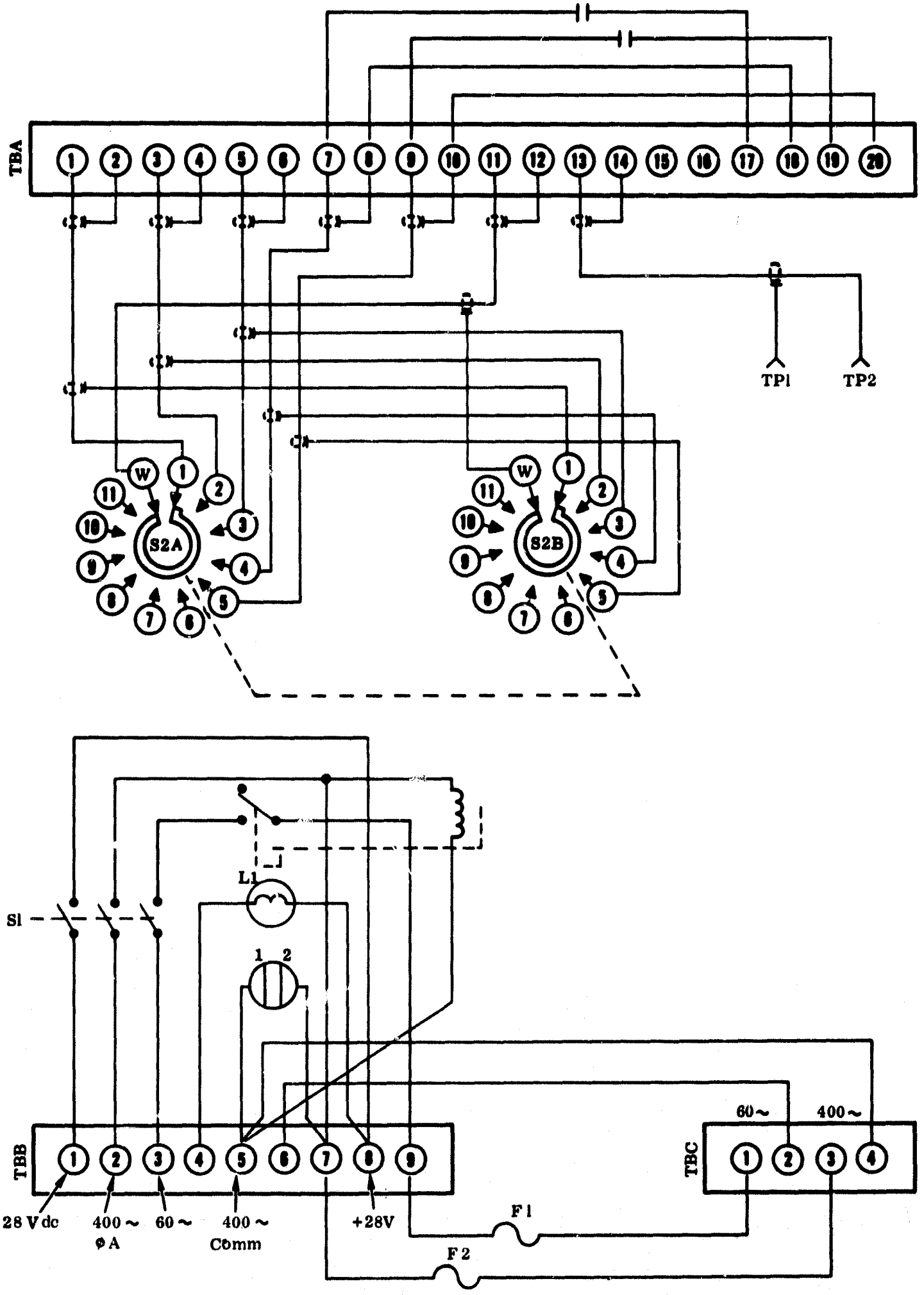


Figure 30 REDOP Control Panel Schematic

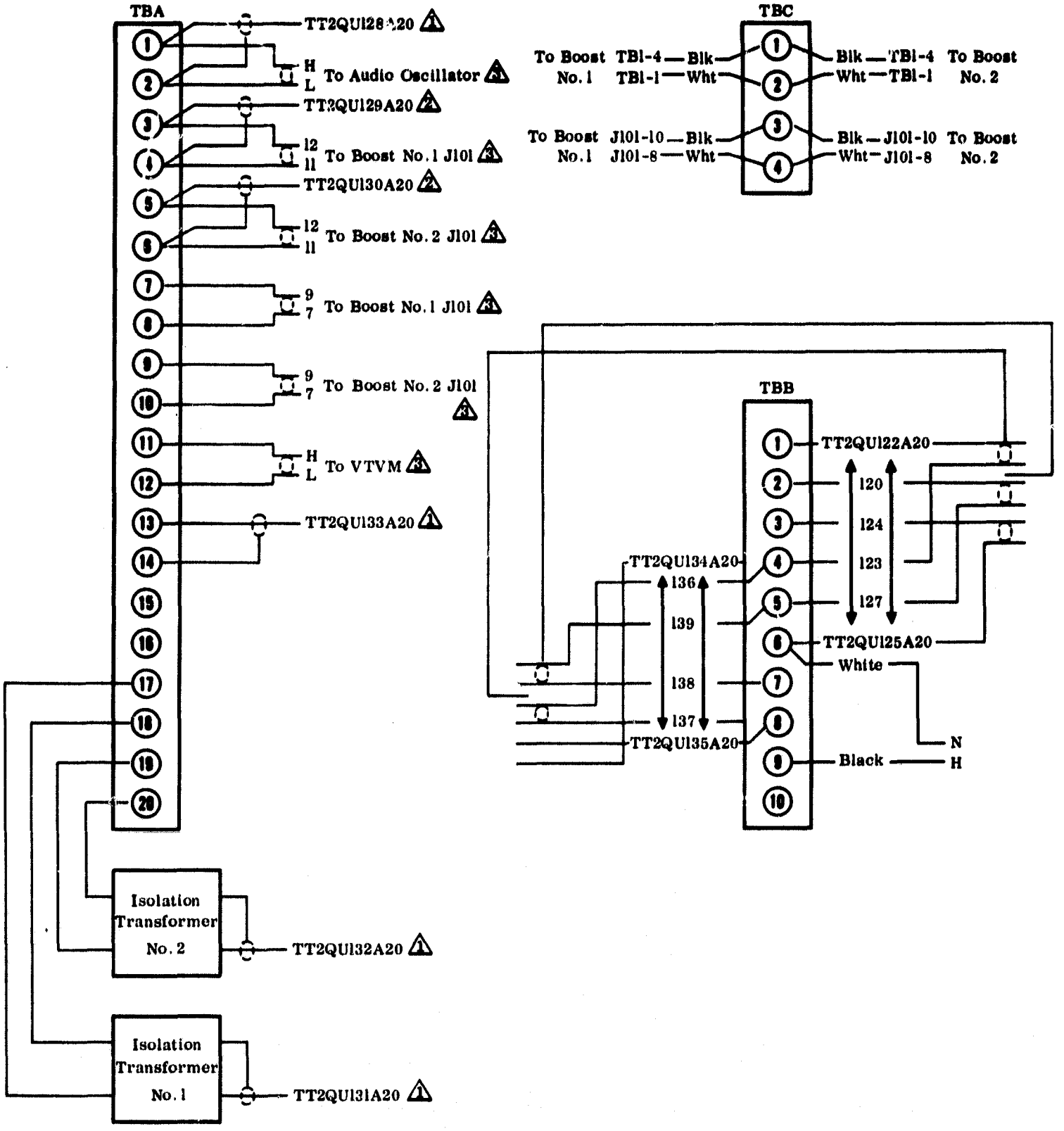


Figure 31 REDOP Control Panel Schematic

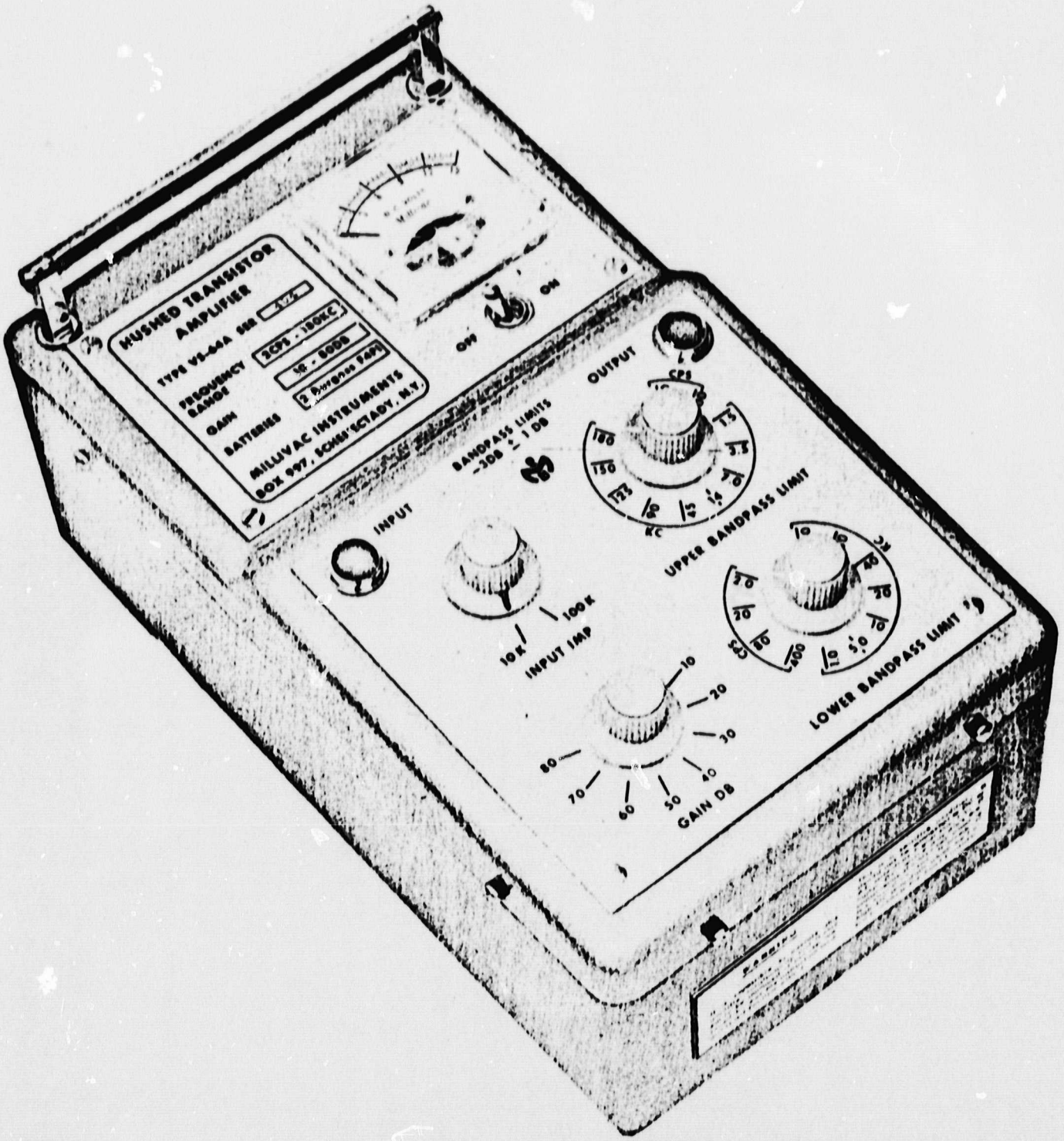


Figure 32 Hushed Transistor Amplifier

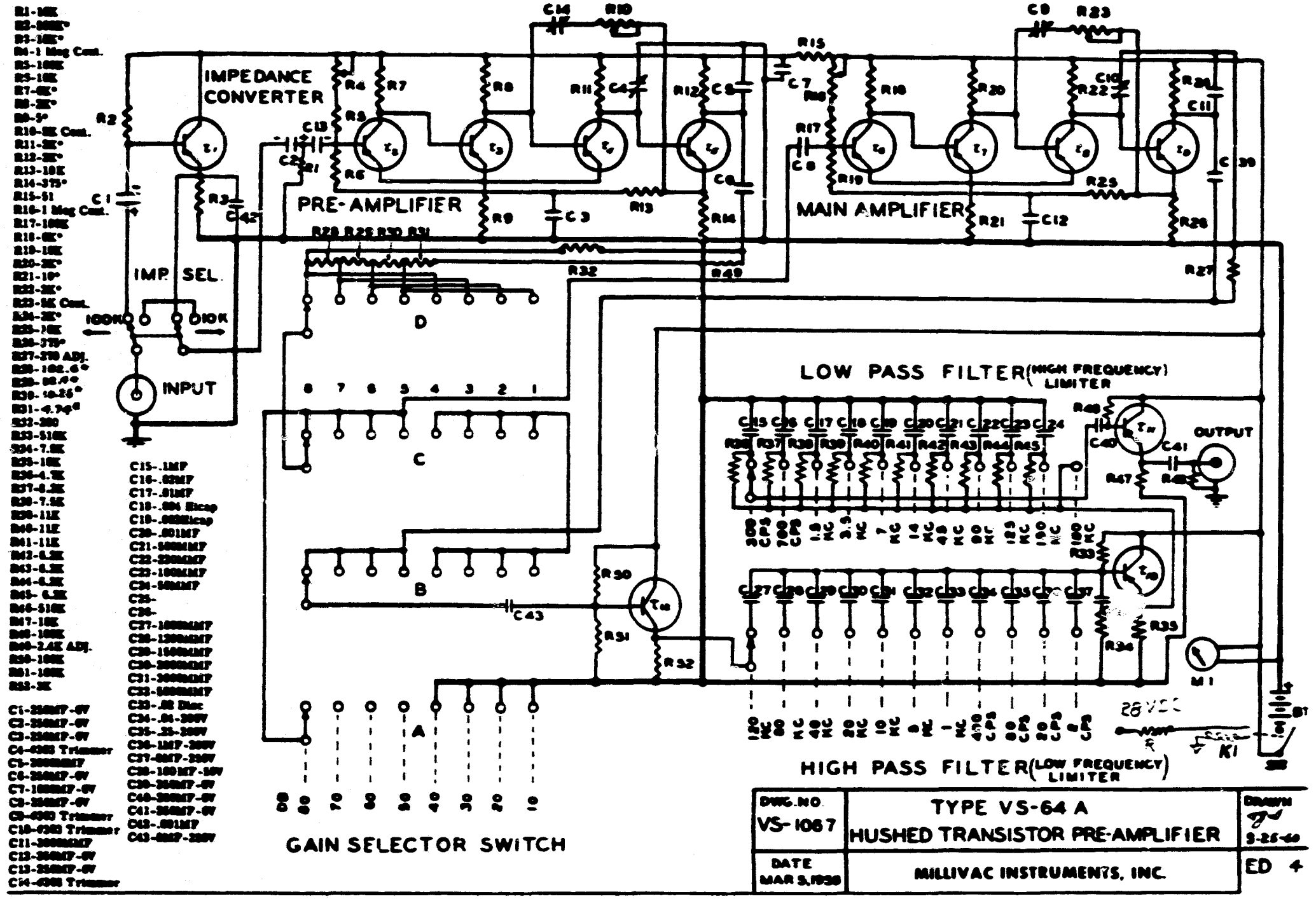
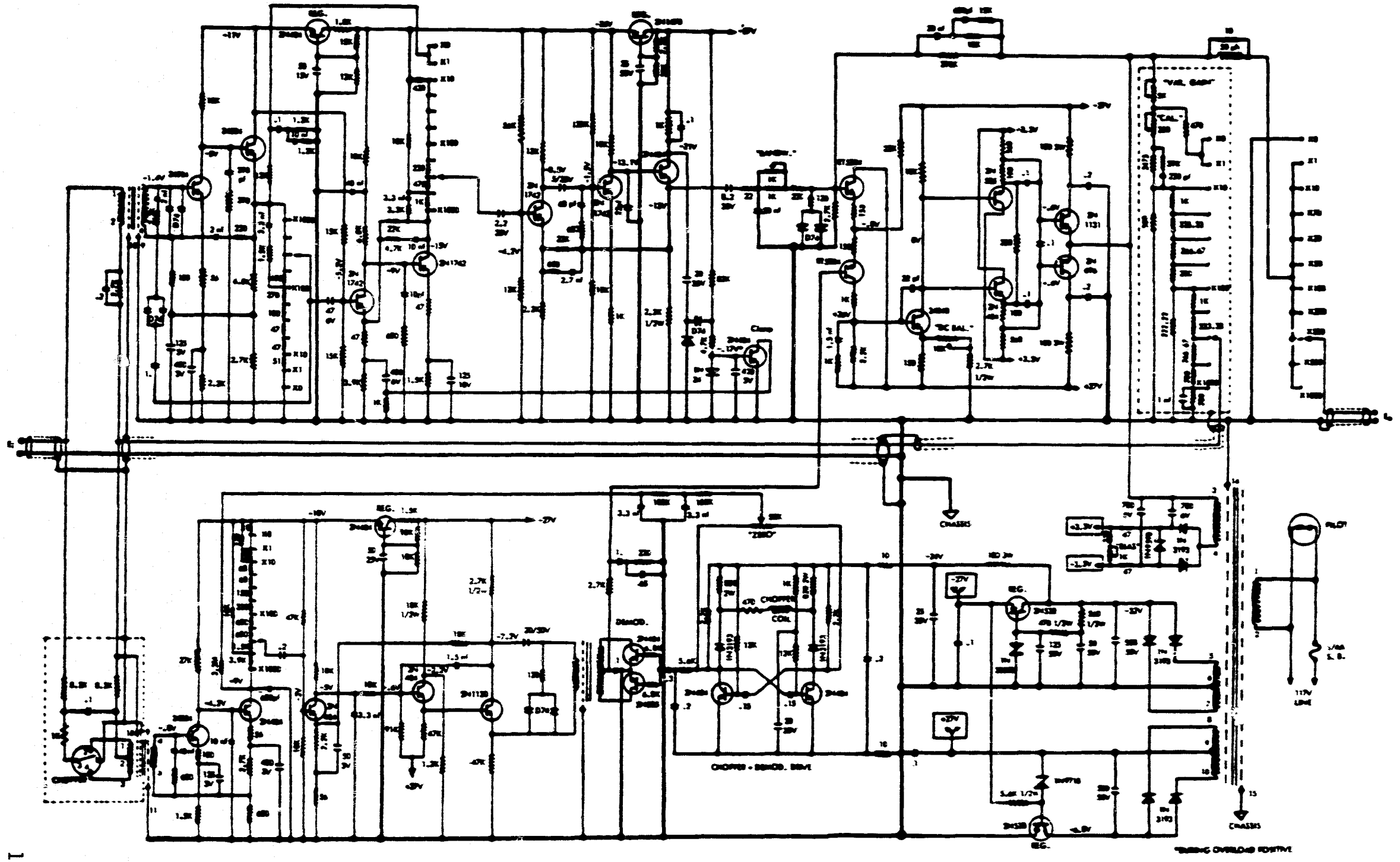


Figure 33 **Preamplifier Schematic**



*Subject to change.

*Schematic Diagram, KIN TEL Model 121A/A Wideband Amplifier

Figure 34 Schematic Diagram of Model 121A Amplifier

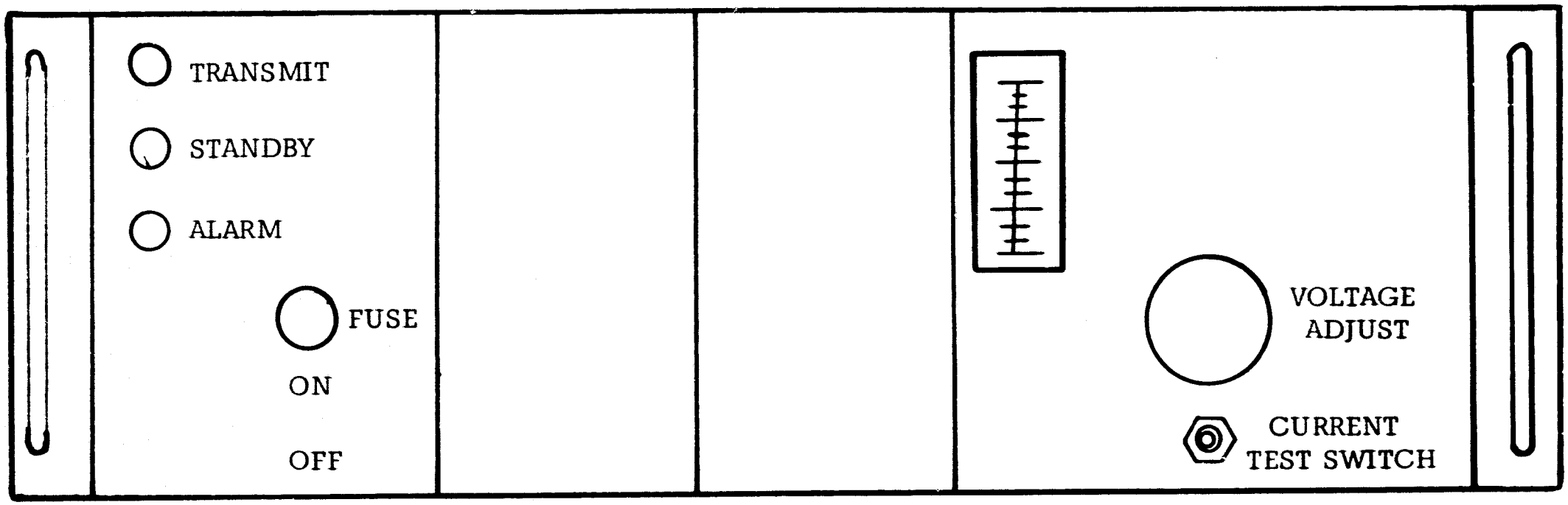
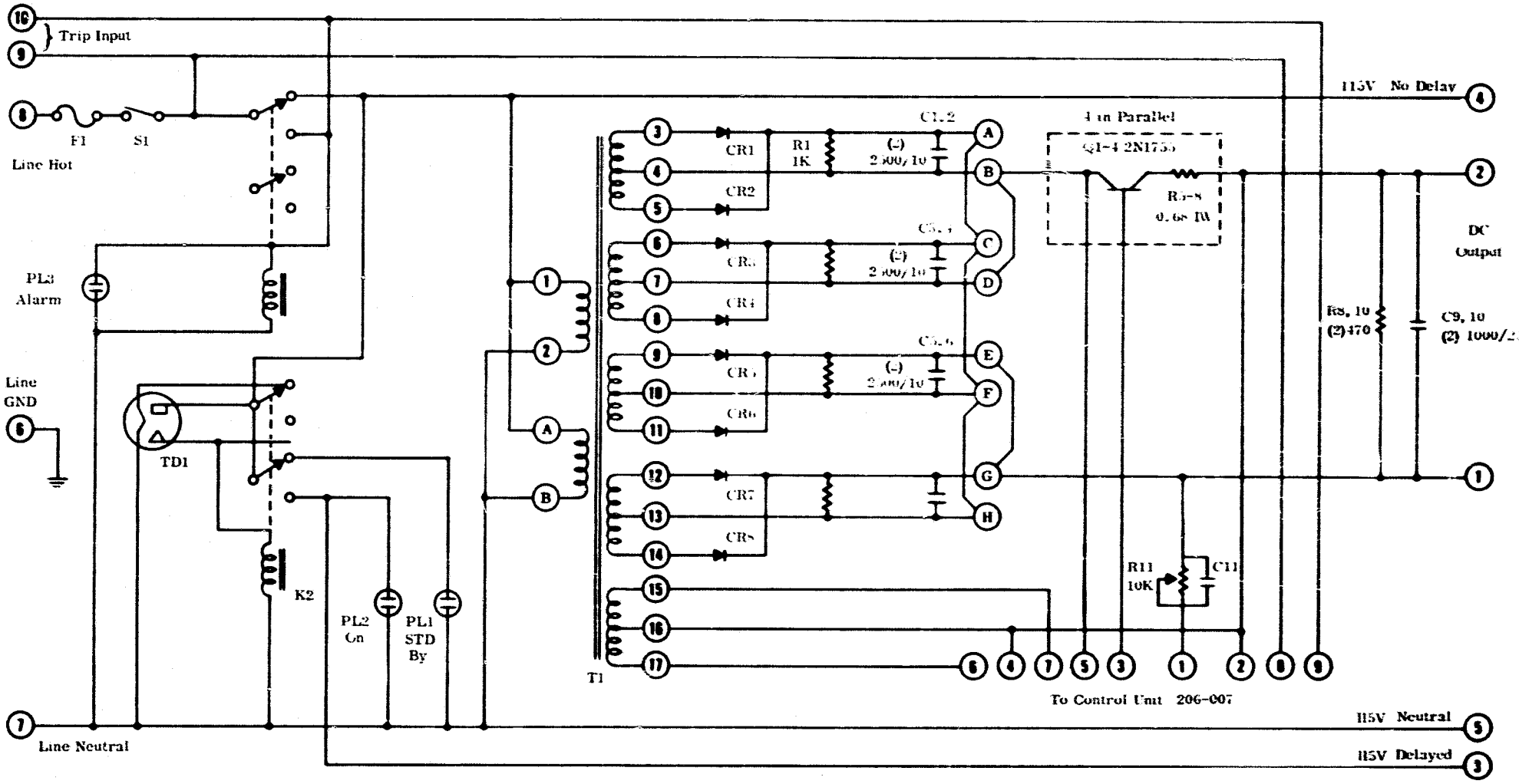


Figure 35 KLYSTRON POWER SUPPLY



Jumper Connections										
Module	Voltage	Amps	Jumper Connections							
FB	2-3	0-3.5	A-C	C-E	E-G	B-D	D-F	F-H		
FC	3-5	0-1.0	A-C	B-D	C-F	E-G	F-H			
FD	5-8	0-2.0	A-C	B-D	C-F	E-G	F-H			
FE	8-10	0-1.1	A-D	C-H						
FF	10-12	0-1.2	A-D	C-H						
FG	13-18	0-1.0	A-D	C-F	E-H					

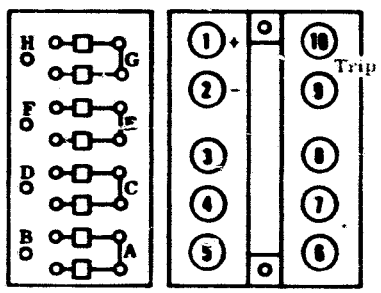
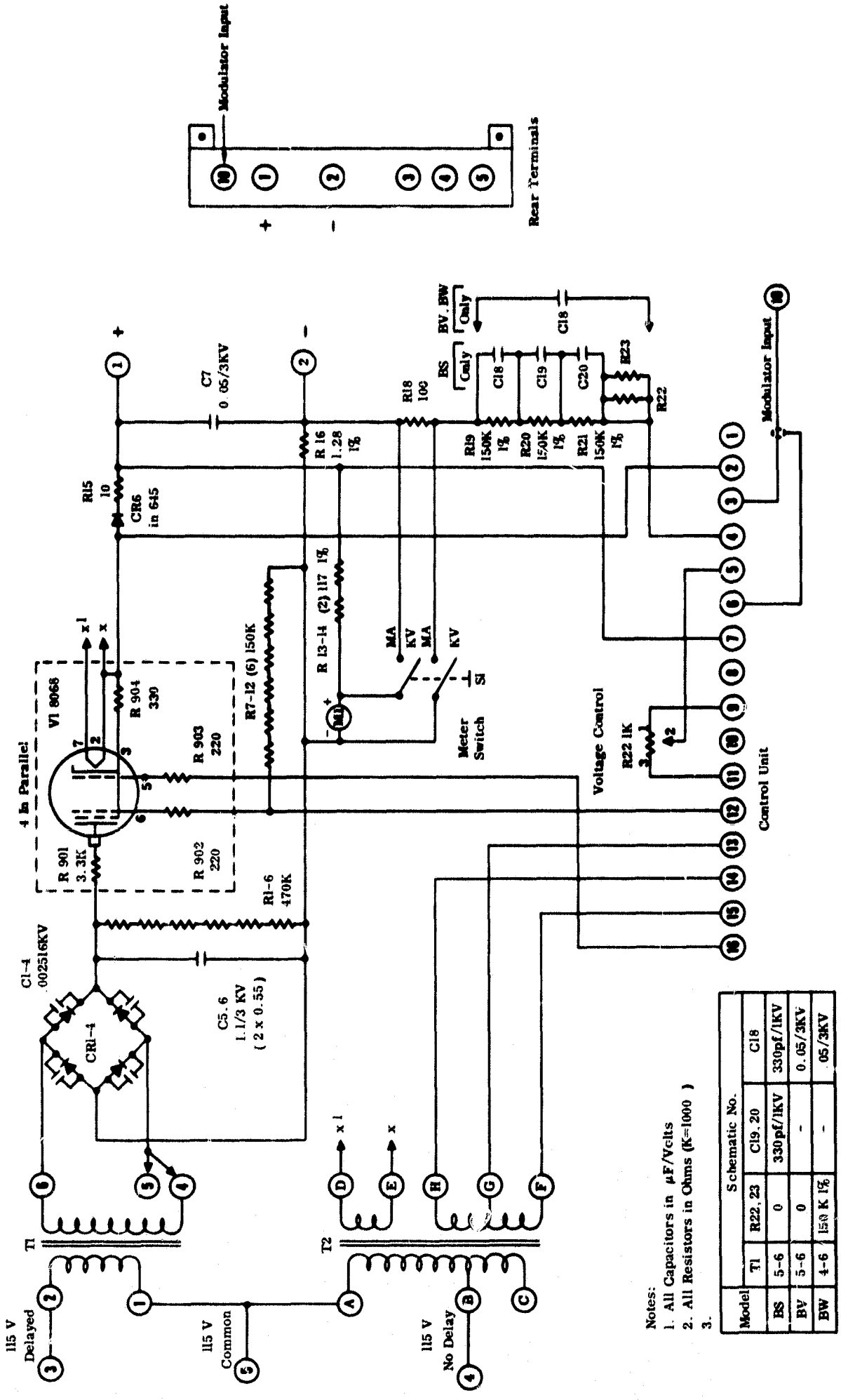


Figure 36 Klystron Filament Supply



Notes:
1. All Capacitors in μF/Volts
2. All Resistors in Ohms (K=1000)
3.

Model	Schematic No.			
	T1	R22, 23	C19, 20	C18
BS	5-6	0	330pf/1KV	330pf/1KV
BV	5-6	0	-	0.05/3KV
BW	4-6	150 K 1%	-	.05/3KV

Figure 37 Klystron High Voltage Power Supply

SECTION 4

DATA REDUCTION

The data reduction portion of this program was performed by NASA personnel. However, it was the responsibility of the contractor to establish the data reduction procedures, review the data quality at each step in the data reduction process, and to supply the equations and techniques to be used in the digital computer program. This Section presents the equations, techniques, and constants used in the data reduction process, including a description of the digital computer programs that were developed.

The first step in the data reduction cycle consisted of processing the recorded doppler audio signal through spectrum analysis equipment. The second step was to convert the output of the spectrum analyzer into a digital form for use in the NASA computer facility. The final step in the data reduction procedure was to correct the filtered and digitized data for system constants and flight parameters in the NASA computer center, and automatically plot the output σ_o curves.

4.1 Spectrum Analysis

The spectrum analysis step consists of several parts. The first part of the spectrum analysis process consists of a determination of signal quality. The recorded doppler audio tape is played back into a speaker and displayed on a dual beam oscilloscope. The

purpose of this part of the spectrum analysis process is to eliminate those runs which have large interference signals superimposed upon the data.

The next part of the spectrum analysis process consisted of feeding short tape loops of the recorded doppler audio signals through a sign sense detector and into a sweeping filter spectrum analyzer. The purpose of the sign sense detector is to separate the fore and aft beam signal power. (The operation of the sign sense detector is described in detail in Section 2.1.3 of this report.) The output of the sweeping filter spectrum analyzer is converted to db by a logarithmic converter, and plotted on an X-Y plotter in the form of relative signal power versus frequency PSD (Power Spectral Density Plot). Figure 38 illustrates this process.

The PSD plots are then reviewed to determine if a sufficient signal-to-noise ratio is available for further data reduction. The PSD is also reviewed for a proper calibration signal level, for proper spectral shape, and for interference signals.

A second mode of operation of the sweeping filter spectrum analyzer is to set the analyzer filter at a fixed frequency (bandwidth determined by analyzer), and run the X-Y plotter in an amplitude-versus-time mode. This process is normally repeated until a "time history" of each incidence angle of interest is plotted along with the calibration signal and the noise threshold.

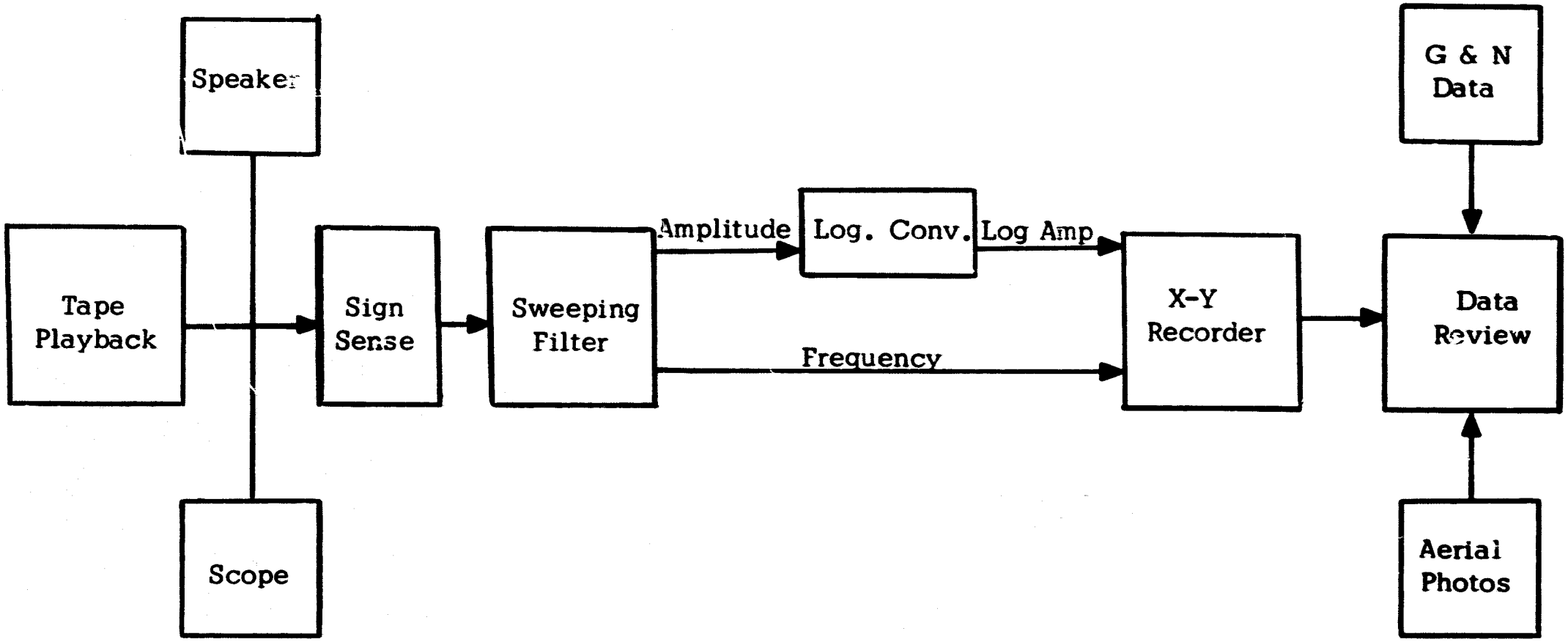


Figure 38 - Sweeping Filter Spectrum Analysis

By use of the time history technique, the entire run can be plotted on one or two plots for data review. The time history provides the flexibility of either obtaining a time stationary plot of σ_o versus θ; or, by proper selection of time intervals between incidence angle plots, obtaining the σ_o versus θ plot of any specified ground cell of the run. However, interference signals cannot be easily detected with the time history plot. Thus, both time history and PSD plots are used in the data verification process.

If any problems exist, the tape copy being used is compared with the original to determine whether the problem appears in the original recording, or if it was generated in the data reduction process. If the data quality is satisfactory, and if the required Guidance and Navigation parameters are available, the Scatterometer data are processed through the regular parallel filter system.

The operation of the analog parallel filter system is illustrated in Figure 39. This process consists of feeding the tape recorder through the sign sense detector and into a bank of filters. The output of each filter is averaged, converted to dc, and recorded on a multiple channel tape recorder. These outputs are also recorded on a multiple channel oscillograph.

The final verification of the wave analysis process consists of a review of the oscillograph data to assure correlation with the time history and PSD plots.

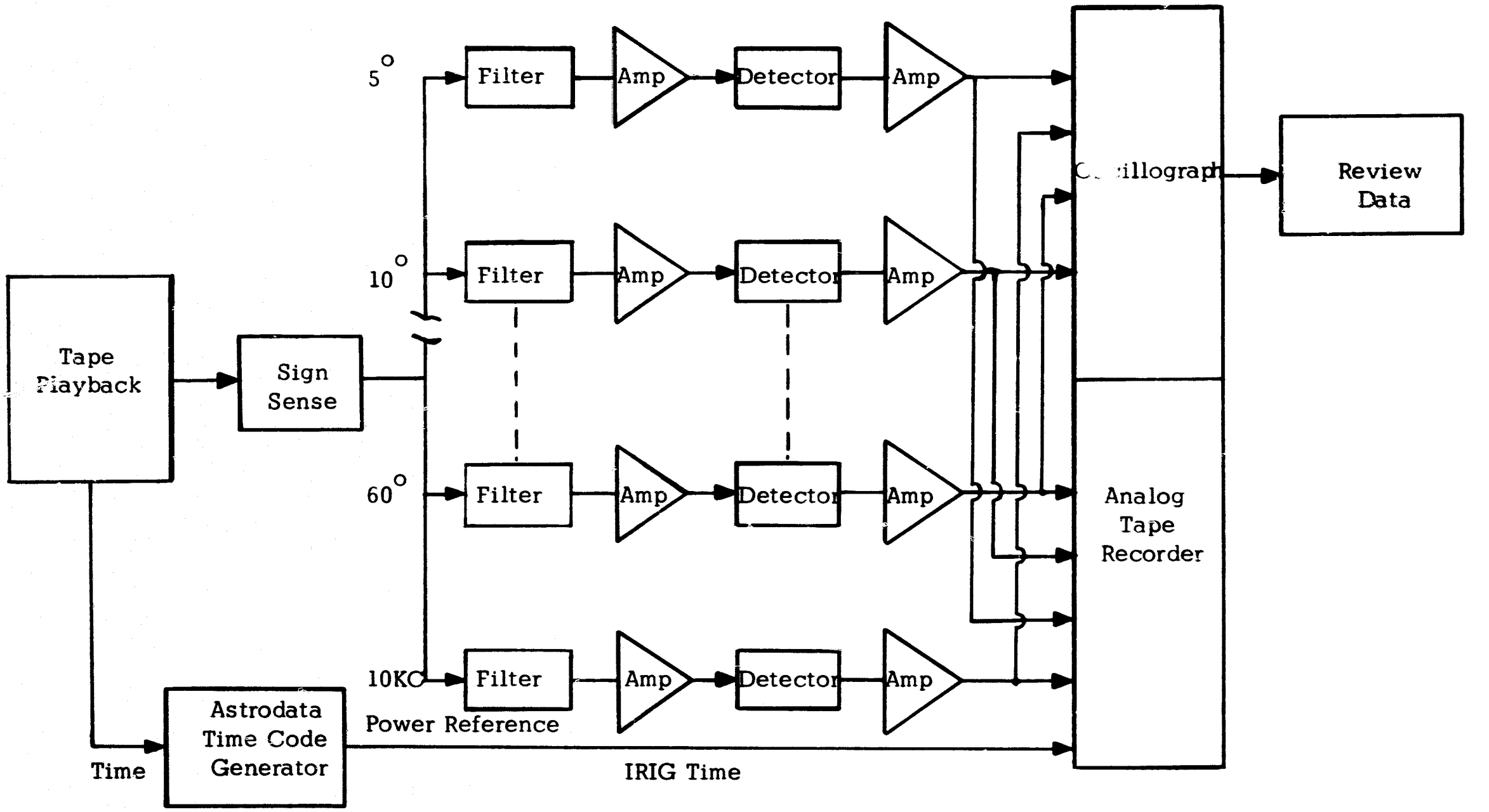


Figure 39 - Analog Parallel Filter Spectrum Analysis

4.2 Digital Spectrum Analysis

The present analog spectrum analysis system is capable of processing about two flight lines per week. However, the present aircraft flight schedule exceeds two lines of data recording per week. Thus a production data processing technique must be developed to satisfy the data reduction requirements. The production data reduction requirements can be satisfied by use of computerized digital filtering techniques.

The one difficulty with computerized digital filtering techniques has been the number of operations required to generate the Fourier series. Techniques have been developed, however, that reduce the required number of calculations.

Digital filtering techniques consist of calculating the complex Fourier Series.

$$X(j) = \sum_{k=0}^{N-1} A(k) \exp(i\ 2\pi \frac{k}{N} j)$$

where $j = 0, 1, \ldots, N-1$ and the Fourier coefficients $A(k)$ are complex.

Conventional processing techniques would require N^2 operations, where an operation is defined as a complex multiplication followed by a complex addition. An Algorithm method developed by Cooley and Tukey (Reference 2) reduces the number of operations to less than $2N \log_2 N$, without increasing the data storage requirements. Therefore, it is recommended that digital filtering techniques be implemented using

either this method,or some other modern method of generating the Fourier coefficients.

4.3 Analog Analysis Equations

This Section contains a derivation of the equations to be used in determining the center frequency and bandwidth of the spectrum analysis filters. The center frequencies of the filters are computed from the equation relating doppler frequency and angle of incidence. The bandwidths of the filters are computed to correspond to a constant size resolution cell on the ground (in the fore-aft direction) for all incidence angles.

The equation relating the doppler frequency to the angle of incidence is,

$$D = \frac{2V}{\lambda} \sin\theta$$

Where the angle of incidence, θ , is measured with respect to the vertical.

The analysis filter center frequency constant for any angle of incidence can thus be computed by the equation,

$$K_{cf} = \frac{2}{\lambda} \sin\theta$$

Values of K_{cf} are given in Table IV for selected incidence angles. The values were computed for a transmitted frequency of 13.3 GHz.

Figure 40 shows the geometry from which the desired filter bandwidth equations are derived. In the figure, $2\Lambda d$ is the length of the resolution cell. The bandwidth of the analysis filters, Λf, are chosen to be,

$$\Delta f = \frac{2V}{\lambda} \quad \sin (\theta + \Delta \theta_2) - \sin (\theta - \Lambda \theta_1)$$

Where,

$$\theta + \Lambda \theta_2 = \tan^{-1} (\tan \theta + \frac{\Delta d}{h})$$

and,

$$\theta - \Lambda \theta_1 = \tan^{-1} (\tan \theta - \frac{\Delta d}{h})$$

In Figure 41, θ_d is the angle at which Δd is defined, that is, the angle of incidence where the resolution cell is a square.

From Figure 41,

$$d = h \sec \theta_d \tan \frac{BW}{2}$$

Where BW is the port-starboard beamwidth.

Or,

$$\frac{\Delta d}{h} = \sec \theta \tan \frac{BW}{2}$$

For any θ the equation for Δf is, therefore, independent of aircraft

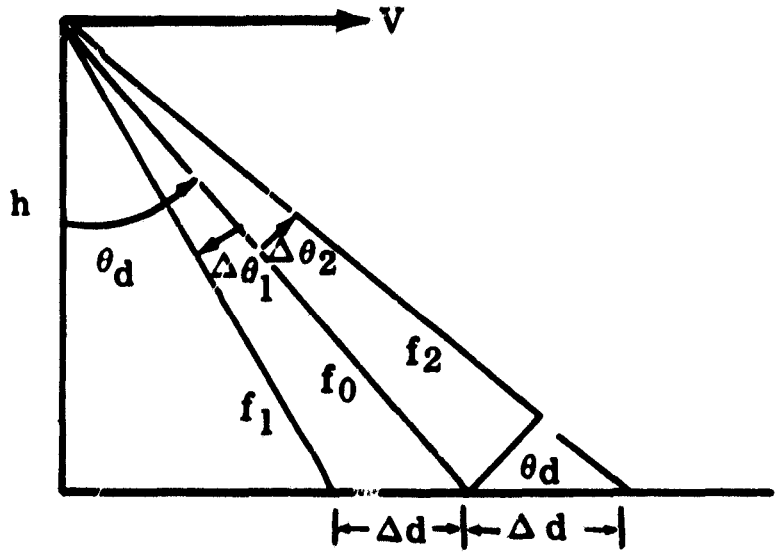


Figure 40. System Geometry

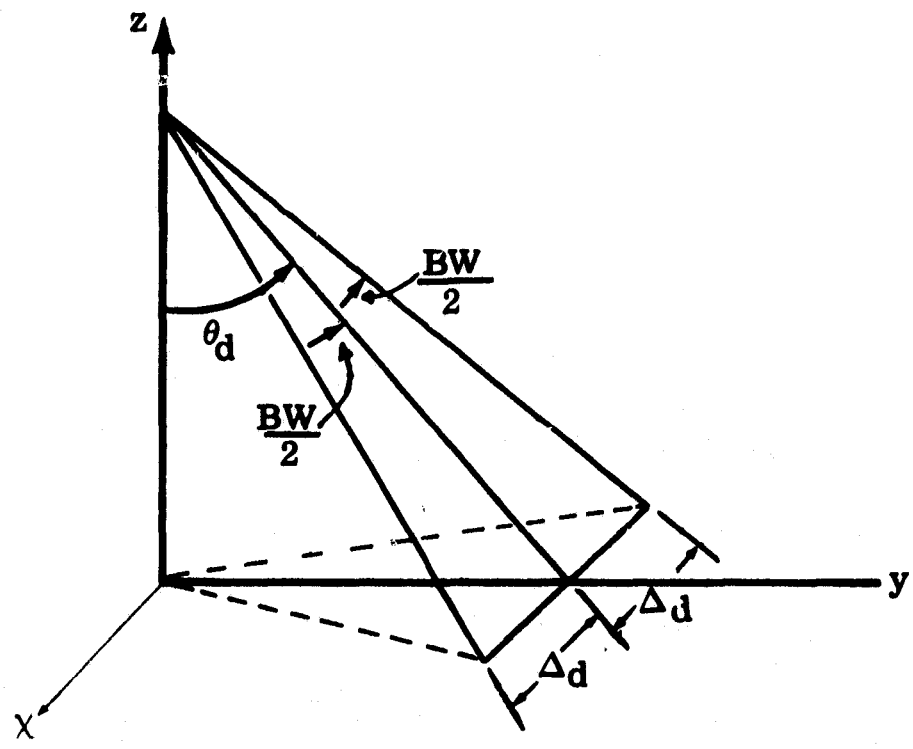


Figure 41. Determination of Resolution Cell Size

altitude and can be simplified to the form ,

$$f = K_{BW}V$$

For the Ryan Scatterometer the port-starboard beamwidth is 2.5 degrees. The deterministic angle of incidence has been chosen as 30^{o}. The constant K_{BW} is given in Table IV for several values of incidence angle.

TABLE IV

Angle	2.5^{o}	5^{o}	10^{o}	15^{o}	20^{o}	30^{o}	40^{o}	50^{o}	60^{o}
K_{cf}	1.991	3.979	7.926	11.814	15.612	22.823	29.341	34.967	38.531
K_{BW}	2.295	2.273	2.196	2.082	1.908	1.492	1.032	0.607	0.298

4.4 Digital Computer Programs

This section describes the various computer programs utilized in the reduction of Scatterometer data.

4.4.1 Digital Computer Program Requirements

This section outlines a procedure for reducing radar reflectivity data. A digital computer will be used for the data reduction.

The input data for a particular test run will consist of several digital tapes. One tape contains attitude, velocity and altitude information as a function of time. The other tapes contain power return as a function of time in 16 frequency channels plus one calibration channel for each tape.

The first step is to align the tapes to establish a data time correspondence and enter the data as matrices with correlated coefficients.

The next step is to select a suitable sampling time increment. The averaging time of the analog equipment is 0.1 seconds. An additional restriction on time resolution is imposed by the geometry of the system. The transverse antenna beamwidth of 2.5^{o} corresponds to a ground resolution cell width of 50.4 feet at an aircraft altitude of 1,000 feet and a beam angle of 30^{o} from the vertical. Fifty feet has been adopted as a reference, and the various frequency channel

filter bandwidths have been adjusted to provide equal fore-aft and port-starboard resolution for this particular geometry. One thousand feet is the minimum altitude at which data will be taken. For a typical aircraft velocity of 150 knots, it requires about 0.2 seconds for the aircraft to fly a distance of one resolution cell at 1,000 feet altitude. The filter bandwidths are constant for constant velocity, resulting in a resolution cell size that is linearly proportional to altitude. Thus, at 5,000 feet and 150 knots, the aircraft travels across one resolution cell per second. Therefore, it is recommended that the sampling rate be made proportional to the resolution cell rate.

Although the method to be described may be scaled to include any number of data points per resolution cell, for simplicity we will consider an altitude of 1,000 feet and a sampling rate of 0.2 seconds, i.e., one data point per resolution cell. Since altitude information is only available every few seconds, rather than assume constant altitude during this period, it seems preferable to linearly interpolate between data points and enter altitude data every 0.2 seconds. This will reduce false "shadowing" of resolution cells on the ground which may actually contribute to the return signal. Horizontal flight will be assumed, and variations in radar altimeter readings will be interpreted as terrain changes rather than changes in barometric altitude.

However, since both barometric and radar altimeter data are available, the altitude data can be normalized to true horizontal flight if necessary.

A five-minute run and a 0.2 second sampling rate will yield:

Altitude	-	1 X 1500 matrix
Velocity	-	1 X 1500 matrix
Power Return	-	16 X 1500 matrix

Storing and processing these matrices, and generating new ones, would use up too much core storage in the computer, but, at the same time, tape storage is inefficient timewise. One solution would be to partition the tape into, say, five one-minute intervals. Another possibility is to process the data one channel at a time. Single channel processing techniques have distinct advantages which are discussed below.

Before the data can be processed, checks should be made to determine if the data points for all incidence angles fall within the desired resolution cells. The required checks are: drift angle $\leq 2.5^{\circ}$, roll angle $\leq 1.25^{\circ}$ and vertical velocity ≤ 360 ft./min. If any of these values are exceeded, some of the data points will fall outside of the desired strip of resolution cells. All cases where these values are exceeded should be noted on the computer output and σ_o versus θ graphs. On runs where drift angle, roll angle and/or vertical velocity are not available, a note should also be made.

Single Channel Processing

The power return matrix is a function of time and frequency. We want to replace this by a power return matrix expressed as a function of time and angle, using the relationship,

$$D = \frac{2V}{\lambda} \sin \theta$$

See Appendix B for a list of symbols. So, θ must be divided into 16 bits ranging from $\theta = -60^{\circ}$ to $\theta = +60^{\circ}$ and corresponding to the 16 frequency channels. For constant velocity, each frequency bit corresponds to a particular angle bit. However, if V varies sufficiently, some crossover will occur. As a first approximation, we will assume V sufficiently constant to prevent crossover. However, sample calculations of the variance of V and also the maximum deviation should be made. The effects of aircraft attitude are removed separately.

Now the problem is going to be primarily keeping track of of subscripts, and this is considerably simplified if we treat one channel at a time. This also avoids partitioning, as there should be ample storage to perform the relatively few calculations necessary on 1500 data points. Computer time should also be materially reduced compared with simultaneous processing of all 16 channels, since repetitive multiplications and generation of trigonometric

functions are not required. Still another advantage of single channel processing is that it is not only possible, but desirable, to use uniform sampling rates.

We first calculate the average aircraft velocity for a given sample of data:

$$\bar{V} = \frac{1}{N}\sum_{i=1}^{N} V_i$$

This can be done as the data is read in - there is no need to store V_i. Next the appropriate "θ bin" is calculated once from the equation for D above, and remains constant over the entire channel. All data calculated for this channel will contain the fixed subscript, say "j", determined by the value calculated for θ.

If the terrain over which the run was made had no altitude variations, each data point representing a spatial location of the aircraft could be associated with a resolution cell on the ground, which is advanced (in the case of a forward beam) a distance given by h tan θ. However, in the more realistic situation of Figure 42, the points of intersection of the radar beam with the ground will tend to bunch on a rising portion of ground (again for a forward beam), and to spread on a downward sloping portion of ground. It seems more realistic to choose uniform resolution cells on the ground, and accept more data from rising than falling sections, than to attempt to establish

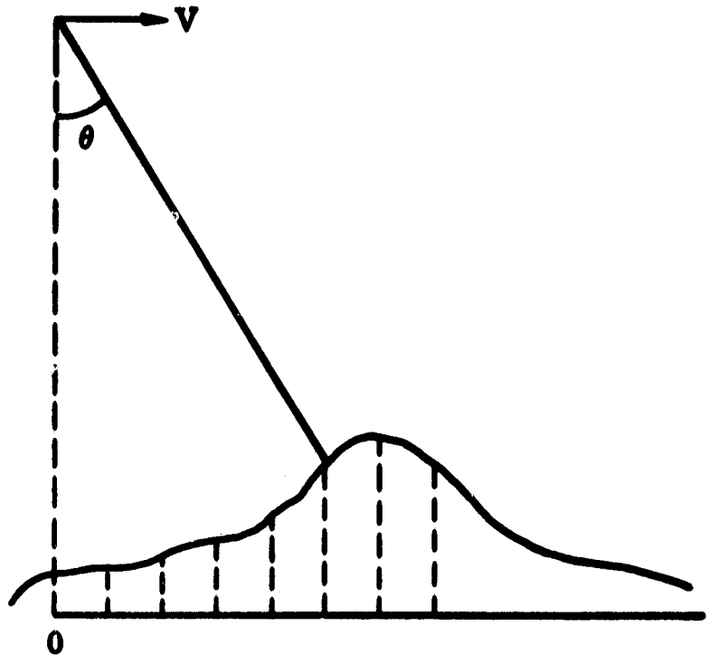


Figure 42 Effect of Irregular Ground on Resolution Cell

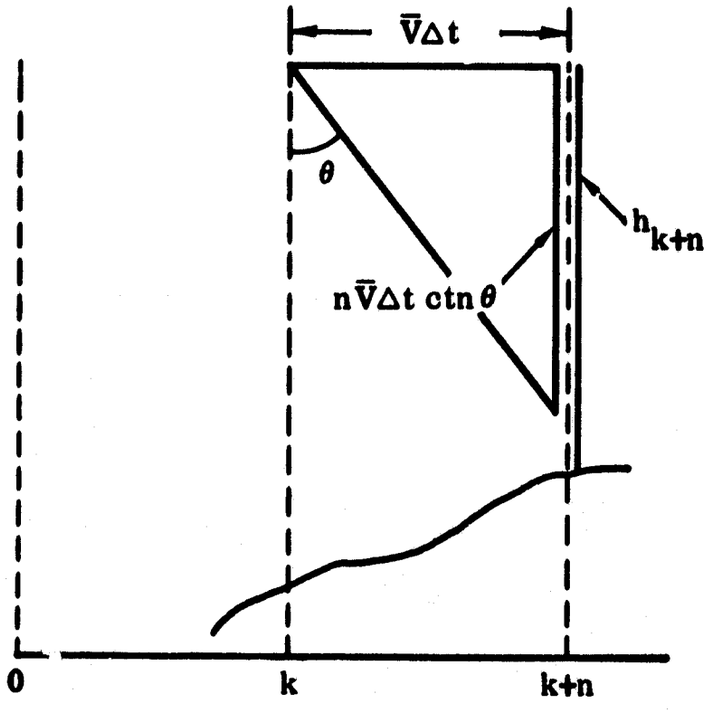


Figure 43 Determination of Point Where Beam Intersects Ground

a 1:1 correspondence between data points and resolution cells.

The radar backscattering cross section will be calculated from the equation,

$$\sigma_o(\theta) = \frac{2(4\pi)^3 V W_s h^2 R(D)}{P_t \lambda^3 G_o^2 f'(\theta)} = W_s h^2 A(\theta) R(D)$$

See Appendix B for a definition of the symbols used in this equation. Tables for $A(\theta)$ and $R(D)$ are presented in Section 4.5. For a particular channel, σ_o is the product of two constants times $W_s h^2$. Two questions arise at this point: (1) What altitude do we use to calculate σ_o for a given θ? (2) How do we correlate resolution cells on the ground with flight test data? Fortunately, both questions may be resolved by the following simple scheme.

Since we are assuming the aircraft moves with constant velocity $\bar{V}$, the equally spaced (in time) sample points correspond to equally spaced positions of the aircraft. The distance between points is $\bar{V}\Delta t$. Starting at some arbitrary point near the beginning of the tape, we call this point "zero" (both on the altitude and power return tapes) and number sequentially to the end of the tape. We divide the ground below the aircraft into resolution cells of the same size ($\bar{V}\Delta t$), and give each cell the same "i" subscript as the aircraft position point directly overhead. Now, at any particular position point, the k^{th} point say, we perform the simple test:

$$\text{is } n\bar{V}\Delta t \cot\theta \geq h_{k+n} ?, \quad n=1, 2, \ldots$$

Figure 43 attempts to illustrate what is being done. As the radar beam extends down towards the ground, $n \bar{V} \Delta t \cot \theta$ measures the vertical drop of the beam n position points out from the origin of the beam (the k^{th} position point in this case). h_{k+n} is the measured radar altitude at this same point. As long as $\bar{V}\Delta t \cot \theta$ is less than h_{k+n} the beam was still above the ground, and the return did not originate at the $k+n^{th}$ resolution cell. Eventually, however, the inequality will be reversed for some value of n, say N. The $k+N^{th}$ resolution cell then should be the actual area on the ground which produced the data point under consideration. The proper value of h to use in calculating the backscattering cross section is then h_{k+N}, and the calculated cross section is labeled $\sigma_{j,\ k+N}$ (again j is a fixed number identifying the particular angle channel being processed). Notice that $\bar{V}\Delta t \cot \theta$ is constant for a particular channel and need only be calculated once.

As successive points along the tape are processed, the "i" subscript on σ_o will increase monotonically (not strictly monotonically, however) except for pathological situations such as the radar beam entering a cave. Since the altimeter cannot handle such "double valued" ground situations, there is no point in attempting to deal with them.

The elements of the resultant two-dimensional σ_o matrix are generated sequentially (in <u>both</u> dimensions if the channels are

processed in order) and there is no need for a sort routine at the end. As pointed out earlier, there may be situations in which several successive data points fall in the same resolution cell,and situations in which no data points originate in a particular cell. Since this is indeed what happens in a typical flight, it is felt that the proper procedure is to test the "i" subscript of $\sigma_{j,i}$,and take the average value of the several data points which may fall into a particular cell before generating the final (single) σ_o matrix element.

Since such data points will always be adjacent, the averaging can be done in the main program loop before the results are stored in the σ_o matrix; thus minimizing addressing problems. Also, clearing to zero and addressing a section of memory before starting the generation of the σ_o matrix,will automatically provide a zero matrix element for each cell which does not contribute to the scattering. If there are storage problems, each complete "line" of the σ_o matrix (corresponding to each channel) can be printed out at the end of a pass.

The test given above may be greatly speeded up by taking advantage of the monotonic property of the time-position subscripts "i". Since each successive data point will be associated with a ground resolution cell which cannot be closer than the cell associated with the preceding data point, there is no need to start with n=1 for any data point except the first. Thereafter each test may begin with n=N, the value found for the immediately preceding point. It should seldom be necessary to increase n=N by more than 1 or 2.

Each channel can be processed in this way. However, if sample calculations show that the computation time is still undesirably long after optimizing the test, the process can be shortened in still another way. Note that once the proper ground resolution cell and corresponding altitude have been located for one channel, the data points in every other channel, corresponding to this same set of resolution cells, may be determined geometrically. As the first channel is being processed, we replace the matrix $(\ldots h_i \ldots)$ by the matrix $(\ldots h_{k+N} \ldots)$ and store the values k+N*. Now for this new "j prime" channel, the power return data point $W_{j',i}$ to be used with,

$$i = k+N - m$$

$$m = \frac{h_{k+N} \tan \theta'}{\bar{V} \Delta t}$$

where "m" is understood to be the integrally terminated quotient above. The backscattering cross section is then computed and labeled $_{j', k+N}$. Note that a new $A(\theta')$ must be used corresponding to the new value θ', but this value again is constant for the entire channel.

---

* Note that "N" varies from point to point and should really carry its own subscript, but for typographical clarity this has been omitted. One should simply regard the quantities (k+N) as a set of monotonically increasing integers.

This modified procedure is less straightforward to program than uniform processing, but it reduces the number of tests by a factor of eight. It also reduces the problem of spreading apart of the uniform-sized resolution cells at the higher angles. It might appear that this projecting back technique would deny us the possibility of more than one data point per resolution cell, but by combining and averaging the power return data over each projected resolution cell before any computations are made, we can use any number of data samples per cell.

This single channel processing procedure will produce one row of the σ_o matrix for each pass. The final result σ_o as a function of θ, will then consist of vertical columns of the σ_o matrix, and if the output is printed sequentially on tape rather than stored in core, the rearrangement can be done on one of the small peripheral computers.

In conclusion, it is felt that, as compared with simultaneous processing, the single channel processing technique discussed above is both faster and easier to program, and in addition, lends itself very naturally to correction for ground irregularities.

Determination of Constants

This section contains the equations and tables used to determine the constants used in the digital computer program. A complete list of symbols is included in Appendix B.

To compute $\sigma_o(\theta)$, the equation,

$$W_s = \frac{P_t \lambda^3 \sigma_o(\theta) G_o^2 f'(\theta)}{2(4\pi)^3 h^2 V R(D)}$$

can be rearranged to yield:

$$\sigma_o(\theta) = \frac{2(4\pi)^3 h^2 V W_s R(D)}{P_t \lambda^3 G_o^2 f'(\theta)}$$

After converting to db, the equation becomes,

$$\sigma_o(\theta) = 69.5 \text{ db} + 20 \log_{10} h + 10 \log_{10} V + W_s + R(D) - G_o^2 f'(\theta)$$

The factor W_s is the corrected channel data, defined in terms of the voltage ratio V_i/V_f, the scale factor $1/K_i$, and the 10 KHz Sideband power output constant of the ferrite modulator.

$$W_s = 20 \log_{10} \frac{V_i}{K_i V_f} + FMC$$

Now, substituting for W_s with the value of FMC included, the equation becomes,

$$\sigma_o(\theta) = -64.2 + 20 \log_{10} h + 10 \log_{10} V + 20 \log_{10} \frac{V_i}{K_i V_f} + R(D) - G_o^2 f'(\theta)$$

The symbol R(D) represents the correction factor for the composite roll-off characteristic of the system. Tables V-VII give listings

of R(D) with proper signs as referenced to 0 db roll-off at the 10 KHz ferrite modulator frequency. For each channel frequency, D, there will be a corresponding roll-off value, R(D), given in db, to be added or subtracted. When a frequency falls between two points in the table, interpolate linearly between the points for the correct value.

Before the $G_o^2 f'(\theta)$ value for a given angle can be obtained from its table, θ must be computed, and a correction made for aircraft pitch angle. The first step is to compute θ from the basic doppler equation,

$$\theta = \sin^{-1} \frac{\lambda D}{2V}$$

The angle θ_t is the corrected theta value to refer to in the $G_o^2 f'(\theta)$ table.

$$\theta_t = \theta - P$$

Punched card data of the photo panel will yield the value of the pitch angle, P. If a value θ_t falls between two theta values in the $G_o^2 f'(\theta)$ table, make a linear interpolation between points.

In some cases the aircraft may be in a climb or glide. Figure 44 contains a diagram of climb or glide angle (C), and a graph of C versus the ratio V_z/V_g. Knowing V_g and V_z, angle C can be found and added to the computed θ to obtain a corrected angle θ_c.

$$\theta_c = \theta + C$$

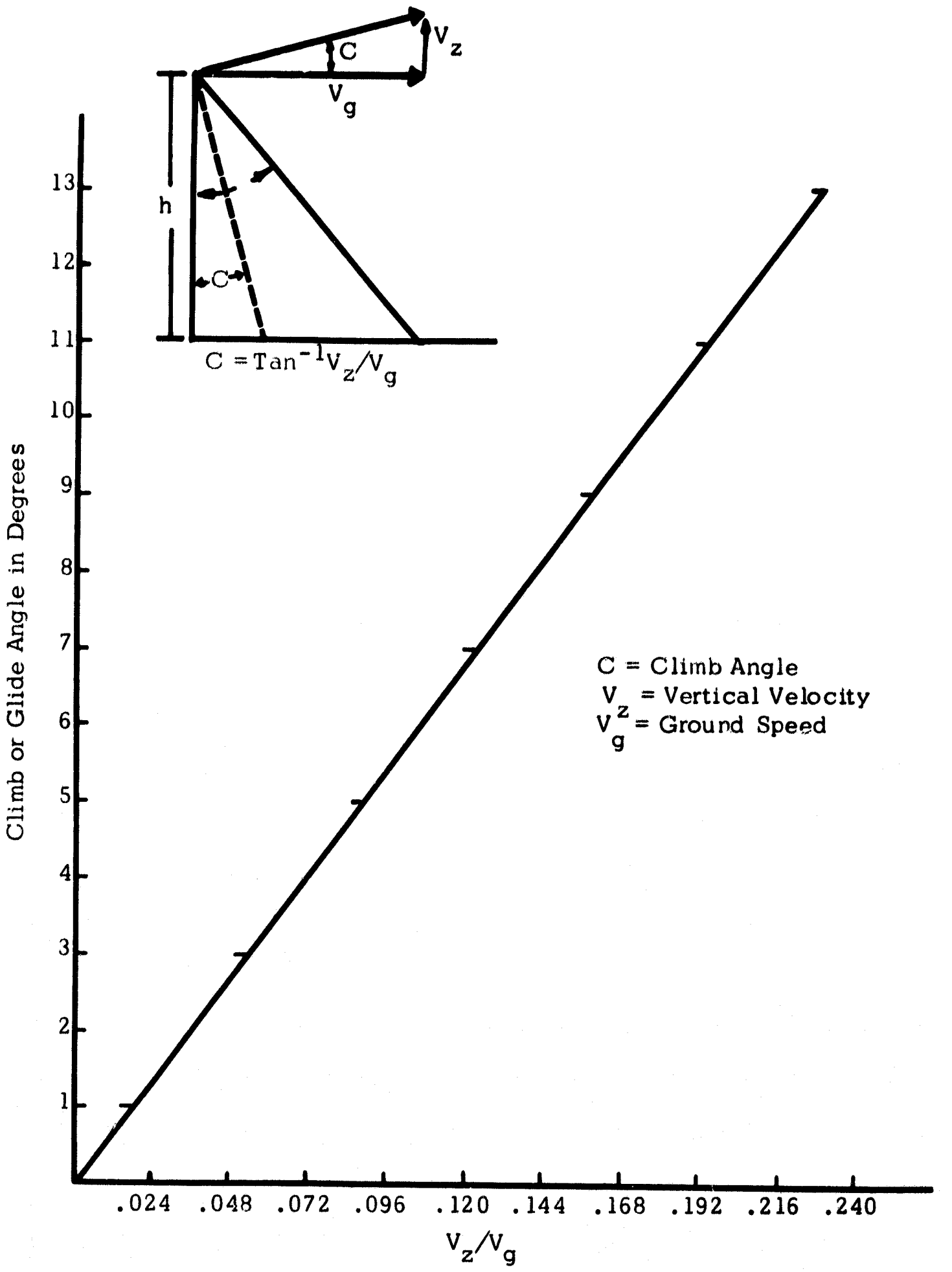


Figure 44 Calculation of Climb or Glide Angle

This θ_c is then used to plot σ_o curves for these flights. In missions where there is a climb or glide angle one theta, $\theta = \theta - P$, will be used to find a $G_o^2 f'(\theta)$ value, and another theta, $\theta_c = \theta + C$, will be used in plotting σ_o versus θ_c graphs.

The result of either procedure outlined above will be a set of σ_o versus θ curves, where each curve will consist of a set of σ_o values at discrete incidence angles. The next step is to derive composite curves for the particular line of data.

Two composite curves will be plotted, one for the position (forward) incidence angles, and one for the negative (rearward) incidence angles. The composite curves will give the average and standard deviation of each angle of incidence in the σ_o matrix. The sample average and standard deviation will be computed with no attempt to fit the results to a predetermined distribution.

The equation for computing the average, $\overline{\sigma_o}$, at each incidence angle is,

$$\overline{\sigma_o} = \frac{1}{N} \sum_{i=1}^{N} \sigma_{oi}$$

where N is the number of samples in the matrix.

The equation for computing the standard deviation about the mean, $\hat{\sigma}_o$, at each incidence angle is,

$$\hat{\sigma}_o = \left[\frac{1}{N} \sum_{i=1}^{N} (\sigma_{oi} - \overline{\sigma_o})^2 \right]^{1/2}$$

where the σ_{oi}'s are the values of σ_o for the samples at a given angle in the matrix, and $\overline{\sigma_o}$ is the average of the samples.

A composite curve will consist of a plot of the $\overline{\sigma_o} + \hat{\sigma}_o$ at each incidence angle.

4.4.2 Basic Computer Program

The basic computer program was written to produce sigma zero versus theta plots for the purpose of checking the flow of data. Variations in altitude and velocity, and the effects of pitch and roll, were not incorporated into this program in order to conserve programming time.

The format of the input data tape is given on the following page. A data flow chart describing the mechanization of the basic program is given on pages 151 through 153.

MAGNETIC TAPE FORMAT

1st File

1st record - 12 BCD character header containing site, flight, and mission

remaining record - ignored

2nd File

typical record - length - 486 BCD characters

mode - 556 BPI, BCD

format - 6 BCD character time, ignored

160 3 BCD character data items

total - 486 BCD characters

high cal record - a typical 2nd file record with all data items greater than 700 counts

low cal record - a typical 2nd file record with all data items less than 75 counts

3rd File

typical record - length - 486 BCD characters

mode - 556 BPI, BCD

format - 8 BCD character time

1 BCD character - hundredths of seconds

2 BCD characters - minutes

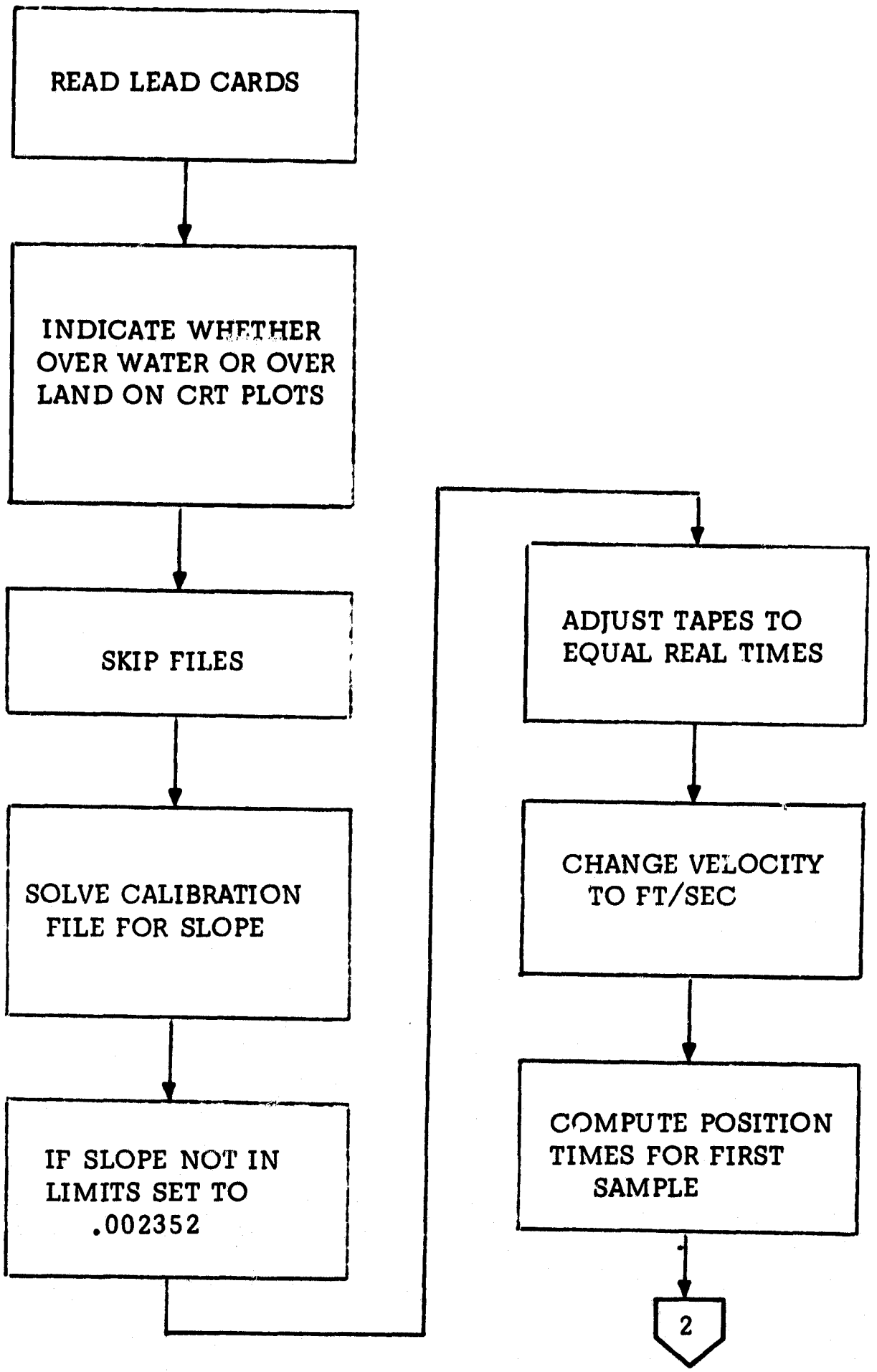
2 BCD characters - seconds

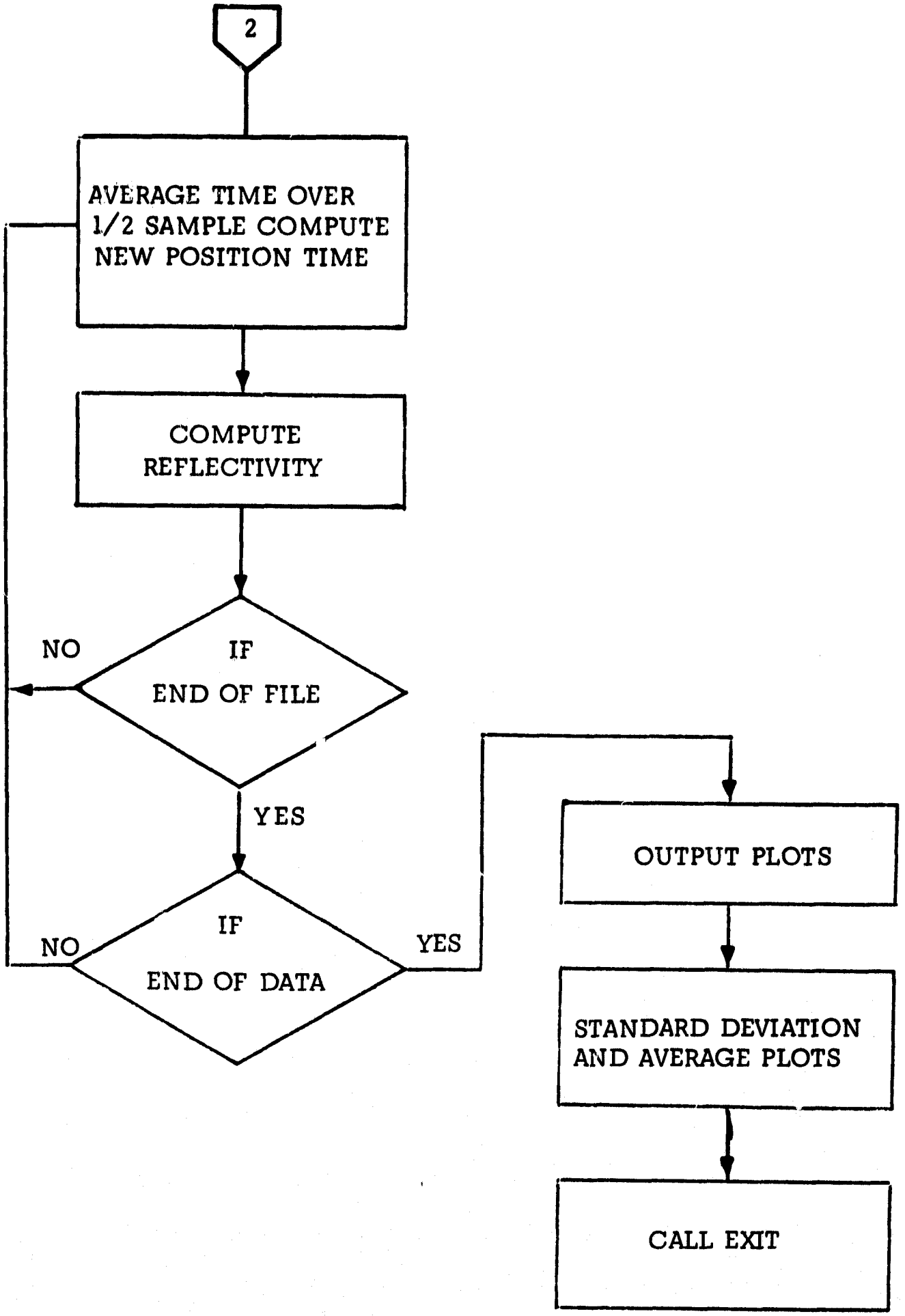
1 BCD character - tenths of seconds

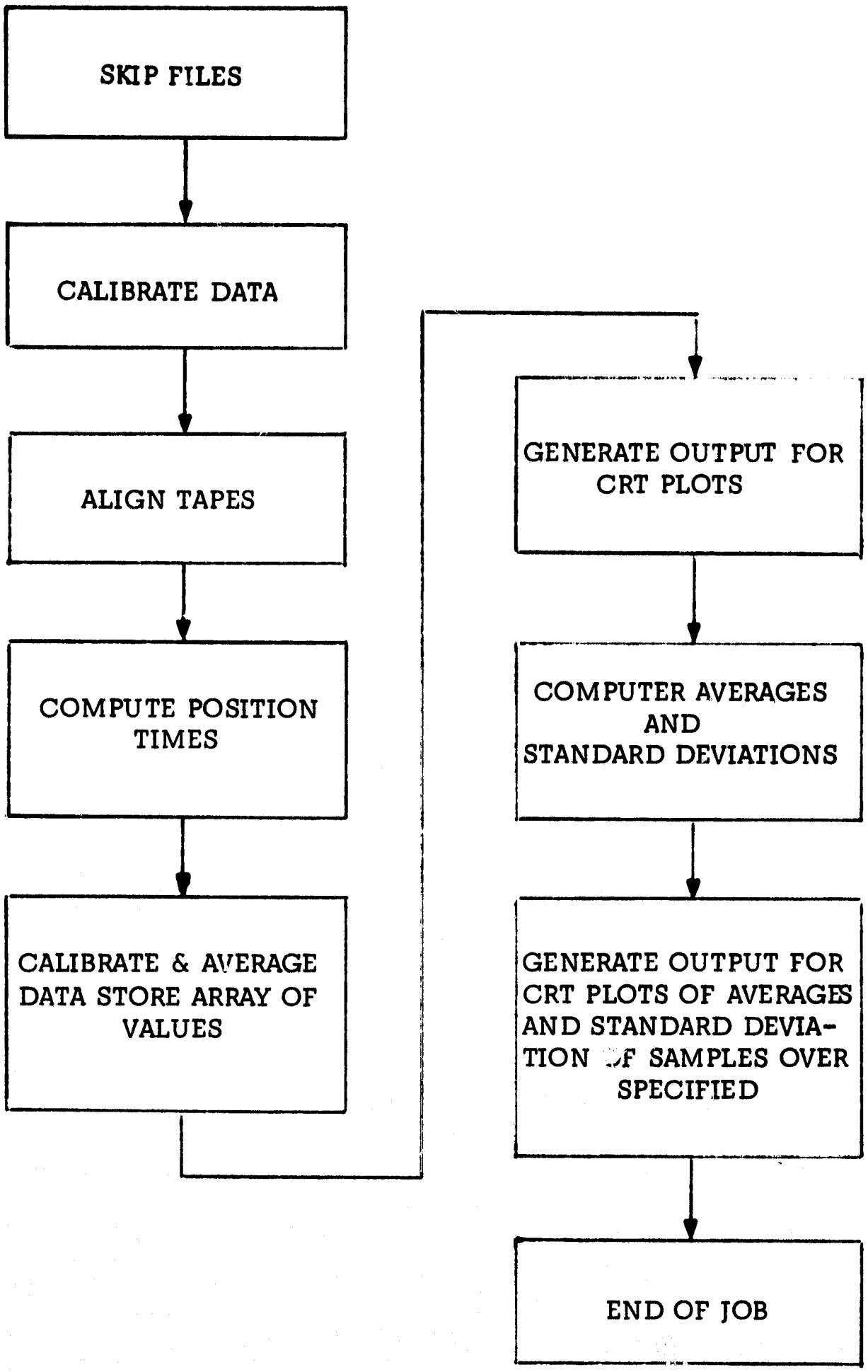
160 3 BCD character data items

total - 486 BCD characters

data range - data items may range from a maximum of 999 counts to a minimum 0 - 99 counts


READ LEAD CARDS
INDICATE WHETHER OVER WATER OR OVER LAND ON CRT PLOTS
SKIP FILES
SOLVE CALIBRATION FILE FOR SLOPE
IF SLOPE NOT IN LIMITS SET TO .002352
ADJUST TAPES TO EQUAL REAL TIMES
CHANGE VELOCITY TO FT/SEC
COMPUTE POSITION TIMES FOR FIRST SAMPLE
2


2
AVERAGE TIME OVER 1/2 SAMPLE COMPUTE NEW POSITION TIME
COMPUTE REFLECTIVITY
IF END OF FILE
NO
YES
IF END OF DATA
NO
YES
OUTPUT PLOTS
STANDARD DEVIATION AND AVERAGE PLOTS
CALL EXIT


SKIP FILES
CALIBRATE DATA
ALIGN TAPES
COMPUTE POSITION TIMES
CALIBRATE & AVERAGE DATA STORE ARRAY OF VALUES
GENERATE OUTPUT FOR CRT PLOTS
COMPUTER AVERAGES AND STANDARD DEVIATIONS
GENERATE OUTPUT FOR CRT PLOTS OF AVERAGES AND STANDARD DEVIATION OF SAMPLES OVER SPECIFIED
END OF JOB

4.4.3 Ryan Advanced Computer Program

Ryan proposed and generated an advanced computer program that was capable of correcting for variations in velocity, altitude and pitch. No correction can be made for roll or drift since their primary effect is to smear the resolution cell. Limits were placed in this program, however, to eliminate any data with excess roll or drift.

This computer program was designed to fulfill the requirements set forth in Section 4.4.1 of this report. The equations used in this program are given below. Figure 45 illustrates the relation between the ground cell and the air cell. Figure 46 illustrates tape data time for the intermediate incidence angles. The remaining pages in Section 4.4.3 are the program flow charts.

1. Doppler Frequency

$$D = \frac{2V}{\lambda} \text{ Sin } \theta$$

D	=	Doppler Frequency = Filter Center Frequency
V	=	Aircraft Velocity
λ	=	Radar Carrier Wavelength
θ	=	Incidence Angle

2. Average Velocity and Radar Altitude

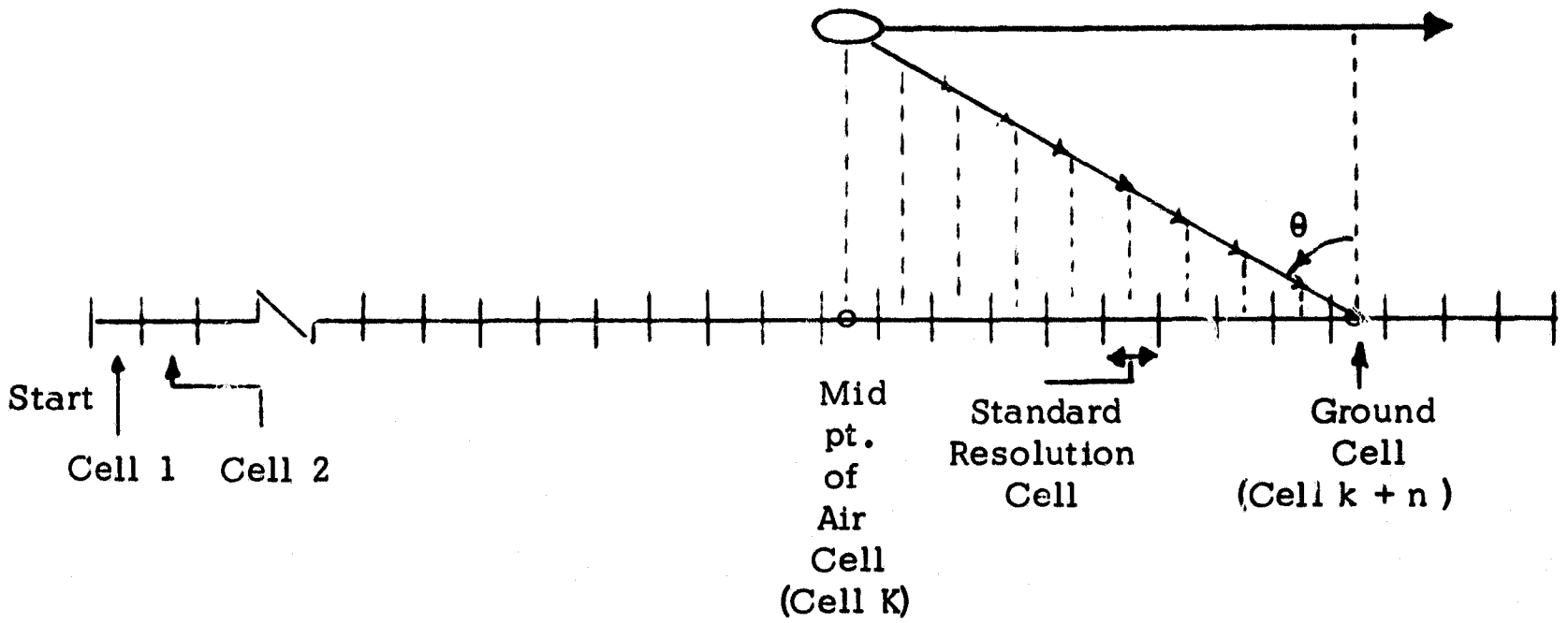
$$\bar{V} = \frac{1}{N}\sum_{i=1}^{N} V_i \qquad \bar{h} = \frac{1}{N}\sum_{i=1}^{N} h_i$$

N	=	Number of velocity or altitude values (on photo panel cards)
V_i	=	Individual velocity values (on photo panel cards)
$\bar{V}$	=	Average velocity for data run
h_i	=	Individual altitude values (from photo panel cards)
$\bar{h}$	=	Average altitude for data run

3. Inequality for Relating Ground Cell to Air Cell

$$n\bar{V}\Delta t \text{ Cot } \theta \geq h_{k+n} \qquad \text{for} \quad n = 1, 2, \ldots\ldots,$$

k	=	Index for air cell of maximum incidence angle
n	=	Difference between ground cell number at maximum incidence angle and air cell number
Δt	=	Average time to traverse one resolution cell
h_{k+n}	=	Radar altitude of ground cell
θ	=	Maximum incidence angle



Note: Terrain need not be smooth as shown for inequality to function.

Figure 45. Relation Between Ground Cell and Air Cell

4. Basic Sigma-Zero Reflectivity Equation

$$\sigma_o(\theta) = -64.4 + 20 \log_{10} h + 10 \log_{10} \overline{V} +$$

$$20 \log_{10} \frac{V_i}{K_i V_f} + R(D) - G_o^2 f'(\theta)$$

h = Radar altitude over ground cell

$\overline{V}$ = Average velocity over entire run

V_i = Radar power (in volts) representing i^{th} channel (i^{th} incidence angle)

K_i = Gain factor for i^{th} channel

$R(D)$ = Roll-off value for frequency corresponding to incidence angle θ (in DB)

$G_o^2 f'(\theta)$ = Antenna factor corresponding to incidence angle θ (in DB)

$\sigma_o(\theta)$ = Radar Backscattering Coefficient

5. Resolution Cell Time

$$T_{cell} = \left(\frac{\bar{h}}{1000}\right)\left(\frac{50}{\bar{V}}\right)^{*}$$

T_{cell} = Time to overfly a standard resolution cell at $\bar{h}$ altitude and $\bar{V}$ velocity

$\bar{h}$ = Average altitude for entire data run

$\bar{V}$ = Average velocity for entire data run

* This is based on arbitrary definition of 50 ft. square cell @ 1000 ft. altitude @ 30° angle

6. Resolution Cell Length

$$S_{cell} = \left(T_{cell}\right)\bar{V}$$

S_{cell} = Length of a standard resolution cell

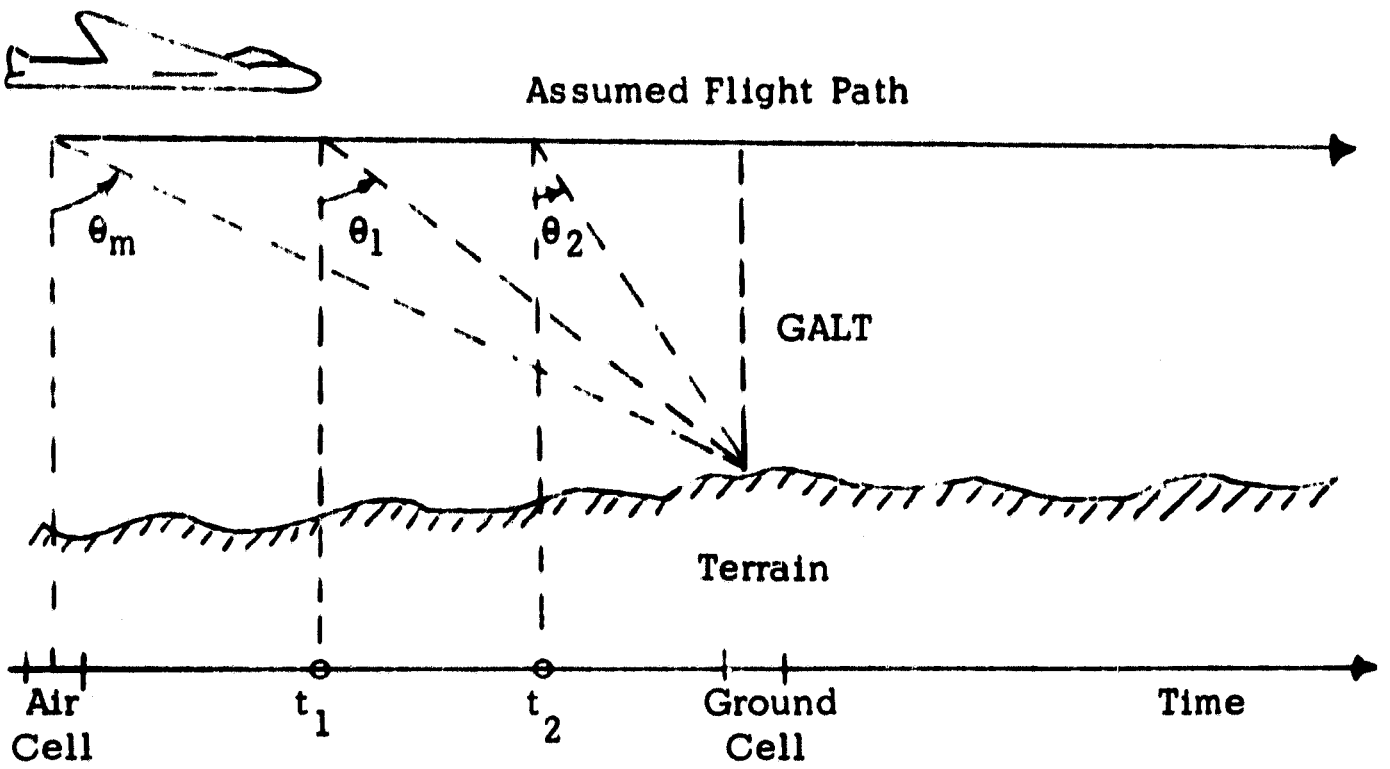
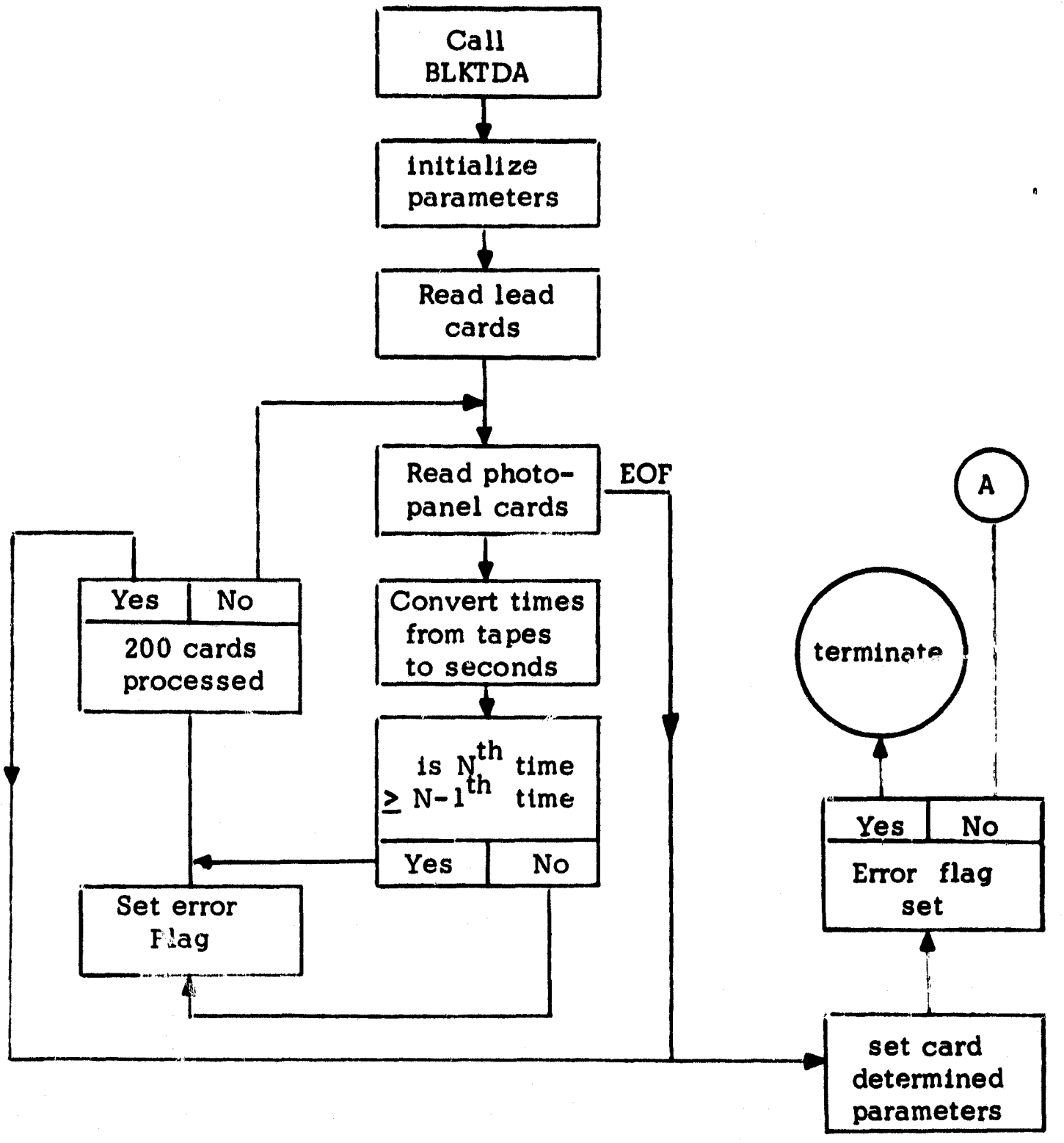
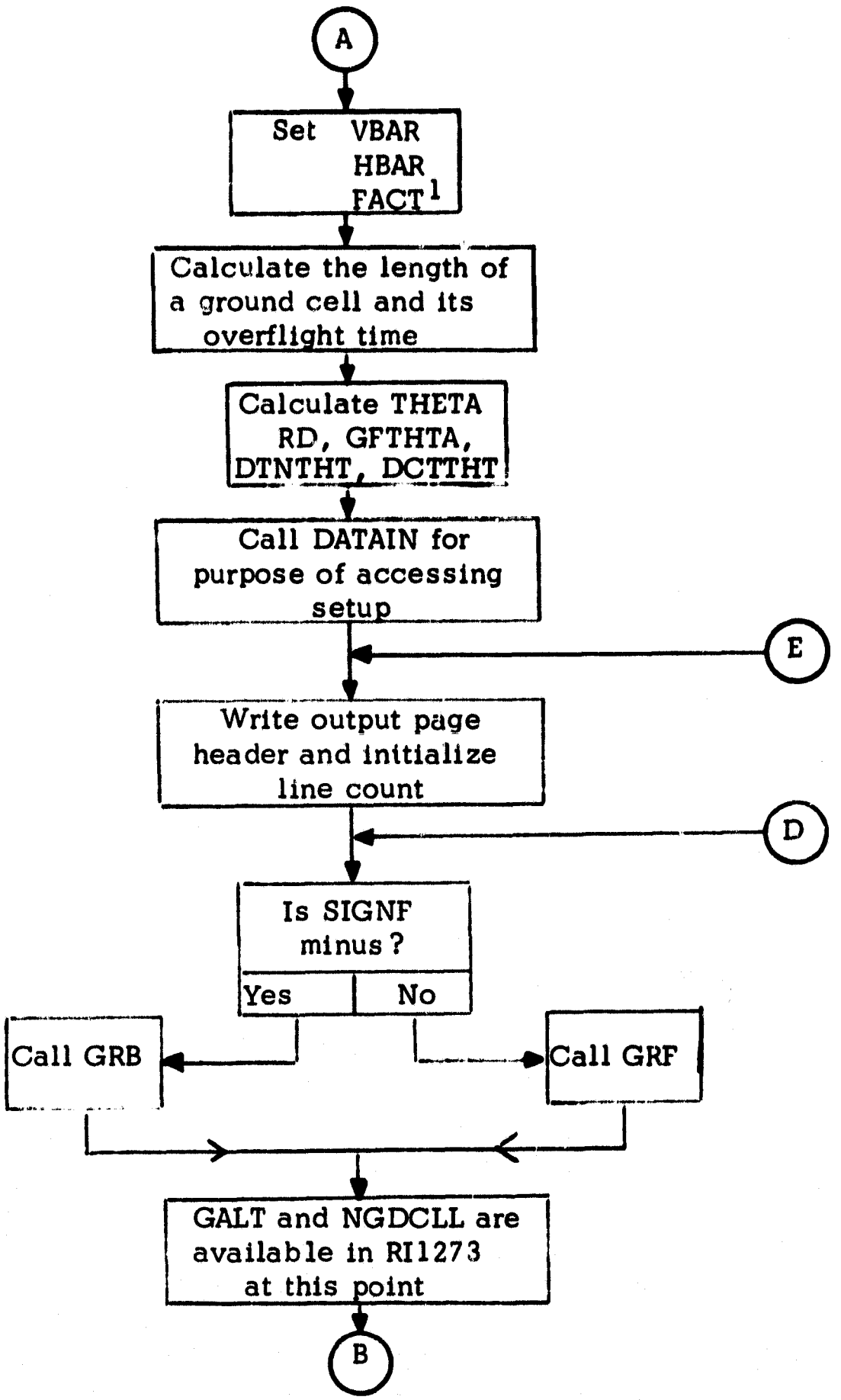


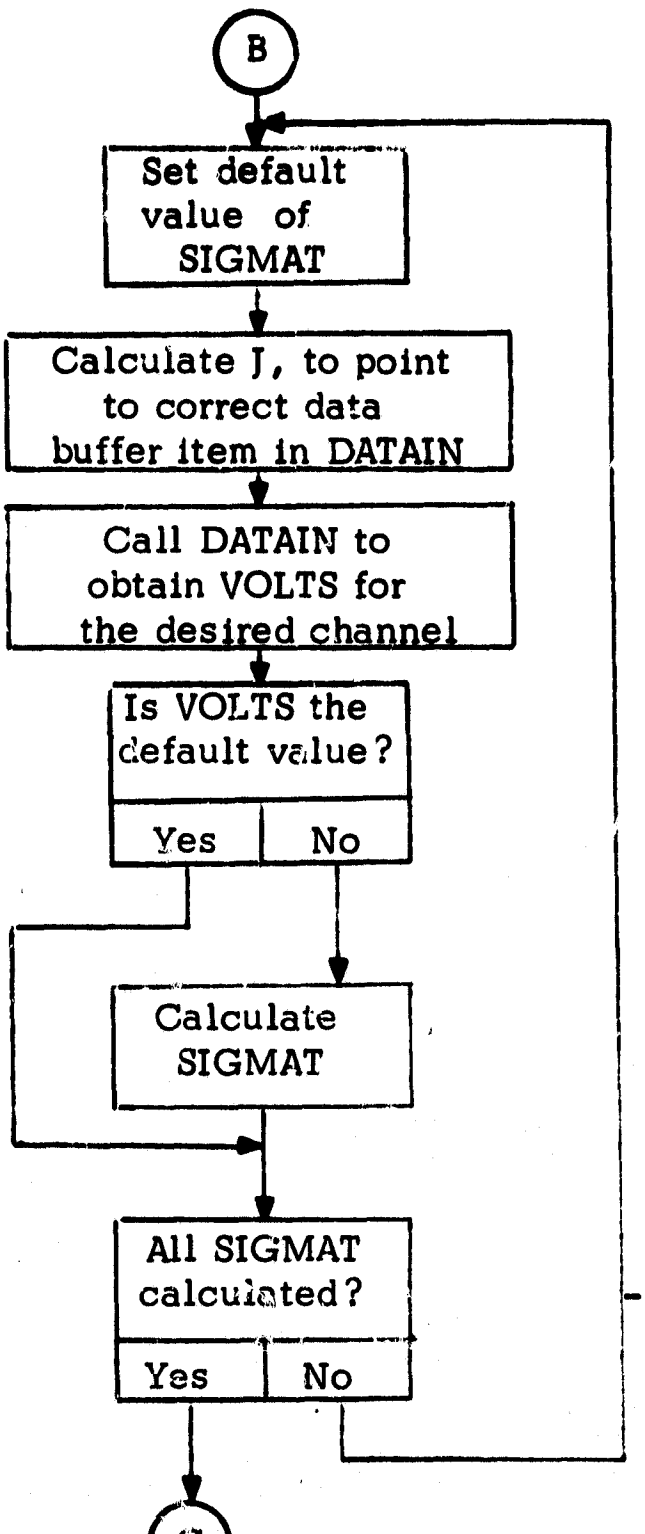
Figure 46. Tape Data Time for Intermediate Incidence Angles

General Flow Chart

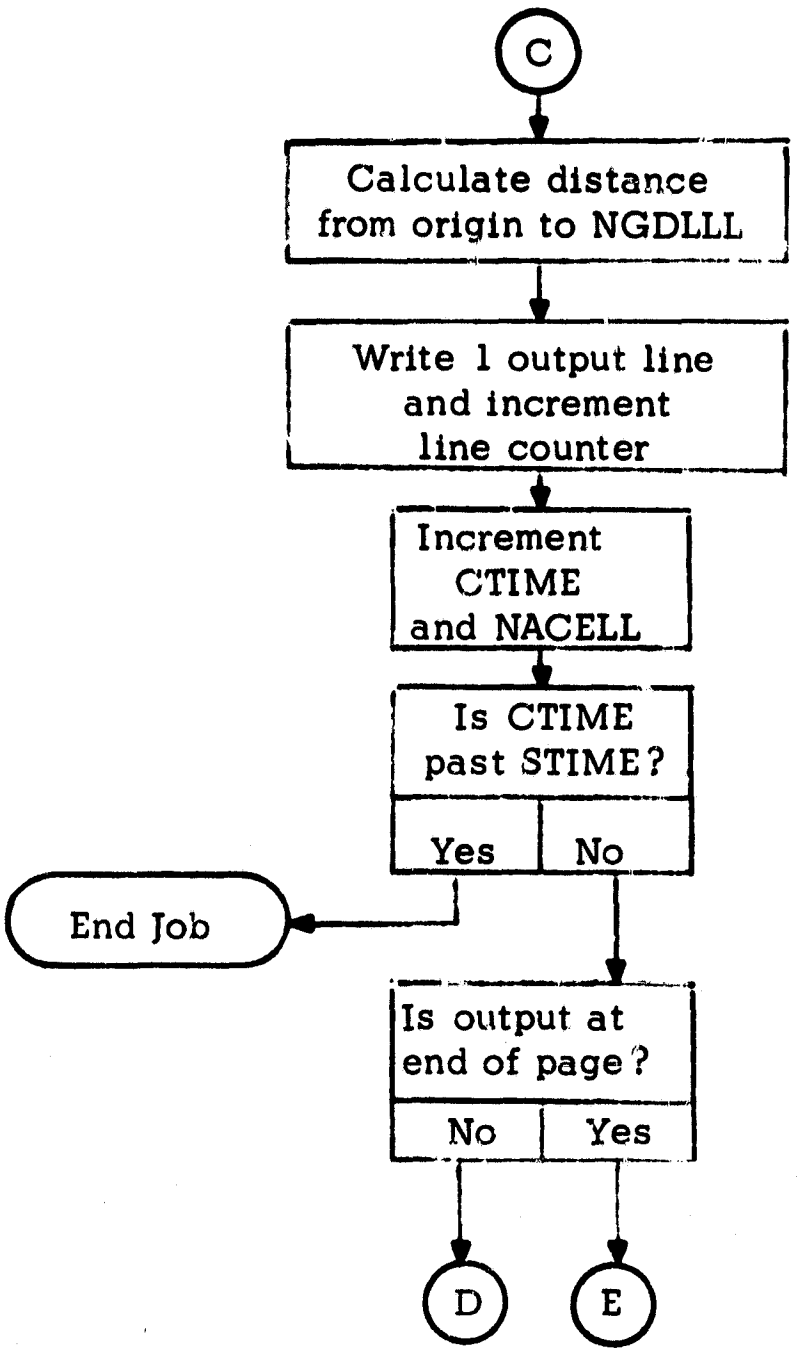



A
Set VBAR
HBAR
FACT1
Calculate the length of a ground cell and its overflight time
Calculate THETA RD, GFTHTA, DTNTHT, DCTTHT
Call DATAIN for purpose of accessing setup
E
Write output page header and initialize line count
D
Is SIGNF minus ?
Yes
No
Call GRB
Call GRF
GALT and NGDCLL are available in RI1273 at this point
B

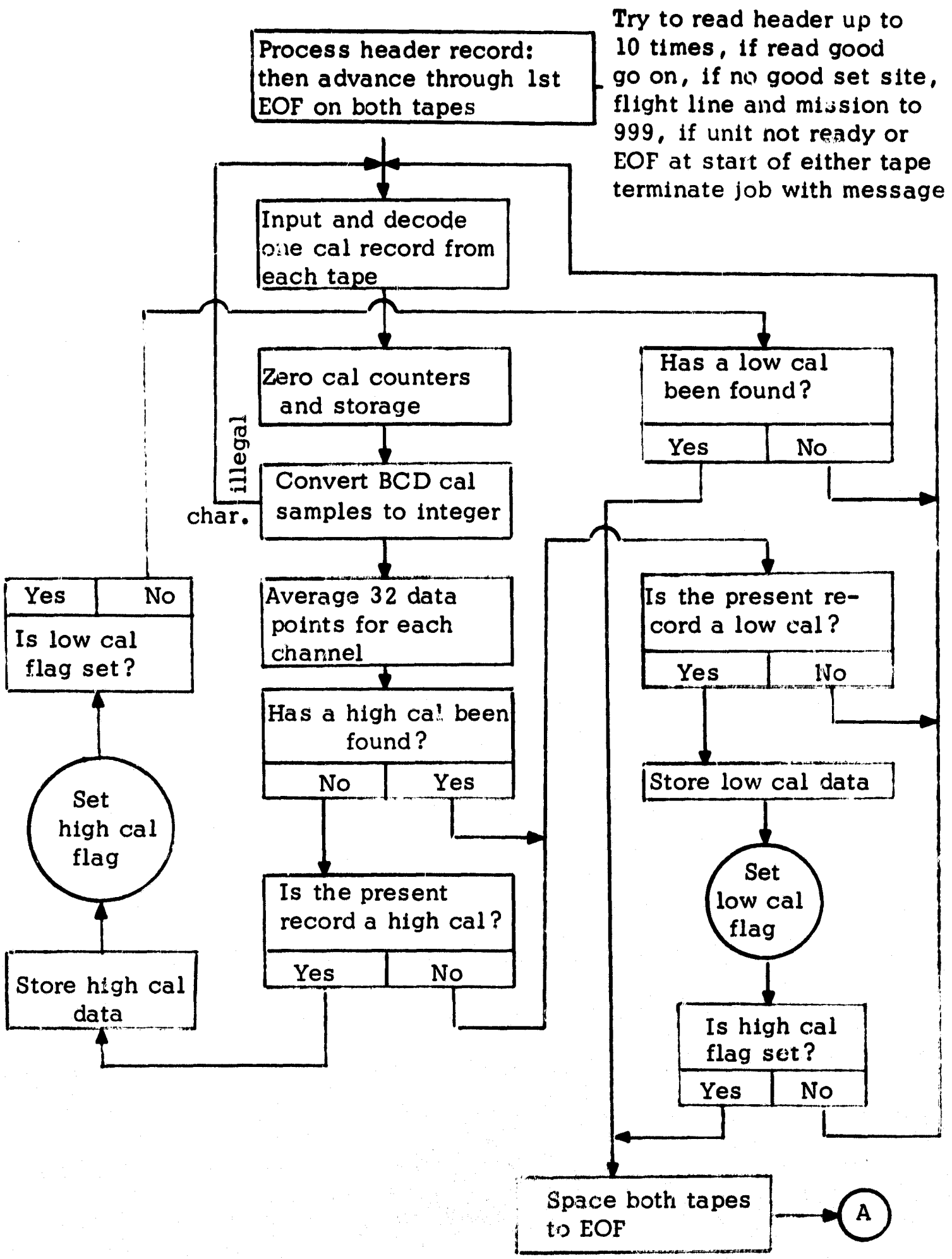
General Flow Chart (Continued)

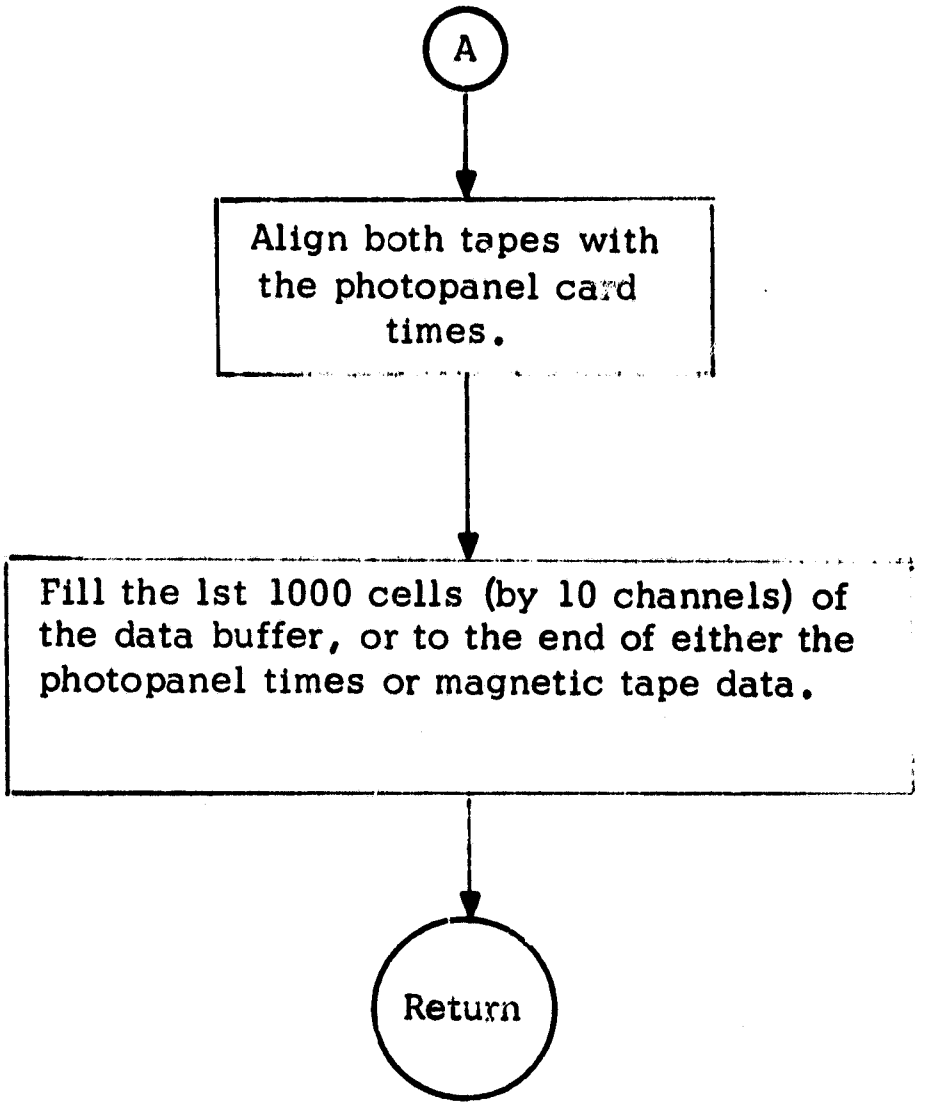


General Flow Chart (Continued)

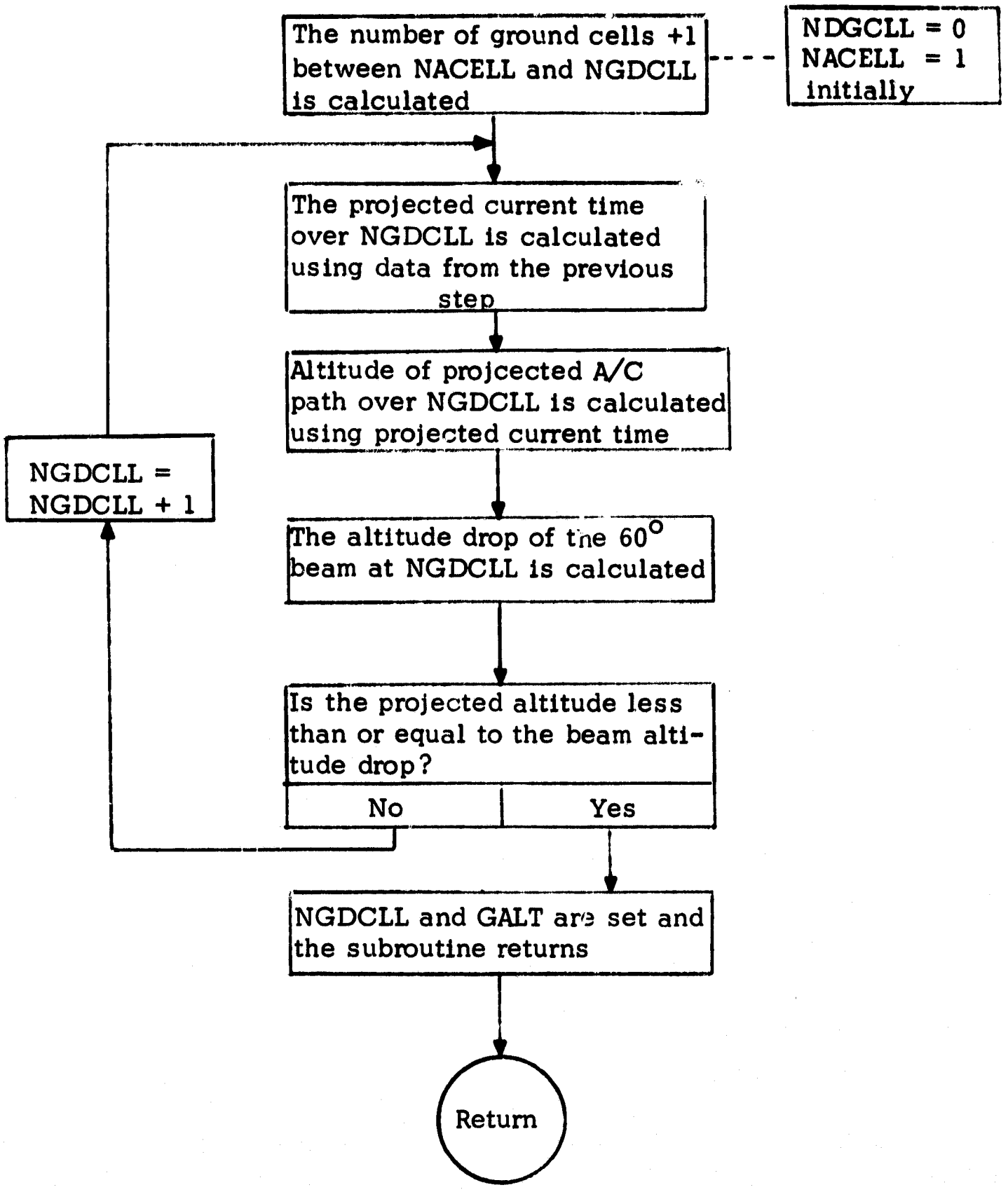


SUBROUTINE SETUP

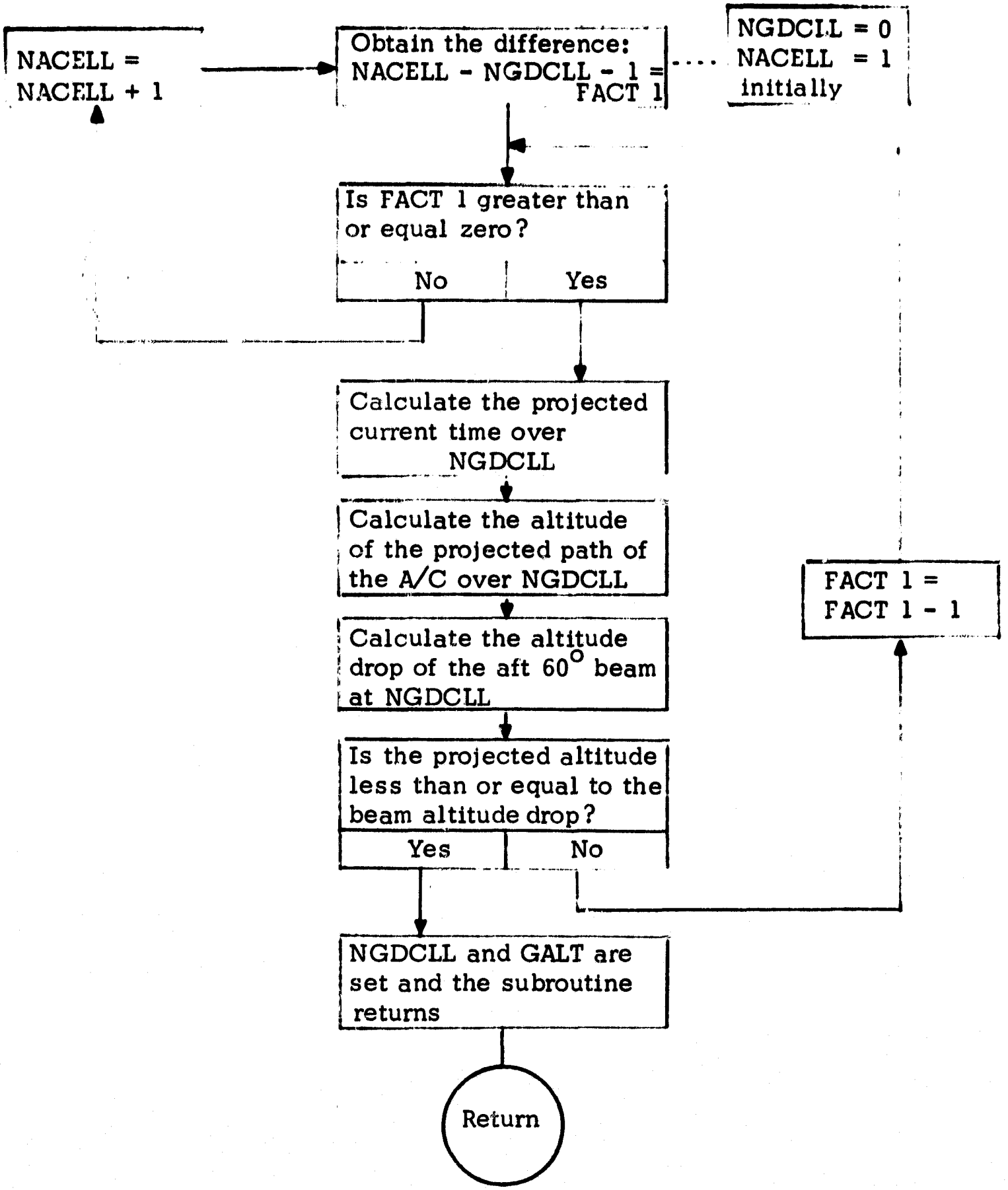



A
Align both tapes with the photopanel card times.
Fill the 1st 1000 cells (by 10 channels) of the data buffer, or to the end of either the photopanel times or magnetic tape data.
Return

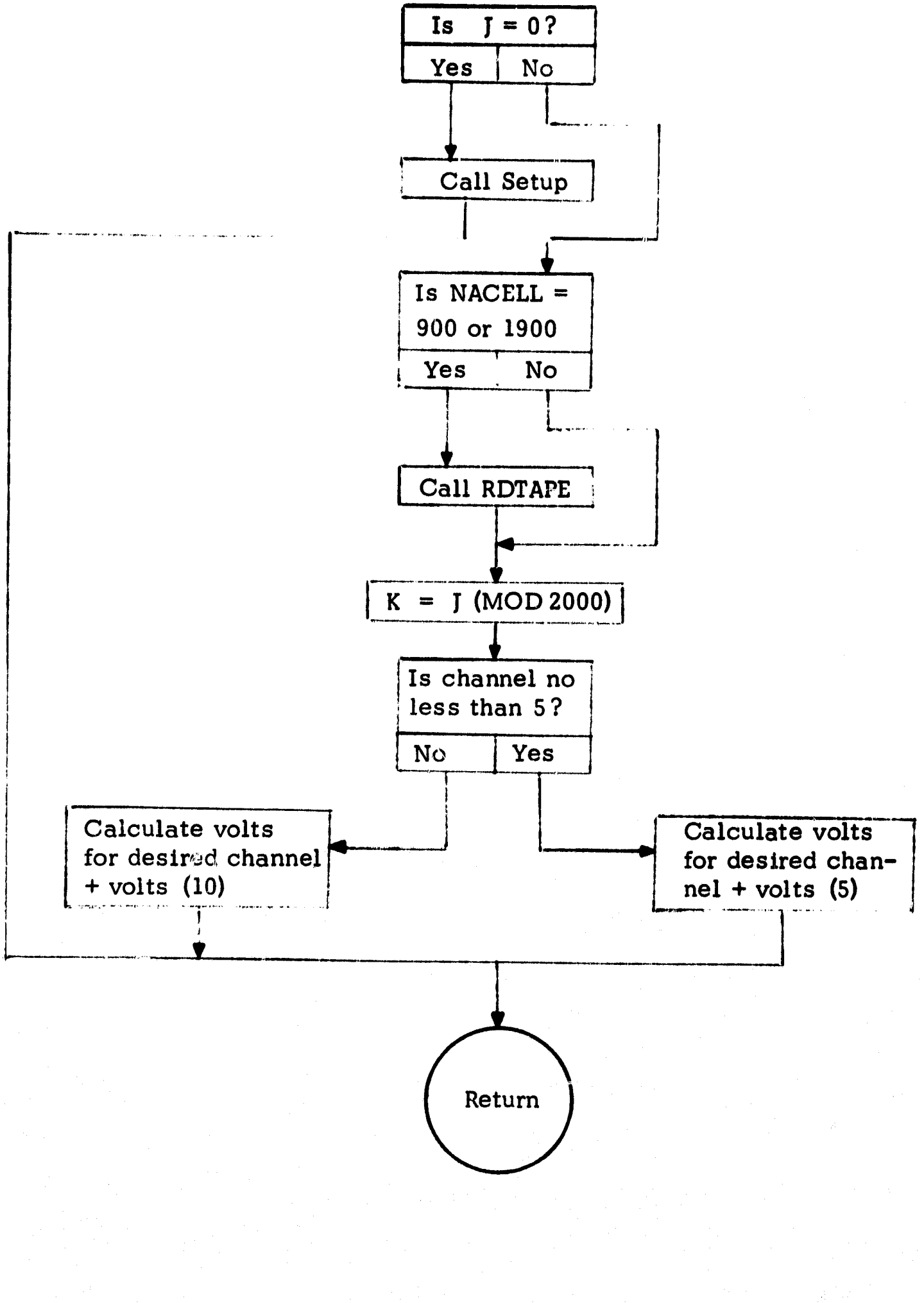
SUBROUTINE GRF



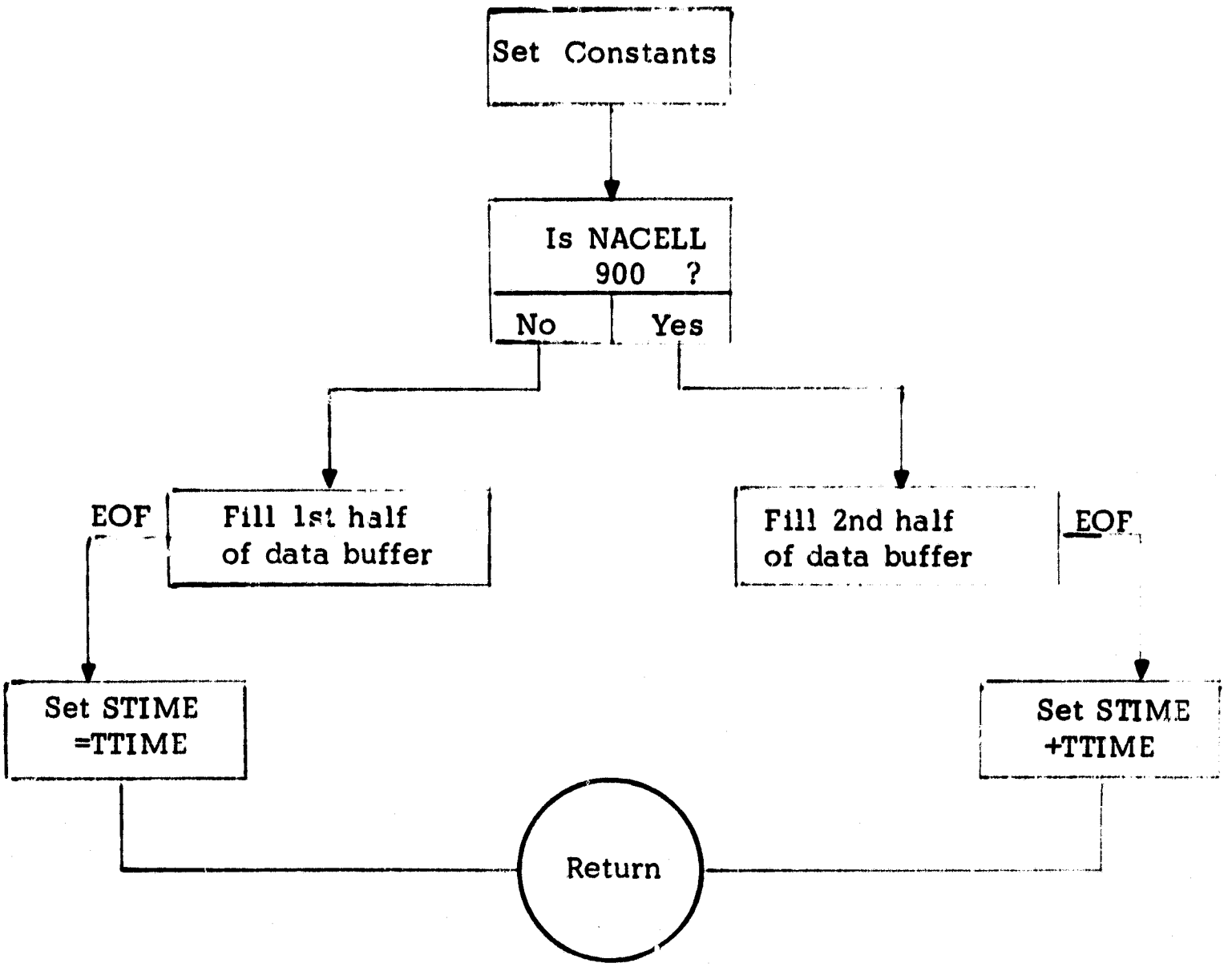
SUBROUTINE GRB



SUBROUTINE DATAIN



SUBROUTINE RDTAPE



4.4.4 Advanced RF Reflectivity Computer Program

This section contains a statement of assumptions of fact or conditions used in the advanced program. Also included is a detailed outline explaining how the program is to operate. Data tables and other peripheral information appears in Section 4.5.

Assumptions

ASQ-90 data to be available on tape at 1/10 second intervals (or 1/40 sec), and to include at least the following: ground speed, barometric altitude, radar altitude, roll angle, pitch angle, and drift angle.

Radar analog data tape to have 11 channels, including a 10 KHz reference channel, 9 separate incident angle channels, and one IRIG time channel.

Radar digital data tape produced from analog data tape will include multiplexed data from the 10 KC reference, and 9 incident angle channels. This digital data will be recorded in records such that each of the 10 channels will be equally represented in a record. Each record will be time coded with the time data on the analog data tape.

Program Outline

Input: there will be three basic inputs:

a. Lead cards

b. ASQ-90 digital data tapes: these will have the data assumed previously at 1/10 second intervals, the exact format of the data will be available.

c. Radar data tapes: these will be assumed previously and will have a "Phase I" format.

Output: There will be two basic outputs, and a possible third may be added at a later date. The first two will be on 40-20 film and are:

a. Radar reflectivity plots of backscattering coefficient (σ_o) in DB vs incident angle (θ).

b. Statistical outputs for stated time intervals. The standard deviation of the averaged data will be calculated, and plots of average plus and minus one standard deviation will be placed on the same grid with the average plot, a total of three plots on one grid.

c. At a later date, there will be a requirement to output a magnetic tape of processed radar data, possibly organized similarly to the data being plotted on 40-20 film. The exact data required and desired format will be specified. It is anticipated that this will not require major computational effort, but will simply output available data values in a form for subsequent computer usage elsewhere.

Basic Equation: The program evaluates the following:

$$\sigma_o(\theta) = -64.2 + 20 \log h + 10 \log v$$

$$+ 10 \log \frac{BW_R}{BW_i} + 20 \log \frac{E_i G_R}{E_R G_i}$$

$$+ R(D) - G_o^2 f'(\theta)$$

Note that above log terms are to base 10, and $\sigma_o(\theta)$ is in DB.

See Appendix B for definitions.

Note further that the analog filter output levels are adjusted to compare to the reference filter. That is, the reference filter output is adjusted (up or down) to a convenient level. Then the i^{th} filter outputs are adjusted (up or down, but usually up, particularly for the higher incident angle filters) to similar convenient levels, and the amount of each adjustment is noted. The object of level adjustment is to ensure that the filtered outputs do not either overdrive the tape recorder, or get lost in tape recorder noise. The computer program then must reestablish the original output levels, but only in a relative sense. Since these data are used to calculate power ratios, there actually is no need to recover the actual original values. Both G_R and G_i then, can be thought of as the amount by which the original data was multiplied before recording. To reestablish ordering, it will be necessary to divide the digital data values by G_R or G_i, whichever is appropriate.

Format for ASQ-90 Data

Time	Barometric Alt.	S	Ground Speed	d	Pitch Angle	Note
t_o	-	-	-	-	-	-
t_1	-	-	-	-	-	-
$\vdots$						
t_i						
$\vdots$						
t_{final}	-	-	-	-	-	-

Note that S and d are not taken directly from the ASQ-90 data, but are processed quantities based on ASQ-90 data. S is the terrain elevation directly beneath the aircraft, and is the difference between the barometric and radar altitudes. d is the distance measured along the horizontal since the start of the data run. It is calculated by:

$$d_i = \int_{t_o}^{t_i} v(t)\, dt \qquad i = 1, 2, \ldots$$

The column headed "note" is reserved for coded references about the quality of the ASQ-90 data. For example, no entry could mean that roll and drift angles were within bounds. A particular entry would mean one or both was marginal. Still another would mean one or both was beyond acceptable limits. It should be noted that the program will include a table of limits for these parameters, as well as others as they are defined.



Figure 56 Pisgah Crater: Northern Lava Flow

It appears that six of seven items will be required for each unit of time. If data is available at 1/10 sec intervals, this could amount to over 4000 items per minute, a figure which easily could exceed the available core for a data run of any length.

There appears to be a number of ways to handle the above situation. However, a simple straightforward way which appears desirable, is to completely preprocess the ASQ-90 data before any time table is constructed, and before any radar data is read. An auxiliary program, or subprogram, which prepared ASQ-90 data to this format on a magnetic tape, would be a solution. Then it would be practical to accept data runs of any length without concern about core storage. It would be necessary to have core available to hold something in excess of one minute of this data for efficient operation, more if possible. The reason for this is that the data representing a single resolution cell can be separated in time on tape by as much as one minute. That is, the nominal 60^{o} data may be recorded one minute prior (FB) to the instant the aircraft was directly over the resolution cell. In this case, if only one minute of data were in core, it would be necessary to shift the data in core, and then read in an additional amount of data for each resolution cell processed. To avoid this extra data handling, it would be desirable to have at least $3.5\ (h_a/v_a)$ seconds of data in core. Note that the (a) subscripts

denote average values, where the extreme values would be h_a of 20,000 ft. and v_a of 200 ft/sec, which would require 350 seconds of data in core for efficient operation. This most likely would be impractical.

To handle the case just presented, it would be appropriate to be able to cut the amount of data by decreasing the number of samples taken from the ASQ-90 data. That is, the program which preprocesses the ASQ-90 data should be able to accept on lead cards, two time increments, which would be the time increment of the input ASQ-90 data tape, and the desired time increment of the processed ASQ-90 data tape. Both of these time increments would normally be equal, probably 1/10 sec. However, the possibility exists that ASQ-90 data may be available (or desired) at a faster or slower rate. Therefore, both the preprocessing program, and the reflectivity program, should be ready to accept variable time increments.

To summarize then, the ASQ-90 preprocessing program (or subprogram) would commence by reading a lead card with input and output time increments plus other pertinent parameters. It will then prepare a magnetic tape with data per the format specified above.

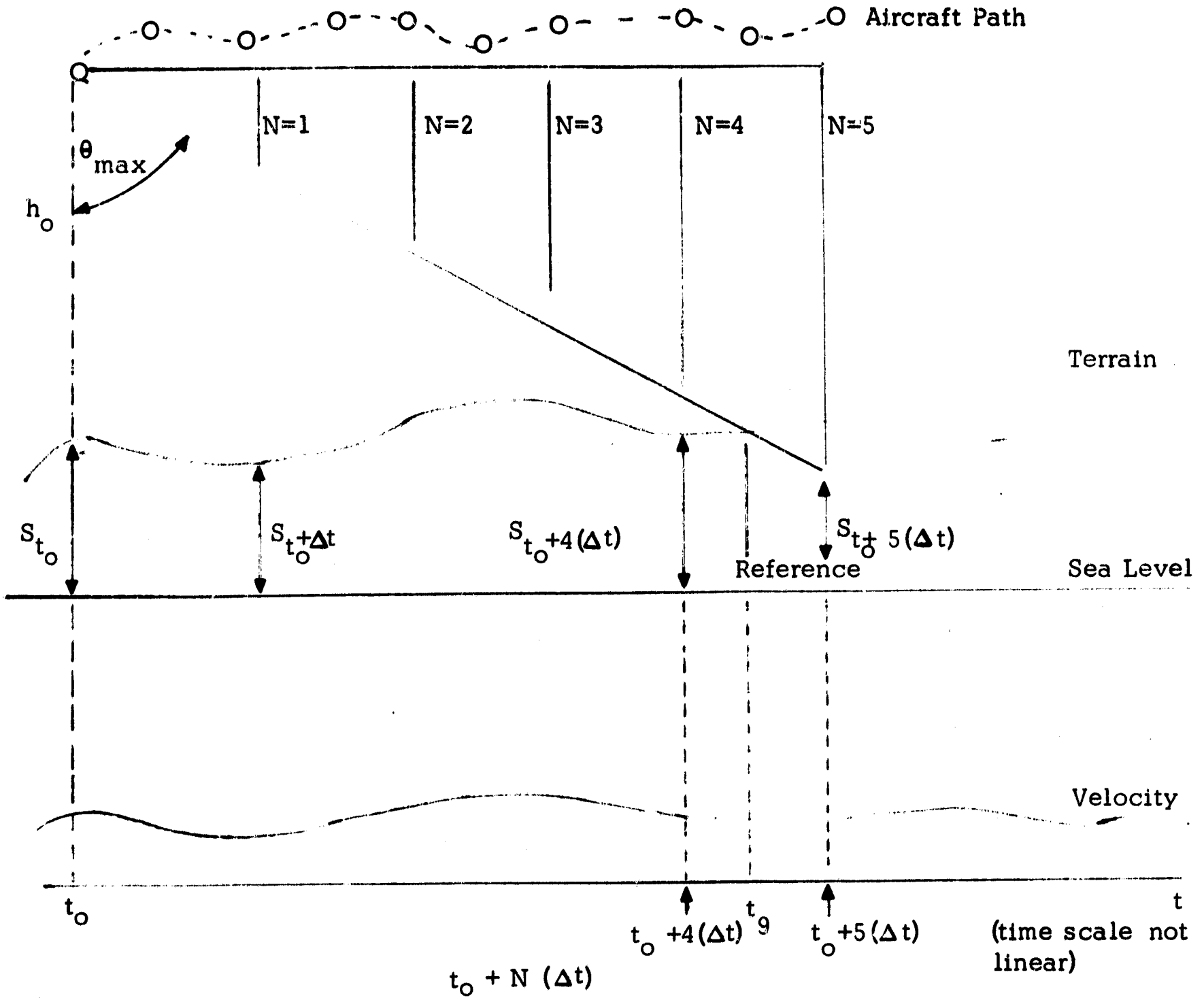
The reflectivity program will commence by reading lead cards with an input processed ASQ-90 data time increment along with other pertinent input parameters. A primary requirement will be to construct a time table from the processed ASQ-90 data. This will be done by reading in the processed ASQ-90 data in quantities as large as practical, repeating till all of the ASQ-90 data has been converted to time table form.

Basic Approach to Building Time Table

For any time t_o, it is possible to establish which particular terrain cell returned radar power at a maximum incident angle (see Figure 47). This can be done by first looking at the velocity profile at t_o to establish the velocity at that time, and from that, the actual maximum incident angle using,

$$\theta_{max} = \text{arc sin } (.5 \lambda f_{max}/v).$$

Note that f_{max} is the center frequency of the maximum incident angle channel. Thus, θ_{max} must be modified by taking into account the pitch angle of the aircraft at time t_o. Using this improved θ_{max}, it is possible to project a line from the aircraft at t_o, intersecting the terrain profile at some later time t_9, where the times $t_o - t_8$ correspond to the times radar power was recorded at the respective incident angles (maximum to minimum for fore beam), and t_9 refers to the time the aircraft was directly over the particular resolution cell, and which will be used to uniquely identify the cell.



$$d_N = \int_{t_o}^{t_o + N(\Delta t)} v(t)\, dt \qquad N = 1, 2, 3, \ldots\ldots\ldots\ldots$$

b_o = barometric altitude at $t_o = h_o + S_{t_o}$

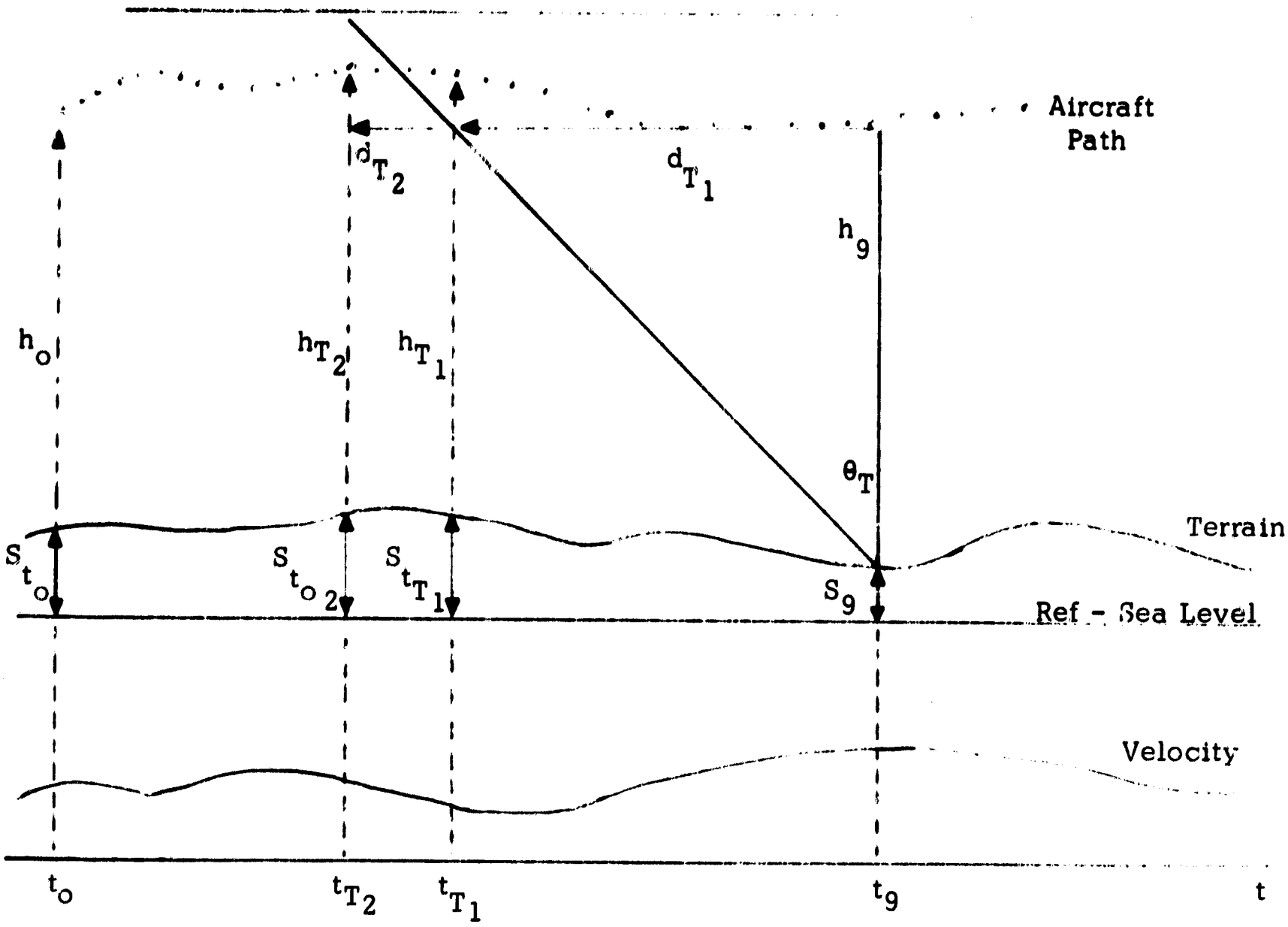
Is $b_o - d_N \cot \theta_{max} \leq S_{t_o} + N(\Delta t)$

Figure 47. Relating θ_{max} to Ground Cell

The method used to find the time t_9 follows. A line at θ_{max} from the aircraft at t_o, drops a vertical distance d cot θ_{max} for a given lateral movement d. It is simple and direct to use the processed ASQ-90 data to find that first point in time, at which the barometric altitude at t_o less the vertical drop d cot θ_{max}, equals, or approximately equals, the terrain elevation s at the time corresponding to lateral movement d. In the event interpolation is required, linearity assumptions are reasonable.

Once t_9 is established, it is required to establish the beginning tape times for the intermediate angle data ($t_1 - t_8$). The procedure for finding any of these times follows. Starting at t_9 (the center of the cell), project a line backward (in time and direction) at the nominal angle. As a first trial, project far enough to reach a barometric altitude equal to that at t_9.

This will be done by referring to the ASQ-90 data using h_9 tan θ_T as the entry key. This will produce a provisional time t_{T1}. The barometric altitude corresponding to time t_{T1} will be found to be greater than b_9 (see Figure 48), which says the aircraft did not receive radar power at this nominal angle and time from the cell at t_9. Therefore the line from the resolution cell must be projected further along the θ_T direction to find the point at which it crosses the aircraft path as defined by the barometric altitude data. It is suggested that the line be projected upward an amount 25 percent



(Note that above time scale is not linear.)

$d_{T_1} = h_9 \tan \theta_T$ θ_T a nominal incident angle such as 5°, 10°, 20°, 30°, 45°

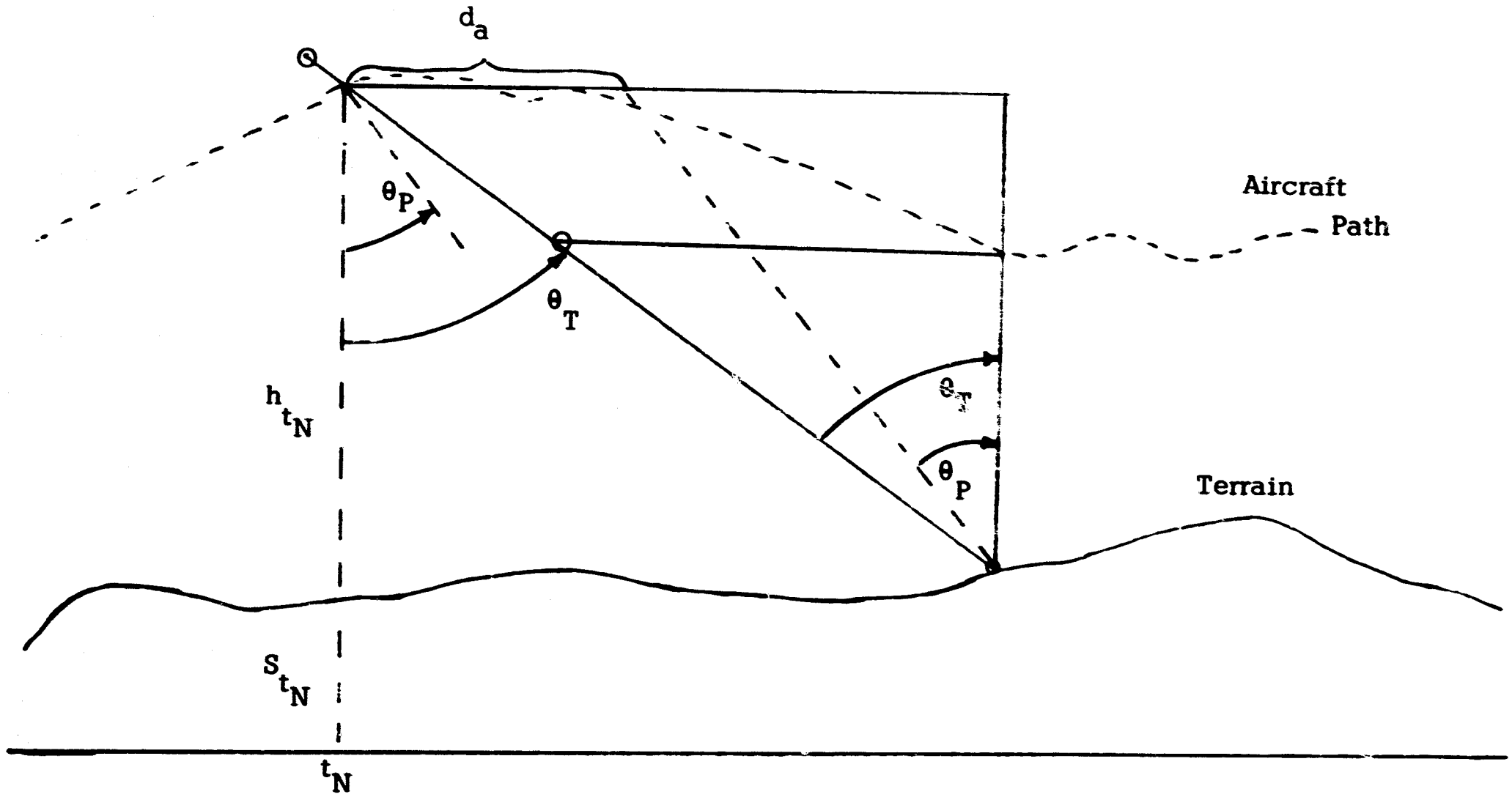
$d_{T_2} = (h_9 + \frac{5}{4} \left\{ b_{T_1} - b_9 \right\}) \tan \theta_T$

Figure 48. Finding Intermediate Angle Radar Data Tape Times

greater than the difference between b_{T1} and b_9 to insure that this second move will cross the aircraft path. It may be found that this is still not enough, and a third move along the θ_T line will be required. Figure 48 shows that the path was crossed on the second move, which corresponded to a second provisional distance d_{T2}, which, used as the key to enter the ASQ-90 data table, gives t_{T2}. Note that the large T subscripts denote "trial" or "test".

The barometric altitude corresponding to time t_{T2} is available from the ASQ-90 table, and was found to be less than the trial barometric altitude. This says that the aircraft passed between the two test altitudes while collecting radar power at nominal angle θ_T from t_9. Since the test altitudes are close together, interpolation with linearity assumed is reasonable to find the nominal point and time on the aircraft path.

Once the nominal time t_N is found at which the radar could have received power at θ_T from the cell at t_9, it is necessary to examine the velocity profile at t_N. If the velocity at t_N is consistant with the nominal θ_T incident angle, then the time t_N is the proper time on tape to look for radar data. If the velocity at t_N is not consistant with θ_T, which is most likely, it then is necessary to make a time adjustment. For example, in Figure 49, the velocity at t_N is v_{t_N}. This velocity and pitch angle data at t_N defines the



$$d_a = b_{t_N} (\tan \theta_T - \tan \theta_p)$$

$$b_{t_N} = h_{t_N} + S_{t_N}$$

Figure 49 Finding Distance and Time Adjustment to Correct Nomina Angles

angle at which radar power was received at t_N, as θ_P could have been greater than θ_T if the velocity and pitch data had been different. Knowing that θ_P is less than θ_T tells us that the data on tape at time t_N is from a cell prior to the cell at t_9. It follows that the data from the t_9 cell is on tape at a time following t_N.

The procedure for finding the proper time adjustment to add to the time t_N for Figure 49 follows. Determine d, the apparent horizontal distance between the t_N point and a point at which θ_P would have intercepted an undeviated aircraft path. The time to travel this distance at velocity v_{t_N} is $\Delta t_a = d_a/v_{t_N}$. This is an estimate of the time adjustment, and may be satisfactory without further correction. A good rule of thumb, however, is to accept the Δt_a whenever it is one second or less. For Δt_a greater than one second (in absolute value), enter the ASQ-90 table with the time key of $t_N + \Delta t_a$ to find the associated velocity. If this velocity, v_a, is different from v_{t_N} by more than 1 knot, repeat the above using the angle θ_p, as the new value of θ_t, and for v_a calculate a new value of θ_p. Thus, to summarize:

$$\Delta t_a = d_a/v_{t_N}$$

If $/\Delta t_a/ \leq 1$ sec, then the desired angle time to $t_N + \Delta t_a$.

If $/ t_a/ > 1$ sec, then find the velocity corresponding to $t_N + t_a$, v_a in ASQ-90 data table.

If $/v_{t_N} - v_a/ \leq 1$ knot, then the desired angle time is $t_N + \Delta t_a$.

If $|v_{t_N} - v_a| > 1$ knot, then repeat the above on time, accepting the results as final.

The structure of the time table will consist of sets of start and stop times. These will specify the tape times of data to be used to compute backscattering coefficients. The start times will correspond to the time data was returned from the center of the terrain cell, and the stop times to the trailing edge of the cell. For a particular cell, then, there will be a time set for each of the nine incident angles, plus a single time value t_9, the aircraft time over cell center, and a single coded entry which will relate the data quality for any or all of the nine data intervals. These add to 20 data values for each cell. See Figure 50. The "note" column as shown, illustrates one way of coding the quality of the G & N data.

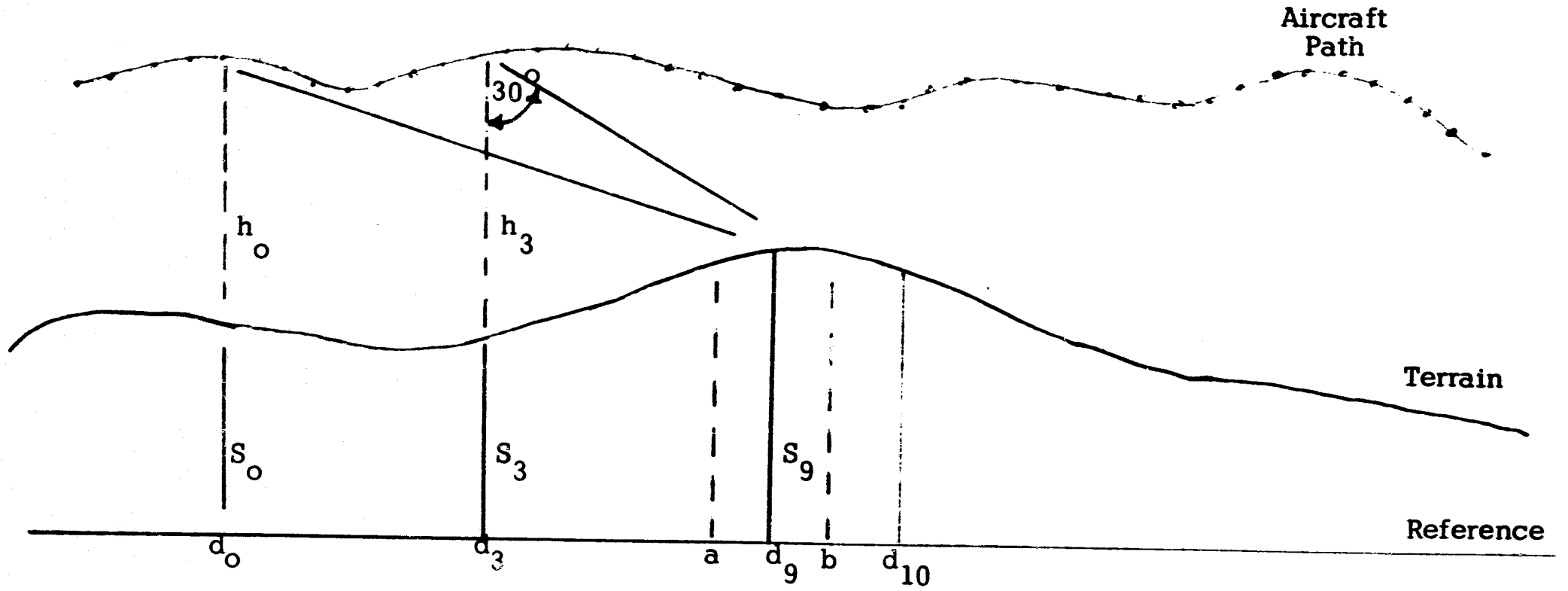
Resolution Cell Size and Time

Aircraft path and velocity vary while traversing a particular cell. It is important, however, that cell size remain constant for a particular plot; that is, the cell should have the same dimension when viewed from 60° as from 5°. To accomplish this, the aircraft 30° barometric altitude and velocity will be used. See Figure 51.

The time between a resolution cell center and the adjacent following cell center will be the same as the time to fly over the first cell at its 30° angle velocity. This will space cells rather

	60	50						10	5	2-1/2	Note/t_9
Start	.501	1.62	2.58					8.21	9.25	10.32	0102
Stop	.98	1.99	3.01					8.73	9.7	10.79	11.09
Start	1.52	2.49	3.57					9.15	10.31	11.28	0100
Stop	1.99	2.98	4.02					9.60	10.79	11.77	12.03
Start	2.49										
Stop	3.02										
Start											
Stop											

Figure 50 Time Table - Partially Filled



Resolution Cell Size = b - a = R = $\frac{h}{20}$

Cell Time = CT = R/V = $\frac{h}{20V}$

Where $h = b_3 - S_9$, $b_3 = h_3 + S_3$

V and b_3 defined at 30^o (nominal).

Note that Cell Time is that time to fly over cell (a to b) and time to fly from cell center (d_9) to adjacent cell center (d_{10}) Cell size and time for cell centered at d_{10} will be based upon b and V data when aircraft at 30^o incident angle from that cell.

Figure 51 Resolution Cell Size and Time Defined at 30^o

regularly along the horizontal reference. They will not necessarily touch one another, or, on the other hand, may overlap very slightly due to the different bases for size definition of adjacent cells. It should be emphasized, however, that the amount of nonincluded and overlapped terrain is extremely small.

It should be remembered that the above was discussed in the fore beam sense. Read beam data would be handled similarly, again using the 30° data for definition.

Averaging of Cell Data

To minimize the effects of "noise" from the radar or reduction system, it is necessary to average the data returned from a given cell. The method to be used is essentially that used in the basic program, namely to average data from one half of the cell, and disregard the data from the other half.

The actual number of points to be averaged will vary with velocity and altitude. Digitizing rate will also directly affect this number. It is intended that there be at least 5 or more points included. This number should be used as a minimum in planning the conversion of the analog filtered tape to a digital tape (see Figure 52). Note that the above averaging procedure, coupled with the existing method of defining analog filter bandwidth, results in cells approximately 150 percent of the desired dimension.

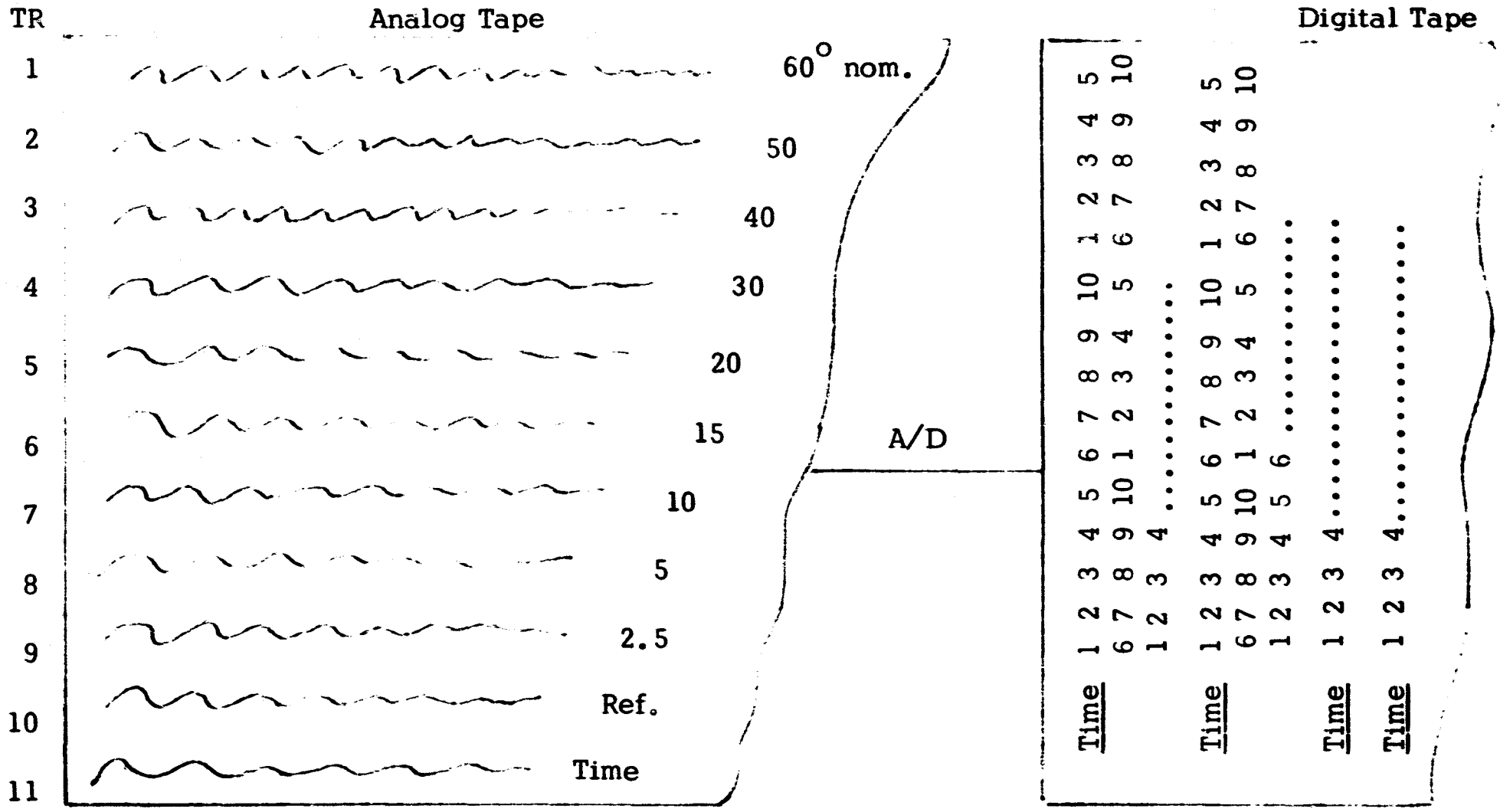


Figure 52 Generalized Desired Analog and Digital Tape Formats for Radar Data Tapes

Guidance and Navigation Parameter Limits

The program should include provision for annotating reflectivity plots with information relating the conditions under which the source data was collected. For instance, if some or all of the incident angle data for a particular plot was collected while the aircraft was undergoing significant movement about its roll axis, the resulting plot will not represent the target resolution cell as well as it might if the movement were not present. Similar statements can be made about drift angle perturbations. Therefore it will be necessary for the reflectivity plot program to include a table of limiting values for critical parameters, and to include mechanism to compare the actual values of these parameters with their limiting values. This comparison can have one of three results, namely that data collected is 1) good, 2) marginal, or 3) unsatisfactory.

A beginning table of limiting values follows:

	Good	Marginal	Unsatisfactory
Roll Angle	$< .5^{o}$	$\leq 1.25^{o}$	$> 1.25^{o}$
Drift Angle	$< .5^{o}$	$\leq 2.5^{o}$	$> 2.5^{o}$
Vertical Velocity	< 2 ft/sec	$\leq$ 6 ft/sec	>6 ft/sec

Other parameters will be added as their limiting values are defined.

Reading Radar Data Per the Time Table

Once the time table (see Figure 50) has been completed, it is time to commence reading the digital radar data tape. This tape will have a format similar to that shown in Figure 52. The data will occur in sets of 10 values ordered from 60^{o} (nominal) data to reference data. Note that the 9 data channels are here referred to by their corresponding nominal incident angles. Time can be interpolated between records such that each set of 10 values has a unique time associated with it. It is desired, then, to consult the time table to find the start time for a given cell at the maximum angle (for FB, minimum otherwise). Then all 60^{o} data values and reference values between the start and stop time will be added. Both of these sums will be used for computation of the σ_o coefficient, similarly, for each of the other angles for the cell. It will be noted, that the angle information for the cells will be intermixed, which will necessitate processing data for a number of cells at the same time. This relates to the process used in the basic program.

The end product will be a table of σ_o plot coefficients. These may be retained in core, or output on tape, depending upon the amount of core available. In either case, they must finally be converted to a plot.

Plot Format

A plot may have the same general format as is currently used in the basic program. It is desired to be able to annotate the plots additionally, however. That is, it should be possible to place a label or line of information on each plot, the line of information to be the same for all plots made from a given computer run.

A second added annotation will be to place the photo number on the reflectivity plot. An effort should be made to use that photo number which places the reflectivity plot nearest the photo center.

Calibration

The calibration procedures used will be similar to those used for the basic program. However, there will be no need for a file of "Station Cals" as presently used. It is anticipated that the analog tape will have a calibration area at the start of each data run, that data runs will typically be 10 minutes of real time data or less, and that the digitizing equipment will be assumed to drift insignificantly over the data run. Thus each of the 10 data channels will have at least 10 seconds of minimum level, followed by at least 10 seconds of maximum level as the calibration.

4.5 Scatterometer Data Tables

The following group of tables represent all the latest constants used in deriving $\sigma_o(\theta)$ plots from PSD and time history RMS plots.

The roll-off tables for over land (Table V), over water (Table VI), and Mission 20 (Table VII), were derived from values gathered on board the aircraft by Ryan. The antenna pattern factors tables (Tables VIII and IX) were prepared from measurements by the Instrumentation and Electronic Systems Division on the NASA antenna range.

When using these tables, linear intepolations can be made between any two successive points with negligible error. When deriving $\sigma_o(\theta)$ values from a composite PSD or RMS plot, the fore and aft $G_o^2 f'(\theta)$ readings should be averaged at each angle of interest.

Table V

COMPOSITE ROLL-OFF FUNCTION
FOR OVER LAND MISSIONS

DOPPLER FREQUENCY (cps)	CHANNEL FREQUENCY (cps)	ROLL-OFF R(D) (db)
10	19,990	30.8
20	19,980	24.3
30	19,970	21.3
40	19,960	18.3
50	19,950	16.8
60	19,940	15.3
70	19,930	13.8
80	19,920	13.3
90	19,910	12.9
100	19,900	11.3
200	19,800	5.8
300	19,700	2.8
400	19,600	1.8
500	19,500	0.8
600	19,400	0.3
700	19,300	-0.1
800	19,200	-0.4
900	19,100	-0.5
1,000	19,000	-0.8
2,000	18,000	-1.0
3,000	17,000	-1.0
4,000	16,000	-0.9
5,000	15,000	-0.9
6,000	14,000	-0.7
7,000	13,000	-0.4
8,000	12,000	-0.3
9,000	11,000	-0.1
10,000	10,000	0.0

Table VI

COMPOSITE ROLL-OFF FUNCTION FOR ALL OVER WATER MISSIONS (EXCLUDING MISSION 20)

DOPPLER FREQUENCY (cps)	CHANNEL FREQUENCY (cps)	ROLL-OFF R(D) (db)
100	19,900	22.9
150	19,850	21.1
200	19,800	20.0
250	19,750	18.9
300	19,700	17.6
400	19,600	15.8
500	19,500	14.3
600	19,400	13.1
700	19,300	12.0
850	19,150	10.3
1,000	19,000	9.0
1,250	18,750	7.5
1,500	18,500	6.3
2,000	18,000	4.3
2,500	17,500	3.2
3,000	17,000	2.1
4,000	16,000	1.0
5,000	15,000	.3
7,000	13,000	-.1
10,000	10,000	0.0

Table VII

COMPOSITE ROLL-OFF FUNCTION FOR MISSION 20 ONLY

DOPPLER FREQUENCY (CPS)	CHANNEL FREQUENCY (CPS)	ROLL-OFF R(D) (db)
40	19,960	37.2
50	19,950	35.9
60	19,940	34.7
70	19,930	33.3
80	19,920	32.2
90	19,910	31.1
100	19,900	30.3
200	19,800	24.3
300	19,700	21.0
400	19,600	18.8
500	19,500	17.0
600	19,400	15.6
700	19,300	14.5
800	19,200	13.4
900	19,100	12.3
1000	19,000	11.5
1250	18,750	9.9
1750	18,250	7.4
2000	18,000	6.6
3000	17,000	4.2
4000	16,000	2.6
5000	15,000	1.7
6000	14,000	1.1
7000	13,000	0.6
8000	12,000	0.3
9000	11,000	0.1
10,000	10,000	0.0

Table VIII

SCATTEROMETER ANTENNA PATTERN F/ CTOR

FORE

θ (degrees)	Beamwidth (db)	$G_o^2 f(\theta)$ (db)	$G_o^2 f'(\theta)$ (db)
0	-13.7	38.1	24.4
1	-13.6	38.3	24.7
2	-13.6	38.4	24.8
3	-13.7	38.5	24.8
4	-13.7	38.5	24.8
5	-13.7	38.5	24.8
6	-13.7	38.6	24.9
7	-13.7	38.6	24.9
8	-13.8	38.5	24.7
9	-13.8	38.4	24.6
10	-13.8	38.3	24.5
11	-13.8	38.2	24.4
12	-13.8	38.1	24.3
13	-13.8	37.9	24.1
14	-13.8	37.7	23.9
15	-13.8	37.8	24.0
16	-13.8	38.0	24.2
17	-13.8	38.2	24.4
18	-13.8	38.5	24.7
19	-13.8	38.6	24.8
20	-13.8	38.8	25.0
21	-13.7	38.8	25.1
22	-13.7	38.9	25.2
23	-13.7	38.9	25.2
24	-13.7	39.1	25.4
25	-13.7	39.0	25.3
26	-13.6	39.1	25.5
27	-13.6	39.2	25.6
28	-13.6	39.2	25.6
29	-13.6	39.1	25.5
30	-13.6	38.9	25.3
31	-13.7	38.7	25.0
32	-13.7	38.6	24.9
33	-13.7	38.1	24.4
34	-13.7	37.8	24.1
35	-13.7	37.3	23.6
36	-13.8	36.7	22.9
37	-13.8	36.3	22.5
38	-13.8	35.7	21.9

Table VIII (Continued)

SCATTEROMETER ANTENNA PATTERN FACTOR

FORE

θ (degrees)	Beamwidth (db)	$G_o^2 f(\theta)$ (db)	$G_o^2 f'(\theta)$ (db)
39	-13.8	35.5	21.7
40	-13.8	35.3	21.5
41	-13.7	35.1	21.4
42	-13.7	35.1	21.4
43	-13.7	35.3	21.6
44	-13.7	35.5	21.8
45	-13.7	35.6	21.9
46	-13.6	35.6	22.0
47	-13.6	35.5	21.9
48	-13.6	35.3	21.7
49	-13.6	35.4	21.8
50	-13.6	35.3	21.7
51	-13.6	35.1	21.5
52	-13.6	34.9	21.3
53	-13.6	34.6	21.0
54	-13.6	34.1	20.5
55	-13.6	33.4	19.8
56	-13.7	32.5	18.8
57	-13.7	31.6	17.9
58	-13.7	30.9	17.2
59	-13.7	30.1	16.4
60	-13.7	29.3	15.6
61	-13.7	29.1	15.4
62	-13.7	28.3	14.6
63	-13.6	27.5	13.9
64	-13.6	26.4	12.8
65	-13.6	25.4	11.8
66	-13.6	24.1	10.5
67	-13.6	22.9	9.3
68	-13.6	22.4	8.8
69	-13.6	21.6	8.0
70	-13.6	20.5	6.9

Table IX

SCATTEROMETER ANTENNA PATTERN FACTOR

AFT

θ (degrees)	Beamwidth (db)	$G_o^2 f(\theta)$ (db)	$G_o^2 f'(\theta)$ (db)
	-13.7	38.1	24.4
1	-13.8	37.9	24.1
2	-13.8	37.8	24.0
3	-13.8	37.7	23.9
4	-13.8	37.4	23.6
5	-13.9	37.1	23.2
6	-13.9	37.1	23.2
7	-13.9	37.3	23.4
8	-13.9	37.7	23.8
9	-13.9	37.9	24.0
10	-13.9	38.1	24.2
11	-13.9	38.3	24.4
12	-13.9	38.6	24.7
13	-13.9	38.9	25.0
14	-13.9	39.1	25.2
15	-13.8	39.4	25.6
16	-13.8	29.6	25.8
17	-13.9	39.7	25.9
18	-13.8	39.9	26.1
19	-13.8	40.0	26.2
20	-13.8	40.1	26.3
21	-13.7	40.0	26.3
22	-13.7	39.8	26.2
23	-13.7	39.7	26.0
24	-13.7	39.5	25.8
25	-13.7	39.1	25.4
26	-13.6	38.6	25.0
27	-13.6	38.1	24.5
28	-13.6	37.5	23.9
29	-13.6	37.1	23.5
30	-13.6	36.8	23.2
31	-13.6	36.9	23.3
32	-13.6	36.8	23.2
33	-13.6	36.8	23.2
34	-13.6	36.7	23.1
35	-13.6	36.7	23.1
36	-13.6	36.9	23.3
37	-13.6	37.1	23.5
38	-13.6	37.5	23.9

Table IX (Continued)

SCATTEROMETER ANTENNA PATTERN FACTOR

AFT

θ (degrees)	Beamwidth (db)	$G_o^2 f(\theta)$ (db)	$G_o^2 f'(\theta)$ (db)
39	-13.6	37.5	23.9
40	-13.6	37.3	23.7
41	-13.7	37.3	23.6
42	-13.7	37.3	23.6
43	-13.7	37.3	23.6
44	-13.7	37.1	23.4
45	-13.7	37.1	23.4
46	-13.8	36.6	22.8
47	-13.8	36.4	22.6
48	-13.8	35.9	22.1
49	-13.8	35.3	21.5
50	-13.8	34.6	20.8
51	-13.7	34.0	20.3
52	-13.7	33.2	19.5
53	-13.7	32.6	18.9
54	-13.7	32.1	18.4
55	-13.7	31.5	17.8
56	-13.6	30.8	17.2
57	-13.6	29.8	16.2
58	-13.6	29.5	15.9
59	-13.6	28.9	15.3
60	-13.6	28.3	14.7
61	-13.6	27.4	13.8
62	-13.5	26.8	13.3
63	-13.5	26.3	12.8
64	-13.4	25.7	12.3
65	-13.4	24.2	10.8
66	-13.4	23.1	9.7
67	-13.4	22.0	8.6
68	-13.4	21.4	8.0
69	-13.4	21.1	7.7
70	-13.4	19.8	6.4

SECTION 5

DATA ANALYSIS

The purpose of the data analysis program was to establish a recommended reflectivity model for the Lunar Module Landing Radar (LMLR). To aid in establishing the recommended LMLR model four sources of information were used. The first was the data collected over various lunar analog sites by the MSC Scatterometer at 13.3 GHz. The second was the measurements made at the University of New Mexico acoustical similator lab (Reference 3). The third was the lunar backscattering data collected by Evans and Pettengill (Reference 4). The last was the data collected by the Surveyor I and Surveyor III Radar Altimeters (12.5 GHz) and Doppler Velocity Sensors (13.3 GHz). Data from these sources are presented in this Section. The correlation between the data collected by these four sources is discussed in Section 6.

Parts 6 and 7 of this Data Analysis Section are two theoretical model studies which were performed to enhance the usefulness of the data and to assist in the correlation between the various data sources. The first study was a general review of theoretical reflectivity models and the second was a review of techniques for use in separation of specular and diffuse return.

An additional study was performed where various mathematical curve fitting techniques were evaluated. The results of this study are presented in Part 8 of this Section.

5.1 Scatterometer Data Analysis Techniques

During the MSC Scatterometer tests a library of magnetic tape recordings of reflectivity data from different types of terrain was collected. The processing of each tape proceeded as follows:

(1) Copies are made of the original mission tapes.

(2) The tape copies are played back through the sign sense detector and fed to a set of comb filters. The comb filter outputs are detected and recorded on multiple-channel magnetic tape. In addition, the filter outputs are recorded on an oscillograph for visual verification of its validity prior to further processing. Sample power spectrum density plots of the unprocessed data and the sign sense detector outputs are also prepared for data verification.

(3) The next step is to process the multiple-channel magnetic tapes through an analog-to-digital converter. The analog-to-digital conversion is accomplished with a CDC-3200 computer. The digitized data is recorded on digital tapes that are compatable with the CDC-3800.

(4) The digital tapes are then processed on the CDC-3800 computer along with aircraft flight parameters. The computer processing consists of computation of the value of σ_o versus θ for each resolution cell of a

run. In addition, the average and standard deviation of σ_o are computed for homogeneous terrain sections.

(5) The σ_o versus θ curves for the fore and aft looking portions of the radar beam are automatically plotted from the computer output.

After reduction of the Scatterometer data to a set of σ_o versus θ curves for each ground cell, the data were correlated with various terrain information.

The terrain information includes aerial photographs showing the flight path (as a function of time) and data on surface conditions (ground truth). The ground truth data includes basic terrain type, surface roughness, soil moisture content, surface temperature and surface bearing strength. These various parameters are used to determine weighting factors for the data in terms of its usefulness as a lunar analog. The ground truth data are also invaluable in establishing correlations with theoretical models (see Parts 6 and 7 of this Section). Confidence in the data is enhanced when a correlation is established between the theoretical and experimental coefficients of σ_o for a particular set of terrain characteristics as described by the ground truth team.

The aircraft flight parameters; altitude, velocity, pitch, yaw and roll, are read out on a specifically designed, central instrument panel. During data runs this information is recorded on film. These

parameters serve a two-fold purpose: (1) they are necessary for σ_o computation and (2) excessive variations in any of the parameters tend to degrade data accuracy and correlation. The data presented in this document were carefully selected for small variations in aircraft performance and were carefully reviewed for signal return quality. Therefore, the data presented are considered to be precise measurements.

All of the scatterometer data were analyzed between incidence angles of 2.5 and 60 degrees. The curves presented in this Section were extrapolated down to zero degrees by the analysis of other experimenters' data, and from theoretical analysis using backscattering model theory.

5.2 Terrain Characteristics of Scatterometer Test Areas

Ground truth data was gathered at White Sands Missile Range (the Lavic area, AFSWC, Scat, Pearl and Salt sites), at the San Francisco Volcanic Fields (the alluvial area, SP Crater and SP Lava Flow), and at Sunset, Amboy and Pisgah Crater. Wind and sea state conditions were also available for one over water mission near Bermuda (Mission 20). This water data is presented separately in Section 5.5. The brief topographical descriptions presented below were obtained from a report by the NASA/MSC Ground Truth Team (Reference 5). A summary of the surface parameters of the lunar analog sites is

compared with the lunar surface parameters in Table X . Information concerning the lunar surface was gleaned from Part II of the Surveyor I Mission Report (Reference 6).

The only available supplemental photography for the White Sands sites are the aerial photos taken by the aircraft cameras during flight. However, for the remaining sites to be discussed, 35mm slides of the surface topography were taken by the ground truth team. These photos were enlarged and are presented in this Section to illustrate particular terrain characteristics.

a. White Sands

The Lavic area consists of a rough lava flow surrounded by relatively smooth desert terrain. This desert area is approximately 25 percent covered with dry vegetation. The micro relief (see Appendix A for a glossary of geologic terms) is on the order of 1 to 2 inches, and the macro relief, due to broken debris and some holes, is from 1 to 2 feet.

In various sections of the lava flow, composed of equal amounts of aa and pohoehoe lava, 15 to 95 percent of the surface is covered with holes 12 feet deep and 20 to 30 feet wide.

This area was chosen for study because of certain similarities to lunar terrain as seen in Surveyor and Lunar Orbitor photography. The most analogous feature to the lunar surface is the holes in the lava bed, which were formed by the collection of gas bubbles and subsequent collapse of the gas pockets.

TABLE X. SURFACE CHARACTERISTICS OF

LUNAR ANALOG SITES AND THE LUNAR SURFACE

MEASURED SURFACE PARAMETERS	White Sands Lavic Area		White Sands	White Sands	White Sands
	Desert	Lava	AFSWC	Gent	Pearl
Average Soil Density (0 to 6"), g/cc	2.0	2.3	1.7	1.55	1.55
Median Soil Grain Size, mm	0.2	Lavic Blocks 100	0.165	0.18	.095
Surface Bearing Capacity, psi	600	1000	560	2160	1380
Soil Moisture Content (0 to 6 in.) %	4.0	1	3.7	8.6	18.4
Macro Relief Structure, feet	1 to 2	12 to 30	1 to 3	.1 to 1	Smooth
Micro Relief Structure, inches	1 to 2	2 to 10	3 to 9	.5	.1 to .5

MEASURED SURFACE PARAMETERS	White Sands	Pisgah Crater		San Francisco Volcanic Fields	Sunset Crater
	Salt	Lavic Dry Lake	Crater and Lava Flow	SP Crater and Lava Flow	Crater Vacinity
Average Soil Density (0 to 6"), g/cc	1.28	1.57	2.29	1.7	2.18
Median Soil Grain Size, mm	0.24	0.6	0.87	13	4.65
Surface Bearing Capacity, psi	67	1176	--*	--*	78
Soil Moisture Content (0 to 6 in.) %	12.3	8.1	1.1	1	0.7
Macro Relief Structure, feet	2 to 3	Smooth	3 to 20	2 to 50	2 to 3
Micro Relief Structure, inches	1 to 4	1	3 to 24	1 to 3	.25 to 3

* too high to measure with available equipment

TABLE X. (Cont'd) SURFACE CHARACTERISTICS OF

LUNAR ANALOG SITES AND THE LUNAR SURFACE

MEASURED SURFACE PARAMETERS	Amboy Crater	San Francisco Volcanic Fields	Sunset Crater	Amboy Crater	Lunar Surface
	Crater Vacinity	Alluvium	Surrounding Cinder Area	Sand Filled Lava Flow	Surveyor I Landing Area
Average Soil Density (0 to 6"), g/cc	2	1.76	1.44	1.8	1.2 to 1.5
Median Soil Grain Size, mm	6.5	0.335	1.5	0.19	1
Surface Bearing Capacity, psi	85	158	--*	69	8(± 2)
Soil Moisture Content (0 to 6 in.) %	.75	7.8	9.3	0.9	--
Macro Relief Structure, feet	.5 to 2	1	3 to 50	4 to 5	--
Micro Relief Structure, inches	1 to 3	1	1	1	1 to 12**

* Not measured

** Estimate

The AFSWC site at White Sands, is used as a bombing site. Radial dirt roads connected to a circular inner road, form the target and cover about five percent of the area. Approximately 40 percent of the surface is covered with clumps of vegetation from 1 to 3 feet in diameter and 3 to 9 inches high. Approximately one percent of the area is covered with craters and mounds. The craters measure from 2 to 10 feet in diameter and 1 to 3 feet in depth; whereas the mounds are from 4 to 8 feet wide by 1 to 5 feet high. Under the United States Department of Agriculture (USDA) soil classification (see Appendix A) the soil in this region is classified as fine sand. This fine grained soil and the small scattered craters prompted scatterometer analysis of this site.

A desert area just northwest of the AFSWC site was over flown during the time the aircraft was in the AFSWC vicinity. At this site, very fine grained sand, has been blown across a very flat surface into random lines of rolling dunes. No ground truth data was taken in the sand dunes area.

The Scat site, also located at White Sands, was leveled and reworked for Surveyor landing system checkouts. The essentially smooth, hard and relatively flat surface of course-to-fine sand has a system of four radial asphalt roads connected to a circular inner road of asphalt. Approximately 1 percent of the area is covered with

vegetation 0.5 inch in height. Undulations with 0.75 inch amplitude and a 12 inch wavelength cover 5 percent of the area. While soil grain size and general topography make the site a candidate as lunar analog terrain; the degree of soil compaction is not, from all available information, lunar like.

The Pearl site at White Sands has also been leveled and reworked for landing system checkouts. The site, composed of medium to very fine sand, is 2000 feet in diameter. Both macro and micro relief of the smooth, compacted surface are excessively small. As in the case of the Scat site, the soil grain size of the area makes it a choice for the scatterometer lunar analog studies. However, the degree of soil compaction is not analogous to the lunar surface.

The last White Sands area discussed here is the Salt site. Ten percent of this, essentially undisturbed, area is covered with mounds of medium to fine grained sand, 1 to 2 feet in diameter. Vegetation in the form of grass and shrubs 6 to 8 inches high, was abundant. The macro and micro relief were 2 to 3 feet and 1 to 4 inches respectively. The general topography and soil grain size of this terrain were the characteristics that prompted testing of this site.

b. San Francisco Volcanic Area

The major features of the San Francisco Volcanic area are similar to those of the Lavic area at White Sands. Flat terrain surrounds

a rough lava flow which eminated from a cinder cone. The surrounding terrain, classified as an alluvial flat, or plain, has a 2 percent slope away from the crater and lava. Thirty to forty percent of its surface is covered with one-foot high grass. The micro relief of this alluvium is on the order of 1 inch. The soil particles range from very coarse to very fine sand. The alluvial flat is a good lunar analog except for the vegetation.

The associated SP lava flow has an estimated age of 1200 years and a depth of more than 170 feet. The 4.5 by 2.5 mile flow is composed entirely of aa lava. The surface, to a depth of 40 feet, resembles a huge rock pile made up of angular basaltic blocks (see Figure 53). The average block size is estimated to be 4 inches by 5 inches by 7 inches. Macro relief due to randomly distributed depressions and mounds is approximately 50 feet. The micro relief, which is 2 to 3 inches, is characterized by the small irregularities and the larger individual rocks comprising the flow.

SP Crater situated at the Southern edge of the flow, is a highly weathered cone rising above the surrounding lava. The slopes of the cone are composed of basaltic cinders which range in diameter from 0.25 to 1.5 inches and are the major contributors to the micro relief.

Aerial photographs of the SP lava flow look similar to some of the Lunar Orbitor photos. However, upon close ground truth investigation it has been found that the SP lava flow does not possess the upper surface of particulate material seen in the Surveyor photos.



Figure 53 Broken Lava

c. Sunset Crater

Sunset crater which is classified as a basaltic cinder cone, developed about 900 years ago. Rising 1000 feet above the surrounding terrain, the cone has an average outside slope of 58 percent and an average inside slope of 46 percent. The surface of the outside lower two-thirds of the crater, which is black in color, is composed of cinders whose average diameter is approximately 0.25 inches. Relief variations due to water runnoff on the surface are in the order of 1 inch. Approximately 1 percent of the area surrounding the crater is covered with scrub brush 2 to 3 feet in height and pine trees up to 30 feet tall. Moisture was evident at a depth of three inches.

The flat cinder area surrounding the crater has a macro relief of 50 feet due to spires of Pahoehoe lava which are covered with loose cinders. Ripples in the surface are 3 to 4 feet high and the micro relief, due to individual cinders, is about 1 inch.

As lunar analog terrain the Sunset crater region can be said to closely resemble portions of the lunar landscape in texture, topography, and color. It was for this reason that the area was chosen for testing. (See Figure 54).



Figure 54 Sunset Crater Cinder Area

d. Amboy Crater

Amboy Crater which is situated at the northern end of a 24 square mile lava flow, rises 250 feet above the surface of the flow and is estimated to be 6000 years old. The slopes of the cone are covered with angular basaltic cinders which have an average equivalent diameter of 1 to 3 inches. Vegetation covers less than 1 percent of the cone.

The associated lava flow is comprised primarily of a pahoehoe, olivine basaltic lava with some block lava. Pressure ridges and tumuli crevasses 4 to 20 feet deep and 2 to 25 feet wide are abundant. Wind blown sand has filled most of these surface irregularities including bowl shaped depressions which are also in abundance. The macro and micro relief are 4 to 5 feet and 1 inch respectively.

The Amboy region is the best lunar analog study area that has been over flown to date. The relief, texture, sparse vegetation, particle distribution and size all contribute to the merits of this analog terrain. (See Figure 55).

e. Pisgah Crater

Three distinct terrain types were studied in the Pisgah Crater area. The first type is a desert area with a five-percent cover of vegetation. Undulations in the sand cause a macro relief of about four to five feet. The micro relief, resulting from small irregularities on the surface, is less than one inch. The second terrain type is a



Figure 55 Ambog Crater Lava Flow

rough lava flow, composed of both pahoehoe and aa lava, surrounding Pisgah Crater itself. The flow to the north of the crater is partially covered with wind-blown sand and is generally smooth. (See Figure 56). South and East of the crater, the area becomes very rough, with macro relief of 12 to 20 feet, and micro relief of one to two feet. This area consists primarily of pressure ridges and fissures two to three feet wide by six to seven feet deep. (See Figure 57).

Figure 58 shows the third terrain type, Lavic Dry Lake, which lies south of the crater and the lava flow. The surface is dry mud, cracked to a depth of about 3/4 of an inch. This essentially flat area has pebbles, cobbles and basaltic fragments (about one to two inches in size) scattered over its surface. The vegetation cover is less than one percent.

The Pisgah Crater area is also a good lunar analog site. The topography, flow texture and color characteristics are similar to those seen in both Lunar Orbitor and Surveyor photos.



Figure 57 Pisgah Crater: Southern Lava Flow

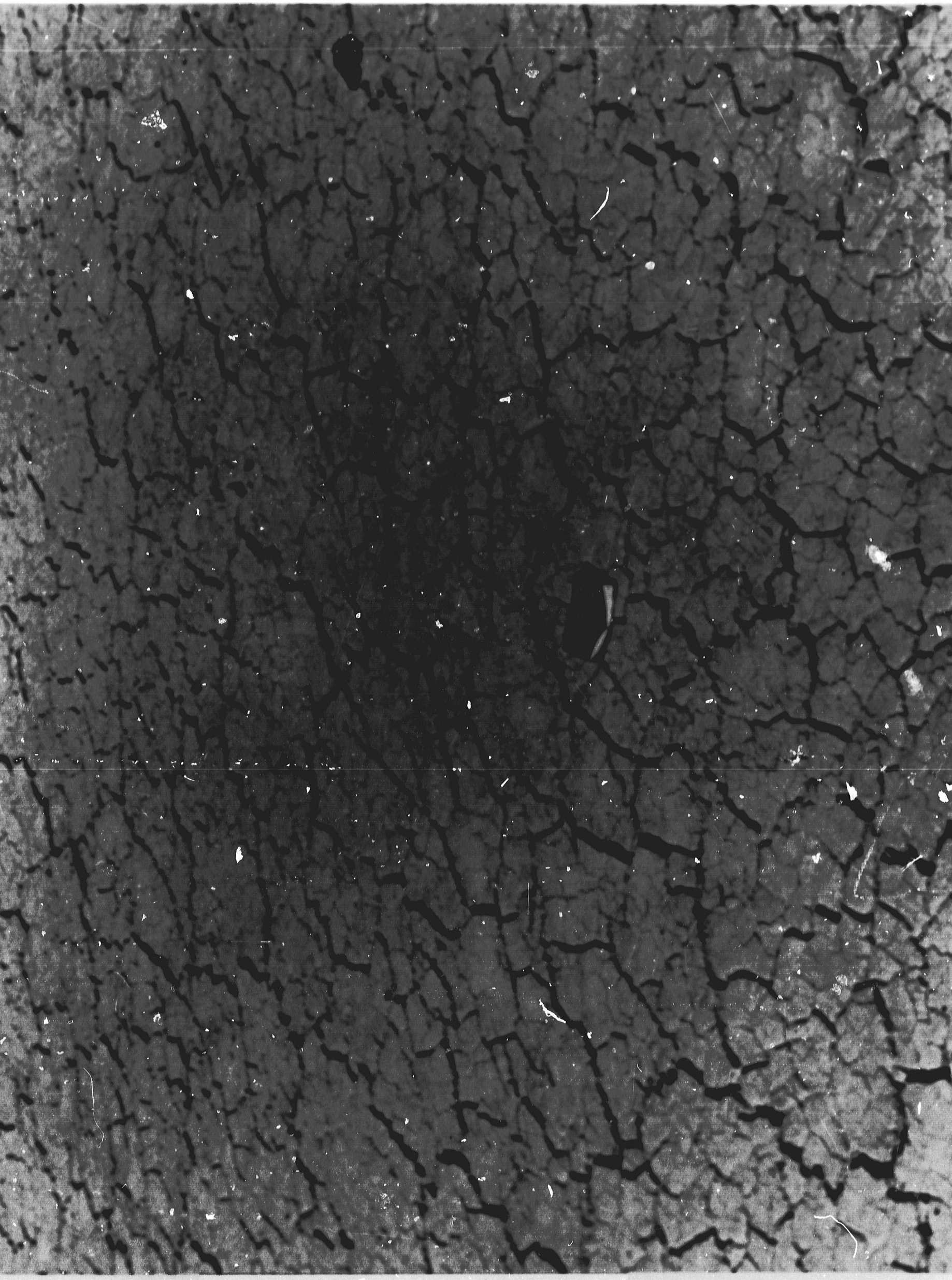


Figure 58 Lavic Dry Lake

5.3 Lunar Analog Data

The scatterometer lunar analog terrain data, presented in Figures 59-72, can be divided into three basic categories according to radar backscattering characteristic. These categories are: 1) those whose return was mostly specular, 2) those whose return was mostly diffuse, and 3) those whose return could neither be classified as specular or diffuse.

The radar backscattering curves from desert areas all had a σ_o value greater than zero db at the nadir and a dynamic range of at least 25 db. Figures 59 through 66 are data from sandy desert areas of the White Sands Missile Range and Pisgah Crater area. The radar backscattering curves from lava flows had a nadir return of about -5db and a dynamic range of about 10 db. Figures 67, 68, 69 are data from three lava fields.

The radar backscattering curves from the alluvial area of the San Francisco Volcanic Fields, the cinder area of Sunset Crater, and the sand filled lava area of Amboy Crater had a nadir return less than 0 db and a dynamic range of between 15 and 20 db (see Figures 70, 71 and 72). These three σ_o curves were selected as the best lunar analogs on the basis of their similarity to the σ_o curve from the Evans and Pettengill data (see Figure 73).

The difference in the radar backscattering characteristic of these terrain types can be attributed to three factors: (1) the difference in macro relief, (2) the difference in micro relief, and

(3) the difference in the median soil grain size.

Model theory predicts that macro relief will have the greatest influence on the signal return near the nadir, and micro relief will have the greatest influence upon the signal return at higher incidence angles. The return near the nadir should decrease with increasing macro relief, but the return at higher incidence angles should increase with increasing macro and micro relief. Median soil grain size should have the effect of increasing the general surface roughness. An inspection of the surface characteristics listed in Table X and the radar backscattering curves shows good agreement with model theory.

Figure 74 shows a comparison of the average, the most diffuse, and the most specular lunar analog data.

5.4 Other Sources of Reflectivity Data

a. University of New Mexico Data

Figure 75 shows the results of measurements with the University of New Mexico acoustical simulator (Reference 3). These measurements were made in 1960 at a frequency of 1 MHz. The wavelength of a 1 MHz acoustical signal in water is 3 cm, or the equivalent of a 10 GHz electromagnetic wave in air. It is interesting to note how the data for slightly rough sand, rough sand and smooth plywood simulate the scatterometer data over desert, lava and specular

sites such as Scat and Lavic Dry Lake. Some comparative curves are shown in Figures 76, a, b, and c where correlation of the data from the two independent sources lends support to their individual validity.

b. Evans and Pettengill Data

The Evans and Pettengill data were accumulated by bouncing a very narrow-beam radar signal off the moon and precisely measuring the return signal as a function of time. A signal return pulse from the moon exhibits a large fading range caused by the many scattering elements of the lunar surface. Thus, it was necessary to average many return pulses to obtain the mean function of return power versus delay time. Averaging times of up to 10 minutes were used.

The Evans and Pettengill data are presented in terms of relative return power versus delay time. Therefore, it is necessary to convert their data into a σ_o versus θ curve. The equations used to make this conversion are derived in Reference 4 , and are presented in Section 2.9. The resultant σ_o curve is plotted in Figure 77 with the three Scatterometer lunar analog curves that most closely approximate the lunar data.

c. Surveyor Radar Altimeter and Doppler Velocity Sensor Data

Lunar reflectivity was measured at two incidence angles by the Surveyor I Radar Altimeter and Doppler Velocity Sensor (RADVS) system.

These measurements were made during the spacecraft's vertical descent to the lunar surface. One incidence angle was zero degrees (the radar altimeter beam) and the other incidence angle was 25 degrees (the three doppler velocity sensor beams). Lunar reflectivity was measured at three incidence angles by Surveyor III RADVS system during its descent. These data were obtained from portions of the descent trajectory where the spacecraft was not vertical. The Surveyor I and III data are plotted in Figure 73. Included in the figure is the Evans and Pettengill lunar reflectivity curve, the average curve of all the scatterometer lunar analog data and the present LMLR model.

5.5 Water Data

The Mission 20 data, gathered near Bermuda, was analyzed to determine the variations in the sigma zero curve with respect to aircraft heading. This water data consisted of a star pattern where the aircraft flew both directions on a North-South line, a Northeast-Southwest line, and a Northwest-Southeast line. The magnitude of sigma zero varied less than $\pm$ 1 db with heading for incidence angles out to 35 degrees. At the 45 and 60 degree incidence angle points the variations in sigma zero with headings were $\pm$ 2.5 db. The wind speed was about four knots during these runs. For greater wind speed the variations of sigma zero with heading should be larger.

Figure 78 is a summary of the eight runs, showing their average and standard deviation. In general the cause for the larger standard deviation at the larger incidence angles is due to (1) the computer program not correcting for aircraft velocity changes, and (2) tape recorder noise.

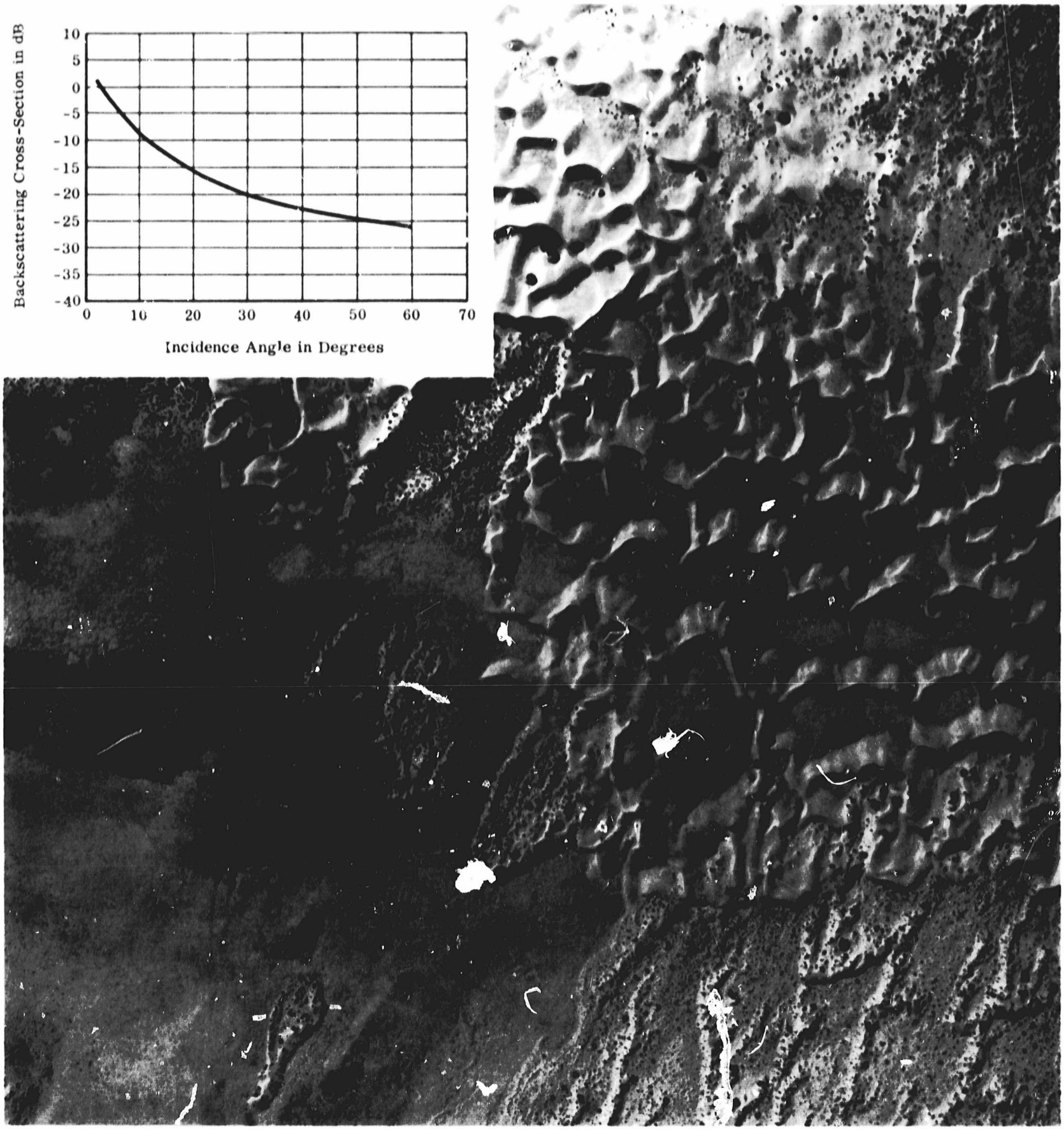


Figure 59. White Sands Missile Range - Desert with Dunes

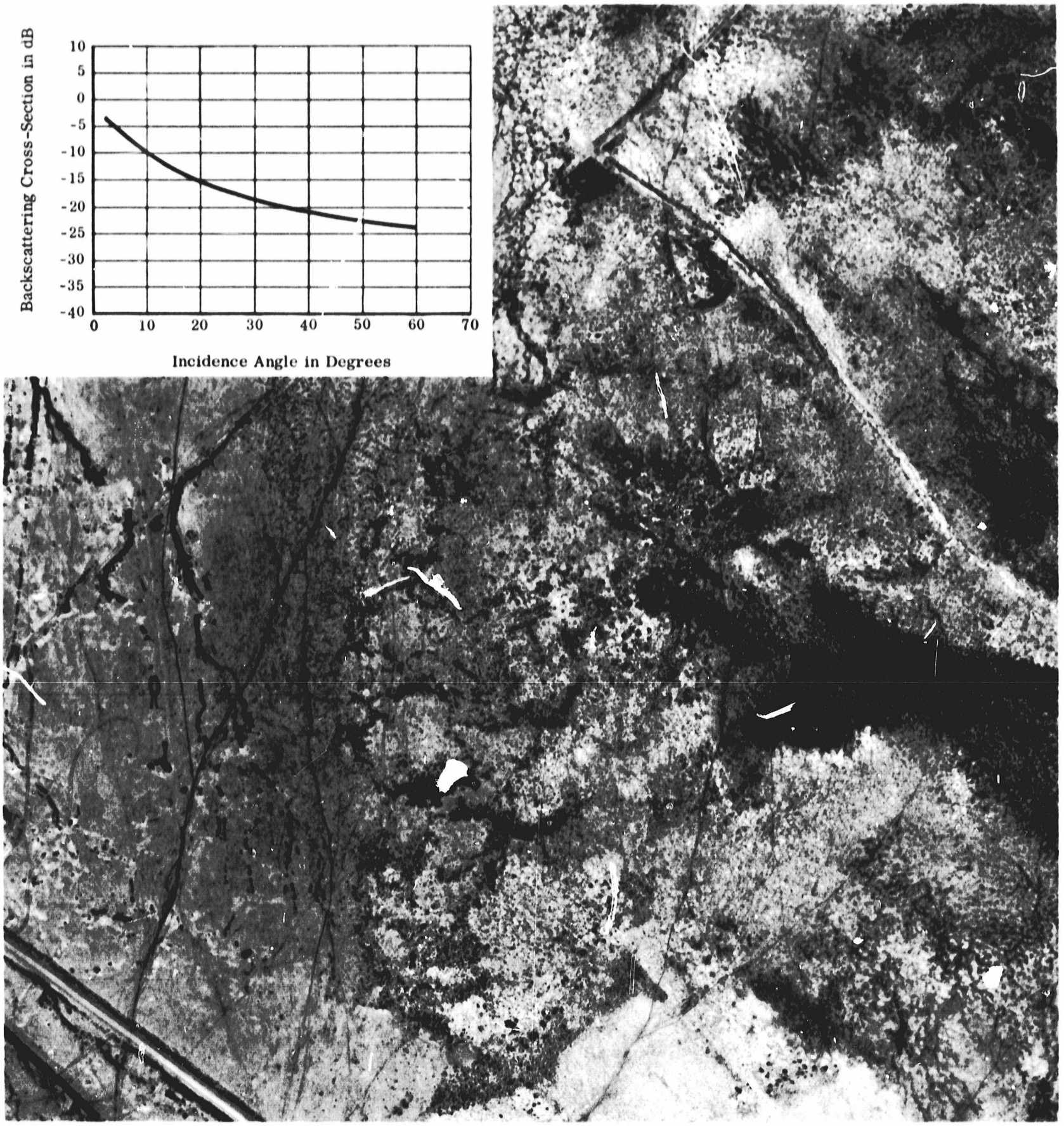


Figure 60. White Sands Missile Range - Desert

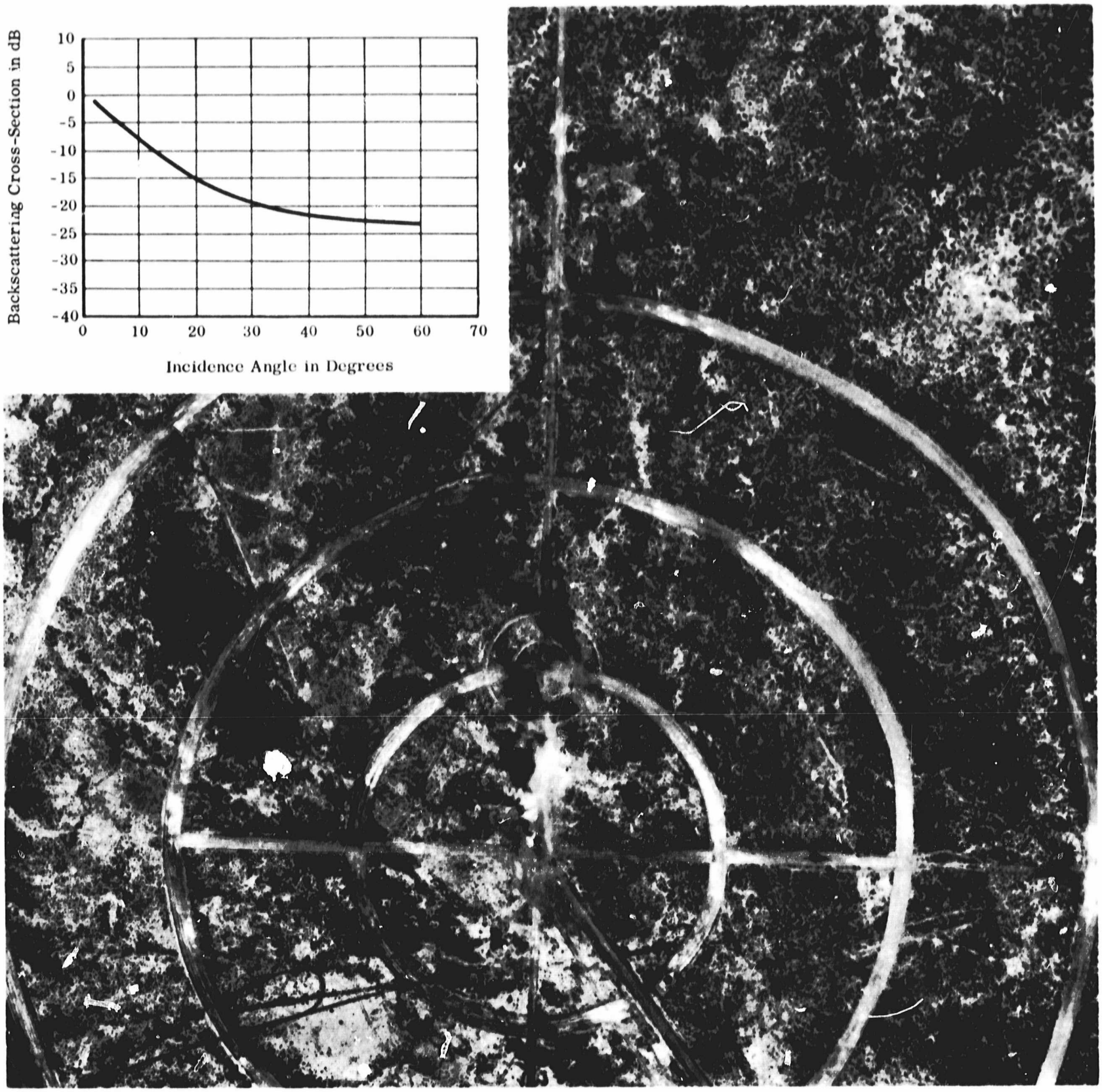


Figure 61. White Sands Missile Range - AFSWC Site

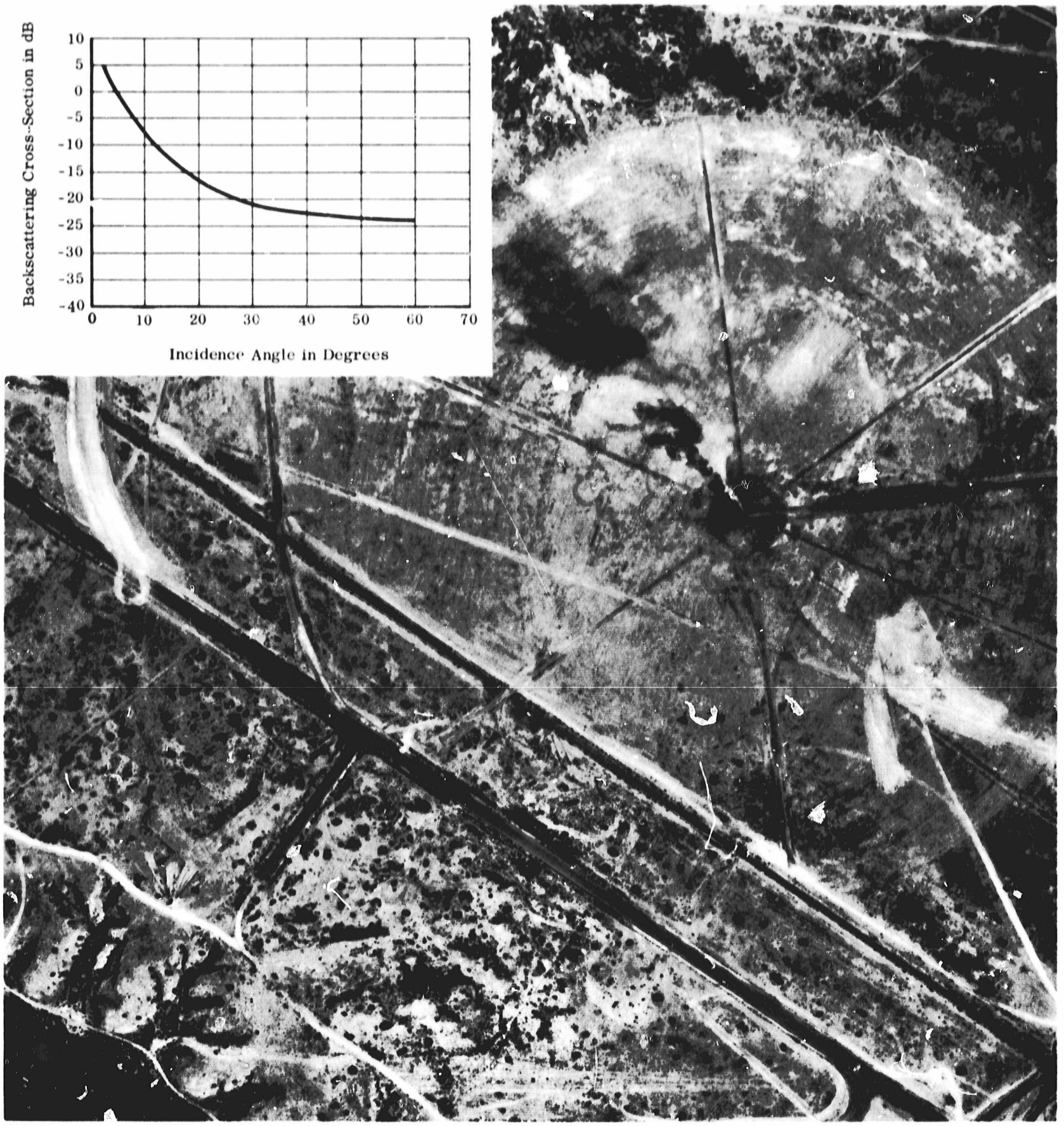


Figure 62. White Sands Missile Range - SS Scat Site

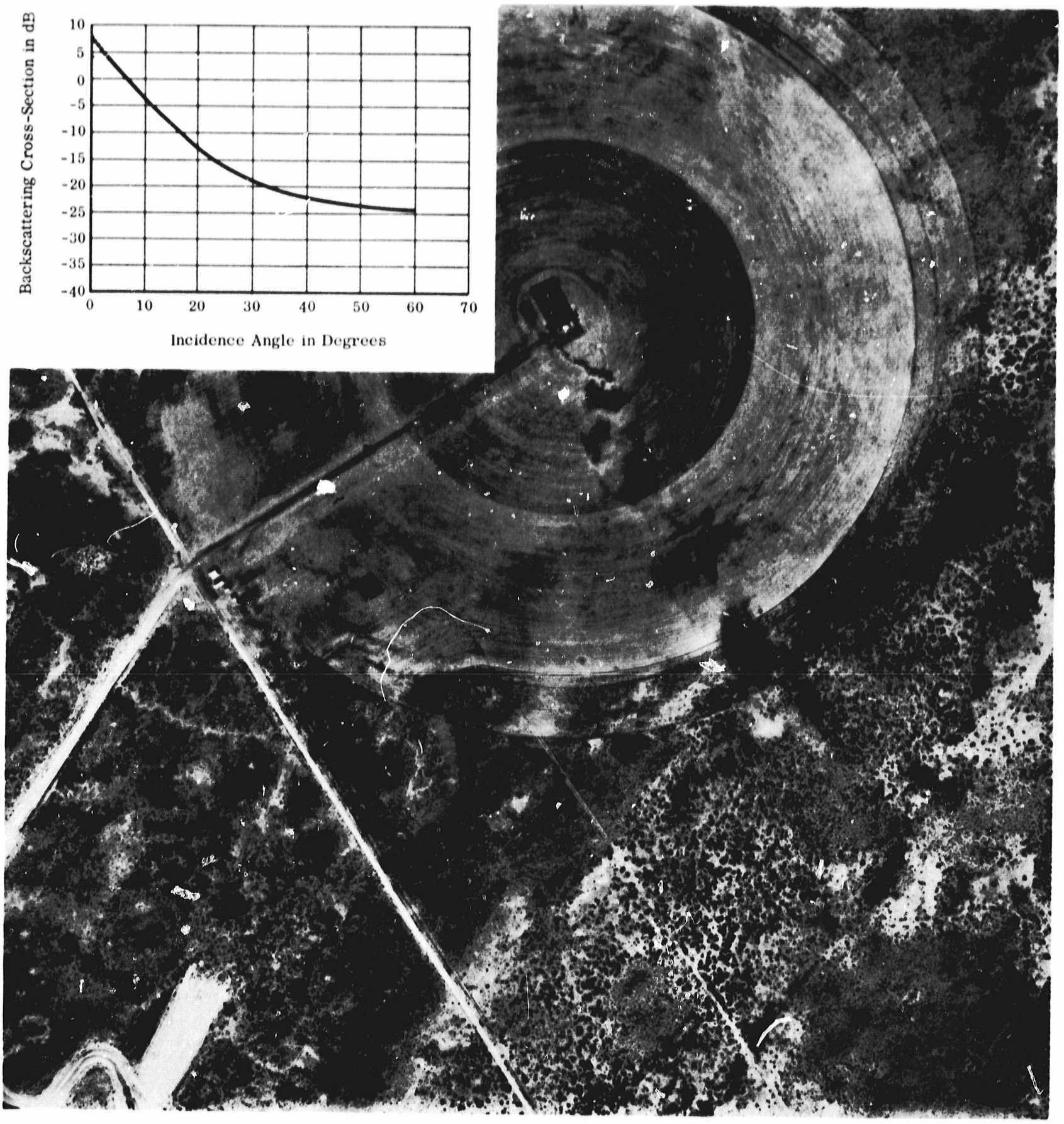


Figure 63. White Sands Missile Range - Pearl Site

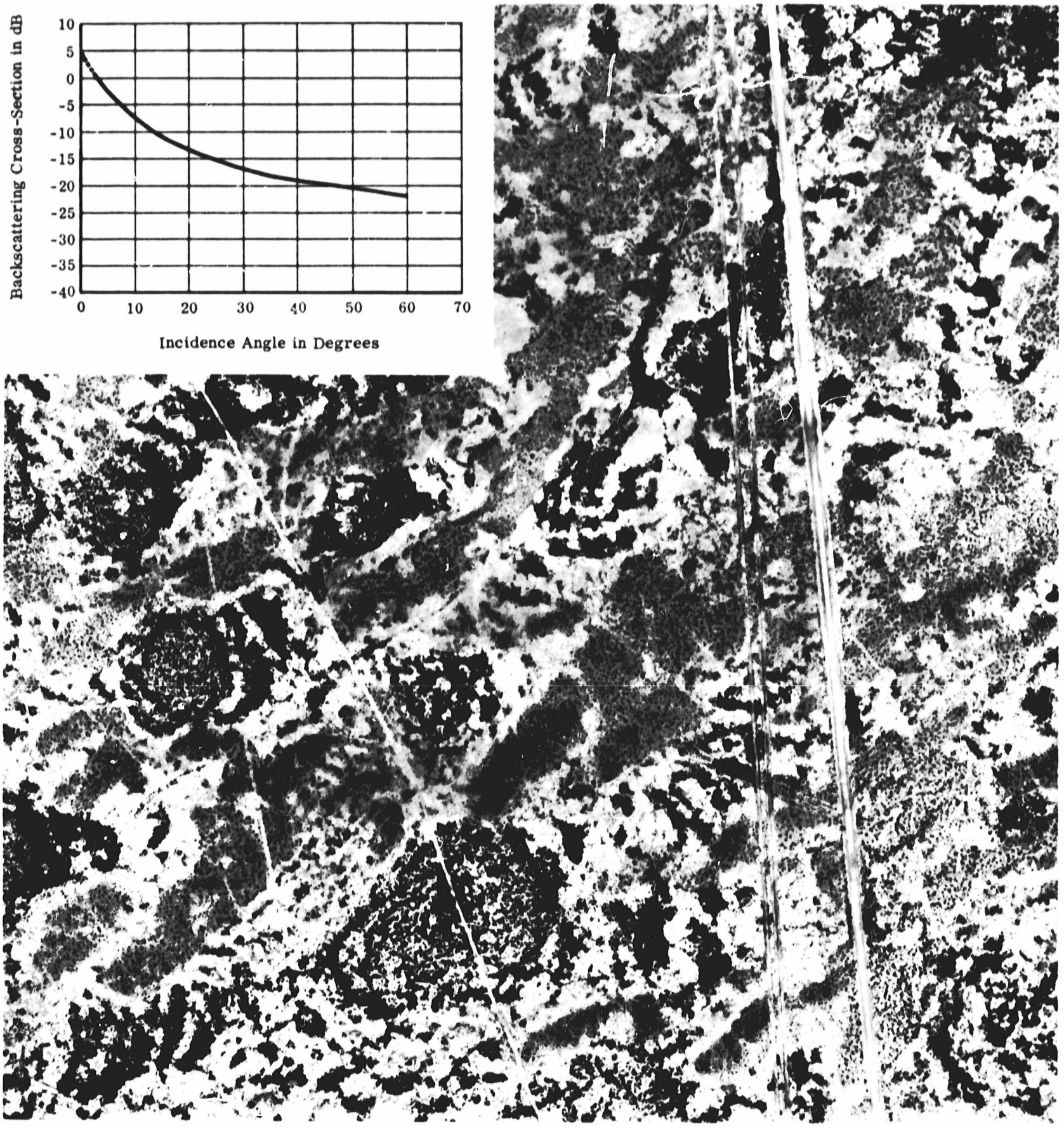


Figure 64. White Sands Missile Range - Salt Site

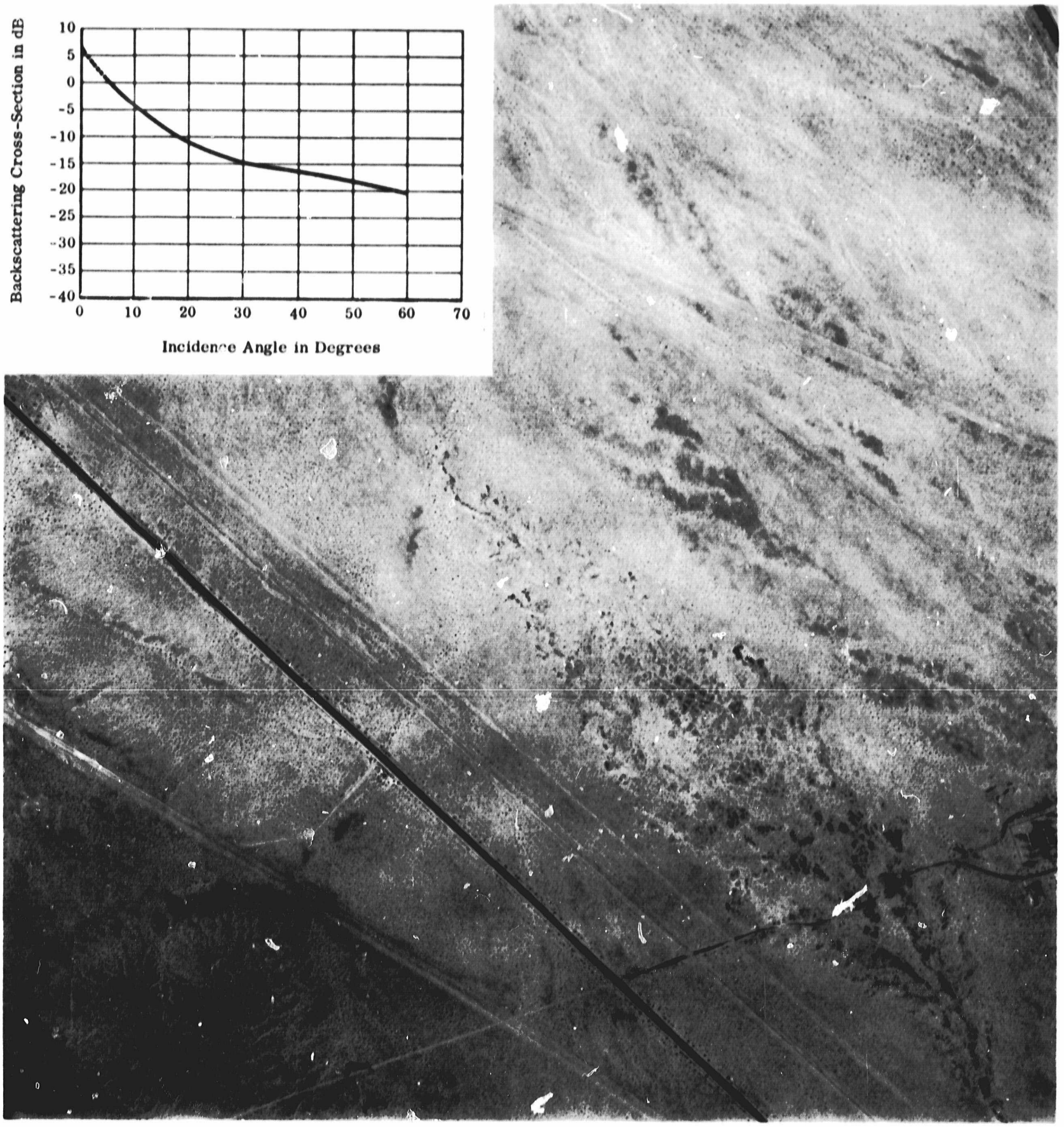


Figure 65. Pisgah Crater Area - Desert

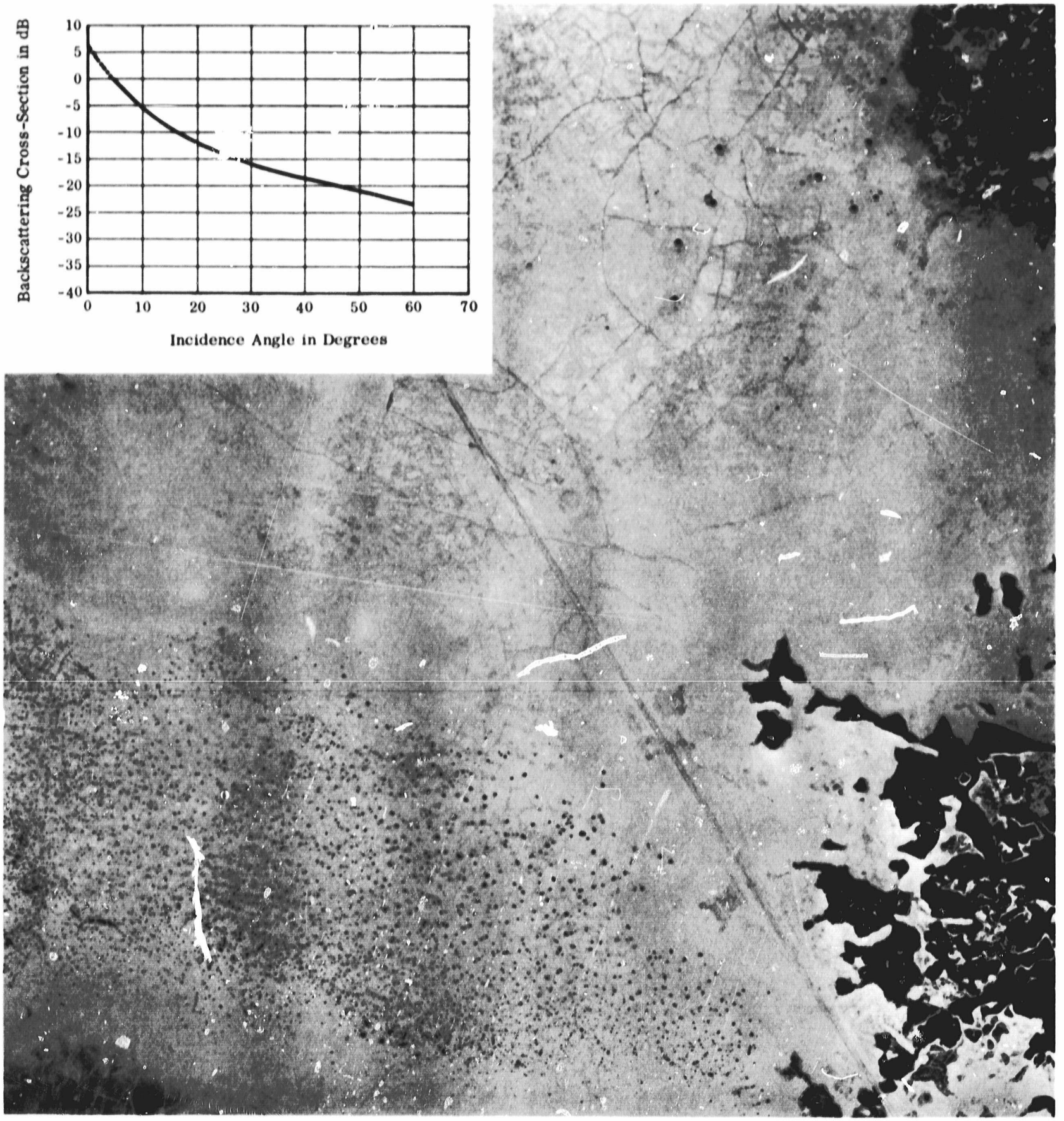


Figure 66. Pisgah Crater Area - Lavic Dry Lake

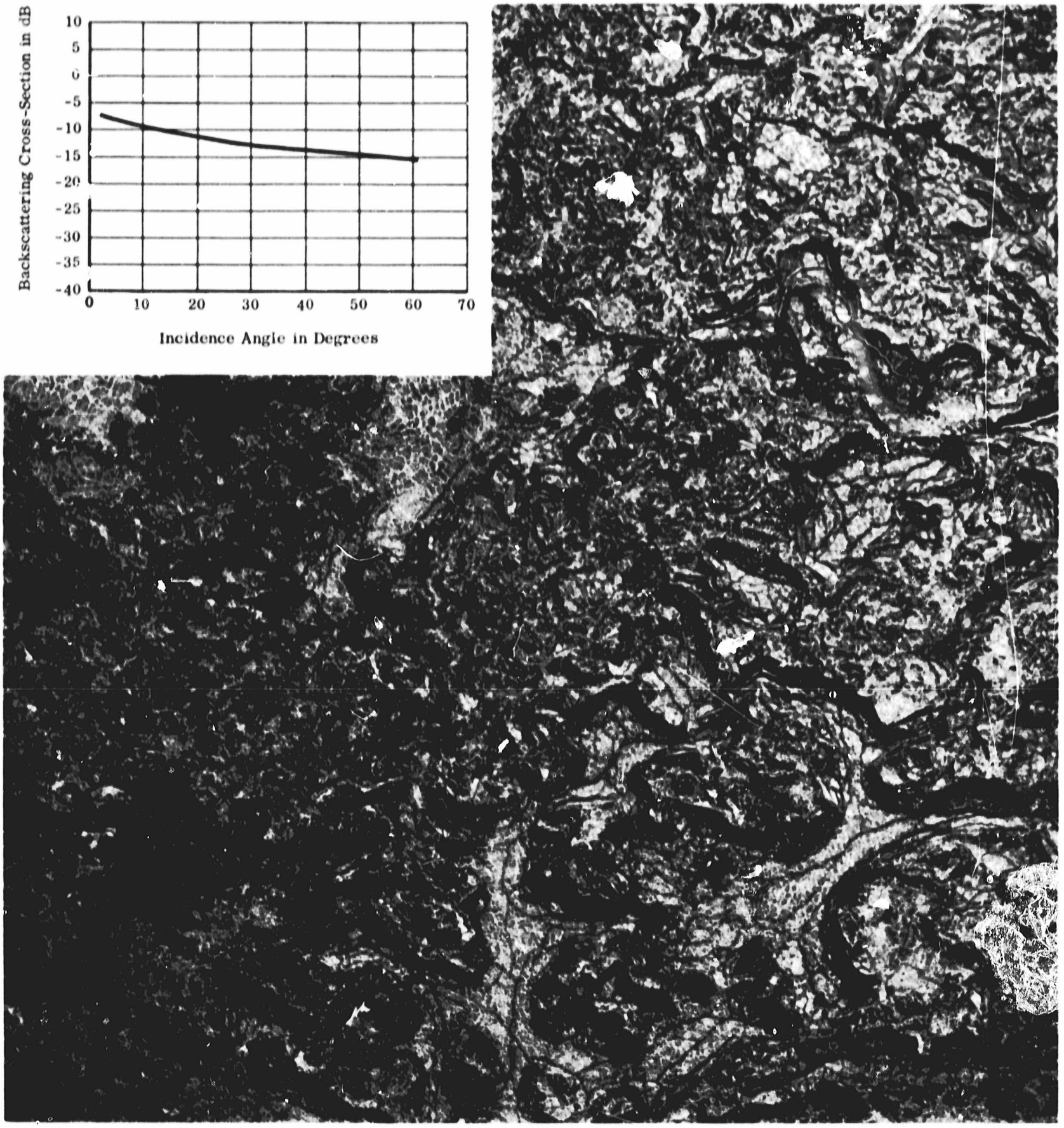


Figure 67. White Sands Missile Range - Lava

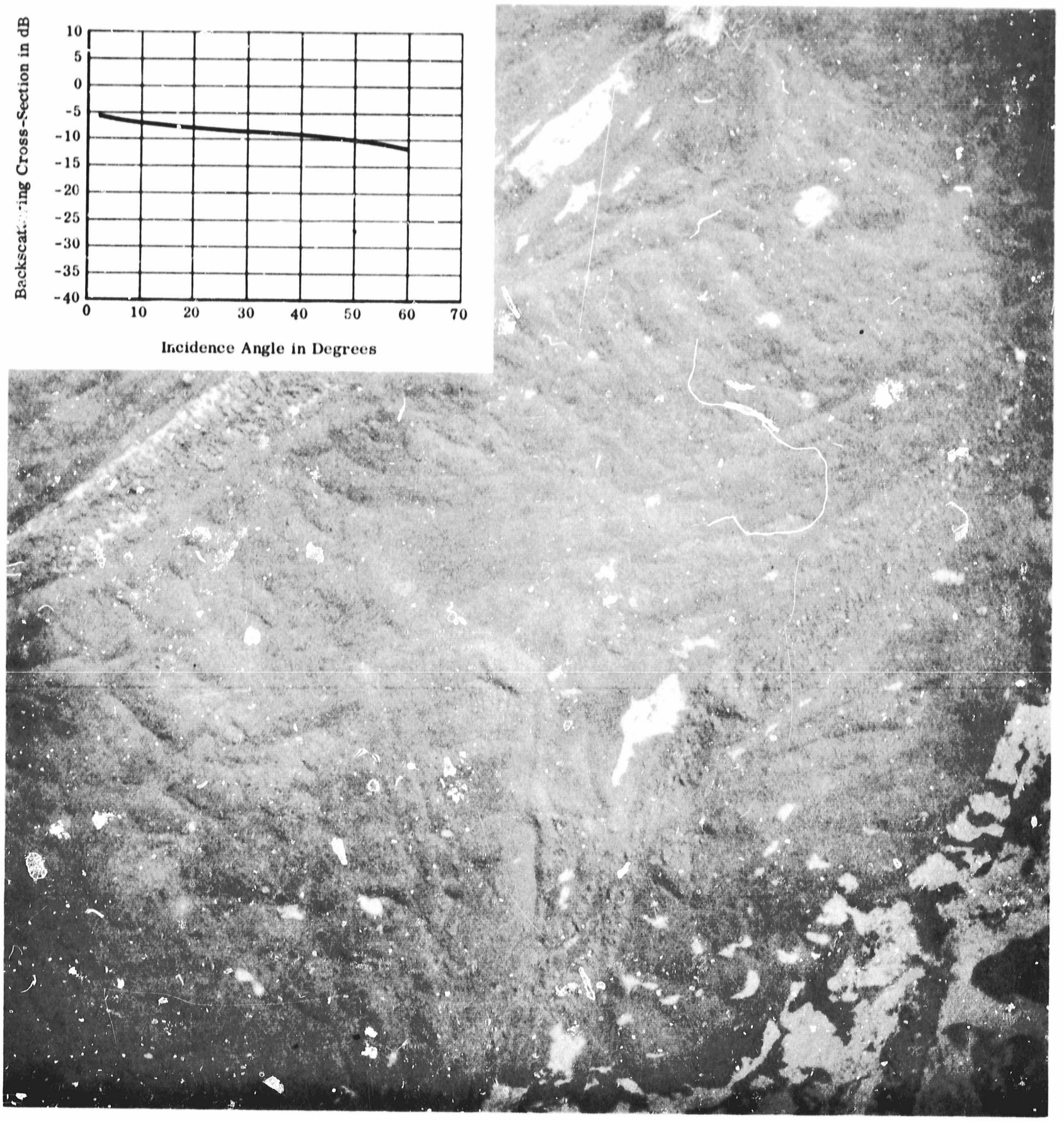


Figure 68. San Francisco Volcanic Fields - Broken Lava

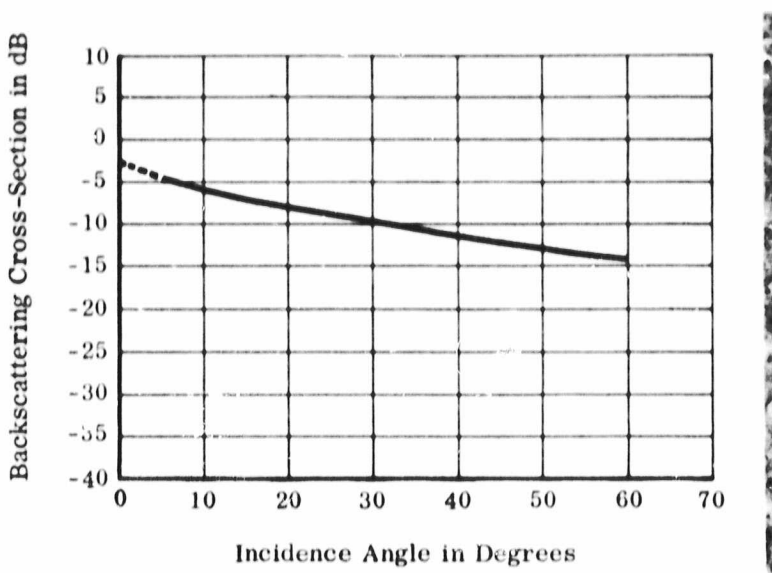


Figure 69. Pisgah Crater Area - Lava Flow

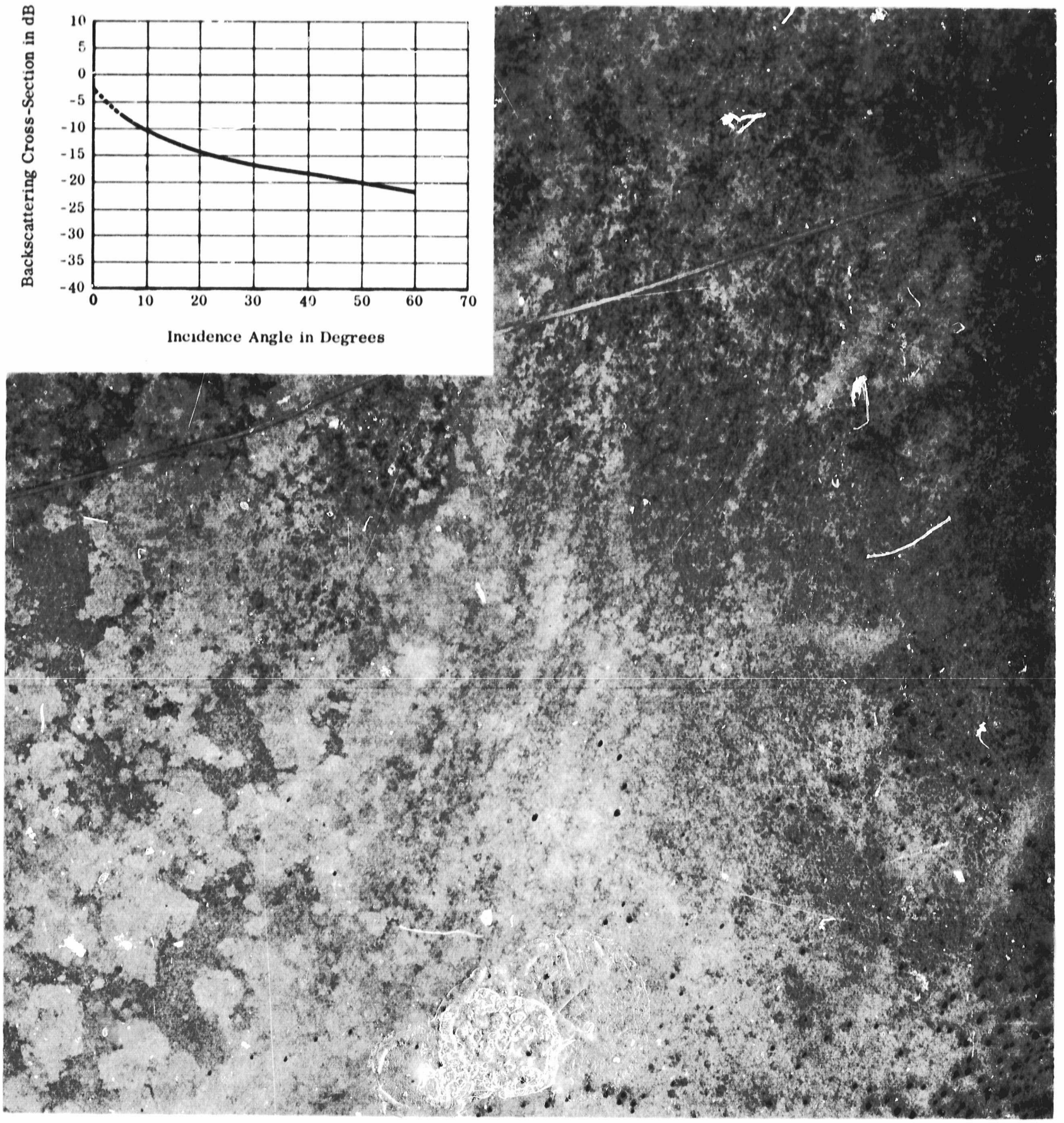


Figure 70. San Francisco Volcanic Fields - Alluvium

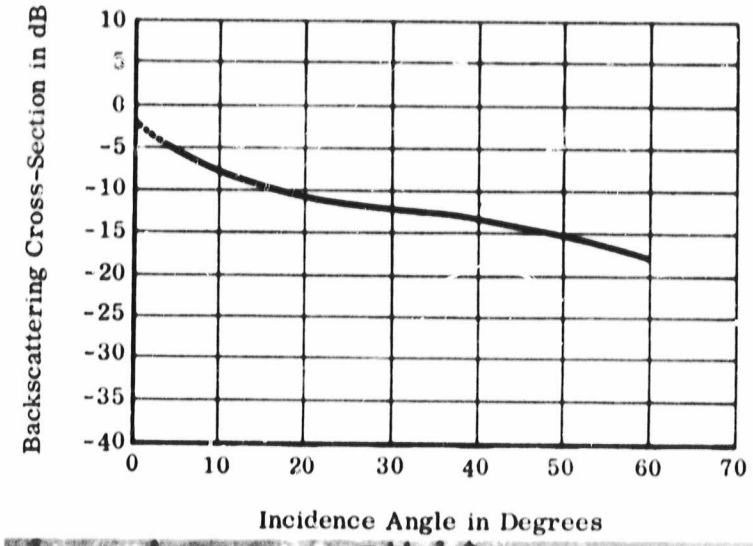


Figure 71. Sunset Crater Area - Cinder Hills

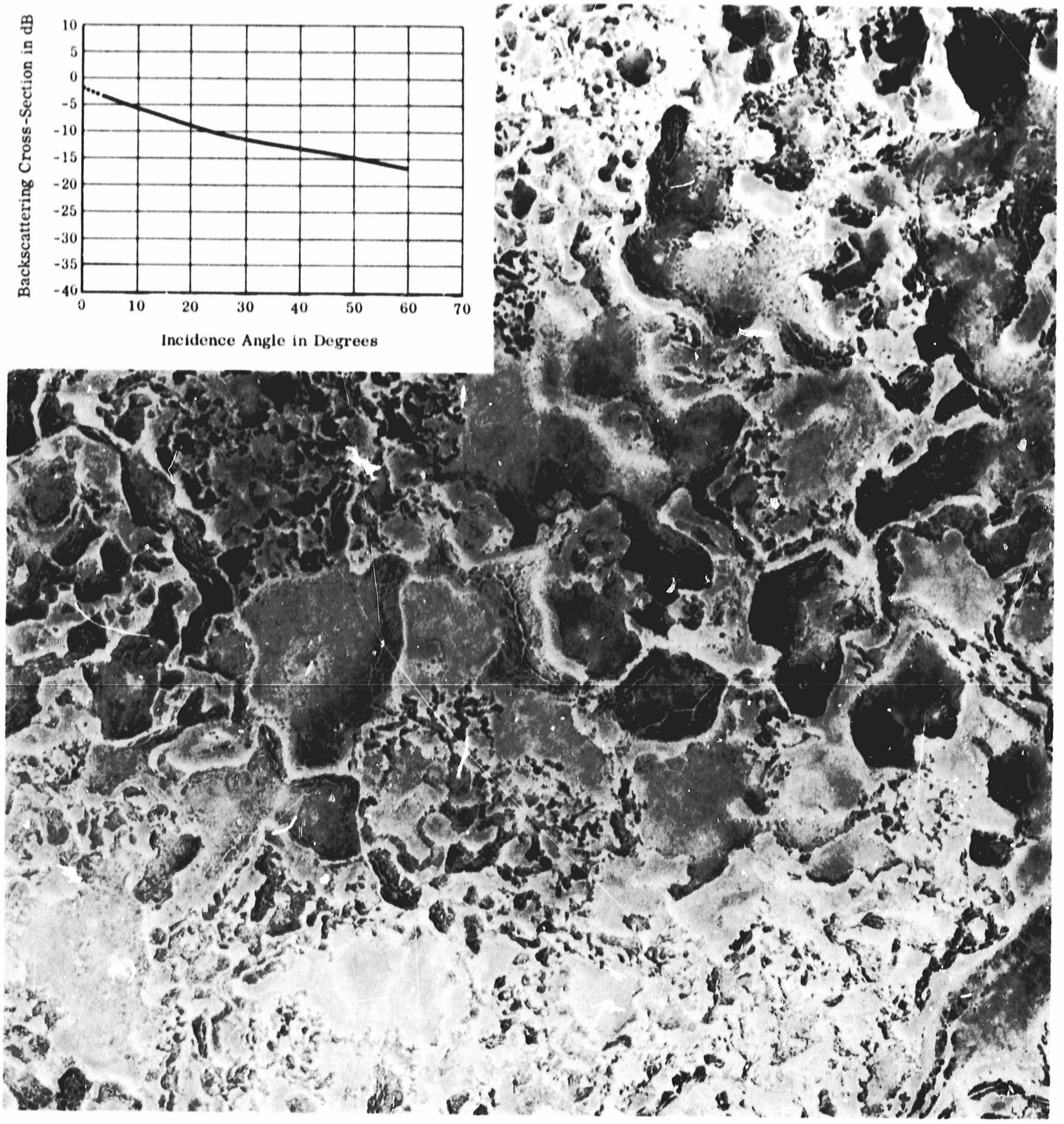


Figure 72. Amboy Crater Area - Sand Filled Lava Flow

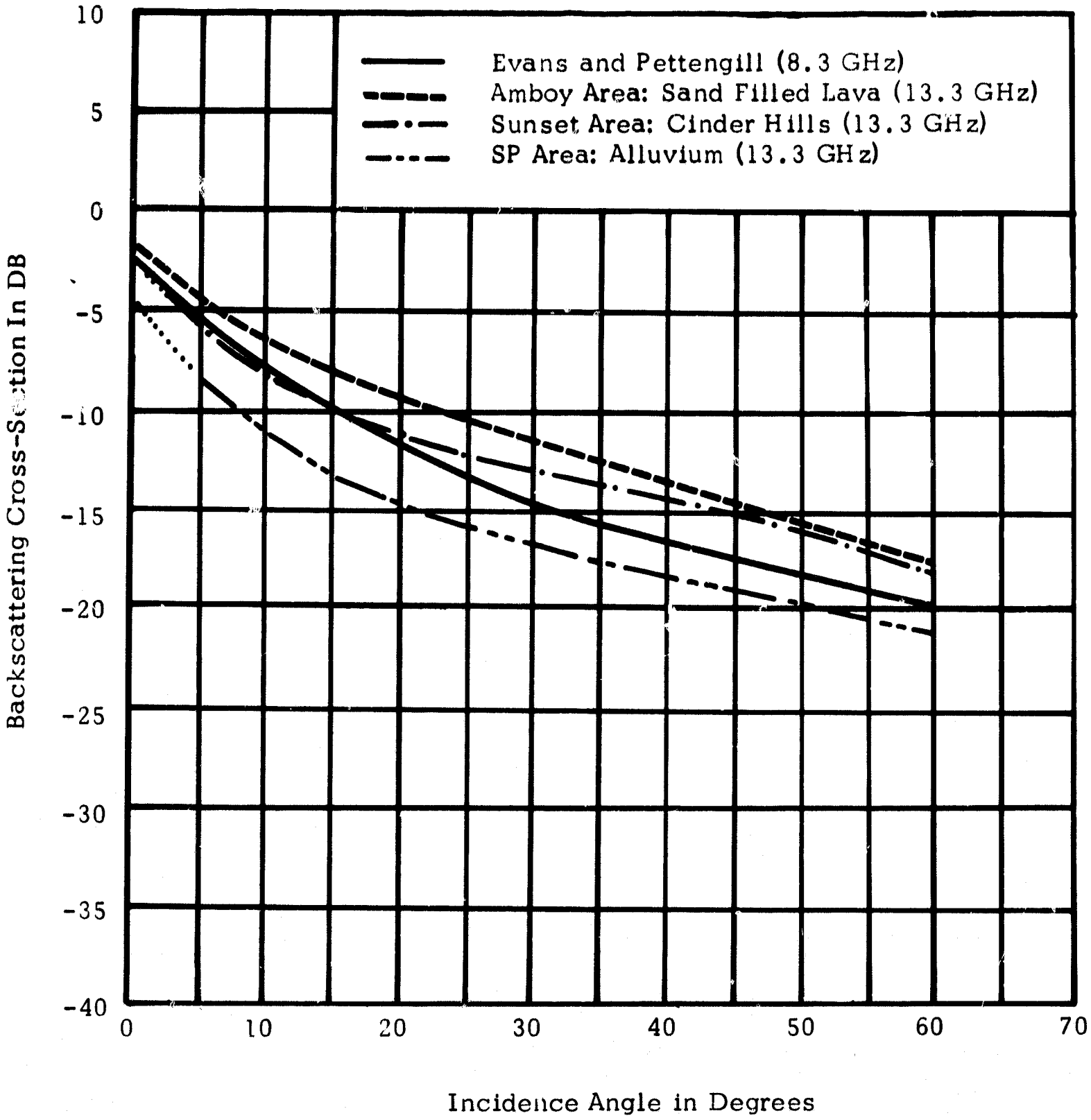


Figure 73 Comparison of Lunar Analog to Lunar Reflectivity Data

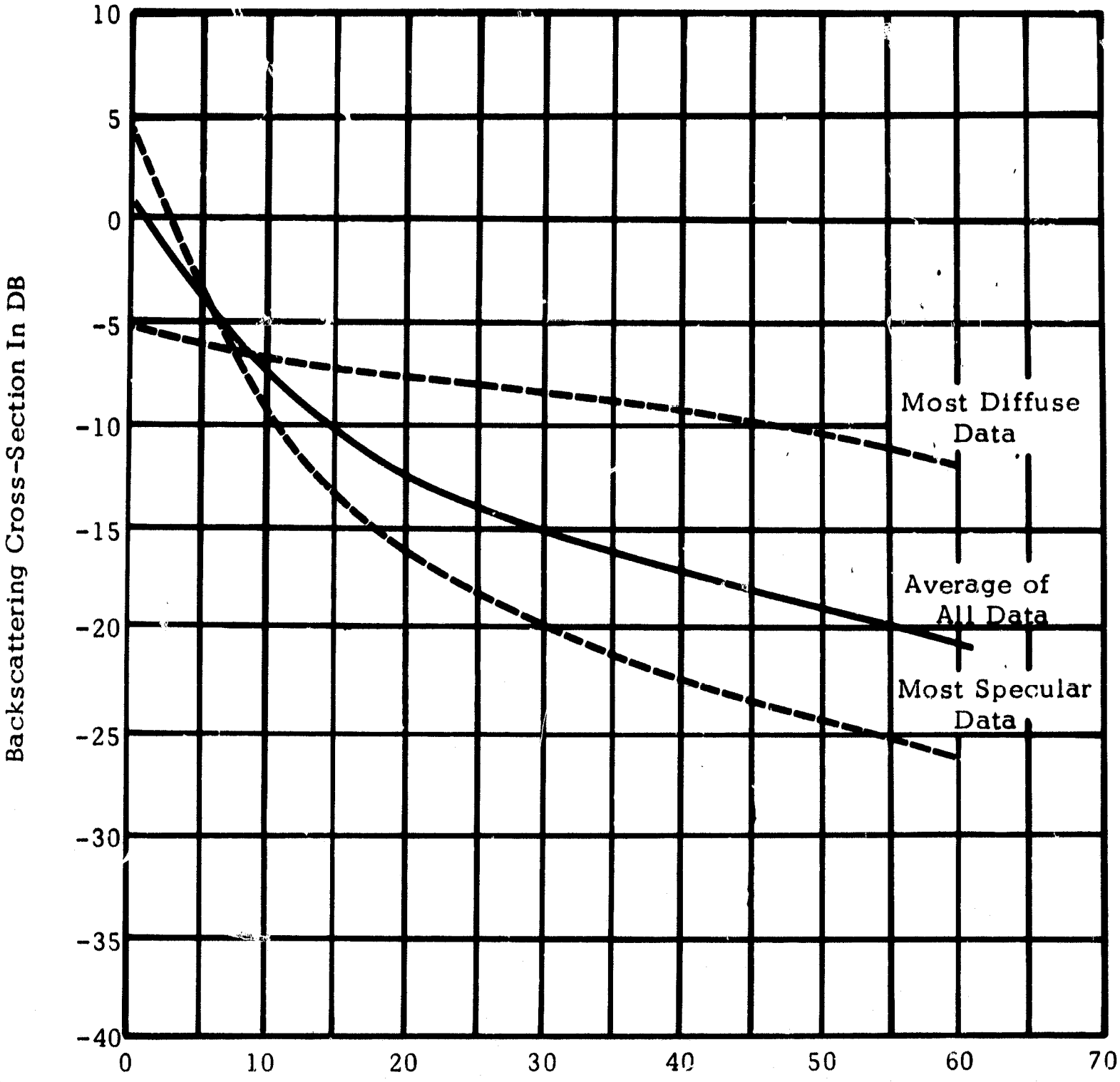


Figure 74 Range of Scatterometer Data

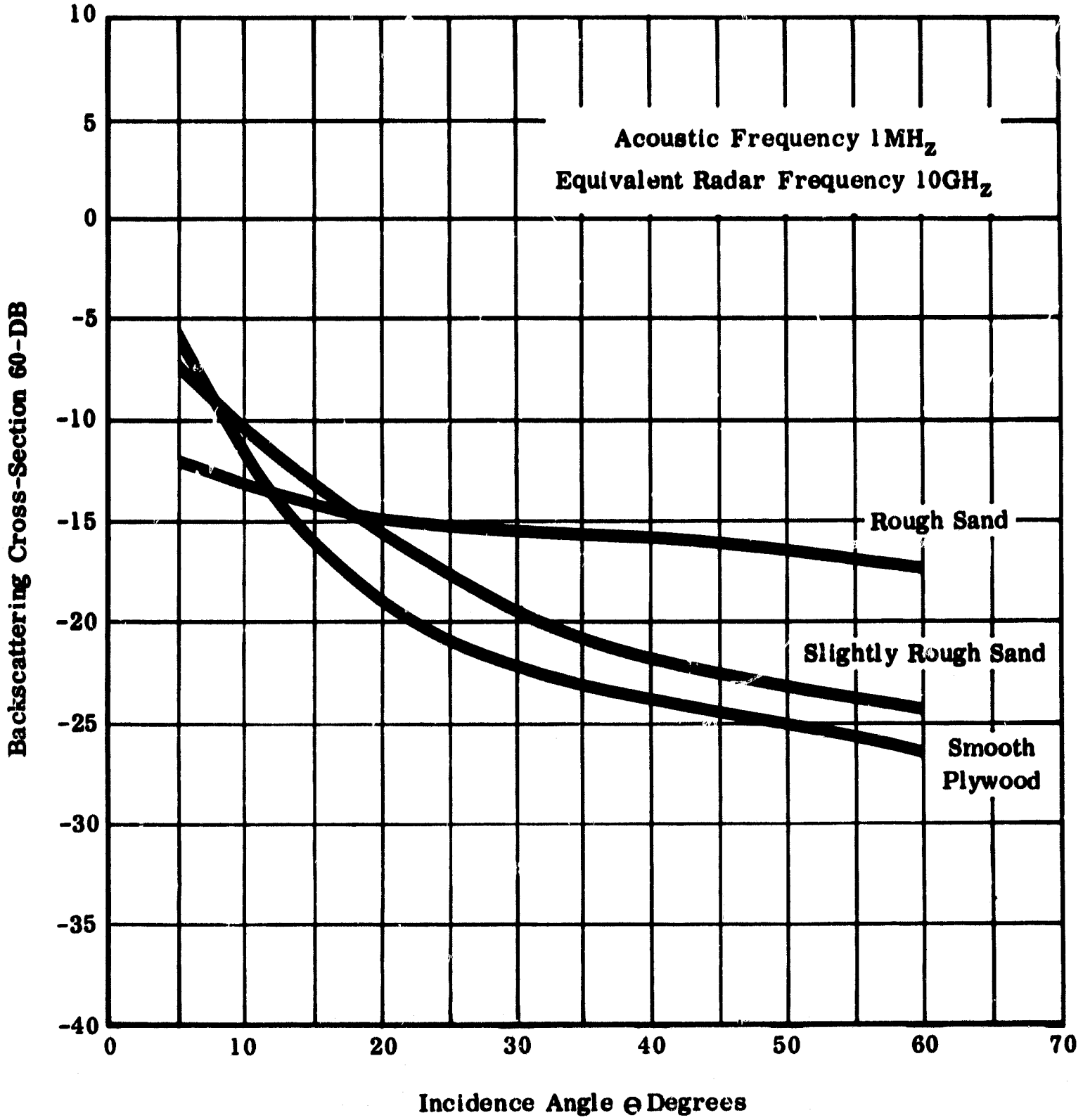


Figure 75 University of New Mexico Reflectivity Data

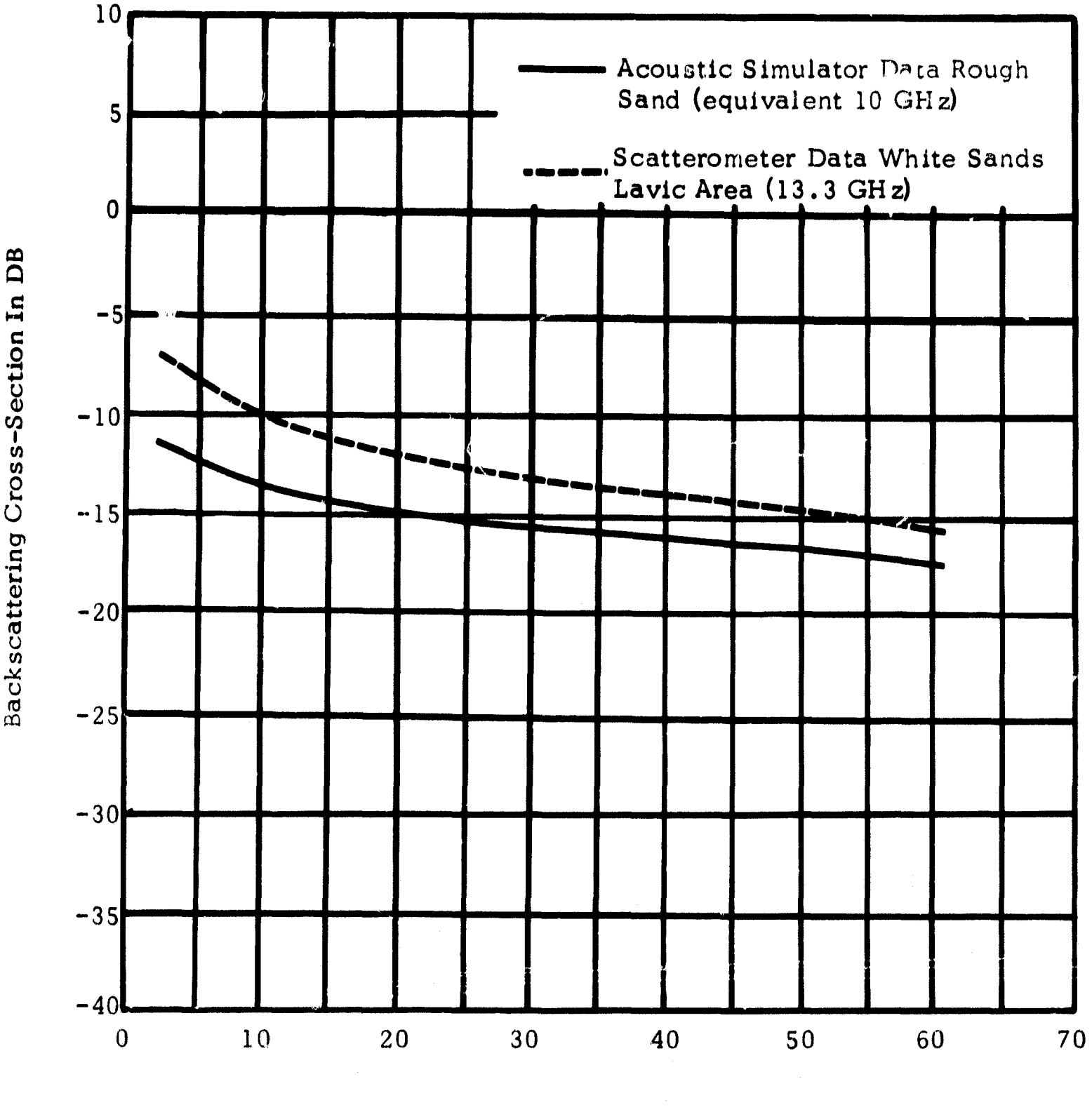


Figure 76a Comparison of Acoustical Data with Scatterometer Data

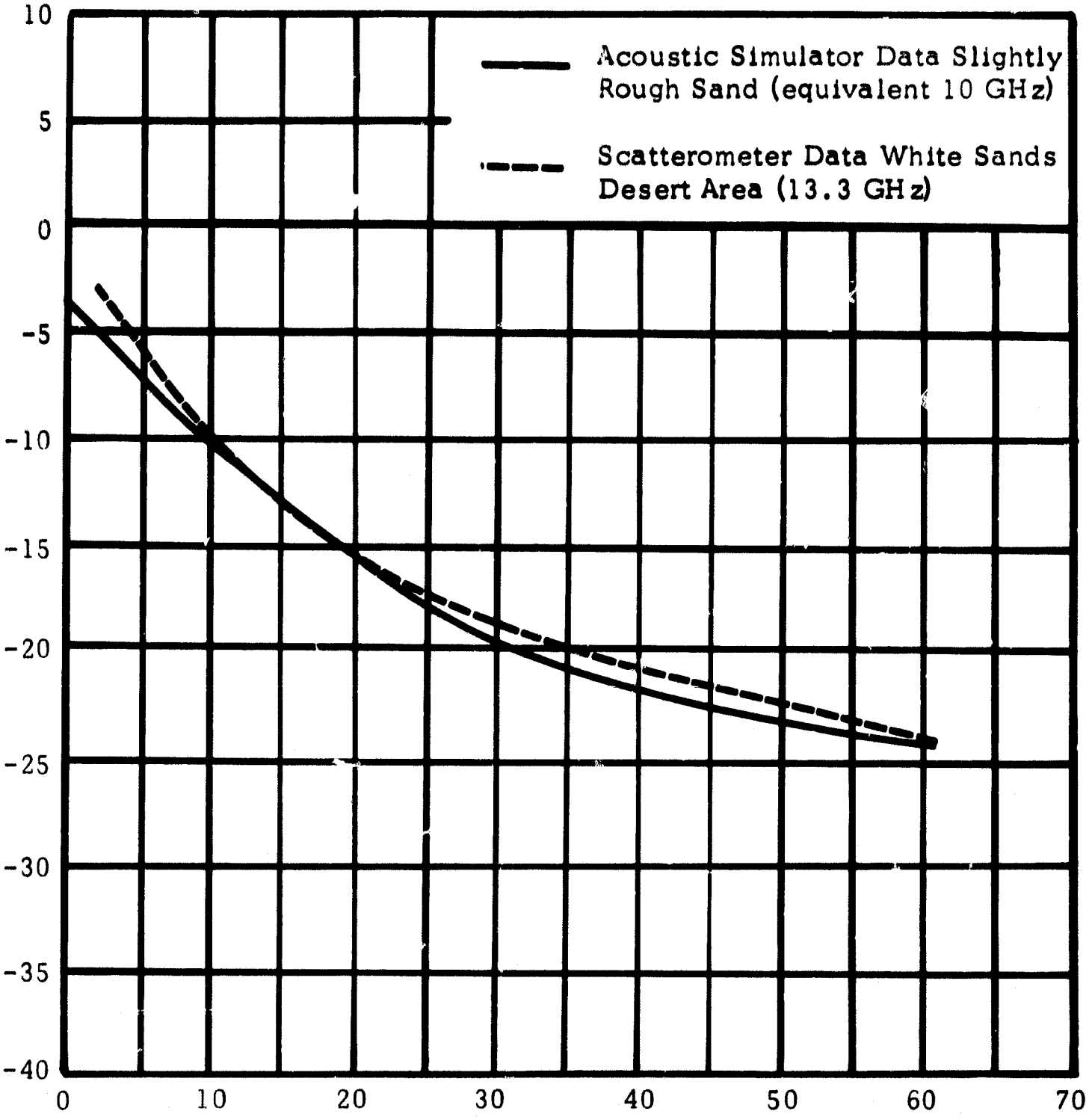


Figure 76b Comparison of Acoustical Data with Scatterometer Data

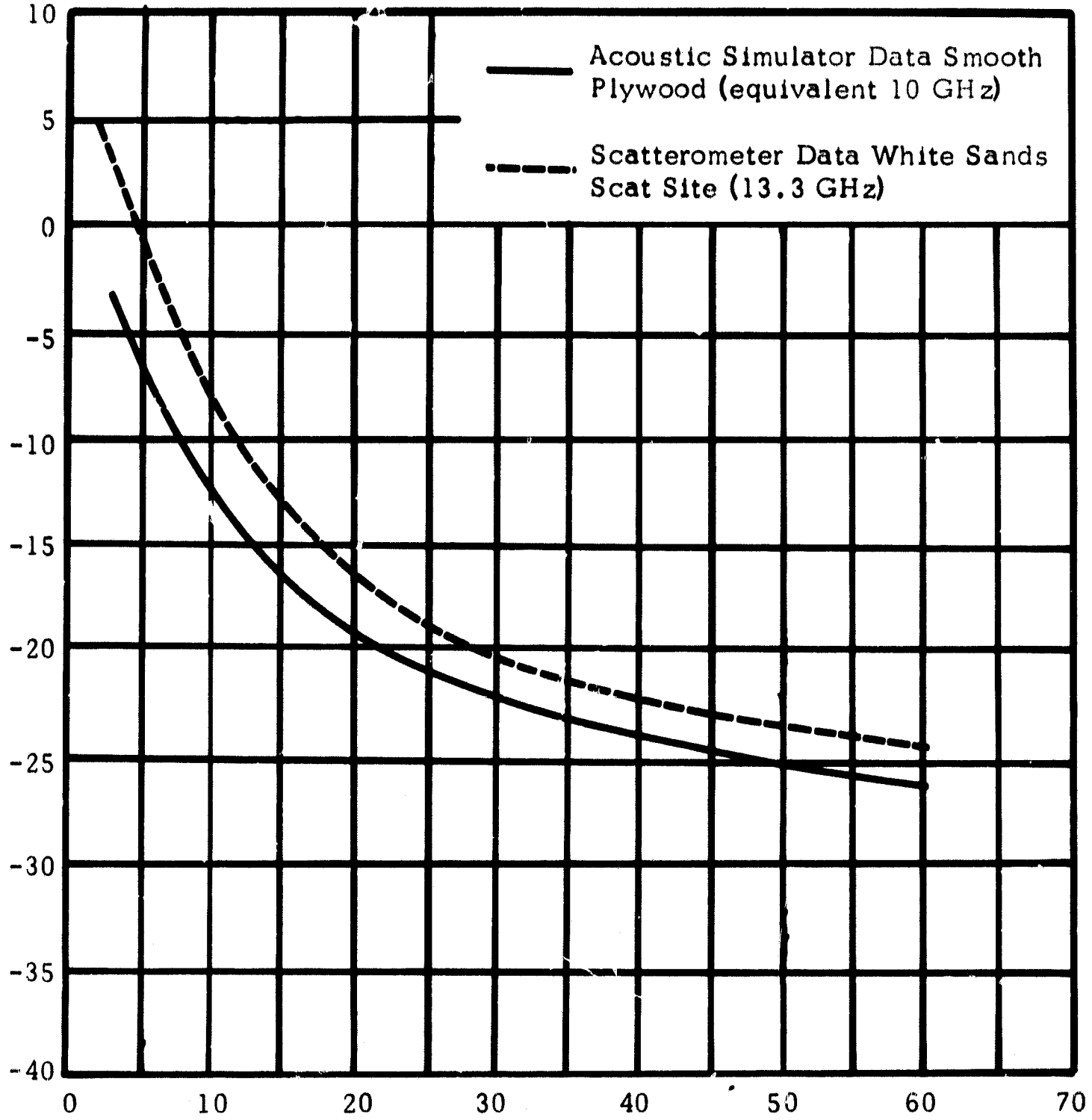


Figure 76c Comparison of Acoustical Data with Scatterometer Data

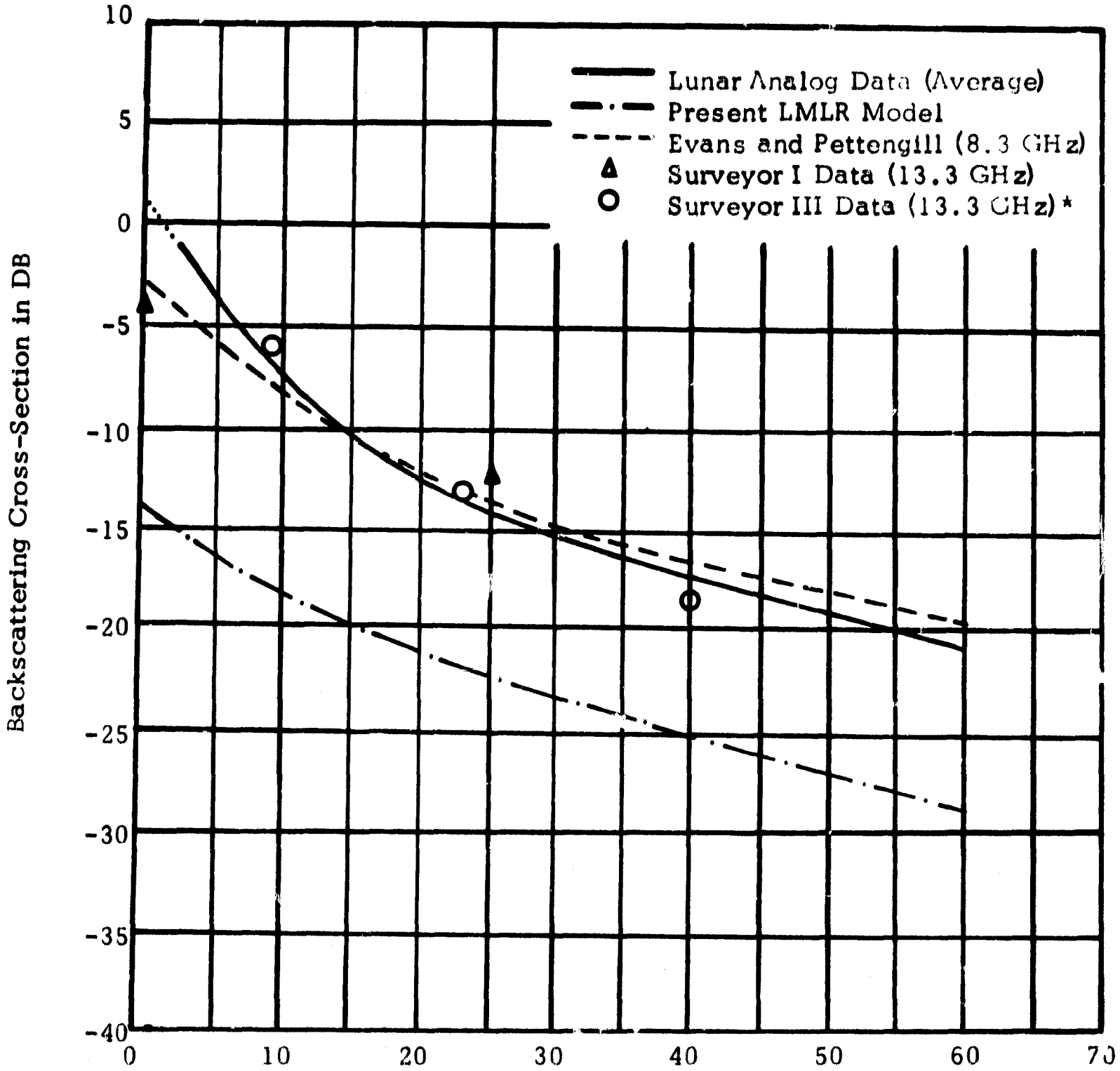


Figure 77. Comparison of Measured Data to LMLR Model

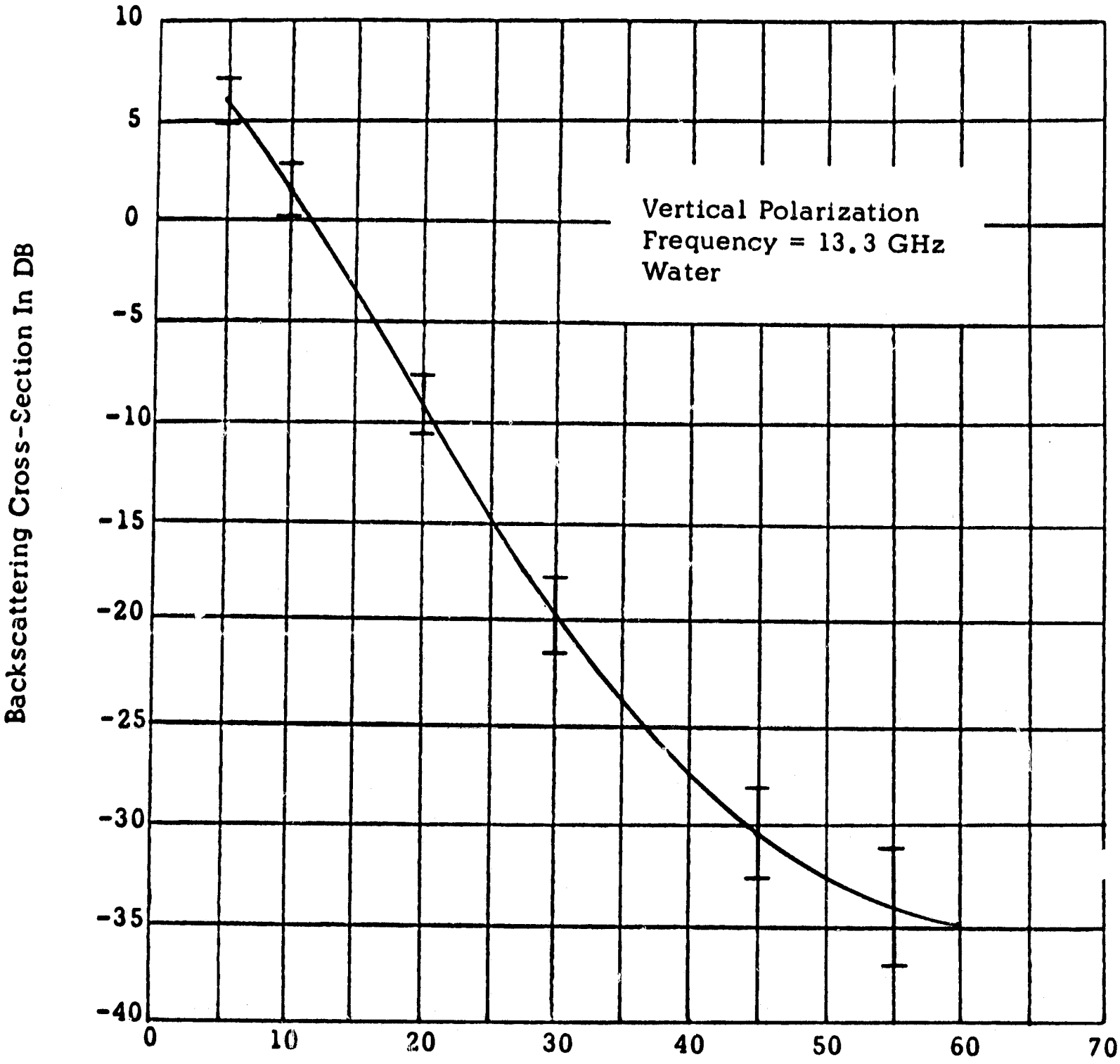


Figure 78 Mission 20, Flight 2, (8 runs), Bermuda Area

5.6 Theoretical Models

The purpose of a theoretical model is to establish a tool for analyzing the scattering mechanism in terms of terrain characteristics. As a part of the Scatterometer Data Analysis Program, various models are being investigated to see how well the differences in radar backscattering can be predicted. The procedure presently used is to obtain curve fits with the theoretical model and then to compare the model-predicted surface parameters with actual measurements of the terrain surface parameters.

After considering the various statistical models that have been applied to the analysis of backscattered radar return signals [7] (Davies), [8] (Moore), [9] (Daniels), [10] (Fung), [11] (Hagfors), [12] (Beckmann and Hayre), there are two candidates that consider the small-scale effects of the scattering surface. These are the models by Fung and Beckmann. The model by Fung is of an empirical nature in which correlation function contains eight adjustable constants. By proper selection of the values for these constants, it is possible to very closely fit almost any σ_o curve for almost the entire angular range, $0^o \leq \theta \leq 90^o$. The model by Beckmann, designed to explain the dependence of the mean backscattered power on the angle of incidence, shows that this dependence may be derived without any artificial assumptions.

The Beckmann model appears to be the most attractive for use in analysis of Scatterometer data at 13.3 GHz and data at other frequencies. The following are some of the more pertinent features of this model:

(1) The statistical model explicitly embodies the parameters necessary to account for both the large-scale and particularly the small-scale effects of the backscattering surface as functions of wavelength, surface height, and slope variations.

(2) Essentially, no artificial assumptions had to be made in the model.

(3) The application of the model to the σ_o (θ) computer-processed plots of the Scatterometer data will require less time and effort in comparison to the other models that also include the small-scale backscattering effects of the surface.

(4) By varying essentially the only two basic dimensionless parameters designated as R and K, a family of σ_o (θ) curves can be readily generated for the desired wavelength. These curves can then be used as overlays to match with the available experimental σ_o (θ) data.

To show how this model can be applied to the Scatterometer and other data, the significance of the various aspects of the model are discussed below, along with their association to backscattering terrain characteristics. The real goal of model application is the association of the parameters with the features and characteristics of the terrain. This will require matching of experimental $\sigma_o(\theta)$ curves before positive associations can be established.

Before discussing the model, it is important to note that the wavelength variable is contained in the model. Almost all investigators active in the study of backscattering from various terrains comment that there is a definite requirement for evaluation of model parameters as a function of wavelength.

Two pieces of pertinent data are available on one of Beckmann's models which show the wavelength dependence. The exponential form of the model was applied to Pettengill's highly accurate radar data from the moon (3.6 and 68 cm) with excellent fits for $0 \leq \theta \leq 90$ degrees. However, Pettengill mentions the need for additional experimental data at other wavelengths to better establish the wavelength dependence. This clearly emphasizes the further need for experimental radar backscattering data over the same terrain, under the same conditions, to establish the wavelength dependence of the measured parameters.

Two general statistical models were developed by Beckmann for random rough surfaces which were applied to the special case of backscattering. The difference in the two models is the form of the

autocorrelation function used. One used a general analytical function (usually Guassian); the other used an exponential form. There is some question posed by different authors as to the validity of the exponential model. As the experimental data are analyzed using model theory, the association of parametric data with ground truth data should be investigated.

Before developing the statistical solutions for the two models, the foundation for these models must be emphasized since it brings out the key to how small-scale scattering effects could be justified for inclusion in the theory. The statistical models of rough surfaces by Davies, Moore and Hayre treat the height variation by a single statistical distribution and a single correlation function. Rough surfaces in nature, however, are in essence composite structures, or better can be treated as such.

The terrain consists of a superposition of a number of kinds of roughness whose modeling parameters are wavelength dependent. For example, rolling hills can be considered as large-scale roughness, trees and houses as median-scale roughness. Plowed fields, rocky surfaces, and grass may be treated as small-scale roughness. Beckmann points out that the surface height variation (a statistical distribution) for each roughness can be identified separately and can be expressed as part of a composite function of the surface $\zeta(x,y)$, where

$$\zeta(x,y) = \zeta_1(x,y) + \zeta_2(x,y) + \ldots$$

For example, $\zeta_1(x,y)$, $\zeta_2(x,y)$ and $\zeta_3(x,y)$ could be associated with the large-, medium-, and small-scale roughnesses, respectively. Also, the ζ_j ($j = 1, 2, \ldots$) are mutually independent stationary random functions of the coordinates, each with its own distribution and correlation function. Thus, ζ represents the height variation of the composite surface. Where ζ was treated before in other models as a single function, the additive effects from the small surface structures were ignored.

It is not too early to point out that one of the important aims of the matching of these models to the Scatterometer σ_o curves, developed from the experimental data, is to break out the ζ_j from the composite ζ's with the aid of the ground truth data and other pertinent information.

It is unnecessary to repeat the mathematical development of the two models. Nevertheless, it is important to present some of the important features of each model, particularly the identification of the model parameters.

(1) Analytical Model - This model was derived for any analytical correlation coefficient such as $C_j(r) = \exp(-r^2/L_j^2)$, where r is the distance between any two points x, y and x', y' in the xy-plane (the scattering surface), and L is the correlation distance ($r = \tau$ and $L = T$ in Beckmann's paper). To show the parameters which need to be

considered in applying this model to fit the σ_o (θ) curves, it is expanded to show clearly all of the detail which will be involved and which will be associated with the terrain if possible.

$$\langle EE^* \rangle = \left(\frac{2\pi}{\lambda}\,\frac{A}{\pi R_o}\right)^2 \frac{1}{\cos 4\theta}\,\frac{\lambda^2}{4\pi A\eta}\,\frac{1}{4\sum_j\left(\frac{\sigma_j/\lambda}{L_j/\lambda}\right)^2}\,\exp\left[\frac{-\tan^2}{4\sum_j\left(\frac{\sigma_j/\lambda}{L_j/\lambda}\right)^2}\right]\cdot S(\theta)$$

$\langle EE^* \rangle$ = mean power backscattered to the receiver.

$*$ = denotes the complex conjugate.

A = equivalent plane surface area.

R_o = distance to area element A at normal incidence.

σ_j = standard deviation of the scattered heights of the jth set of scatterers. $j = 1, 2, \ldots$

L_j = correlation distance for the jth set of scatterers. $j = 1, 2, \ldots$

θ = angle measured from vertical (independent variable for the curve fitting process).

$S(\theta)$ = shadowing factor (percent value) to account for reduction in signal due to shadowing, takes effect past 30^o.

η = the impedance of the medium on the incident side of the interface formed by the rough surface.

In more compact form, this equation can be written:

$$[EE^*] = \frac{P_o}{\cos^4 \theta} S(\theta) \exp(-Q \tan^2 \theta)$$

where

$$P_o = \frac{E_o^2 \lambda^2 Q}{4\pi \eta A}$$

$$E_o = \frac{KA}{\eta R_o}$$

$$K = 2\pi/\lambda$$

$Q = 1/2 \sum_j s_j^2$ where $s_j = \sqrt{2}\sigma_j/L_j$ = the RMS slope of the jth set of scatters.

(2) Exponential Model - Because of the lack of available information on correlation functions associated with various terrain types, Hayre (Reference 6) analyzed a large number of terrain types using maps prepared by the Army Corps of Engineers and the U. S. Department of Commerce. His studies showed that the exponential form for the correlation function was predominant and seemed to describe very large perturbations in a surface in addition to small-scale roughness. It probably also presents microscopic surface elevation variations.

Based upon this information, Beckmann's choice of the exponential correlation coeft. ient for the curve fitting Pettengill's moon data appears justified. There are still those who contend that analytic forms are required to fit the data at near-vertical incidence. Some experience, however, will have to be gained through inspection of ground-truth data to ascertain which correlation function actually applies.

Derived from an exponential correlation function such as $C_j = \exp(-|r|/L_j)$, the second model is given by,

$$\langle EE^* \rangle = \frac{S(\theta)}{128\pi^3 A(\Sigma_j r_j s_j)^2 \left\{\cos^4\theta + \frac{\sin^2\theta}{(4\pi\Sigma_j r_j s_j)^2}\right\}^{3/2}}$$

or in more compact form,

$$\langle EE^* \rangle = \frac{P_o \# S(\theta)}{(\cos^4\theta + R\sin^2\theta)^{3/2}}$$

where

$$P_o \# = \frac{E_o^2 \lambda^2 R}{8\pi\pi A}$$

The first models for backscattering did not contain the shadowing function, $S(\theta)$, to account for the fact that the shaded parts of the surface do not contribute to the backscattered power. "$S(\theta)$"in a sense is an adjustment factor developed using

geometric optics concepts, but does not consider diffraction effects. The most important features of this function are that it decreases the contributions of the fields scattered by a rough surface at large angles of incidence, and it contains the important parameters, s_j, the RMS slopes of the scatterer groups.

The value of the $S(\theta)$ function is given by,

$$S(\theta) = \exp\left[-1/4 \tan\theta \operatorname{erfc}\left(\sqrt{Q} \cot\theta\right)\right]$$

where $\operatorname{erfc}(x) = 1 - \operatorname{erf}(x)$, which is the complementary error function.

Thus,

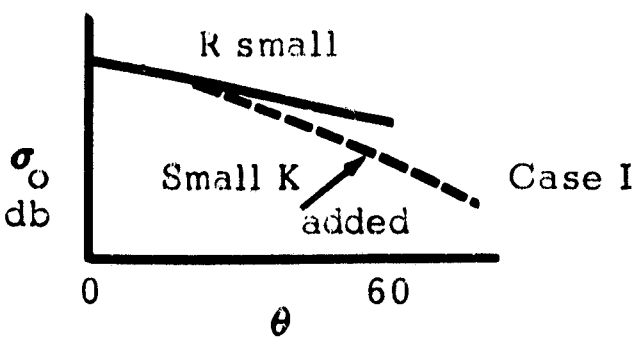
$$\operatorname{erfc} x = \frac{2}{\sqrt{\pi}} \int_x^\infty \exp\left(-t^2/2\right) dt$$

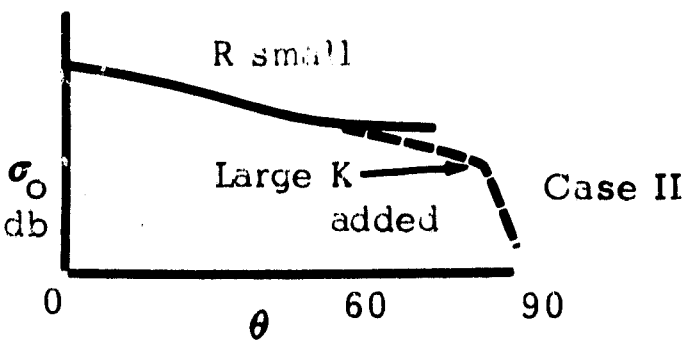
The effects of R and K upon the σ_o curve are presented in Figure 79, along with the respective terrain predictions. Figure 80 illustrates these effects.

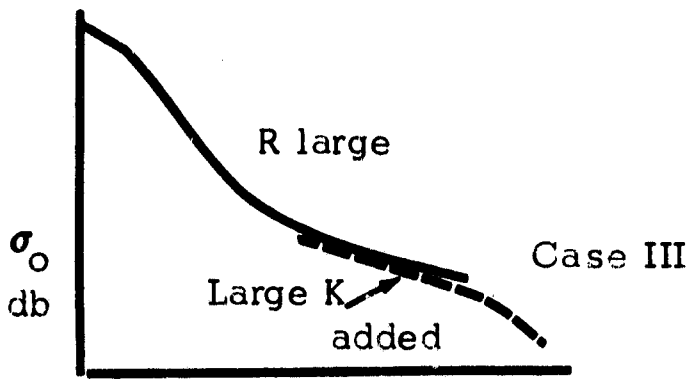
Figure 79
Terrain Prediction through R and K Values

Case	R	K	σ	s	Anticipated Structure
I	small	small	large	large	Terrain rough, large peaks close together
II	small	large	large	small	Terrain rough, large peaks far apart
III	large	large	small	small	Terrain smooth, small mounds far apart
IV	large	small	small	large	Terrain smooth, small mounds close together

$$R = \frac{1}{\left(4\pi \sum_j r_j s_j\right)^2} \qquad K = \frac{1}{\left(2 \sum_j s_j^2\right)^{1/2}} \qquad r = \frac{\sigma}{\lambda} \qquad s = \frac{\sigma}{T}$$







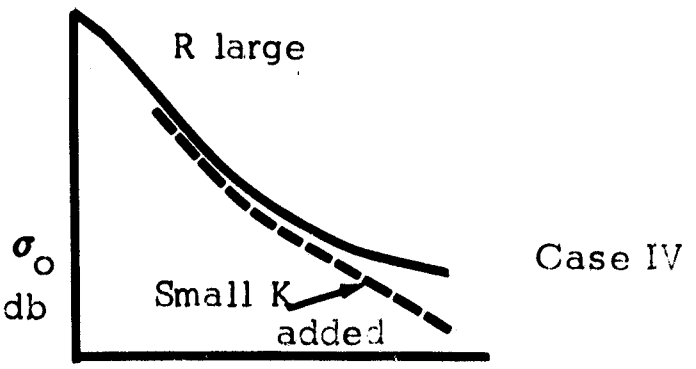


Figure 80 Terrain Prediction

5.7 Separation of Specular and Scatter Components

As a further method for identifying the terrain from radar return data, the ratio of the specular to the scatter content of the returned signal was proposed quite early as a feasible way of obtaining such definitive information. The early radar return data were obtained with pulse systems so, naturally, means were devised to separate the average radar "pulse" data into the specular and scatter components. Very little effort was expended in applying this concept to CW or Doppler systems. A brief discussion will be presented on some of the early graphical methods used in making such separations. Certain mathematical models and methods were brought forth to explain the complex transition between the specular and scattered return signals. A brief discussion will be presented of this area along with the success obtained by applying the models and methods to radar return data.

After reviewing the existing methods of separation of specular and scatter components for pulse systems, a plan is proposed for obtaining information of a similar nature from the Ryan Scatterometer data.

I. Models for Separating Specular and Scatter Components.

1. Moore's[14] (1957) method, is a mathematical development which is based upon the normal distribution of the heights of the scattering elements and a first approximation of normal distribution of phases. A summation is made

of all the electric field contributions from the scattering facets at the receiver for the radar-backscatter case. Of significance in this model is the appearance of a separation, or attenuation, constant "a" with the specular term,

$$a^2 = e^{-4\left(\frac{2\pi}{\lambda}\sigma\right)^2}$$

(squared for power)

where σ is the standard deviation of the scattering heights and λ is the wavelength. The particulars of this model are:

a) It provides a separation constant for the specular and scatter components as functions of σ and λ .

b) The specular to scatter ratio resulting is a function of σ only.

c) Results of this method cannot be verified with confidence using simulation.

d) The method does provide an insight to the possible mechanisms generating the specular and scatter components of the return.

e) If "a" is the specular portion, then (1-a) is the scattered portion.

2. Davies [15] (1954) treats the specular-scatter problem for the general case (radiation in any direction) for a slightly rough surface where the scattering heights also have a normal distribution. The surface is made up of an ensemble of reflectors. The average field is computed by averaging over the ensemble and integrating to obtain the usual far-field diffraction expression. The maximum field is found to be in the specular direction. Davies refers to this as the "coherent" or dc component. The "incoherent" or scatter component is then determined by taking an ensemble average of the ac, or scatter, component where the method of the complex conjugate is used in conjunction with an auto-correlation function of the height of the surface. The particulars of this model are:

a) A separation constant $a_1^2 = \exp\left[-4\left(\frac{\pi}{\lambda}\sigma\right)^2\left(\cos\theta + \cos\psi\right)^2\right]$ results which multiplies the familiar $\left(\frac{\sin x}{x}\right)^2$ diffraction expression for a rectangular facet. For normal incidence, this reduces to the separation constant by Moore.

b) The coherent component is shown to be related to diffraction theory where the larger the scattering rectangular aperture the more directive the beam. Also the smaller σ and the larger λ, the larger the magnitude of the specular component.

c) The incoherent component is found to be a cone of radiation about the specular direction; however, the magnitude is a function of the horizontal correlation distance B, the standard deviation of scatterer heights σ, and the size of the scatterers of dimension ℓ by m.

d) The expression for the specular-to-scatter ratio for the Davies model for the general case is given by,

$$\frac{\text{Specular power}}{\text{Scattered power}} = \frac{(dc)^2}{(ac)^2} = \frac{\langle E\rangle^2}{\langle |E - \langle E\rangle|^2\rangle} =$$

$$= \frac{\left\{\frac{E_o}{2\lambda r}(\cos\theta + \cos\psi)\frac{\sin\left[\frac{\pi\ell}{\lambda}(\sin\theta\cos\phi - \sin\psi)\right]}{\frac{\pi}{\lambda}(\sin\theta\cos\phi - \sin\psi)}\cdot\frac{\sin\left[\frac{\pi m}{\lambda}(\sin\theta\sin\phi)\right]}{\frac{\pi}{\lambda}\sin\theta\sin\phi}\exp\left\{-2\left[\frac{\pi\sigma}{\lambda}(\cos\theta+\cos\psi)\right]^2\right\}\right\}^2}{\frac{\pi^3 E_o^2 a^2\sigma^2\ell m}{\lambda^4 r^2}(\cos\theta+\cos\psi)^4\exp\left\{-\left(\frac{\pi a}{\lambda}\right)^2\left[(\sin\theta\cos\phi-\sin\psi)^2+\sin^2\theta\sin^2\phi\right]\right\}}$$

where ψ is the angle of incidence, θ and ϕ give the direction of the specular component, r gives the distance, and E_o the field intensity.

e) Parkins (1965) treats the problem of the separation of specular and scatter power and obtains expressions similar to those above.

3. Hayre[16] (1962) modified the Davies model for backscattering by replacing the spatial-height normal auto-correlation function with an exponential form. The resulting expression for the radar cross section per unit area was found to be

$$\sigma_o = 4\sqrt{2}\,\pi\left(\frac{B}{\lambda}\right)^2\frac{\theta\cos^2\theta}{\sin\theta}e^{-4\left(\frac{2\pi}{\lambda}\sigma\cos\theta\right)^2}\sum_{n=1}^{\infty}\frac{4^n\left(\frac{2\pi}{\lambda}\sigma\cos\theta\right)^{2n}}{(n-1)!\left[2\left(\frac{B2\pi}{\lambda}\sin\theta\right)^2+n^2\right]^{3/2}}$$

The significant aspects of this expression for the separation of the specular and scatter components are:

a) An attenuation constant appears which is the same as for Moore and Davies for normal incidence ($\theta = 0.$),

$$a^2 = e^{-4\left(\frac{2\pi}{\lambda}\sigma \cos\theta\right)^2}$$

b) Arbitrarily the argument of the exponent can be set to unity to define a transition region between the specular and scattered returns, thus,

$$\frac{\sigma}{\lambda} = 0.079 \sec\theta$$

Sometimes σ/λ is designated as the transitional value of the vertical roughness in going from a specular (or quasi smooth) surface to a rough surface.

c) For a nearly smooth surface, the general expression for Hayre's σ_o becomes,

$$\sigma_o \approx \frac{4\sigma^2}{B\lambda}\ \theta\ \cot^4\theta \qquad \theta \neq 0$$

This expression could be applied to specular type returns for near vertical incidence where a separation of the specular component is attempted.

4. Brown[17] (1960) presents a number of methods of determining the specular-to-scatter ratio for the CW radar return case. Of the three cases considered

which include spatial, frequency and polarization effects as well as the effects of beamwidth and pulse-width limitations, none treat the specular-to-scatter ratio in terms of the important statistical parameters of the reradiating terrain such as the mean, the standard deviation and the auto-correlation of the scatterers. The aspects of these models are:

a) Reported test results on lunar data were found not to agree adequately with the model.

b) Experimental data are essential to determine the specular-to-scatter ratio.

5. Welch[18] (1955) proposed a mathematical model for designating the specular-to-scatter ratio. A Rayleigh type scattering surface was assumed that was made up of a large number of scatterers whose power spectrum is continuous, and each frequency (included the Doppler effects) contributes a small amount to the total received signal. The pulse case is considered as a sampling of the CW standing wave, and the changes occurring from pulse to pulse are due to variations in the phase of the return signals. The first case treated was for a large number of scatterers of uniform size and distribution of the phases. Other cases treated included one, two, and more very large specular targets interspersed with the many small scatterers.

For these models the ratios of specular (dc) to scatter (ac) power (the square of the variance) components were computed. The following significant aspects of these models are:

a) The specular (non-fading dc value) to scatter (fading ac value) for a Rayleigh ground is unity.

b) The model was used to determine the dc to ac ratios for 1, 2, and 3 very strong scatterers. The models were modified accordingly.

c) The determination of ratios of $\frac{(dc)^2}{\text{variance}}$ from pulsed radar data for some 50 flights showed that only the returns from Elephant Butte Reservoir indicated high ratios (around 100), The ocean and various seas had ratios around 5, and the rest of the data (desert, farmland, cities, wooded land) appeared to be from Rayleigh ground. Warner (1958) used the ratio of the median/mean power return to show the specular to scatter aspects of the ground.....for a Rayleigh ground this value is 0.693. For 6 different terrain types the ratios were close to 0.693 which does not insure that a Rayleigh distribution exists, but does provide evidence in its favor.

d) Experimental data obtained by an acoustical simulator (Hayre) showed the ratio of $\frac{(dc)^2}{\text{variance}}$ could not be applied to radar return data for depicting the surface roughness. It was shown that the ratio increased linearly with height (transmitter-target distance) for only one simulated surface. This was in agreement with Williams (1959) who showed that for a plane surface the specular component of a pulse radar with $\frac{c\tau}{2} << h$ (c = free space velocity, τ the pulse length)

increases with h over the scatter component, also given by

$$\frac{\text{specular power}}{\text{scatter power}} = \frac{a^2 h}{2 c \tau (1-a^2)}, \text{ Moore, 1958 .}$$

The other surfaces did not confirm this analysis.

II. Graphical Methods

1. Warner[19] (1958) devised a means whereby the average return power for a pulsed radar could be separated into specular and scatter components by solving for the value of the separation constant, a. Previously, the scatter component of the σ_o (θ) plot was determined by an application of Davies' directivity, or scattering, model of a rough surface for the backscattering case. The average pulse return expression separating the specular and scatter components is given by,

$$\langle P_r(d) \rangle = a^2 \left[\frac{P_D \left(d - \frac{2h}{c}\right) G^2(0) \lambda^2 K^2}{(4\pi)^2 (2h)^2} \right] + (1-a^2) \frac{c \lambda^2 \beta}{64 \pi^2} \int_{T_1}^{T_2} \frac{P_D (d-T) G^2(T) \sigma_o(T) dT}{(h + cT/2)^3}$$

$\overbrace{\qquad\qquad}$ $P_r(d)$ specular

$\overbrace{\qquad\qquad\qquad\qquad}$ $P_r(d)$ scatter

where $[P_r(d)]$ = average power return (not a time average), P_D= transmitted power, G= antenna gain, β = scatter power absorption coefficient, d= radar delay time, and T= delay time for difference in range r and altitude h. All other parameters have been defined previously. The specular component can be eliminated by working with times greater than the pulse length τ. Thus the first part of the equation can be ignored. The specular component is the difference between the total measured value $[P_r(d)]$ and the scattered component above.

Thus $a^2 = \frac{1}{K^2} \frac{(4\pi)^2 (2h)^2}{P_D (d - \frac{2h}{c}) G^2(0) \lambda^2} [P_r(d)]$ specular

The following important comments about this method are:

a) The values of **K** and β are unknown.

b) The spatial-height correlation distance in Davies' scattering model, β, can be graphically estimated

c) Successful application of this method requires having available continuous data on the average power return.

2. Glascock[20] (1958) designed a pulsed radar experiment to be conducted by the U. S. Naval Research Laboratory that would provide specular and scatter radar data for targets previously covered by the Sandia Corp radar backscatter program. This was a direct approach that by-passed the short-comings of an analytical model (unattainable values for the statistical constants) and was to provide positive values of the specular and scatter components for verifying the model theory.

A pulsed radar switched alternately to a very narrow-beam and a broad-beam antenna at a fairly high pulse repetition rate would result in specular and scatter returns taken, for all practical purposes, over the same surface.

The power returned for the beamwidth-limited case for the narrow-beam antenna (a limited number of Fresnel zones) is,

$$P_1 = P_{1\ \text{specular}} + P_{1\ \text{scatter}}$$

and the power for the broadbeam antenna (essentially an infinite number of Fresnel zones).

$$P_2 = P_{2\ \text{specular}} + P_{2\ \text{scatter}}$$

where $P_{1\ \text{specular}}$ should equal $P_{2\ \text{specular}}$ since the radar return due to the specular component is essentially independent of the irradiated area, provided the gain for both antennas $G_1(0) = G_2(0)$. $P_1 \approx P_{1\ \text{specular}}$ since $P_{1\ \text{scatter}}$ is negligible, thus, $P_2 \approx P_{1\ \text{specular}} + P_{2\ \text{scatter}}$.

Subtracting $P_{1\ \text{specular}}$ from the total return from the broadbeam antenna yields the scatter component and finally,

$$\frac{\text{Specular power}}{\text{Scattered power}} \approx \frac{P_{1\ \text{specular}}}{P_{2\ \text{scatter}}}$$

There are a number of ways of irradiating a small area and a large area to obtain essentially the specular and scatter components as follows:

(1) Use a very short pulse (pulse-width limited) and a long pulse alternately at a sufficient pulse repetition rate.

(2) Use a narrow-beam and wide-beam antenna for alternate runs over the same target area.

(3) Use a dual-antenna system and pulse each one alternately.

III. Applications

There appear to be two possible ways of separating the Ryan Doppler Scatterometer data: (1) an analytical approach, and (2) an experimental approach. The analytical approach appears the more feasible at the present time, since there is an abundance of tape recorded data on the Doppler spectrum by Ryan for a number of terrain types. It would require an integration over the specular portion of the Doppler spectrum to obtain the specular contribution from the candidate

ground surface, thus,

$$P = \int_{f=0}^{f=f_1} P(f)\, df$$

An analysis would have to be made of this method to determine what limits would have to be placed upon the integral to include the coherent component other than the return associated with zero Doppler. Correspondingly, the limits to define the scatter component can be determined and finally, a ratio of specular-to-scatter power could be determined and associated with the terrain type. This method has not been investigated in any depth, but it appears to be feasible.

An experimental approach using alternately-switched narrow and broad-beam antennas, though more involved, offers a more positive means of obtaining the specular and scatter components. Correlation between the analytical and experimental methods would establish a level of confidence in the separation values.

Both of these methods should be studied to determine feasibility, but, of greater importance, a study should be made to determine the utility of this separation concept in providing information about the scattering surface that is not already available elsewhere ---- like the separation of $\sigma_o(\theta)$ plots.

IV. Summary

A number of mathematical models and methods applicable to the separation of the specular and scatter power components in a back-scattered signal (also forward-scattered signal) were briefly presented, others by Twersky[21] (1957),

Basore[22] (1962), Peake[23] (1960), Katz[24] (1959) and Beard[25,26] (1956) are to be considered in a more complete study.

To the authors knowledge, very little information is published which evaluates either the mathematical models or the separation methods with substantiated experimental data. This is readily understandable when one looks for actual radar return data which has been separated into its specular and scatter components. A limited amount of such work has been done by Warner and Glascock.

The separation constants by Davies, Moore, Hayre, and others should be tested to ascertain their validity, or rather applicability, in pointing out the transition region between the specular and scatter components.

The application of "scattering" mathematical models to separate out the scatter component, and by analytical continuation to extend it to the normal ($\theta = 0$), has been attemped; however, important parameters such as σ, β, and K need to be known. Since an experimental program is required to evaluate these parameters, it appears expedient to obtain the separation values of the specular and scatter components experimentally by possibly a dual-beam Doppler radar system where these parameters are implicit in the return data. These parameters are already implicit in the Doppler spectra of the various Scatterometer data taken by Ryan. Investigations should be made to determine how these magnetically taped Doppler spectra data can be separated for the specular and scatter components.

5.8 Best Fit Curves

To further enhance the quality of the plotted Scatterometer data, various curve fitting techniques were explored using computer routir presently available at the Computation and Analysis Division. To date, two methods of curve fitting have been used experimentally. The results have been promising, but until the total number of data points are further defined, the degree of the curve fit cannot be determined. In addition, these techniques can be applied to fitting the curves from the various models to the actual experimental data by computized methods. A brief explanation of the methods used is as follows:

Least Squares Method

A standard technique for fitting a curve to a set of experimental data is the method of least squares. This technique simply involves selecting a polynomial of the form,

$$Y(X) = \sum_{n=0}^{N} a_n X^n$$

and adjusting the coefficients a_n to minimize the expression,

$$D^2 = \sum_{m=1}^{M} D_m^2$$

where the D_m are the differences between the measured data and the polynomial ordinate at the M points X_m; m = 1, M. Clearly, if the order of the polynomial, N, is chosen to be equal to the number of data points M, the polynomial can be made to pass exactly through every data point. In practice, however, this is neither desirable nor practical and we choose $N \ll M$. Denoting the measured data points by Y_m; m = 1, M, we may express the differences D_m by,

$$D_m = Y_m - \sum_{m=0}^{N} a_n X_m^n$$

Substituting in the expression for D^2 yields,

$$D^2 (a_0, a_1, \ldots, a_n) = \sum_{m=1}^{M} \left[Y_m - \sum_{n=0}^{N} a_n X_m^n \right]^2$$

Now, in order for this expression to yield an absolute minimum with respect to the N + 1 parameters a_n; n=0, N, each partial derivative must be equal to 0, i.e.,

$$\frac{\partial D^2}{\partial a_o} (a_o, a_1, \ldots, a_n) = \sum_{m=1}^{M} 2 \left[Y_m - \sum_{n=0}^{N} a_n X_m^n \right] (-1) = 0$$

$$\frac{\partial D^2}{\partial a_1} (a_0, a_1, \ldots, a_n) = \sum_{m=1}^{M} 2 \left[Y_m - \sum_{n=0}^{N} a_n X_m^n \right] (-X_m) = 0$$

$$\frac{\partial D^2}{\partial a_n} (a_0, a_1, \ldots, a_n) = \sum_{m=1}^{M} 2 \left[Y_m - \sum_{m=0}^{N} a_n X_m^n \right] (-X_m^N) = 0$$

And we have N + 1 equations which must be solved for the N + 1 quantities a_n; n=0, N. A sample curve using this method is shown in Figure 81. In general a curve may be fitted to the highest order required, but the present curve fit program is limited to the fifth order.

Power Function Method

Another method of curve fitting may be accomplished through the use of power functions. This is accomplished by taking the log of the X value of the data coordinates (X, Y) which now become (log X, Y), and using the resultant values to form a curve on the Cartesian coordinate system as represented in Figure 82. By taking these new coordinates we can obtain a polynomial fit using the least squares technique. The equation of the computed coefficients is:

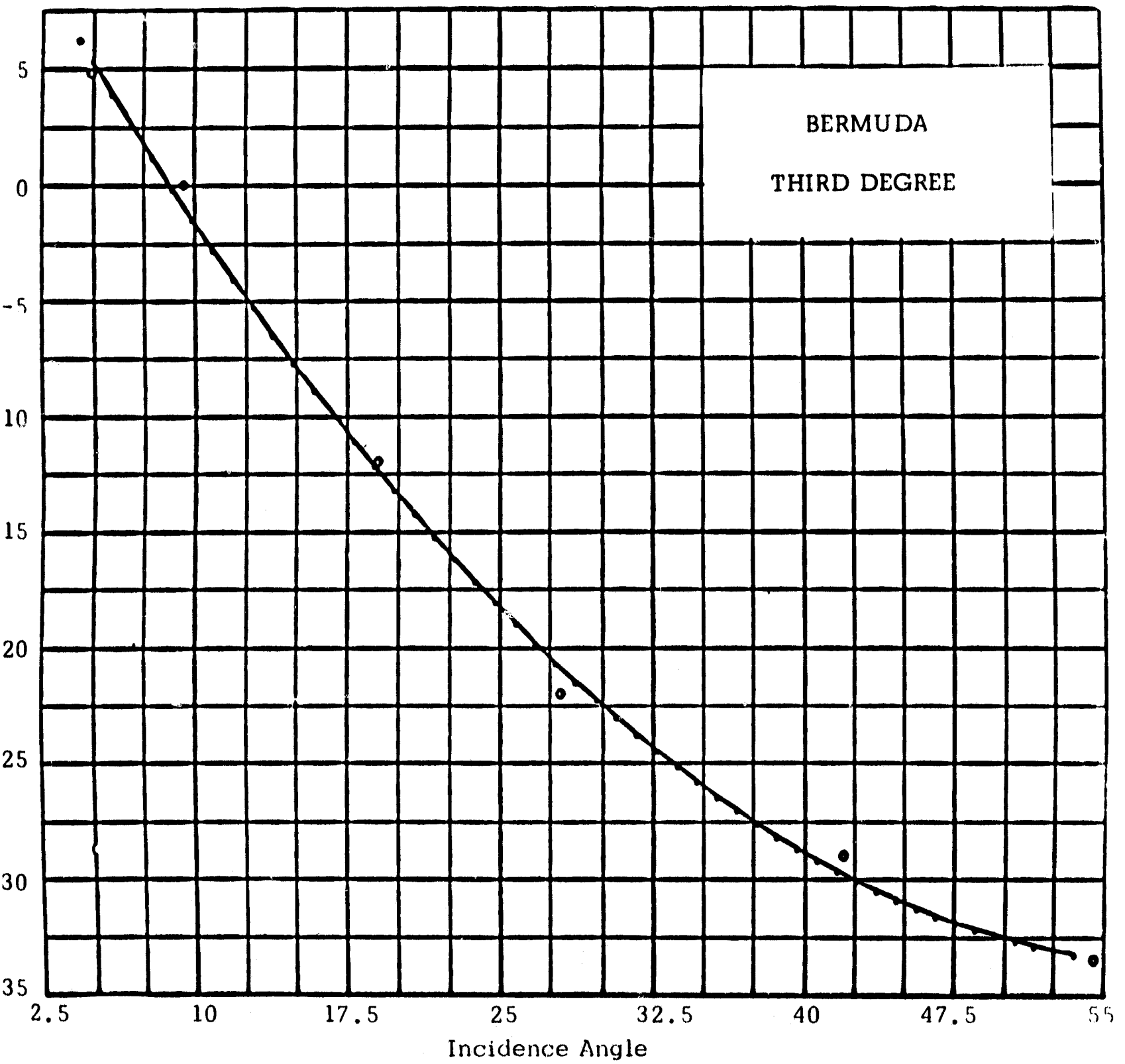
$$Y = A_0 + A_1 (\log X) + A_2 (\log X)^2 + \ldots + A_N (\log X)^N$$

These polynomials may also be used to obtain a dependent value by taking the logarithm of the new independent value and plotting the results on semi-log paper to obtain the same curve. The results are given in Figure 83.

Using the present number of data points in their designated position, a third degree curve fit using the least squares method is most representative of the Scatterometer data. However, as other angles or data points are defined, a curve fit utilizing the

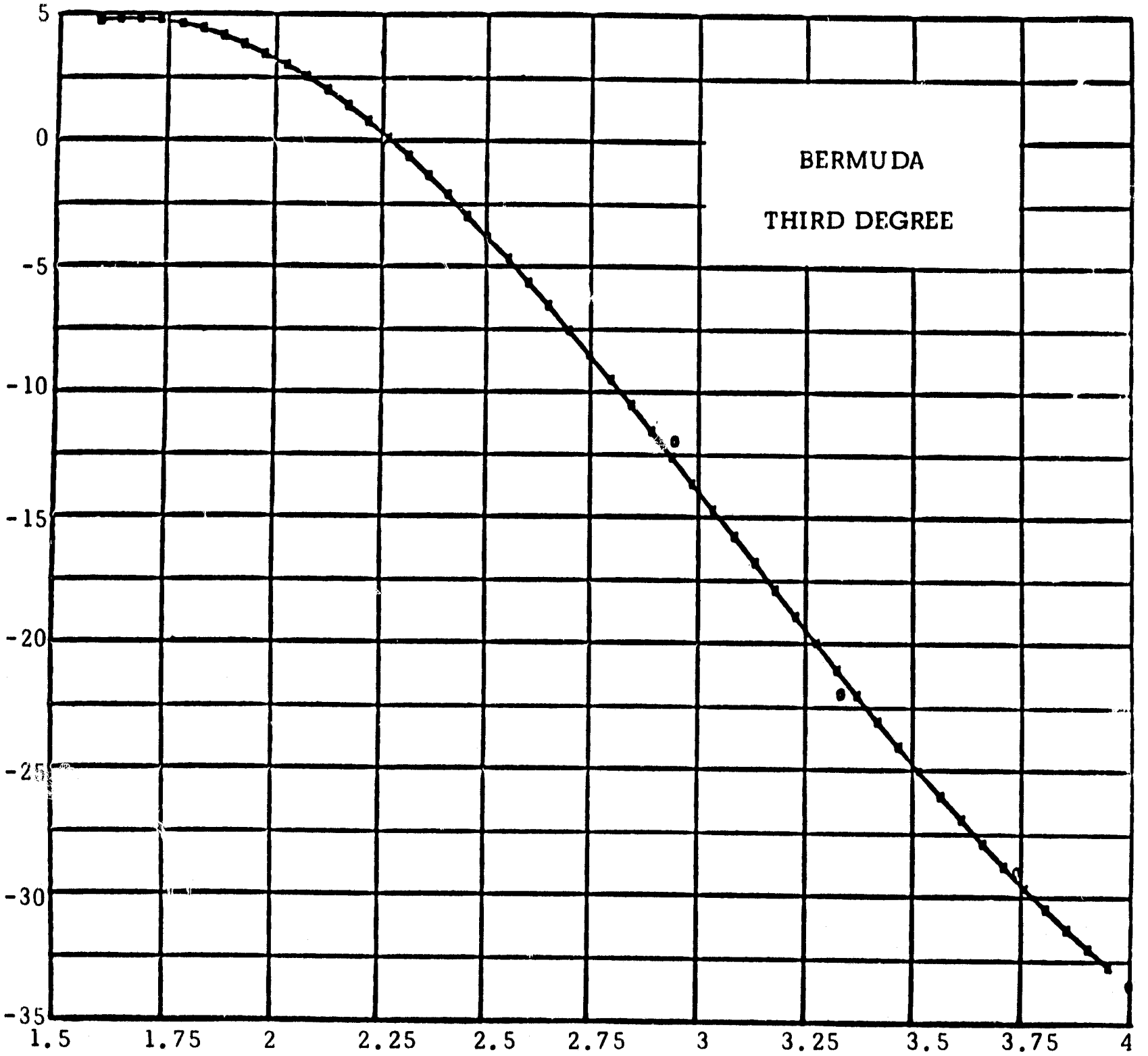
fourth or fifth degree curve should produce the best fit. The fourth and fifth degree curve fits presently result in the smallest percentage of error, but tend to turn down too rapidly at the larger angles.

It is recommended that a study be conducted on the feasibility of fitting a curve to the statistical data summaries utilizing the original computer program grid size and dimensions. The present curve fit program determines its own grid and limits. Distribution of the independent variable should be considered in determining the degree of curve fit to be used.



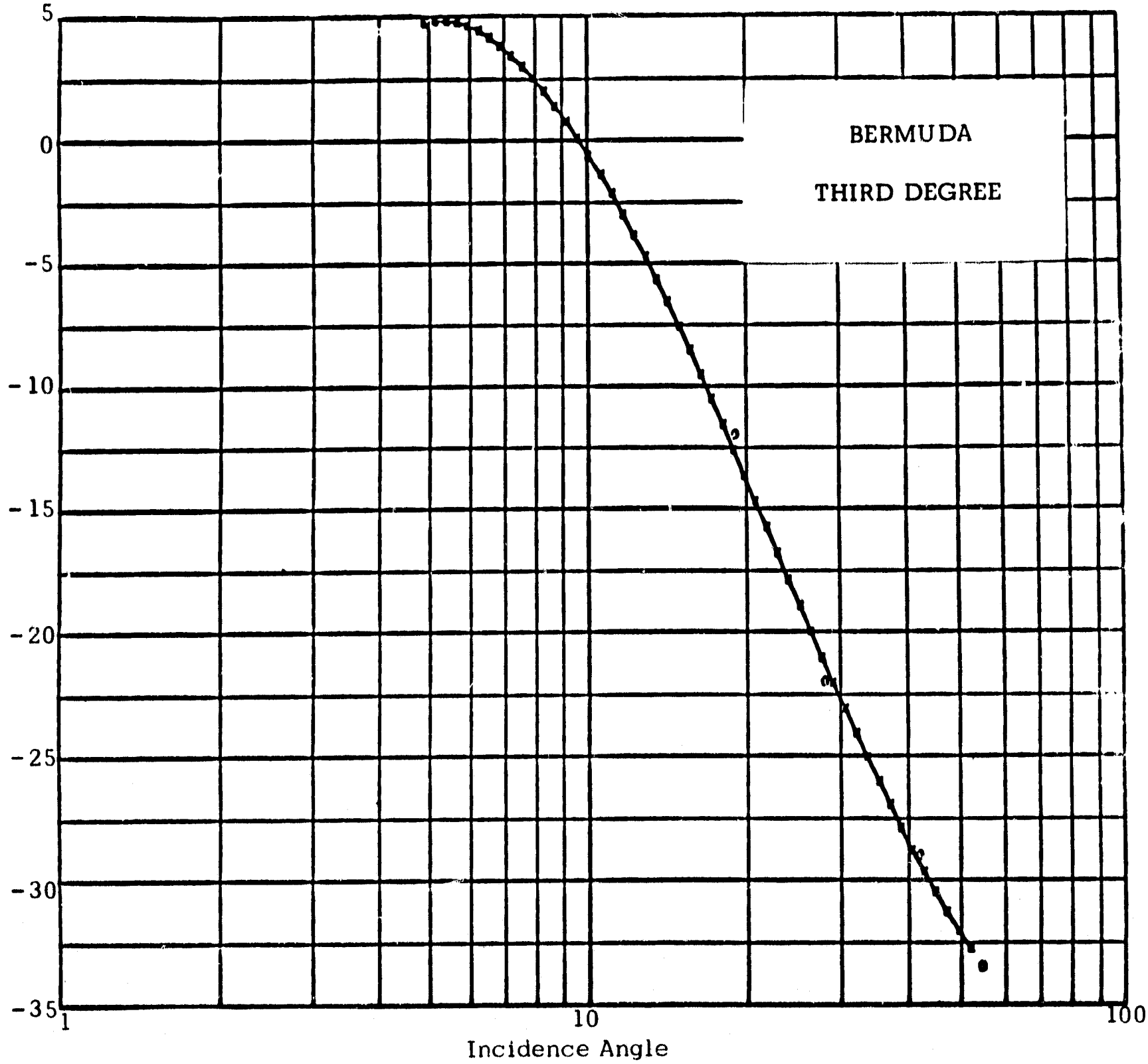
LEAST SQUARES CURVE FIT

Figure 81



POWER FUNCTION CURVE FIT

Figure 82



POWER FUNCTION CURVE FIT ON SEMI-LOG GRID

Figure 83

SECTION 6

SUMMARY

The results of the data analysis program are summarized in this section. Figure 84 is a summary of the detailed scatterometer lunar analog data displayed in the previous section. The solid curve is the average of all the lunar analog curves. The two dotted curves represent reflectivity data from the most diffuse and most specular areas analyzed.

The σ_o curves from the three areas that were selected by the ground truth team as being the best lunar analog sites showed close agreement with the σ_o curve from the Evans and Pettengill data (see Figure 85). The relief texture, color, particle size, particle distribution and sparse vegetation of these areas were considered by the ground truth team before selecting them as the best lunar analogs. Thus a high correlation was seen between terrain characteristics and reflectivity data.

Figure 86 shows a comparison of the average Scatterometer lunar analog, the Evans and Pettengill lunar data, the Surveyor I and III lunar data, and the LMLR Reflectivity Model. The measured reflectivity curves are higher than the LMLR model for all incidence angles. Thus it is recommended that the LMLR model be modified to agree more closely with the average value of the measured data.

A 3σ value for the range of values in the new LMLR model can be established from Figure 84 which shows the range of σ_o values encountered for lunar analog terrain.

6.1 Refinements in the New LMLR Model

The LMLR model can be further refined by comparing the slopes of the curves in Figure 86 and by evaluating the effects of altitude upon σ_o. The only significant difference in the four sets of measured data is the slightly greater slope of the Scatterometer data for the lunar analog terrain at incidence angles between zero and 15 degrees.

The lunar analog terrain was more smooth, more compact and more moist than the lunar surface. (Except for the lava beds, which were very rough and dry.) These factors are believed to account for the higher specular component of the radar return from the lunar analog surface. Figure 87 supports this assumption. The two pictures of the lunar surface photographed by Surveyor I show two important surface characteristics: (1) the lunar surface is rough compared to the exploratory wavelength (2.2 cm) and (2) the surface is partially covered with rough, rocky material. As can be seen, the environmental and gravitational characteristics of the moon have resulted in the surface being fluffy and rough. The reflectivity data from such terrain is expected to be less specular (i.e. return less signal at the smaller incidence angles) than the sandy areas on the earth which, due to weathering, moisture and gravity will return higher signals from incidence angles near the vertical.

The effects of altitude upon the LMLR model have not been precisely determined. The data analyzed does not show any variation

for altitudes above 1000 feet. A program is presently in progress to determine the characteristics of the σ_o curve for altitudes below 1000 feet. This program will assist in establishing the transients that will be encountered by the LM Landing Radar at low altitudes.

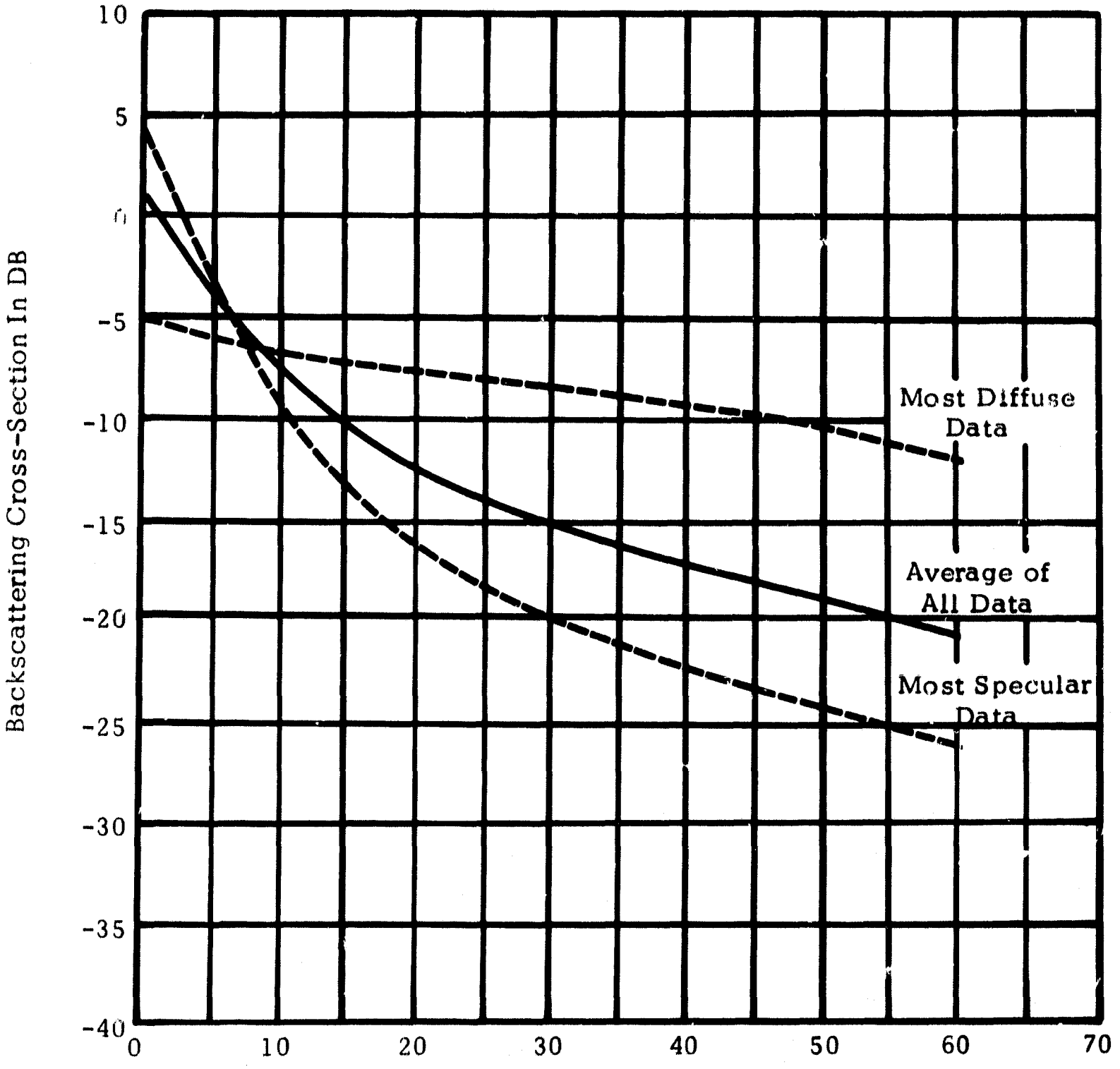


Figure 84 Range of Scatterometer Data

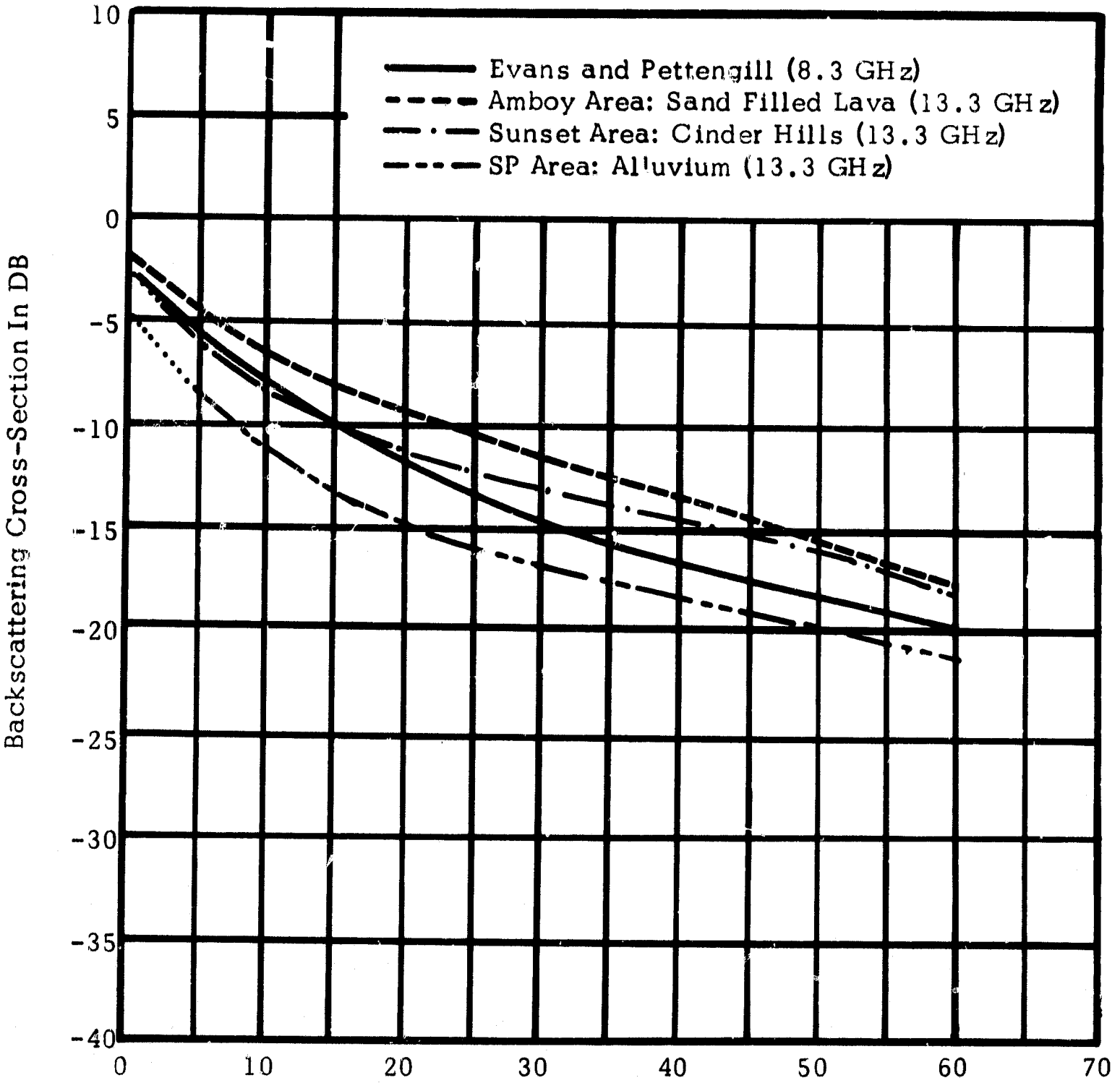


Figure 85 Comparison of Lunar Analog to Lunar Reflectivity Data

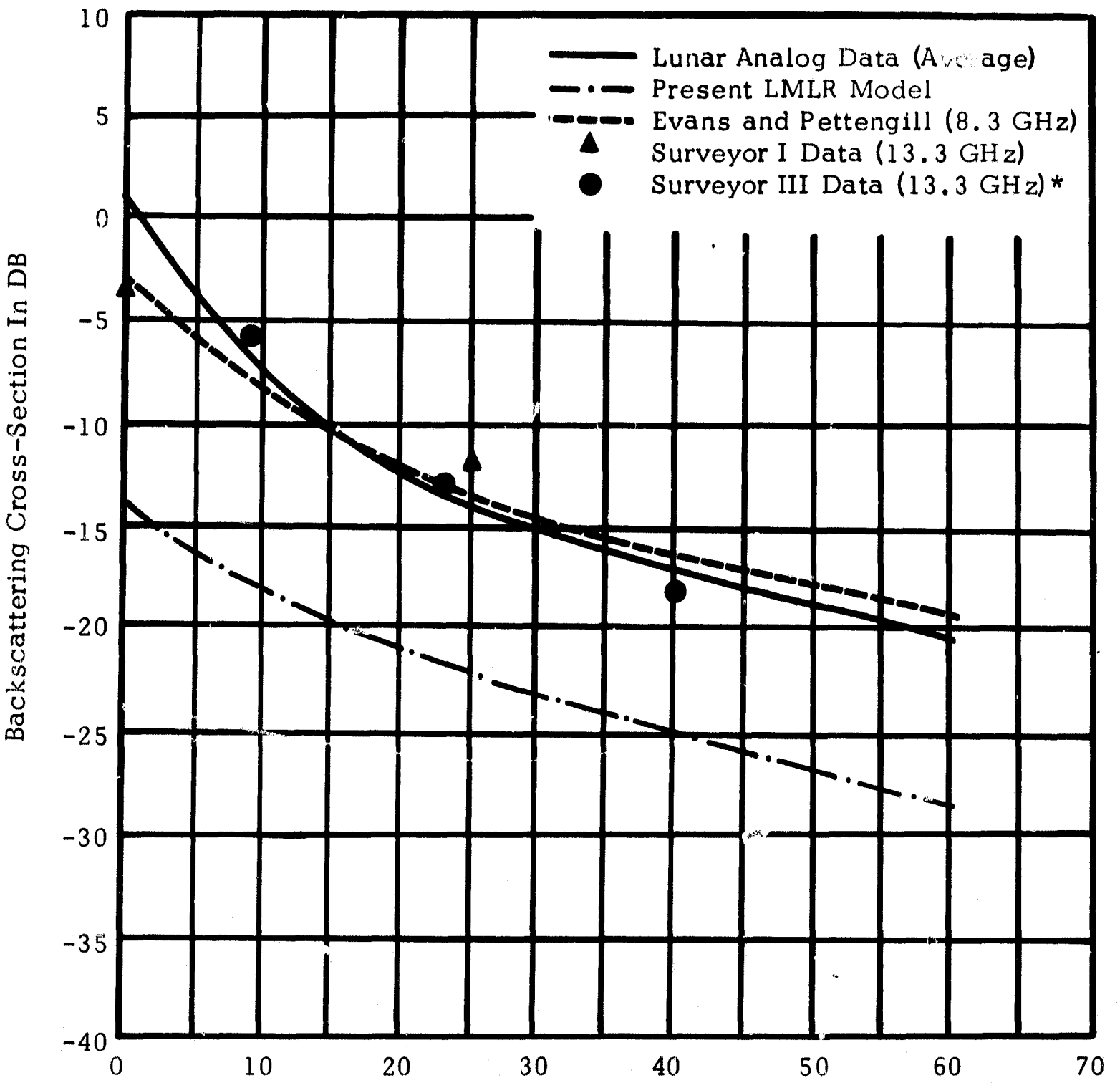


Figure 86 Comparison of Measured Data to LMLR Model

* Preliminary



Figure 87 Surveyor 1 Photos of Lunar Surface

SECTION 7

CONCLUSIONS AND RECOMMENDATIONS

This program has resulted in an improved reflectivity model for the LM Landing Radar for altitudes above 1000 feet. In addition, theoretical model studies have been performed to use for correlating the Scatterometer data with data from other sources and with ground truth information.

The data that have been the most valuable to this program are those missions where adequate ground truth information were available. This program has resulted in a better knowledge of the relative importance of the various parameters obtained by the ground trutn team.

It is recommended that the following study areas be considered for future programs associated with Scatterometer Data Analysis. A recognition of the need for these studies developed as a direct result of this program.

1. Low Altitude Reflectivity Study - The MSC Scatterometer has been installed on a helicopter and flights are being made at altitudes below 1000 feet. The data from these flights should be carefully analyzed to determine the exact properties of the signal return. This data must be carefully correlated with acoustical simulator and theoretical model data. Presently no satisfactory model exists for data below 1000 feet. Thus one of the most important

aspects of this study will be to develop a low altitude math model.

2. Application of Theoretical Models - The theoretical model studies performed during this program should be applied to a large volume of data to determine their usefulness as an analysis tool. This study should include, but not be limited to, analysis of specular return and doppler chirps.

3. Surface Reflectivity Range Study - It is recommended that a study and hardware development program be initiated to assist NASA in establishing a surface reflectivity test range. This range would consist of a multiple frequency reflectivity measuring system on an arch shaped track. This system could be used to measure reflectivity as a function of incidence angle, frequency, and polarization for various carefully controlled soil samples. In addition, soil penetration studies could be conducted.

4. Remote Sensor Test Range - It is recommended that a study be initiated to establish the optimum design of a test area for use in flight calibration of remote sensor systems.

5. Aircraft Instrumentation Study - It is recommended that a study be initiated to evaluate the flight instrumentation

on board the NASA 926 and 927 aircraft. The purpose of this study would be to recommend those changes in the aircraft instrumentation that will optimize data processing or improve measurement precision.

APPENDIX A

GLOSSARY OF GEOLOGIC TERMS

Aa Lava	A hardened lava sheet which is extremely rough. Its top is a chaotic assemblage of blocks and slag-like fragments, with innumerable sharp points.
Alluvium	Small fragmental particles; pebbles, sand etc., usually deposited on a plain from some higher terrain by errosion.
Basalt	A magma of low-silica content.
Blocks	Pieces of fragmental material blown out from a volcanic vent are called blocks if the pieces are larger than 1.25 inches in diameter and ejected as solid fragments and hence angular.
Cinder	Rough, slag-like fragment from a hundreth of an inch to an inch across, formed from magma blown into the air during a volcanic eruption.
Cinder Cone	Built exclusively or in large part of cinder size fragmented material formed and ejected during volcanic action. Parasitic to a major volcano, it seldom exceeds 1500 feet in height. Slopes of 30° to 40° are common.
Density	The weight (solids plus water) per unit of total volume of soil mass, irrespective of the degree of saturation.
Fissures	A narrow opening made by the parting of any substance.
Lava	Magma that has poured out onto the surface of the earth, or rock that has solidified from such magma.
Macrc Relief	As used herein, all relief that can be described in terms of feet, greater than one foot relief.
Magma	Molten material within the earth which through cooling and crystallization results in the formation of different types of rock.

Median Grain Size	The median point on a grain size distribution curve, which indicates the proportion of material of each grain size present in a given soil.
Micro Relief	As used herein, all relief that can be described in terms of inches, less than one foot relief.
Moisture Content	The ratio, expressed as a percentage, of: (1) the weight of water in a given soil mass, to (2) the weight of solid particles.
Olivine	A small group of ferromagnesian silicates that crystallize early from a magma and weather readily at the surface of the earth.
Pahoehoe Lava	A hardened lava flow with smooth surfaces, which have curious twisted, curved, and billowy forms.
Pressure Ridge	A ridge produced on a congealing lava flow by the continued movement of its liquid interior. Large open fissures along the crest with smaller fissures on the sides of the ridges are prominent features of the pressure ridges.
Soil Classification, (USDA).	The USDA soil classification classified gravel as anything over 2.0 mm in diameter; very coarse sand, 2.0 to 1.0 mm; coarse sand, 1.0 to 0.5 mm; medium sand, 0.5 to 0.25 mm; fine sand, 0.25 to 0.10 mm; 0.10 to 0.05 very fine sand; silt, 0.05 to 0.002 mm; and clay as anything smaller than 0.002 mm. in diameter.
Surface Bearing Capacity	The average load per unit of area required to produce failure by rupture of a supporting soil mass.
Tumuli	Lava flow features which are characteristically elongated domes that are elliptical in plan, roughly symmetrical in cross-section, and marked by prominent open fissures along the crest.

APPENDIX B

LIST OF SYMBOLS

SYMBOL	DEFINITION
B	Transmitter-receiver coupling factor
B_i	Bandwidth of the i^{th} analog reduction filter
BW	Port-Starboard antenna beamwidth
C	Climb angle
D	Doppler frequency
FMC	The 10KHz sideband power output constant of the ferrite modulator
f(t)	Time domain function of filter output
f_c	Filter center frequency
f_t	Filter output random variable
$f'(\theta)$	Two-way antenna pattern factor
G_f	Voltage gain of ferrite modulator
G_i	Voltage gain of the i^{th} analog reduction filter
G_o	Antenna gain
$G_o^2 f'(\theta)$	Product of the two-way antenna gain times the integral of the port-starboard beamwidth for any incidence angle
h	Radar Altitude
J	The Jacobian
K_i	Gain-bandwidth constant of i^{th} analog reduction filter

L_f	Ferrite modulator insertion loss
n	Summing index
P	Aircraft pitch angle
p(i)	Probability density function of the variable i
p(i, j)	Joint probability density function of variables i and j
P_M	Measured power density
P_m	Ferrite modulator sideband power
P_N	Noise power density
P_t	Transmitted power
P_S	Actual signal power density
$\overline{R}$	Roll angle
R(D)	Correction factor for the composite roll-off characteristic of the Scatterometer system
R(t), ϕ(t)	Envelope and phase angle time domain functions of filter output
R_t, ϕ_t	Envelope and phase angle random variables
V, Vg	Aircraft ground speed
V_c	Ferrite modulator coil voltage
V_f	Voltage output of the ferrite modulator
V_i	Voltage output of the i^{th} analog reduction filter
V_z	Vertical velocity of aircraft
W_s	Signal power density
X(t), y(t)	Orthogonal coordinates of f(t)
x_n, y_n	Coefficients of Fourier series of f(t)

$x(t)$, $y(t)$	Random variables which represent possible values of $x(t)$ and $y(t)$
θ	Incidence angle - measured from the nadir
θ_c	Incidence angle corrected for aircraft climb or glide
$\vec{\theta}_i$	Compound incidence angle
$\vec{\theta}_o$	Incidence angle for zero roll
λ	Transmitter wavelength
ϵ	Half bandwidth of notch filter
	Error in measured signal power
	Variance of the random variable i
(θ, ϕ)	Radar backscattering cross section per unit area at the compound angle (θ, ϕ)
$\hat{\sigma}_o$	Standard deviation of σ_o (θ) at each angle of incidence
$\frac{\Delta\sigma_o}{\sigma_o}$	The ratio of the error in sigma zero to sigma zero
	$2 \pi f_c$
ω_o	Fourier analysis frequency variable

APPENDIX C

SYSTEM TEST PROCEDURES

This Appendix presents the procedures to be used to operate, test, and maintain the Ryan REDOP installation on the NASA Convair 240 aircraft.

This procedure is designed to give assurance of proper system operation without excessive expenditure of time or unnecessary system operation. Because the klystron life is limited by the turn-on cycle, particular effort has been included to avoid needless operation of the klystron.

The system calibration schedule is to be a normal six-month cycle on all components. Because aircraft scheduling is critical, the aircraft schedule should be monitored and every effort made to correlate the calibration with a maintenance period of the aircraft to avoid loss of valuable data collection time. Intermediate checks are made by the REDOP Operational Ground Check to detect any variations which normally would not be detected in preflight or inflight operation. Klystron power, amplifier gains and signal quality are continuously monitored in flight and will detect a failure in the system as soon as it occurs.

C.1 PREFLIGHT PROCEDURE

The following paragraphs describe the procedure to be used to preflight the REDOP system.

1. Check the REDOP installation for correct connection. Secure connectors, and general appearance of all cables and components. (See Figure 88 for a block diagram of the system.)
2. Make the following settings on the REDOP components. Record the required information in the preflight section of the REDOP Mission Report Sheet. (See Figure 89).

Preamplifiers

Gain Setting - 40 db

Input Impedance - 10 K

Upper Bandpass Limit - 14 KC

Lower Bandpass Limit - 400 CPS if the flight is to be over land, 5.0 KC if the flight is to be over water.

Boost Amplifiers

Gain - X 100

Variable Gain - Maximum CCW

Master Power Control Panel

REDOP Power Switch - ON

Ballantine 302C

Voltage Setting - 10 volts full scale

Power - ON

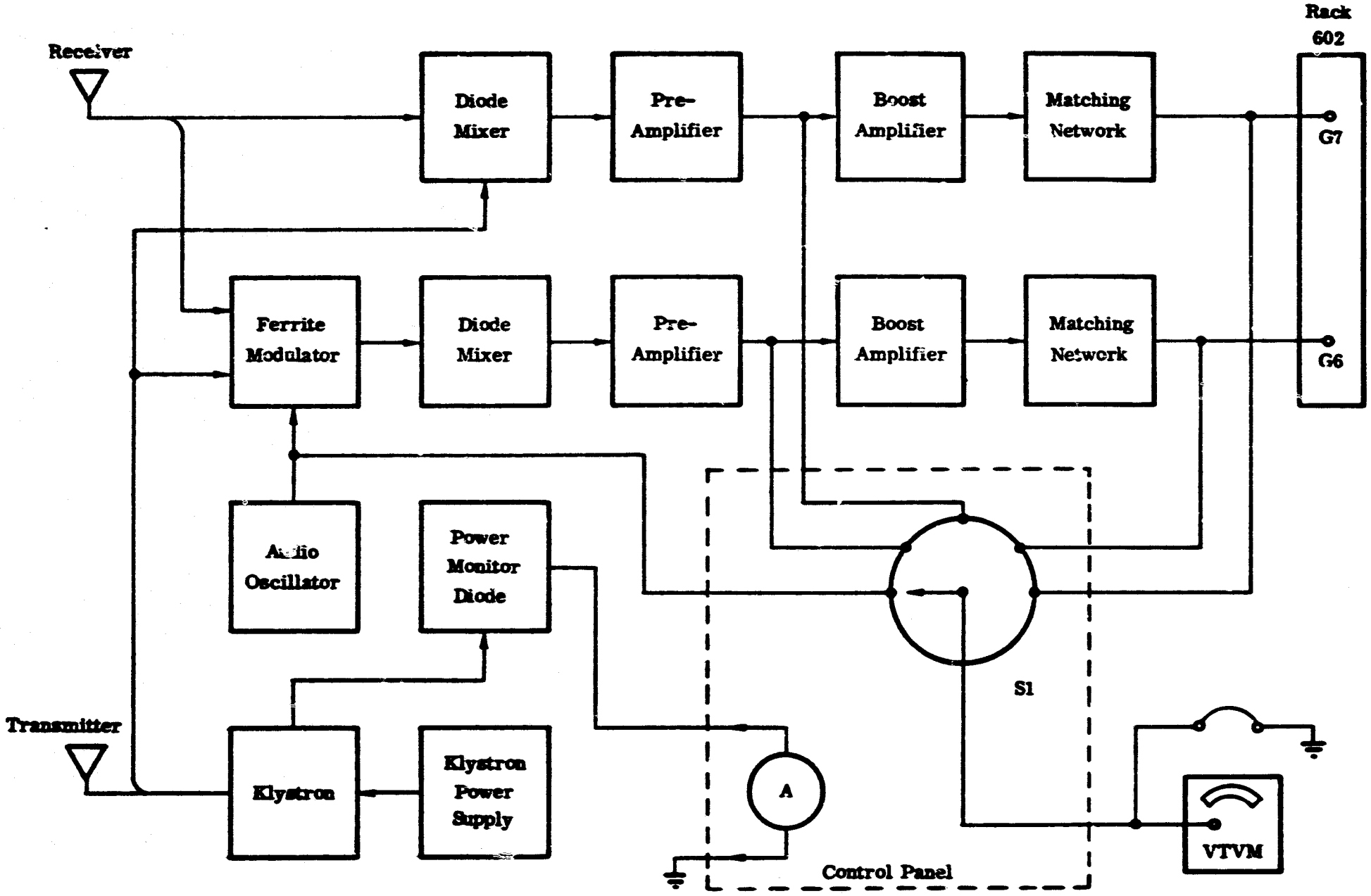


Figure 8 Ryan Redop System Block Diagram

REDOP MISSION REPORT SHEET

PREFLIGHT

Mission		Flight		Date	Time
Elapsed Time	Start		Stop	Voltmeter Batt.	
Preamp Batt.	#1		#2	Power Monitor	
Preamp #1	Input Z		Gain	Bandpass	Lower	Upper
Preamp #2	Input Z		Gain	Bandpass	Lower	Upper
Boost Amp #1 Gain				Boost Amp #2 Gain	

READINGS	Osc. OFF	Preamp.	#1	#2	Boost	#1	#2
	Osc. ON	Preamp.	#1	#2	Boost	#1	#2

Comments:

IN FLIGHT

LINE	RUN	TIME START	TIME STOP	GAIN	REMARKS

/s/ _____

Figure 89

REDOP Control Panel

Monitor Switch - Audio Oscillator position

Power - ON

Power Supply

Power - ON

CAUTION: DO NOT TURN POWER SUPPLY ON UNLESS BLOWER INDICATOR LIGHT ON REDOP CONTROL PANEL IS ON.

HP-241A Audio Oscillator

Power - OFF

3. Place the Ecco-sorb sheet over the antenna.

4. REDOP System Tests

   1. Adjust the High Voltage Adjust for a maximum reading on the Power Monitor Meter.

   2. Complete the tests necessary to fill in the Preflight section of the REDOP Mission Report Sheet (See Figure 89). The HP-241A Audio Oscillator will be turned on as indicated and the output adjusted for 10 KHz and 1.0 volts amplitude.

   3. Remove the Ecco-sorb from the antenna.

   4. Place the REDOP Monitor Switch in the Boost 1 position. Create movement of the aircraft by jumping. The doppler return should be detected in the headset and on the meter.

CAUTION: ALWAYS REMOVE THE HEADSET BEFORE CHANGING THE POSITION OF THE REDOP MONITOR SWITCH.

5. Place the REDOP Monitor Switch in the Boost 2 position. Create movement of the aircraft by jumping. The doppler return should be detected in the headset and on the meter.
6. Turn the Power Supply, Test Equipment, REDOP Control and REDOP Switches on Master Power Panel OFF.

C.2 IN-FLIGHT PROCEDURE

The following paragraphs describe the procedure to be used to operate the REDOP system.

C.2.1 Turn On Procedure

The following steps will turn the REDOP sytem ON:

1. Turn thw REDOP Power Switch ON.
2. Turn the Power Switch on REDOP Control Panel ON.
3. Turn the Power Supply ON.
4. Turn the Audio Oscillator and Ballantine 302C Voltmeter ON.
5. Place the REDOP Monitor Switch in the Audio Oscillator position.
6. Adjust the Audio Oscillator for a 10 KHz and 1.0 volt amplitude output.

7. Adjust the High Voltage on the Power Supply for a maximum reading on the Power Monitor Meter.

C.2.2 Data Acquisition Procedure

The following steps outline the procedure for Data acquisition:

1. Set the voltmeter at 1.0 volt full scale.
2. Place the REDOP Monitor Switch in the Boost 1 position.
3. Just before run begins, adjust the decade gain for the highest gain possible without exceeding 300 m V on the meter (if the tape recorder is set for $\pm$ 1 volt dc for $\pm$ 40% deviation, for higher tape recorder calibration use proportionately higher REDOP system output levels).
4. Place the REDOP Monitor Switch in the Boost 2 position
5. Place the Decade Gain of Boost Amplifier 2 to the same gain setting as Boost Amplifier 1.
6. Adjust the Variable Gain of Boost Amplifier 2 until the output on the meter is the same as the Boost 1 position.
7. Continually monitor the REDOP system in flight for an indication of a failure. This can be accomplished by the REDOP Monitor Switch, Power Monitor Meter, Signal Quality in the Headset and Oscilloscope presentation on the Tape Recorder Monitoring Oscilloscope. Keep the REDOP Mission Report Sheet up-dated.

8. When runs are complete, turn the Power Supply Test Equipment, REDOP Control and REDOP Switch on the Master Power Panel OFF.
9. Record the elapsed time meter reading in the REDOP Mission Report Sheet.
10. Record the required data for each run in the REDOP Mission Report Sheet.

C.3 Post-Flight Check

After each flight and prior to turning the equipment off:

1. Check the REDOP installation for secure connectors and general appearance of all cables and components.
2. Check for correct settings of the preamplifiers, boost amplifiers and audio oscillator.
3. Note any differences from intended conditions on mission flight log.

C.4 Operational Ground Check

The operational ground check is designed to give assurance of REDOP operation and calibration without removal from the aircraft. Any change in system parameters will be detected so that corrective action may be initiated if necessary. The operational ground check should be made at the following times.

1. Every 60 days or 100 hours of operation, whichever occurs first.
2. After each calibration of system components.

3. Any time a component of the system is removed for repair.

4. Any time a failure is suspected or abnormal operation is experienced.

C.4.1 List of Test Equipment

Simpson VOM

HP-241A Audio Oscillator

Ballantine 302C Voltmeter

HP-403B Voltmeter

Divider Probe, Millivac Instruments 10,000/1

Fairchild Oscilloscope

Ecco-sorb Sheet

NOTE: ALL EQUIPMENT EXCEPT THE DIVIDER PROBE IS INSTALLED AS PART OF THE REDOP SYSTEM OR THE NASA 926 AIRCRAFT SYSTEM.

C.4.2 Preliminary Connection of Test Equipment

A. Using the Divider Probe, connect the Audio Oscillator to the #1 Preamplifier. Connect the HP-403B Voltmeter to monitor the Audio Oscillator output.

B. Connect the oscilloscope to the Ballantine Voltmeter input.

C.4.3 Preliminary Settings of Equipment

1. Preamplifiers

   Input Impedance - 10 K

   Lower Bandpass Limit - 400 Hz

   Upper Bandpass Limit - 14 KHz

   Gain Setting - 40 db

2. Boost Amplifiers

   Gain - X 50

3. REDOP Monitor Switch in Boost Amplifier #1 position.

C.4.4 Operational Ground Check Procedure

1. Turn-on REDOP master power control switches, REDOP control panel power switch, Ballantine Voltmeter, H-P Voltmeter, audio oscillator and oscilloscope (Do not turn the Power Supply ON).
2. Adjust the audio oscillator for an output of 1.0 volt and a frequency of 1 KHz.
3. Note the reading of the output on the Ballantine meter. (This should be approximately 500 mV.) Also observe the amplitude and shape of the waveforms on the oscilloscope.
4. Increase the Boost Amplifier #1 decade gain to X 100. The meter and oscilloscope readings should double.

5. Decrease the Boost Amplifier #1 decade gain to X 30. The meter and oscilloscope readings should decrease 70%. Set the Boost Amplifier decade gain at X 50.

6. Keeping the Audio Oscillator output at 1.0 volt amplitude output, run a frequency response curve using the frequencies listed in the REDOP Operational Ground Check Sheet (See Figure 90).

7. Place the lower bandpass limit of Preamplifier #1 to 5 KC. Repeat the frequency response check as in step 6.

8. Repeat steps 2 through 7 for Channel 2.

9. Disconnect the test equipment and connect the system for normal operation.

10. Place the Ecco-sorb sheet over the antenna.

11. Turn the Power Supply ON. (All other equipment should already be ON.) Turn the High Voltage Adjust CCW until the stop is reached.

12. With the Simpson VOM, read the filament voltage. This should be 6.8 VDC. If necessary, adjust the filament voltage to 6.8 VDC with R11 on the power supply.

NOTE: THE FILAMENT VOLTAGE IS ADJUSTED TO 6.8 VDC TO ALLOW FOR LINE DROP IN THE FILAMENT LEADS. THE ACTUAL FILAMENT VOLTAGE AT THE KLYSTRON IS 6.3 VDC.

REDOP OPERATIONAL GROUND CHECK SHEET

Date:		Elapsed Time		Start	Stop		Voltmeter Batt.	
Preamp Batt.	#1	#2		Power Monitor				
Boost Amps.	Gain: X 100			Variable Gain: Max. CCW				
Preamps.	Input Z: 10K			Gain db: 40			Bandpass Limits: See Columns	
READINGS	Osc. OFF	Preamp.	#1	#2	Boost	#1	#2	
	Osc. ON	Preamp.	#1	#2	Boost	#1	#2	

Freq. in Hz	CHANNEL 1		CHANNEL 2	
	400 Hz & 14 KHz	5 KHz & 14 KHz	400 KHz & 14 KHz	5 KHz & 14 KHz
10				
20				
30				
40				
50				
60				
70				
80				
90				
100				
150				
200				
300				
400				
500				
700				
1K				
2K				
3K				
4K				
5K				
7K				
10K				
12K				
14K				
20K				

/s/ _____

Figure 90

13. Set the High Voltage Adjust for a maximum reading on the Power Monitor Meter.
14. Adjust the Audio Oscillator for 1.0 volt at a frequency of 10 KHz.
15. Make the readings indicated in the READINGS section of the REDOP Operational Ground Check Sheet.
16. Turn the Power Supply, Test Equipment, REDOP Control and REDOP Switches on Master Power Panel OFF.
17. Remove the Ecco-sorb sheet from the antenna.

C.5 In-Flight Preventive Maintenance

The in-flight maintenance is limited to replacement of fuses and tightening connectors. No replacement of parts or components should be accomplished.

C.6 Periodic Maintenance

The following periodic maintenance should be accomplished as indicated:

1. Every 90 days or 100 hours, whichever occurs first, lubricate the blower motors in the Boost Amplifier Rack Module. Use a MIL approved lightweight oil.
2. Every 90 days or 100 hours, whichever occurs first, perform an operation ground check as outlined in Section C.4.

3. Perform an operation ground check after any equipment repair or after a periodic calibration of the equipment.

4. Every six months remove all equipment and test equipment for calibration. The antennas, ferrite modulator, klystron and diodes shall be calibrated at the factory. All other units shall be calibrated at the MSC Calibration Laboratory.

5. Record all calibration data in the REDOP Calibration Log (See Figure 91).

C.7 Pre-Mission Tests

The purpose of these tests is to evaluate the performance of the scatterometer prior to each mission.

Preflight Procedure

The first pre-mission test to be performed on the equipment shall be the pre-flight procedure specified in Section C.1 of this Appendix.

In-Flight Procedure

The techniques specified in Section C.2 of this Appendix shall be used as the basic in-flight procedures during the pre-mission tests. The following additional information shall be recorded during the flight to expedite post-flight data evaluation:

REDOP CALIBRATION LOG

COMPONENT	SERIAL NUMBER	CALIBRATION		CALIBRATION		CALIBRATION		CALIBRATION	
		Due	Accomp.	Due	Accomp.	Due	Accomp.	Due	Accomp.
VS-64A	541								
VS-64A	560								
KIN-TEL 121A	PO-3902								
KIN-TEL 121A	PO-3903								
HVPS	1429								
HP-241A	43581								
HP-403B	49443								
BALLANTINE 302C	231830								
(SCOPE)	?								
ANTENNA ASSY.	-								
DIODE	1								
DIODE	2								
DIODE	3								
DIODE	4								
FERRITE	-								

Figure 91

(1) Aircraft ground speed

(2) Aircraft drift angle

(3) Radar Altitude

(4) Barometric altitude

(5) Pitch angle

(6) Roll angle

(7) Ground track angle

In addition, the following information shall be recorded: terrain, location, changes in terrain and sea state (for over water runs).

The flight shall be made at a relative (radar) altitude of 2000 feet. Both over land and over water runs should be made if at all possible. Runs should be made at aircraft cruise speed. Both upwind and down wind runs should be flown. Two sea states can normally be obtained by flying over Galveston Bay and then out over the Gulf. Care must be taken to note any ships or islands that are flown over as these will distort the σ_o curve. The over water runs shall start at least 30 seconds after leaving land. The length of all runs should be one minute.

It is desirable that the over land runs be flown above homogeneous terrain. It is also desirable that the terrain characteristics be affected as little as possible by seasonal variation. Therefore, it is recommended that an area covered entirely with pine trees be used.

REFERENCES

1. Barnes, F. A., "Radar Backscattering Coefficient for the Lunar Surface," RCA Report No. LTM-P-3600-4-9100-8, 28 June 1965.

2. Cooley, James W., "Applications of the Fast Fourier Transform Method," IBM Scientific Computing Smposium on Digital Simulation of Continuous Systems, June 1966.

3. Edison, A. R., "An Acoustic Simulator for Modeling Backscatter of Electromagnetic Waves," Tech. report EE-62, University of New Mexico Engr. Exp. Sta., Sept. 1961.

4. Evans, J. V., and G. H. Pettengill, "The Scattering of the Moon at Wavelengths of 3.6, 68, and 784 Centimeters,", J. Geophys, Res., V.68, 15 January 1963, pp. 423-447.

5. Nordmeyer, E. F. and Werner, R. A., "Terrain Quantification in Support of the IESD-RF Reflectivity Program," MSC Document 67-TH-3, July 1967.

6. Jaffe, L. D., et. al. "Surveyor 1 Mission Report, Part II. Scientific Data and Results," JPL Technical Report No. 32-1023, 10 September 1966.

7. Davies, H., "The Reflection of Electromagnetic Waves from a Rough Surface," Jour. IEE (London) pt. 4., Vol. 101, 209-215, August, 1954.

8. Moore, R. K., "Resolution of Vertical Incidence Radar Return Into Random and Specular Components," Tech. Report EE-6, Univ. of New Mexico Engr. Exp. Sta., July, 1957.

9. Daniels, F. B., "A Theory of Radar Reflection from the Moon and Planets," J. Geophys. Res., Vol. 66, p. 1787, 1961.

   Daniels, F. B., "Radar Determination of the Root Mean Square Slope of the Lunar Surface," J. Geophys. Res., Vol. 68, p. 449, 1963.

10. Fung, A. R., "Scattering Theories and Radar Return," Univ. of Kansas Eng. Science Division, Lawrence, Kansas, Report #48-3.

11. Hagfors, T., "Some Properties of Radio Waves Reflected from the Moon and Their Relation to the Lunar Surface," J. Geophys. Res., Vol. 66, No. 3, P. 777, March 1961.

Hagfors, T., "Backscatter from an Undulating Surface with Applications to Radar Returns from the Moon." J. Geophys. Res., Vol. 69, pp. 3779-3784, 1964.

12. Beckmann, P., "Scattering by Composite Rough Surfaces," Proc. IEEE, August 1965, pp. 1012-1025.

13. Hayre, H. S., "Radar Back-Scatter Theories for Near Vertical Incidence and Their Application to an Estimate of the Lunar Surface Roughness." Tech. Report EE-67, Univ. of New Mexico Engr. Exp. Sta., January, 1962.

14. Moore, R. K., "Resolution of Vertical Incidence Radar Return Into Random and Specular Components." Tech. Report EE-6, Univ. of New Mexico Engr. Exp. Sta., July, 1957.

15. Davies, H. "The Reflection of Electromagnetic Waves from a Rough Surface." Jour. IEE (London) pt. 4., Vol. 101, P. 209-215, August 1954.

16. Hayre, H. S., "Radar Back-Scatter Theories for Near Vertical Incidence and Their Application to an Estimate of the Lunar Surface Roughness." Tech. Report EE-67, Univ. of New Mexico Engr. Exp. Sta., January, 1962.

17. Brown, W. E., Jr., "A Lunar and Planetary Echo Theory." Jour. Geophys. Res., Vol. 65, 3087-3095, October, 1960.

18. Welch, P. D., "Interpretation and Prediction of Radar Terrain Return Fading Spectra." Progress Report AER-14W, New Mexico College of Agr. and Mechanic Arts, May 25, 1955. Sandia Corp. Reprint SCR-212, July, 1960.

19. Warner, B. D., "Radar Terrain Return from the Sperical Earth at Near-Vertical Incidence," Tech. Report No. EE-46, Univ. of New Mexico Engr. Exp. Sta., May, 1961.

20. Glascock, R. B., "Design of an Experiment to Separate Specular and Scattered Radar Returns." Tech. Report EE-9, Univ. of New Mexico Engr. Exp. Sta., May, 1958.

21. Twersky, V., "On Scattering and Reflection of Electromagnetic Waves by Rough Surfaces." IRE Trans., PGAP, Vol. AP-5, 81, 1957.

22. Basore, B. L., "The Impulse Response of a Reflecting Surface." Report OTR-4, The Dikewood Corp., Albuquerque, New Mexico, January, 1962.

23. Cosgriff, R. L., W. H. Peake, and R. C. Taylor, "Terrain Scattering Properties for Sensor System Design," Terrain Handbook II, Engr. Exp. Sta., Ohio State Univ., Awetwa Lab., Columbus, Ohio, May, 1960.

24. Katz, I. and L. M. Spectner, Radar Terrain Return: "A Theoretical Model, 1959 Radar Return Symposium, U. S. Naval Ordnance Test Station and the University of New Mexico Engr. Exp. Sta., May 1959.

25. Beard, C. I., I. Katz, and L. M. Spetner, "Phenomenological Vector Model of Microwave Reflections from the Ocean," IRE Trans., PGAP, Vol. AP-4, 162-167, April, 1956.

26. Beard, C. I., "Coherent and Incoherent Scattering of Microwaves from the Ocean," IRE Trans. PGAP, Vol. AP-9, 470-483, September, 1961.